Dynamics of the Subpolar North Atlantic Ocean Circulation—the Role of Surface Forcing and Topography



James Boneham

Linacre College

University of Oxford

A thesis submitted for the degree of

Doctor of Philosophy

Michaelmas 2022

Acknowledgements

First and foremost, I thank my supervisors David Marshall and Helen Johnson for their advice, encouragement and endless enthusiasm. I have lost count of the number of meetings we have had where I have gone in feeling stuck or listless, and left re-energised. I will always be grateful for the kindness they have shown me over the past four years. I still cannot believe my luck in having not one but two such supportive supervisors.

I am grateful to many members of the Oxford Atmospheric, Oceanic, and Planetary Physics department, who have been immensely generous with their time and effort in helping me at various points over the past few years. Thanks go, in particular, to Andrew Wells, but also to Philip Stier, Antje Weisheimer, and Myles Allen, among others.

I thank all the friends I have made in Oxford for keeping me sane over the years. Thanks especially to Alex, Abbie and Andrew for all their support (and for tolerating my messiness). To my parents, Carol and David, and to my siblings, Harry and Alice, thank you for keeping me going whenever I felt I was stalling. Finally, special thanks to the late Catherine Dendy, whose guidance I could always rely on.

Funding

This work was supported by the Natural Environmental Research Council (NERC)

Abstract

The ocean is a fundamental component of the global climate system, acting as a colossal sink of heat and carbon dioxide. Its effectiveness as a sink is enhanced by the transport of these tracers into the deep ocean by the Atlantic Meridional Overturning Circulation (AMOC). Hence, due to its location near the northern terminus of the AMOC, the subpolar North Atlantic plays a crucial role within the global climate system. Unfortunately, this is a fiendishly difficult region to model. As such, a better understanding of the physical mechanisms setting the large-scale flow at these latitudes is required.

In this thesis, the roles played by wind stress, surface buoyancy forcing, and topography in determining the mean barotropic and overturning circulations in the subpolar North Atlantic Ocean are explored. An idealised model of the region is introduced, and the response of the mean circulation to different combinations of wind, buoyancy forcing and bathymetry is presented. The overturning circulations in both depth, and density, space are split into shear, Ekman, and external mode components.

A novel diagnostic is then derived allowing for the isolation of the force balances controlling the large-scale flow. This diagnostic is based on the previously proposed rotational momentum framework, whereby the rotational component of an applied force is extracted in the form of a set of *force functions*. An error in the original derivation of this framework is highlighted which limits its utility to domains without topography. A new derivation generalising the approach to apply to domains with arbitrary topography is presented, and the derived force functions are related to the barotropic and overturning circulations.

This diagnostic is then applied to the aforementioned experiments, allowing the dominant force balances in each to be identified. A key result emerging from this analysis is that the presence of sloping sidewalls drastically alters the dominant force balance in the mean barotropic circulation.

Contents

Acknowledgements ii

Abstract iii

Contents iv

List of Figures vii

List of Abbreviations ix

1 Introduction 1
1.1 The AMOC . . . 1
1.2 The Subpolar North Atlantic . . . 4
1.3 Understanding Subpolar Ocean Circulation . . . 6
1.4 Rotational Momentum Balance . . . 10
1.5 Thesis Outline . . . 12

2 Model 13
2.1 Introduction . . . 13
2.2 MITgcm . . . 15
2.2.1 Approximated Equations of Motion . . . 15
2.2.2 Mixing Parametrisations . . . 17
2.2.3 Grid Geometry . . . 20
2.2.4 Notation and Discretised Operators . . . 22
2.3 An Idealised Model of the Subpolar North Atlantic . . . 25
2.3.1 Model Configuration . . . 25
2.3.2 Control State . . . 29
2.4 Summary . . . 35

3 Decomposing the Subpolar AMOC Subject to Different Forcings 36
3.1 Subpolar Overturning . . . 36
3.1.1 Depth Space vs. Density Space . . . 38
3.1.2 The Importance of Topography . . . 41
3.2 Decomposition of the AMOC . . . 43

3.2.1 Shear Component . . . 45
3.2.2 Ekman Component . . . 47
3.2.3 External Mode Component . . . 47
3.2.4 Numerical Implementation of Decomposition . . . 49
3.3 Numerical Sensitivity Experiments . . . 51
3.3.1 Horizontal Gyre Circulation . . . 52
3.3.2 Overturning in Depth Space . . . 55
3.3.3 Overturning in Density Space . . . 60
3.4 Summary . . . 65

4 Rotational Momentum Equation Decomposition 67
4.1 Introduction . . . 67
4.2 The Rotational Momentum Equation . . . 69
4.3 Boundary Conditions . . . 72
4.3.1 Helmholtz Decomposition . . . 73
4.3.2 The Surface & Bottom Boundaries . . . 77
4.4 Overturning and Barotropic Force Functions . . . 78
4.5 Finding the Overturning Force Functions . . . 80
4.6 Finding the Barotropic Force Function . . . 81
4.7 Simplifying the Forcing Terms . . . 87
4.7.1 Eliminating 3-D Differential Operators . . . 87
4.7.2 Horizontal and Vertical Forces . . . 90
4.8 Boundary Condition on Barotropic Force Function . . . 92
4.9 Relating Force Functions to Transport Streamfunctions . . . 96
4.9.1 Overturning Circulation . . . 96
4.9.2 Barotropic Circulation . . . 98
4.9.3 Barotropic Potential Vorticity Equation and JEBAR . . . 99
4.10 Summary . . . 100

5 Application of Decomposition to Sensitivity Experiments 103
5.1 Introduction . . . 103
5.2 Numerical Implementation . . . 104
5.2.1 Solving for the Overturning Force Functions . . . 104
5.2.2 Solving for the Depth-Integrated Force Function . . . 105
5.2.3 Further Decomposition of the Barotropic Rotational Momentum Equation . . . 109
5.3 Rotational Momentum Balance of the Barotropic Circulation . 114
5.4 Rotational Momentum Balance of the Overturning Circulation 120
5.4.1 The Overturning Force Function . . . 120
5.4.2 The Overturning Circulation in Depth Space . . . 128

5.4.3 The Overturning Circulation in Density Space 136
5.4.4 Shear and External Mode Components 144
5.5 Summary 148

6 Conclusions 150
6.1 Summary 151
6.2 Future Work 157
6.3 Concluding Remarks 159

References 161

List of Figures

1.1 Schematic of the AMOC . . . 2
1.2 Schematic of currents in subpolar gyre . . . 5
1.3 Schematic illustrating net rotational force . . . 11

2.1 Schematic of Arakawa C-grid continuity cell . . . 21
2.2 Schematics illustrating vertical grid structure . . . 22
2.3 Model Configuration . . . 27
2.4 Relaxation temperature profiles . . . 28
2.5 Control Ψ_{BT} . . . 30
2.6 Control $\Psi^{(z)}_{\mathrm{MOC}}$ . . . 32
2.7 Control flow field . . . 34

3.1 Mean velocity and potential density across the OSNAP section . . . 37
3.2 Schematic highlighting difference between overturning in depth and density space . . . 40
3.3 Schematic showing overturning due to barotropic circulation in presence of topography . . . 43
3.4 Full Ψ_{BT} for different model configurations . . . 53
3.5 Surface flow field for different spun-up model configurations . . . 54
3.6 Full $\Psi^{(z)}_{\mathrm{MOC}}$ for different model configurations . . . 56
3.7 Shear component of $\Psi^{(z)}_{\mathrm{MOC}}$ for different model configurations . . . 57
3.8 External mode component of $\Psi^{(z)}_{\mathrm{MOC}}$ for different model configurations . . . 58
3.9 Ekman component of $\Psi^{(z)}_{\mathrm{MOC}}$ for different model configurations . . . 61
3.10 Full $\Psi^{(\rho)}_{\mathrm{MOC}}$ for different model configurations . . . 61
3.11 Shear component of $\Psi^{(\rho)}_{\mathrm{MOC}}$ for different model configurations . . . 63
3.12 External mode component of $\Psi^{(\rho)}_{\mathrm{MOC}}$ for different model configurations . . . 64
3.13 Ekman component of $\Psi^{(\rho)}_{\mathrm{MOC}}$ for different model configurations . . . 65

4.1 Schematic illustrating decomposition of force into rotational and divergent parts . . . 68

5.1 Different methods of calculating HA^{BT} . . . 108

5.2 Two ways of obtaining HA^{BT} for buoyancy force 109
5.3 Closure of the rotational momentum equation 110
5.4 Decomposition of HA^{BT} into topography-independent and topography-dependent terms 113
5.5 HA^{BT} for vertical sidewalls configuration 115
5.6 HA^{BT} for no-buoyancy-forcing configuration 117
5.7 HA^{BT} for no-wind-stress configuration 118
5.8 HA^{BT} for control configuration 120
5.9 $A^{\mathrm{OT}x}$ for control configuration 124
5.10 $A^{\mathrm{OT}x}$ for no-wind-stress configuration 125
5.11 $A^{\mathrm{OT}x}$ for no-buoyancy-forcing configuration 126
5.12 $A^{\mathrm{OT}x}$ for vertical sidewalls configuration 127
5.13 $\partial \Psi^{(z)}_{\mathrm{MOC}} / \partial t$ in vertical sidewalls configuration 129
5.14 $\partial \Psi^{(z)}_{\mathrm{MOC}} / \partial t$ in no-buoyancy-forcing configuration 131
5.15 $\partial \Psi^{(z)}_{\mathrm{MOC}} / \partial t$ in no-wind-stress configuration 134
5.16 $\partial \Psi^{(z)}_{\mathrm{MOC}} / \partial t$ in control configuration 135
5.17 $\partial \Psi^{(\rho)}_{\mathrm{MOC}} / \partial t$ in vertical sidewalls configuration 137
5.18 $\partial \Psi^{(\rho)}_{\mathrm{MOC}} / \partial t$ in no-buoyancy-forcing configuration 139
5.19 $\partial \Psi^{(\rho)}_{\mathrm{MOC}} / \partial t$ in no-wind-stress configuration 141
5.20 $\partial \Psi^{(\rho)}_{\mathrm{MOC}} / \partial t$ in control configuration 142
5.21 Decomposition of $\partial \Psi_{\mathrm{MOC}} / \partial t$ for Coriolis force in control configuration 145
5.22 Decomposition of $\partial \Psi_{\mathrm{MOC}} / \partial t$ for wind stress in control configuration 146
5.23 Decomposition of $\partial \Psi_{\mathrm{MOC}} / \partial t$ for viscosity in control configuration 147

List of Abbreviations

AMOC	Atlantic Meridional Overturning Circulation
GCM	General circulation model
GM	Gent-McWilliams (eddy parametrisation scheme)
JEBAR	Joint effect of baroclinicity and relief
KPP	K-profile parametrisation (of surface mixing)
LSW	Labrador Sea Water
MITgcm	Massachusetts Institute of Technology general circulation model
NADW	North Atlantic Deep Water
OSNAP	Overturning in the Subpolar North Atlantic Program
RAPID	Rapid Climate Change Programme
SST	Sea surface temperature

1 Introduction

1.1 The AMOC 1
1.2 The Subpolar North Atlantic 4
1.3 Understanding Subpolar Ocean Circulation 6
1.4 Rotational Momentum Balance 10
1.5 Thesis Outline 12

1.1 The Atlantic Meridional Overturning Circulation

The Atlantic Meridional Overturning Circulation (AMOC) is the zonally-integrated northward flow of warm surface waters (the upper limb of the AMOC), with a return flow of cold, dense water at depth (the lower limb). This zonally-integrated, two-dimensional, view of the AMOC, however, hides the true three-dimensional nature of the overturning circulation—shown schematically in Figure 1.1.

Warm water crosses the equator on the western boundary of the Atlantic basin in the North Brazil Current. North of the Caribbean Sea, this northward flow joins the North Atlantic subtropical gyre and continues along the eastern seaboard of the United States as part of the Gulf Stream, until it reaches Cape Hatteras, where it separates from the coast and continues northeast, while the coastline curves back to the west. When it reaches the Grand Banks off

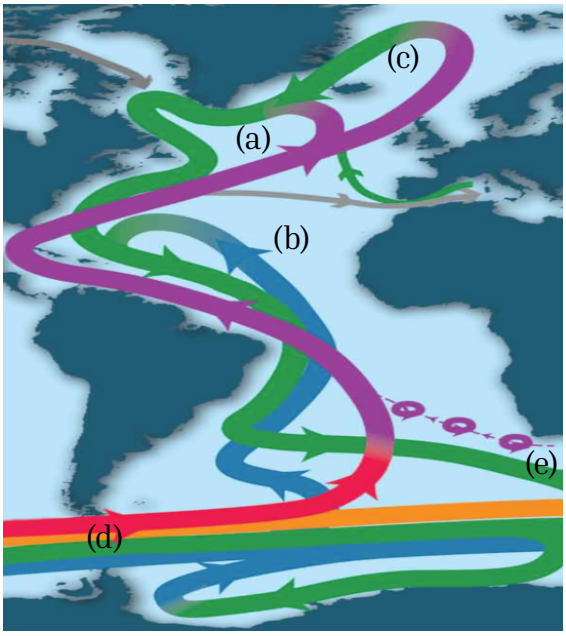


FIGURE 1.1: Schematic of the Atlantic Meridional Overturning Circulation, adapted from Talley (2013). The arrows show the main pathways for constituent currents of the AMOC. Purple indicates upper-ocean water, green indicates North Atlantic Deep Water, blue indicates Antarctic Bottom Water, and (for completeness) orange indicates Indian/Pacific Deep Water. The subpolar gyre **(a)**, subtropical gyre **(b)**, Nordic Seas **(c)**, Drake Passage **(d)** and Cape Agulhas **(e)** are all shown.

the coast of Newfoundland, the Gulf Stream meets the Labrador Current at the southern extent of the subpolar gyre, forming the North Atlantic Current. The North Atlantic Current separates the subpolar and subtropical gyres as it flows northeast across the Atlantic basin (Buckley and Marshall 2016).

This warm current splits as it enters the subpolar basin. Some of this water continues into the Nordic Seas, where it undergoes vigorous buoyancy loss. The transformed water returns over the Greenland-Scotland ridge either as Denmark Strait Overflow Water to the west of Iceland, or as Iceland-Scotland Overflow Water to the east. These overflow waters form the densest components of the lower limb of the AMOC, and make their way around the gyre in a deep boundary current along the coast of Greenland and subsequently around the Labrador Sea (Quadfasel and Käse 2007). The upper limb water that does not enter the Nordic Seas recirculates in the subpolar gyre. As it recirculates, it undergoes transformation by convection and mixing, forming

Labrador Sea Water (LSW)—the shallowest water mass in the dense lower limb of the AMOC (Lozier et al. 2017). Collectively, these cold, dense water masses in the AMOC lower limb are referred to as North Atlantic Deep Water (NADW).

The balancing transformation of cold, dense, lower-limb water back into upper-ocean, thermocline waters occurs primarily in the Southern Ocean. The strong westerly winds and associated northwards Ekman transport bring deep water to the surface adiabatically along sloping isopycnals that outcrop in these latitudes (Buckley and Marshall 2016). This acts to steepen these isopycnals and the resultant baroclinic instability induces a strong opposing meridional eddy transport (Marshall and Speer 2012). The residual of these opposing overturning transports forms the southern end of the global meridional overturning cell.

In addition, some of the southward flowing lower limb water is transformed into Antarctic Bottom Water in the Southern Ocean, and is subsequently diapycnally upwelled (Talley 2013). Waters upwelled in the Pacific and Indian Oceans then re-enter the Atlantic, either through the Drake Passage, or around Cape Agulhas via the Agulhas Leakage (Garzoli and Matano 2011). A small fraction of southward-flowing NADW upwells within the Atlantic itself (Cimoli et al. 2022).

The AMOC is of fundamental importance to global climate: the overturning cell extends from the high latitudes of the North Atlantic into the Southern Ocean. Consequently, it carries warm water and heat northwards in both hemispheres. This leads to a convergence of heat in the northern hemisphere, as the AMOC carries around 0.5PW of heat across the equator (Marshall et al. 2013). As a result of this heat convergence, surface air temperatures in the North Atlantic can be as much as 3 degrees warmer than corresponding latitudes in the North Pacific, which lacks a sustained cross-equatorial overturning cell (Feulner et al. 2013).

The process of NADW formation allows the North Atlantic to function as a conduit for transferring heat and carbon into the deep ocean. The air-sea flux of CO2 in the North Atlantic accounts for 41% of the global total (Takahashi et al. 2009), and the North Atlantic is the most intense sink for anthropogenic

carbon on the planet per unit area (McKinley et al. 2017). As most NADW is formed in the regions comprising (or directly linked to) the subpolar latitudes of the North Atlantic, it is therefore not surprising that conditions in this region can have a profound effect on both ocean heat and carbon uptake. For example, Desbruyères et al. (2016) find from hydrographic data that, due to changes in the rate of NADW formation in the subpolar North Atlantic, this was the only region in the global ocean to oppose the global mean warming trend in the deep ocean over the period from 1991 to 2010. Also, Watson et al. (2011) attribute the observed decrease in strength of the North Atlantic carbon sink over a similar period to a decline in the size and strength of the subpolar gyre and hence a lower rate of deep convection within the gyre.

The climatic impacts of the AMOC are not limited to heat and carbon uptake. Variability in the AMOC is one of the key drivers of Atlantic Multidecadal Variability (AMV; see Zhang et al. 2019, for a review). Through its connection to North Atlantic sea surface temperature (SST) anomalies, the AMOC has a wide range of impacts on European weather and climate (Josey et al. 2018). For example, these SST anomalies can influence summer precipitation (Dunstone et al. 2018) and heat waves (Duchez et al. 2016) over Europe, as well as the frequency and intensity of Atlantic hurricanes (Klotzbach et al. 2015; Yan et al. 2017).

Two of the strong surface current constituents of the AMOC flow along the densely populated—and economically important—east coast of North America: the Labrador Current and the Gulf Stream. It is unsurprising therefore, that changes in the strength of the overturning circulation are predicted to impact sea level along this coastline, with a decrease in AMOC transport associated with an increase in sea level in both model simulations and observations (Little et al. 2019).

1.2 The Subpolar North Atlantic

The transformation of water from the upper limb of the AMOC to the lower limb occurs in the high latitudes of the North Atlantic, and hence the subpolar North

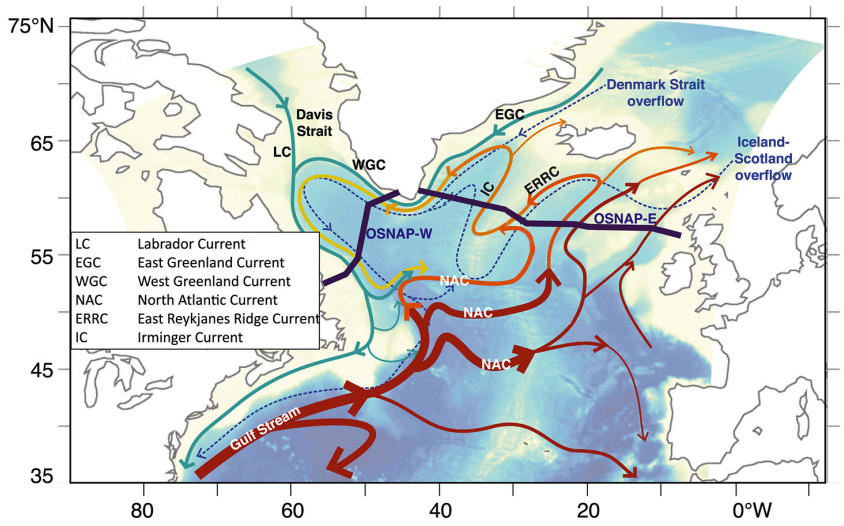


FIGURE 1.2: Schematic—adapted from Holliday et al. (2018)—showing the regional circulation of the subpolar North Atlantic, as well as the location of the two sections of the OSNAP array. The dashed lines indicate overflow waters.

Atlantic circulation, shown in Figure 1.2, plays a central role in the overturning circulation. Buoyancy loss of the upper-limb waters occurs in the surface layer all along the flow path, but is most intense in certain distinct regions of deep convection, for example the Labrador, Greenland, and Irminger Seas (e.g., Petit et al. 2021; Pickart et al. 2003; Marshall and Schott 1999).

Although water is transformed in the interior of these marginal seas by the above convective process, there is very little net downwelling in these convective regions or in the basin interior as a whole (Send and Marshall 1995; Spall and Pickart 2001). Instead, the downwelling occurs primarily in a narrow boundary layer with a width that scales with the deformation radius (Pedlosky 2003; Spall 2003), and therefore within the boundary current. The transformed water in the basin interior is exchanged via eddies with the boundary current, which provides the source of buoyancy to balance the buoyancy loss to the atmosphere in the interior. This eddy flux of heat into the boundary current reduces property gradients between the current and the interior and therefore requires downwelling within the boundary current to remain in geostrophic balance (Straneo 2006). From the thermal wind relation, the vertical shear in the boundary current velocity is proportional to the density gradient between

the boundary current and the interior. Therefore, as this density gradient decreases along the flow path, the vertical shear in the boundary current velocity must also decrease—and hence the current becomes more barotropic—to remain geostrophically balanced. This barotropisation of the boundary current implies a net downwelling, and so the erosion of density gradients between the boundary current and the interior generates a net downwelling within the boundary current.

The traditional view of NADW export is that NADW formed in the high latitudes is exported to the subtropics through the DWBC. Tracer experiments have confirmed that young deep water is present in higher concentrations in the DWBC than in the ocean interior: Rhein et al. (2015), for example, find from tracer concentrations that southward transport of young LSW in the DWBC at 26°N is still 39% of its formation rate. There is evidence from both float experiments (Lozier et al. 2022; Bower et al. 2019; Bower et al. 2011) and model studies (Gary et al. 2011; Lozier et al. 2013), however, that a significant proportion of NADW exported from the subpolar gyre to the subtropics is transported southwards via interior pathways.

1.3 Understanding Subpolar Ocean Circulation

Measuring the overturning circulation directly is challenging. Due to its fully three-dimensional structure it is not feasible to directly measure current strength over large spatial regions. As such, measurements of overturning are generally based around the taking of two density profiles and subsequent integration of the thermal wind balance to infer the zonally-integrated meridional transport between the two profiles (McCarthy et al. 2020). As this approach only yields the geostrophic shear, a reference velocity, as well as the ageostrophic Ekman flow, must be evaluated by other means.

The overturning circulation can be calculated as a cumulative integral either over depth, in which case it is a measure of Eulerian upwelling and downwelling, or over density, giving a measure of transformation between

density classes. In regions where the two differ substantially, the latter framework is a more appropriate measure of the strength of the AMOC (Lozier et al. 2019). In the subtropical North Atlantic, isopycnals and isobaths are broadly parallel, and so it is generally sufficient to measure overturning in depth space, which greatly simplifies the calculation of the overturning (Hirschi and Marotzke 2007). At subpolar latitudes, however, the zonal tilt of isopycnals across the basin and complex regional bathymetry mean that the overturning calculated in depth space differs significantly from that calculated in density space (Frajka-Williams et al. 2019). The overturning must therefore be calculated in density space to provide an accurate picture of transformation between density classes, making inferral of the geostrophic transport far more difficult (Waldman et al. 2021).

The approach outlined above forms the basis for the subtropical RAPID array at 26°N (McCarthy et al. 2015) and the subpolar OSNAP array (Lozier et al. 2017), comprising one section from Labrador to Greenland and one from Greenland to Scotland. In both observational programmes, current strengths on the boundaries are measured directly, with the geostrophic transports across the basin interiors inferred from density profiles as outlined above. The location of the OSNAP array is shown in Figure 1.2.

The deployment of the RAPID array provided continuous observations of the subtropical AMOC where previously only snapshots had been available (with the exception of the Gulf Stream transport through the Florida Straits, which has been continuously monitored via submarine cables since 1982; Baringer and Larsen 2001). The data from the RAPID array motivated a flurry of studies, resulting in a far clearer understanding of the strength and variability of the AMOC in the subtropical North Atlantic (e.g., Srokosz and Bryden 2015; Zhao and Johns 2014; Jackson et al. 2016; Smeed et al. 2018).

Following on from the success of the RAPID programme, the OSNAP observing system was deployed in the subpolar North Atlantic aiming to provide a similar leap in our understanding of subpolar overturning. Early results

revealed a subpolar AMOC dominated by watermass transformation to the east of Greenland, not in the Labrador Sea as had previously been thought (Lozier et al. 2019). Subsequent studies have attempted to explain the comparatively small overturning signal across the western section of the OSNAP array. Zou et al. (2020) find that the competing influences of thermal and haline anomalies within the Labrador Sea counteract each other, leading to only a small net density transformation across the basin. Further, Li et al. (2021) find that deep convection within the Labrador Sea—previously thought to be one of the primary mechanisms driving subpolar overturning—has very little effect on density in the boundary current. Petit et al. (2020) show that, in fact, it is in the Iceland Basin and Irminger Sea, to the east of Greenland, where that dominant transformation of upper limb to lower limb water takes place.

The subpolar gyre, however, is a difficult region to model due to intense surface forcing, highly non-uniform bathymetry, and the complex network of constituent currents (see Figure 1.2). As such, coupled and ocean-only models often exhibit strong biases in this region (Wang et al. 2014; Jong et al. 2009). While models often struggle for consistency with observations at these latitudes, some model studies do agree with the results from the OSNAP programme. For example, Menary et al. (2020) find that—consistent with observations—overturning variability across OSNAP East dominates the variability across the full section in a high-resolution coupled model. Further, in an eddy-permitting ocean model, MacGilchrist et al. (2020) find that a Lagrangian analysis of the origins of LSW shows that ocean ventilation occurs primarily at the Labrador Sea boundary—i.e., not in the basin interior where mixing by deep convection occurs—in agreement with measurements from OSNAP moorings (Le Bras et al. 2020).

With such a wide range of factors potentially impacting the circulation in the subpolar North Atlantic, isolating the key processes is difficult. For example, direct wind forcing (via Ekman transport) only accounts for a small proportion of the overall AMOC variability across the OSNAP section (Lozier et al. 2019).

Kostov et al. (2021) find, however, that when remote wind forcing is taken into account, wind stress and surface buoyancy forcing explain similar fractions of the overall variability on interannual to decadal timescales. This is in stark contrast to the subtropics, where the impact of buoyancy forcing on variability is restricted to decadal timescales and wind forcing dominates variability on shorter timescales (Pillar et al. 2016).

The difficulty in ascertaining the key processes determining the circulation in the subpolar North Atlantic highlights the need for idealised and conceptual models to provide a theoretical basis for understanding the mechanisms governing watermass transformation in the subpolar North Atlantic. Comparing solutions obtained from a two-layered variable-density ocean model to those from an ocean circulation model, Schloesser et al. (2012) study the response of a flat-bottomed ocean in a rectangular basin to surface buoyancy forcing. They find that the presence of a meridional temperature gradient leads to a deepening of the thermocline along the eastern boundary, which is then communicated westwards into the ocean interior by Rossby waves, and that sinking occurs primarily in the northeast corner of the domain. In a follow-up paper, Schloesser et al. (2014) include the effects of wind forcing, finding a similar structure, but with the addition of a wind-driven gyre, which drives water northwards, enhancing buoyancy loss in the North Atlantic.

Gjermundsen and LaCasce (2017) take a similar approach, forcing an idealised model in a rectangular basin with surface buoyancy forcing alone, noting that this is sufficient to drive a meridional overturning circulation. In a subsequent paper applying the same buoyancy-forcing-only approach but to the global circulation, Gjermundsen et al. (2018) find that they are able to recreate many of the features of the observed ocean circulation—for example, an overturning circulation, baroclinic western boundary currents and a strong Antarctic circumpolar Current.

On a more local scale, experiments using idealised analogues of the marginal seas of the subpolar North Atlantic—both using theoretical models (e.g., Stra-

neo 2006; Spall 2015) and high-resolution numerical models (e.g., Spall 2004, 2015)—have demonstrated the importance of eddy fluxes between the interior of a convective basin and the surrounding boundary current in determining the export of dense water from the basin.

Given the understanding gained from these idealised experiments, it may therefore provide further insight into the mechanisms determining subpolar North Atlantic circulation to adopt a similar strategy in this region. The approach towards modelling adopted is therefore to keep only the essential physics, removing as much extraneous detail as possible and to cleanly separate the effects of wind, buoyancy and topography in an idealised domain.

One potential technique, which has already generated some insight into the overturning and barotropic circulations in the North Atlantic (Marshall and Pillar 2011), is consideration of the rotational force balance. This approach, however, has not yet been applied to the subpolar North Atlantic specifically—indeed, it has not been successfully implemented in any domain with non-uniform topography, and so needs first to be adapted.

1.4 Rotational Momentum Balance

In the large scale ocean, the steady state horizontal force balance is dominated by geostrophic balance between the Coriolis force and the pressure gradient force. Similarly, the vertical momentum equation in the steady state is dominated by hydrostatic balance between the buoyancy force and the pressure gradient force. The time evolution of the flow is therefore determined by small departures from these geostrophic and hydrostatic balances. As a result, many of the foundational theoretical models of ocean circulation are derived in terms of vorticity, in order to eliminate pressure gradient terms (e.g., Stommel 1948; Munk 1950).

Marshall and Pillar (2011) take a different approach to isolating the net effect of an applied force on the evolution of the flow. When a force is applied

to a Boussinesq (and hence incompressible) fluid, a pressure gradient is instantaneously established to ensure the flow remains non-divergent. Noting this, they represent the effect of a force on the flow as the—purely rotational—sum of the applied force and the resulting pressure gradient force (illustrated schematically in Figure 1.3).

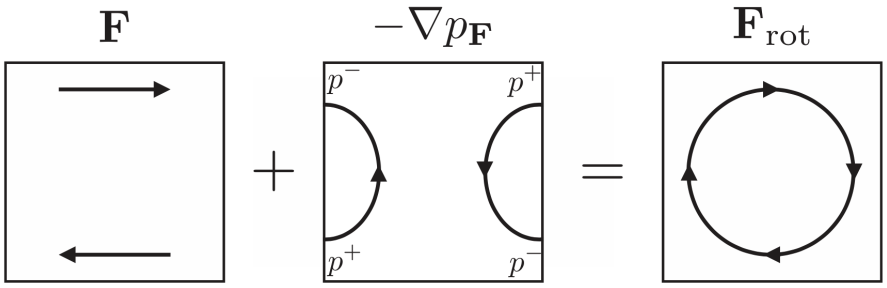


FIGURE 1.3: Schematic, adapted from Marshall and Pillar (2011), showing the net rotational force arising from a purely zonal applied force and the resulting pressure gradient force.

Marshall and Pillar (2011) find this rotational force through the application of Helmholtz's theorem (Helmholtz 1858; English translation, Helmholtz 1867) to extract the solenoidal component of the force in the form of a vector potential. Then, similarly to how the velocity field may be derived by forming and inverting a Poisson equation relating a streamfunction to the known vorticity (e.g., Vallis 2006), they derive equations relating the curl of the applied forcings to barotropic and overturning *force functions*—which act to accelerate the depth-integrated and overturning circulations respectively.

The rotational force from these force functions includes both the locally applied force, and the nonlocal pressure gradient forces arising from the requirements to satisfy conservation of mass and the kinematic boundary conditions. The force function therefore neatly encapsulates the net effect of an applied force, and allows us to immediately diagnose the primary force balances maintaining the flow. Although the two frameworks describe ultimately equivalent dynamics, conceptualising the dynamics of the circulation in terms of rotational forces acting on the flow instead of sources and sinks of vorticity is appealing and provides additional insight.

In their derivation of the three-dimensional force function, however, Marshall and Pillar are missing a key term, accounting for the interaction between the barotropic force function and sloping topography. As they consider only a model with a flat bottom in applying their framework, this missing term had no effect on their results. Retaining this term makes decoupling the horizontal and vertical components of the force function non-trivial.

1.5 Thesis Outline

This thesis aims to explore the roles played by surface wind and buoyancy forcing, as well as topography, in determining the barotropic and overturning circulations in the subpolar North Atlantic. Using an idealised model of the North Atlantic to make the isolation of the specific mechanisms driving the ocean circulation an easier task, two separate techniques are employed. First, the overturning circulation is split into components using a decomposition similar to that used by the monitoring programmes at RAPID and OSNAP; with the full model property fields available, this decomposition can be extended to density space and applied across all latitudes. Second, a corrected reworking of the rotational momentum equation approach of Marshall and Pillar (2011) is derived, and subsequently applied to the model output to highlight the force balances underlying the ocean circulation.

The thesis is structured as follows. In Chapter 2, the idealised model of the North Atlantic used throughout the rest of this thesis is introduced. Chapter 3 then presents the decomposition of the AMOC in depth space, and generalises it to use density as a vertical coordinate. These diagnostics are then applied to the results of numerical experiments altering wind-stress, buoyancy forcing, and topography. A correct version of the rotational momentum balance decomposition in Marshall and Pillar (2011) is derived in Chapter 4. This corrected framework is then applied to the aforementioned numerical experiments in Chapter 5. Finally, conclusions and potential avenues for future work are presented in Chapter 6.

2 Model

2.1 Introduction 13
2.2 MITgcm 15
2.2.1 Approximated Equations of Motion 15
2.2.2 Mixing Parametrisations 17
2.2.3 Grid Geometry 20
2.2.4 Notation and Discretised Operators 22
2.3 An Idealised Model of the Subpolar North Atlantic 25
2.3.1 Model Configuration 25
2.3.2 Control State 29
2.4 Summary 35

2.1 Introduction

The ocean is an enormously complex system, the dynamics of which are governed by the Navier-Stokes equations, as well as the equation of state of seawater, and the conservation of heat and salt. It gains and loses both momentum and tracers, via external boundary interactions, as well as by internal geochemical processes (Griffies and Treguier 2013). It is evidently not possible to directly perform experiments on the large-scale ocean circulation, and so numerical models are a vital tool in providing a controlled environment in which these experiments can be simulated.

To be able to fully simulate the ocean, it would be necessary to resolve an implausible range of scales: from gyre circulations with a horizontal length scale of the order of $\sim 10^6$ m down to the smallest turbulent length scale, given by the Kolmogorov length, which is of order $\sim 10^{-2}$ m (Smyth et al. 2001). The equations solved by numerical ocean models are therefore generally a truncated version of the full Navier-Stokes equations where processes occurring at scales too small to be resolved are included as subgrid scale parametrizations. Further simplifications can be obtained via scale analysis of the system being modelled. Le Sommer et al. (2018) give the example of the approximation of the ocean as a thin shell on a sphere—such that variations in the radius of the Earth with latitude, in deviations of the gravitational force from the radial direction, and in the Coriolis acceleration with depth, can be neglected—as an approximation that is valid in the majority of oceanographic cases.

As the available computing power has grown exponentially from the early ocean models of the 1960s and 1970s (e.g., Bryan 1969), so has the resolution of ocean models, with it now possible to run basin-scale simulations with resolution as high as 1/50° (e.g., Chassignet and Xu 2017). As the resolution increases, more physical processes are explicitly resolved, and so the model should become less dependent on parametrizations and provide a solution which is closer to reality (Fox-Kemper et al. 2019; Chassignet and Xu 2021).

Despite this vast increase in computing power, the prospect of a direct numerical simulation (i.e., one which resolves all processes down to the Kolmogorov scale) of the large-scale ocean in the near future is unrealistic—indeed, the maximum domain size of such simulations currently possible is of order 10 m (Yeung et al. 2015). Further, high-resolution models are expensive to run and so are often less well tuned and validated. As such, the model configuration selected will depend on the scope and application of the experiment. The highest-resolution models with the most processes explicitly resolved are too computationally expensive to run repeatedly over long times, so tend to be used for short-term forecasts, whereas models towards the simpler end of

the hierarchy are more often used to better understand the physical processes driving the system (Le Sommer et al. 2018).

The model used in the experiments presented in this thesis is very much towards the more idealised end of the model hierarchy. It was hoped that the simplicity of the model would make it easier to isolate the mechanisms underlying the overturning and horizontal gyre circulations in the subpolar North Atlantic. The guiding principle behind the choice of model configuration was to keep the model as simple as possible, including only as much physics as required for a first-order description of the effects of wind stress, buoyancy forcing, and sloping bathymetry on the circulation—and to be able to relate results to observations of the region.

This chapter is set out as follows: Section 2.2 introduces the model and the various approximations and parametrizations used, as well as the notation used in later chapters to describe any discrete equations. Section 2.3 then describes the model configuration, the specific parameters chosen, and the spun-up control state.

2.2 The Massachusetts Institute of Technology General Circulation Model

The model used is an idealised ocean-only configuration of the Massachusetts Institute of Technology general circulation model (MITgcm; e.g., Marshall et al. 1997; Marshall et al. 2004; Adcroft et al. 2004). The MITgcm was chosen as its modularity and its well-maintained documentation make it easy to modify to suit the problem at hand, and it has excellent support for running on parallel systems (Marshall et al. 1997).

2.2.1 Approximated Equations of Motion

The model used here solves the hydrostatic primitive equations in vector invariant form—discretized via the finite volume method—on a spherical polar

grid using depth as the vertical coordinate (Campin et al. 2021). It has a nominal horizontal resolution of $1/2^\circ \times 1/2^\circ$, but meridional resolution scales with latitude to keep grid cells approximately square. The zonal and meridional grid spacings are therefore given by:

$$\Delta\phi = \left(\frac{1}{2}\right)^\circ \qquad \text{and} \qquad \Delta\lambda = \left(\frac{\cos\lambda}{2}\right)^\circ.$$

The model has 30 levels in the vertical, ranging in thickness from 26 m at the surface to 250 m at depth.

Several simplifying assumptions are made about the dynamics of the system in addition to the thin spherical shell approximation outlined in Section 2.1. First, the ocean is assumed to be in hydrostatic balance, whereby the dominant force balance in the vertical direction is between the vertical pressure gradient and the buoyancy force. For this approximation to hold, the condition on the flow is that the aspect ratio must be must less than one or, equivalently, $L_z \ll L_h$ where L_z and L_h are the characteristic vertical and horizontal length scales of the flow. This condition is generally well satisfied in the ocean, away from regions of intense convection where stratification is weak and so the vertical length scale is comparatively large (Vallis 2006).

Secondly, the ocean is further assumed to be Boussinesq. As such the density is decomposed into a constant reference density ρ_0 and a density anomaly ρ', where it is assumed that $\rho_0 \gg \rho'$. A consequence of this approximation is that the ocean now conserves total volume, instead of the more physical mass conservation of a non-Boussinesq ocean (Griffies 2004). In the single-basin, highly idealised, modelling context within this thesis, however, the value of the increased simplicity outweighs any downside from the potential loss of accuracy associated with treating the ocean as a Boussinesq fluid.

Two further approximations made, which are perhaps harder to justify physically, are the treatment of the ocean surface as a rigid lid, and the choice of an equation of state that is a linear function of temperature only. The rationale behind these approximations is that the resulting loss in accuracy

and/or generality of the model is outweighed by the gains in numerical and physical simplicity, respectively. In assuming the ocean to have a rigid lid, the simulation of external gravity waves, tides, and freshwater fluxes across the ocean surface is lost (Griffies 2004). In the idealised experiments presented in this thesis, however, the former are of little direct interest, and the latter is irrelevant with an equation of state with no explicit representation of salinity. The benefits behind assuming a rigid lid present themselves largely in the rotational momentum balance derivation in Chapter 4, where the presence of a fixed boundary at the surface simplifies certain calculations.

The use of a linear equation of state dependent solely on temperature means that the effects on density of salinity are included only implicitly and so the model is unable to distinguish between the responses to thermal and haline forcing. The differing effects on density of salinity and temperature are generally important in the subpolar North Atlantic (Born and Stocker 2014; Menary et al. 2016; Zou et al. 2020). The following chapters, however, are concerned more with the circulations driven by wind stress and the buoyancy force in general, as opposed to those of its thermal and haline components individually. As a result, adhering to the previously stated principle of keeping the model as simple as possible, the inclusion of a more realistic equation of state, along with a free surface, is left for future work.

2.2.2 Mixing and Subgrid-Scale Parametrisations

In the real ocean, mixing of tracers is primarily mediated by eddies and occurs overwhelmingly along isopycnals or, more strictly, along neutral surfaces. This is true particularly in the ocean interior away from boundaries and rough topography (Ledwell et al. 1993). These eddies only begin to be resolved around the Rossby radius of deformation, which is not well resolved by the $1/2^\circ \times 1/2^\circ$ grid used in this thesis—particularly at higher latitudes. As such, the mixing effects of these eddies must be parametrised. Attempting to represent this mixing as a primarily horizontal diffusion leads to spurious mixing across

density surfaces (Veronis 1975). Although it might intuitively seem that this issue would diminish with increased resolution, this is not the case, as spurious mixing remains an issue even in eddying ocean models (Gibson et al. 2017; Fox-Kemper et al. 2019).

This issue is addressed in the model by the inclusion of parametrisations first proposed by Redi (1982), Gent and McWilliams (1990), and Gent et al. (1995). The Redi scheme represents the mixing of tracers by eddies by rotating the diffusion tensor such that the gradient of the tracer is projected onto the neutral surface and so diffusion of the tracer now occurs primarily along isentropes. The Gent-McWilliams (GM) parametrisation of Gent et al. (1995) represents the advection of tracer by eddies by an adiabatic flux, the magnitude of which depends on the extent of the misalignment between surfaces of constant depth and neutral surfaces. The form used in the model, however, is the adaptation proposed by Griffies (1998), who rewrites the advective flux of the GM scheme as a skew flux. Writing this skew flux in tensor form, and combining it with the rotated diffusion tensor of Redi (1982) then allows both parametrisations to be included through a single term in the tracer equation.

Vertical mixing in the surface boundary layer is parametrised using the K-profile parametrisation scheme (KPP) proposed by Large et al. (1994). The KPP scheme represents the surface mixed layer as the combination of a shallow turbulent layer—where mixing is governed by the similarity theory of Monin and Obukhov (1954)—with a deeper mixed layer of varying thickness where vertical mixing results from local Richardson number instability, internal wave breaking, and double diffusion. The assumptions underlying the scheme are summarised by McWilliams (2000) as twofold: first, that the thickness of the boundary layer adjusts to maintain a bulk Richardson number at some critical value of order $\mathcal{O}(1)$. The second assumption is that the diffusivity profile remains smooth across the two layer boundaries: one between the turbulent surface layer and the deeper mixed layer, and the other between the mixed layer and the ocean interior. To ensure compatibility between the GM and KPP

parametrisations, an additional adaptation proposed by Large et al. (1997) is used to taper the GM scheme near the surface mixed layer.

Despite the inclusion of the above subgrid-scale mixing parametrisations, frictional dissipation is still required to maintain the numerical stability of the model (Griffies 2004). As it is included for numerical reasons, it is defined in such a way as to reduce its influence on the circulation as much as possible while still retaining the factors ensuring stability. These requirements on friction are that it is able to suppress grid-scale noise associated with advection (Bryan et al. 1975; this also has the effect of reducing spurious diapycnal mixing, as shown by Ilıcak et al. 2012), as well as providing a sink of vorticity and kinetic energy at unresolved scales (Griffies et al. 2000). Viscous dissipation, therefore, should be as scale-selective as possible. To that end, the model uses a biharmonic viscosity in addition to a Laplacian one, to preferentially dissipate motions at the grid-scale.

The magnitude of the viscosity required for numerical stability decreases as horizontal resolution increases. Seeing as the horizontal grid spacing in the model varies with the cosine of latitude, the resolution at high latitudes is significantly higher than that at low latitudes. This means that the amount of viscous dissipation required for stability is significantly lower at subpolar latitudes than in the subtropics. Setting the viscosity coefficients to a constant which ensures stability would therefore result in a model with unnecessarily high viscous dissipation at high latitudes. As such, the Laplacian and biharmonic viscosity coefficients are allowed to vary with grid size to minimise extraneous dissipation. The respective coefficients are set in the model via the non-dimensional parameters $\hat{\nu}_h$ and $\hat{\nu}_4$, which vary with grid cell size as:

$$\hat{\nu}_h = \frac{4\,\nu_h(x,y)\,\Delta t}{\Delta(x,y)^2} \qquad \text{and} \qquad \hat{\nu}_4 = \frac{32\,\nu_4(x,y)\,\Delta t}{\Delta(x,y)^4}\,. \tag{2.1}$$

Here, ν_h and ν_4 are the Laplacian and biharmonic viscosity parameters and Δt is the model timestep. Δ is the grid length scale, given by the harmonic

mean of the zonal and meridional grid spacings:

$$\Delta = \frac{2\,\Delta x^f\,\Delta y^f}{\Delta x^f + \Delta y^f}\,, \tag{2.2}$$

where Δx^f and Δy^f are the distances in the x and y directions between the faces of the continuity cell—which will be introduced in the next section—and are therefore defined at the cell centers.

2.2.3 Grid Geometry

The model grid is constructed such that the variables stepped forward by the momentum equations are staggered in space. The way this staggering is organised in the model is in the form of the Arakawa C-grid (Arakawa and Lamb 1977). The C-grid is based around the idea of the continuity cell (shown in Figure 2.1): the positioning of the velocities on the faces of the cell makes enforcing non-divergence of the flow simple, with no spatial averaging of velocities required. One problem with the C-grid representation, however, is that the calculation of the Coriolis force requires averaging of the horizontal velocities (because the zonal component depends on the meridional velocity, but is defined at the u-point, and vice versa). This averaging introduces a computational mode and makes handling of the Coriolis force problematic on coarse resolution grids (Arakawa 2000). The MITgcm does provide one potential solution to this problem, through the C-D scheme of Adcroft et al. (1999). The advantages of this scheme are most prominent at lower resolutions, however, and it introduces another tunable parameter. The impact of this parameter on the flow is not easily diagnosed, which runs counter to the motivation for using an idealised model in the first place, and so it is not used here.

As mentioned at the beginning of Section 2.2.1, the model has 30 levels in the vertical, with resolution decreasing with depth. This increase in level thickness with depth is a common tactic in z-coordinate models as, for no significant increase in required computation time, it focuses resolution on shallower

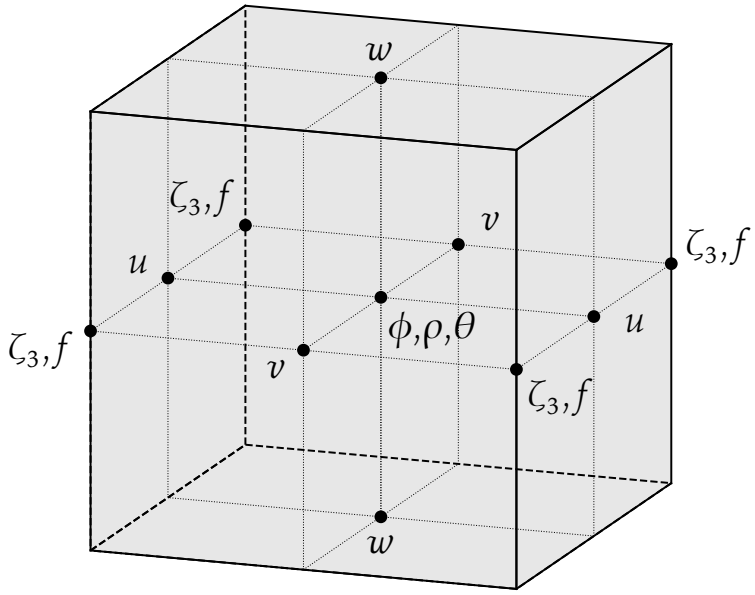


FIGURE 2.1: Arakawa C-grid continuity cell. The pressure (ϕ), density (ρ), and temperature (θ) are all defined at the cell center, the *tracer-point* (or *T-point*). Zonal, meridional, and vertical velocities (u, v and w) are defined at the centers of the east and west, north and south, and upper and lower cell faces, respectively. These points are then referred to as the *u-point*, the *v-point*, and the *w-point*. The relative vorticity (ζ_3) and Coriolis parameter (f) are defined at the cell corners, at the *ζ-point*.

depths with more vigorous dynamics. A rule of thumb given by Lindzen and Fox-Rabinovitz (1989) is that the ratio of horizontal to vertical grid spacing should scale with the aspect ratio of the motion. For the large scale ocean circulation, this heuristic would imply that resolution should vary with the stratification, giving higher resolutions near the surface and lower resolution at depth.

In the context of this thesis, where we are concerned with the effects of topography on the flow, an important issue with this coarse vertical resolution at depth is that the ability of the model to accurately represent deep bathymetry is degraded. To address this issue, the partial cell scheme—shown schematically in Figure 2.2(a)—of Adcroft et al. (1997) is incorporated, whereby vertical distances are multiplied by scaling factors to adjust cell volume to match the topography.

While this does not *strictly* increase the vertical resolution, the simulation of flow over deep topography is greatly improved. Another pertinent issue with the vertical structure of the model grid, specifically with the step-like nature of the

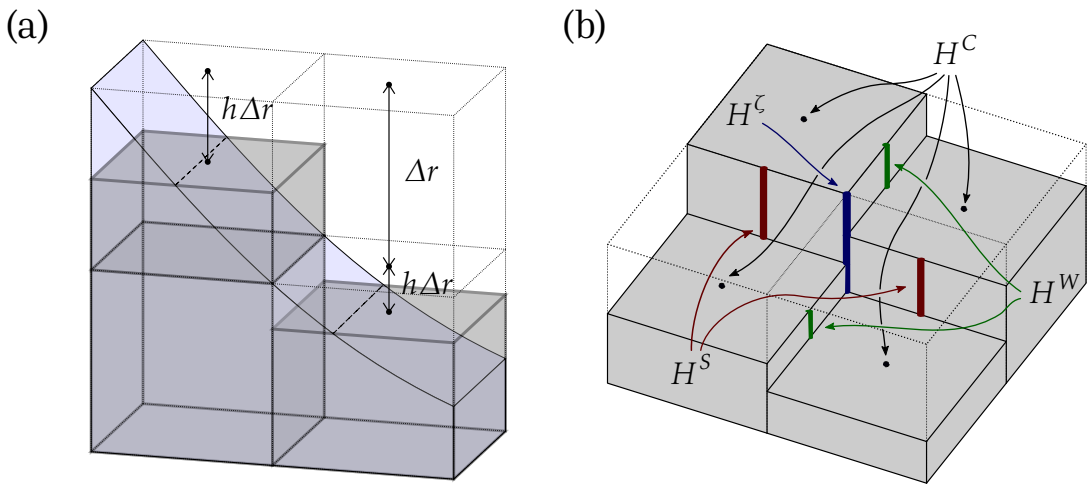


FIGURE 2.2: Schematics illustrating the vertical grid structure. (a) the partial cell representation of topography of Adcroft et al. (1997). h are the fractions of the cell not occupied by topography, and Δr are the level thicknesses. In this example, if the partial cells were not enabled, the topography shown in blue would be represented as flat in the model. (b) the degeneracy in the calculation of depth at the various grid points (H^C is at the tracer-point, H^W is at the u-point, H^S is at the v-point, and H^ζ is at the ζ-point). Although H^C is well-defined, there is ambiguity in the definition of H^W, H^S and H^ζ, shown in the schematic by the colored columns.

representation, is the degeneracy in model depth when calculated anywhere other than at the tracer-point. This problem, illustrated in Figure 2.2(b), will be adressed in greater detail in later chapters, but generally complicates the calculation of any diagnostic that is dependent on vertical distances and is defined outside the tracer-point.

2.2.4 Discrete Notation and Discretisation of Operators

The validity of the diagnostics introduced in the following two chapters depends on various conservation properties. The successful numerical implementation of these diagnostics therefore relies on these conservation properties being preserved in their discrete form. The precise discretisation scheme, particularly that of horizontal differential operators, is therefore important and is outlined in this section.

The specific discretised equations solved by the model are not included here, but can be found in Section 2.15 of the MITgcm manual (Campin et al. 2021). The purpose of this section is to specify the notation used in any subsequent

discrete equations and to introduce the discretised form of the differential operators *grad*, *div*, and *curl* used in the computation of the diagnostics introduced in Chapter 3 and Chapter 5.

The notation used closely follows that used in the MITgcm documentation (Campin et al. 2021), and is presented in Table 2.1. The first thing to notice is that, due to the C-grid staggering of variables (see Figure 2.1), when taking the difference of a variable in a certain direction, the result is defined at a different point on the grid in that direction. For example, consider a variable defined on the u-point (i.e., the zonal faces of the continuity cell), taking the difference of this variable in the x direction will result in a new variable defined at the cell center. Variables located at different points on the grid cannot be directly combined, and so to estimate the value of a variable defined at one point on the continuity cell at a different point it needs to be interpolated using the averaging operator. This interpolation comes at the cost of a loss in accuracy and so, wherever possible, diagnostics are calculated in such a way as to minimise the need for averaging—although eliminating it entirely is often not possible.

The finite volume formulation of the MITgcm, coupled with the C-grid staggering of variables, gives the model some very useful conservation properties (see Marshall et al. 1997; Adcroft et al. 2004). Preservation of these properties under the application of differential operators, particularly on a grid with non-uniform spacing, requires a careful discretisation of the operator applied. The simplest of the three aforementioned operators is the gradient, which is just the derivative taken in each direction, and so is discretised as:

$$\nabla\Phi \approx \frac{\delta_i \Phi}{\Delta x}\,\hat{\boldsymbol{e}}_x + \frac{\delta_j \Phi}{\Delta y}\,\hat{\boldsymbol{e}}_y + \frac{\delta_k \Phi}{\Delta r}\,\hat{\boldsymbol{e}}_z\ , \tag{2.3}$$

where Φ is an arbitrary scalar field.

The curl and divergence, however, require more care. For the divergence, because of the grid geometry, while the vertical component can be calculated

i, j, k	Indices in the x, y, and z directions
Δx, Δy, Δr	Generic grid spacings in the x, y, and z directions
Δx^f, Δx^c, Δx^g, Δx^v	Specific grid spacings in the x direction, defined at the T, u, v, and ζ-points
Δy^f, Δy^c, Δy^g, Δy^u	Specific grid spacings in the y direction, defined at the T, v, u, and ζ-points
Δr^f, Δr^c	Specific grid spacings in the z direction, defined at the T and w-points
h^c, h^{W}, h^{S}, h^ζ	Partial cell thicknesses (a fraction between 0 and 1) at the T, u, v, and ζ-points
H^c, H^{W}, H^{S}, H^ζ	Ocean depth (positive) at the T, u, v, and ζ-points
$\mathcal{A}^c$, $\mathcal{A}^{\mathrm{W}}$, $\mathcal{A}^{\mathrm{S}}$, $\mathcal{A}^\zeta$	Horizontal grid cell areas at the T, u, v, and ζ-points
$\delta_{i,j,k}$	The difference operator: $\delta_i \Phi = \Phi_{i+\frac{1}{2}} - \Phi_{i-\frac{1}{2}}$
$\overline{}^{i,j,k}$	The averaging operator: $\overline{\Phi}^{\,i} = \frac{1}{2}\left(\Phi_{i+\frac{1}{2}} + \Phi_{i-\frac{1}{2}}\right)$

TABLE 2.1: Notation for discrete equations. The superscripts follow MITgcm conventions. For the grid spacings, the superscripts *f*, *c*, *g*, *v*, and *u* denote spacings between *faces*, *centers*, *gridpoints* (or vertices), *v-points*, and *u-points*, respectively. For other grid descriptors, the superscripts *c*, *W*, *S*, and ζ imply that the variable is defined at the *center*, the *western* edge (or *u*-point), the *southern* edge (or *v*-point), and the ζ*-point* of the continuity cell, respectively.

simply as a vertical difference, the integral definition of the horizontal divergence must be used to calculate the horizontal component. For a two-dimensional divergence:

$$\boldsymbol{\nabla}_h \cdot \boldsymbol{\Psi} = \lim_{A \to 0} \frac{1}{A} \oint_{l=\partial A} \boldsymbol{\Psi} \cdot \hat{\boldsymbol{n}} \, \mathrm{d}l \,, \tag{2.4}$$

where l is the closed curve bounding area A, $\hat{\boldsymbol{n}}$ is the unit normal to this curve, and $\boldsymbol{\Psi}$ is an arbitrary vector. On the model grid, the smallest discrete horizontal surface is the cell area $\mathcal{A}$, bounded by Δx and Δy, which may not be equal on each side. The line integral in (2.4) therefore discretises to

$$\boldsymbol{\nabla}_h \cdot \boldsymbol{\Psi} \approx \frac{\delta_i \left(\Psi^x \Delta y\right) + \delta_j \left(\Psi^y \Delta x\right)}{\mathcal{A}} \,, \tag{2.5}$$

and the full 3D divergence is calculated as

$$\boldsymbol{\nabla} \cdot \boldsymbol{\Psi} \approx \frac{\delta_i \left(\Psi^x \Delta y\right) + \delta_j \left(\Psi^y \Delta x\right)}{\mathcal{A}} + \frac{\delta_k \Psi^z}{\Delta r} \,. \tag{2.6}$$

In the same way that the horizontal divergence must be calculated from its integral definition as the flux of a vector out of a cell, the components of the curl of a vector must be calculated from the circulation around the cell. Considering the z component of the curl, for example:

$$\hat{\boldsymbol{e}}_z \cdot \boldsymbol{\nabla} \times \boldsymbol{\Psi} = \lim_{A \to 0} \frac{1}{A} \oint_{l=\partial A} \boldsymbol{\Psi} \cdot \mathrm{d}\hat{\boldsymbol{l}} \,, \tag{2.7}$$

where A here is an area in the horizontal plane, and $\mathrm{d}\hat{\boldsymbol{l}}$ is the vector line element along closed curve l. This discretises to:

$$\hat{\boldsymbol{e}}_z \cdot \boldsymbol{\nabla} \times \boldsymbol{\Psi} \approx \frac{\delta_i \left(\Psi^y \Delta y\right) - \delta_j \left(\Psi^x \Delta x\right)}{\mathcal{A}} \,. \tag{2.8}$$

The x and y components of the curl are treated in a similar way, but the area used to calculate the circulation must be calculated using Δr and taking the partial cell heights into account. Coupled with issues arising from the large aspect ratio, this renders these components of the curl more difficult to deal with accurately.

Due to these natural discretisations of divergence and curl and the lack of something similar for the dot and cross products, wherever possible, expressions containing dot or cross products are manipulated using various vector calculus identities into ones containing only divergences and curls to avoid the need to average quantities across grid cells.

2.3 An Idealised Model of the Subpolar North Atlantic

2.3.1 Model Configuration

The model domain aims to capture the main characteristics of the subpolar North Atlantic while remaining as simple as possible. To that end, the domain consists of one large, “Atlantic”, basin, and a smaller “Nordic” basin in the

north-east corner. The Atlantic basin extends zonally from 50°W to 10°W, and meridionally from 20°N to 60°N: this region roughly corresponds to the area of ocean bounded by the Iberian peninsula and Northwest Africa in the east, Greenland and Iceland in the north, Newfoundland to the west, and the North Equatorial Current to the south. The Nordic basin is much smaller: extending meridionally from roughly 60°N to 70°N, and zonally from 30°W to 10°W. The basins both have a maximum depth of 4000 m, and are connected by two channels either side of an idealised "Iceland". These channels contain a zonal sill, the depth of which rises from 4000 m to 1000 m and then falls again with a sinusoidal profile in the meridional direction.

At all boundaries except the northernmost and southernmost, the model sidewalls slope linearly from zero depth at the domain boundaries to maximum depth around 200 km away from the boundary. The exceptions for the northern and southern boundaries are due to the fact that these boundaries are considered "open". This characteristic is simulated by the presence of sponge regions, where the temperature—and hence the buoyancy—is relaxed to a prescribed stratification. In the "subtropical" sponge, which occupies the region south of 30°N, the stratification is reset to the initial reference stratification, shown in Figure 2.4(a). Note that the coldest water formed by the model is formed at depth in the subtropical sponge. This is to simulate Antarctic bottom water, which is colder and denser than the North Atlantic deep water formed at high latitudes in the Atlantic.

In the "Nordic" sponge, on the other hand, temperature is relaxed to 5°C over the full ocean depth, to simulate the formation of deep water in the Nordic Seas. The intensity of the sponges is gradually increased as the "open" boundaries are approached, with the goal of relaxing strongly enough to set the desired water properties and dissipate any wave features entering the sponge, but not so strongly that incoming waves reflect off the sponges. The domain bathymetry, along with the location of the two sponge regions, is shown in Figure 2.3(b). Both the southern boundary within the tropical sponge and the northern boundary

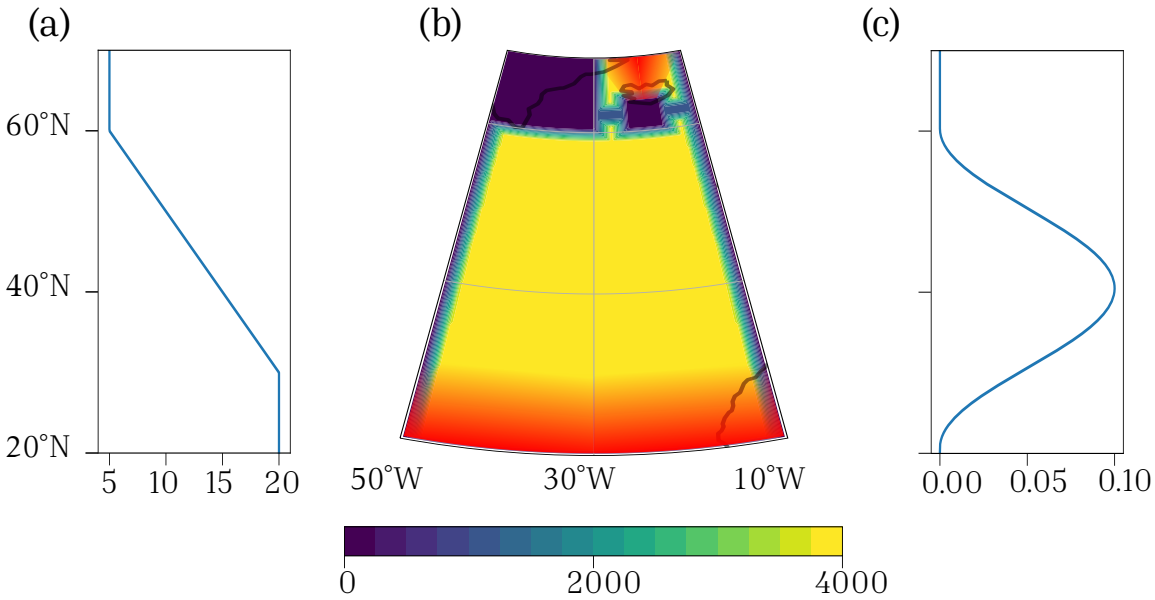


FIGURE 2.3: Model configuration. **(a)** the surface relaxation temperature as a function of latitude, units are in °C (i.e., θ_{relax} from equation (2.9)). **(b)** colormap shows model depth in metres. Red shaded regions indicate the presence and intensity of sponge regions. Any landmasses which would be present in the analogous region in reality are overlaid as black contours. These landmasses are included purely to help situate the model domain, they are not present in any simulations and have no effects. **(c)** the wind stress forcing profile; the units are $\mathrm{N\,m^{-2}}$ and the maximum wind stress is $0.1\ \mathrm{N\,m^{-2}}$ and occurs at 40°N.

within the Nordic sponge are vertical walls. Hence while the sponges *simulate* open boundaries, the domain is closed.

In the base configuration, the other source of buoyancy forcing is via surface forcing. This is also represented as a simple relaxation to a prescribed temperature (a function of latitude), this time in the surface layer only. The temperature is restored to a constant value of 20°C at latitudes below 30°N, and to a constant value of 5°C at latitudes above 60°N. This ensures that surface forcing and the sponge regions relax to consistent temperatures. The relaxation temperature then varies linearly with latitude between these two parallels to give a meridional gradient in buoyancy forcing, as shown in Figure 2.3(a).

Each of these sources of buoyancy forcing introduces an additional forcing term into the temperature tendency equation of the form:

$$\mathcal{F}(\boldsymbol{x}, t) = -\frac{M_\theta(\boldsymbol{x})}{\tau_\theta}\left[\theta(\boldsymbol{x}, t) - \theta_{\text{relax}}(\boldsymbol{x})\right] . \tag{2.9}$$

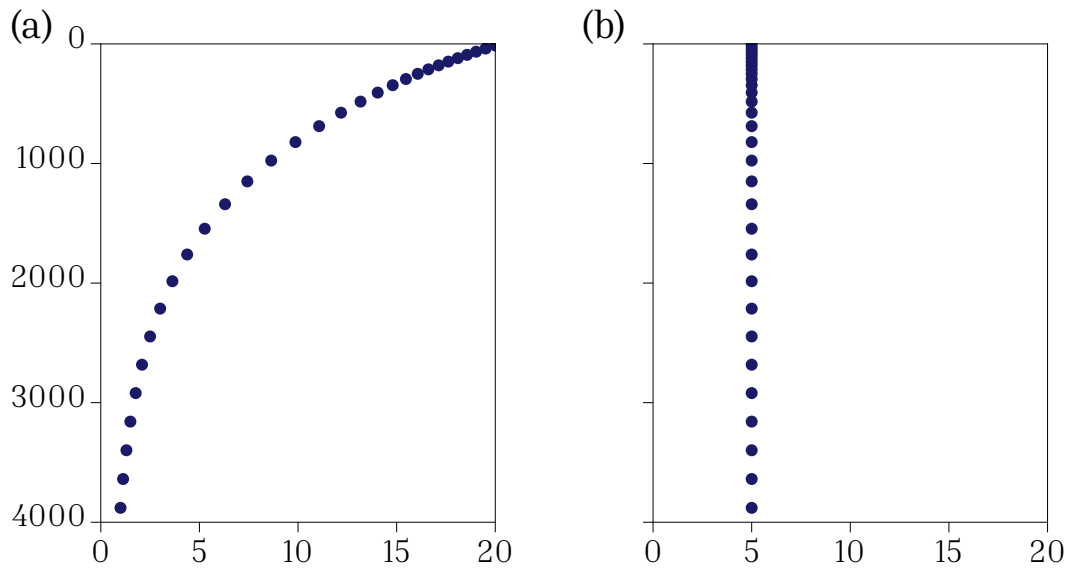


FIGURE 2.4: The temperature profiles relaxed to in (a) the subtropical sponge, and (b) the Nordic sponge. The temperature profile in (a) is also the initial stratification, as well as the profile to which any temperature anomalies are referenced. Temperatures are in °C and depths are in m.

The effective timescale on which temperature is restored to the given temperature (θ_{relax}) is therefore controlled by specifying a constant relaxation time scale (τ_θ) and a masking function (M_θ), which varies between zero and one sinusoidally with distance from the sponge boundary. For the subtropical sponge, the boundary is 30°N, whereas the boundaries for the Nordic sponge are lines connecting the northern corners of Iceland with the northern corners of the domain (see Figure 2.3(b)). In the case of the sponges, this allows for a gradual decrease in relaxation time scale, whereas for the surface buoyancy forcing it is set to one in the surface level and zero elsewhere.

The model is also forced by a zonal wind stress which varies sinusoidally with latitude, but is zonally uniform. This wind stress has a maximum amplitude at 40°N, and vanishes smoothly at the northern and southern boundaries of the Atlantic basin, so that there are no discontinuities in the wind stress curl, nor is there any wind forcing in the Nordic basin. The profile of the wind stress is shown in Figure 2.3(c), and has a peak amplitude of 0.1 N m^{-2}, broadly consistent with observed values (e.g., Gulev and Hasse 1998).

Zonal cell thickness	Δx	(18.5 km–52.2 km)
Meridional cell thickness	Δy	(18.9 km–52.1 km)
Vertical cell thickness	Δr	(26 m–241 m)
Time step	Δt	600 s
Lateral boundary conditions		No normal flow, free-slip
Vertical boundary conditions		No normal flow, free-slip
Maximum zonal wind stress	$\tau^{(x)}_{\max}$	$0.1\,\mathrm{N\,m^{-2}}$
Non-dimensional Laplacian viscosity	$\hat{\nu}_h$	2.5×10^{-3}
Non-dimensional biharmonic viscosity	$\hat{\nu}_4$	2.5×10^{-3}
Vertical viscosity	ν_z	$1 \times 10^{-2}\,\mathrm{m^2\,s^{-1}}$
Reference density	ρ_0	$1025\,\mathrm{kg\,m^{-3}}$
Thermal expansion coefficient	α_θ	$2 \times 10^{-4}\,\mathrm{K^{-1}}$
Reference temperature profile	θ_{ref}	(1°C–20°C)
Surface temperature relaxation timescale	$\tau^{(\mathrm{surf})}_\theta$	60 days
Sponge temperature relaxation timescale	$\tau^{(\mathrm{sponge})}_\theta$	50 days
Horizontal diffusivity	κ_h	$400\,\mathrm{m^2\,s^{-1}}$
Vertical diffusivity	κ_z	$1 \times 10^{-5}\,\mathrm{m^2\,s^{-1}}$
GM eddy diffusivity	κ_{GM}	$1 \times 10^{3}\,\mathrm{m^2\,s^{-1}}$
Minimum GM diffusivity after tapering	$\kappa^{\min}_{\mathrm{GM}}$	$50\,\mathrm{m^2\,s^{-1}}$

TABLE 2.2: Model parameters, bracketed ranges indicate minimum and maximum values.

Other important model parameters and their values are summarised in Table 2.2. Where parameter values are not constant—i.e., if they vary in space—they are given as a range in parentheses. Any available physical model parameters not mentioned in Table 2.2 are either omitted or set to their default values, documented in Sections 3.8 and 8.4 of the MITgcm manual (Campin et al. 2021).

2.3.2 Model Control State

The model is initialised with the parameters given in Table 2.2, and the bathymetry and forcings shown in Figure 2.3. It is then spun up from rest with the initial stratification shown in Figure 2.4(a) for 300 years, after which time there are no readily discernible trends in the flow. The model is therefore assumed to have reached equilibrium. Convergence to this equilibrium state is comparatively fast, and in fact there is little difference between the flow fields after 100 years and those after 300 years.

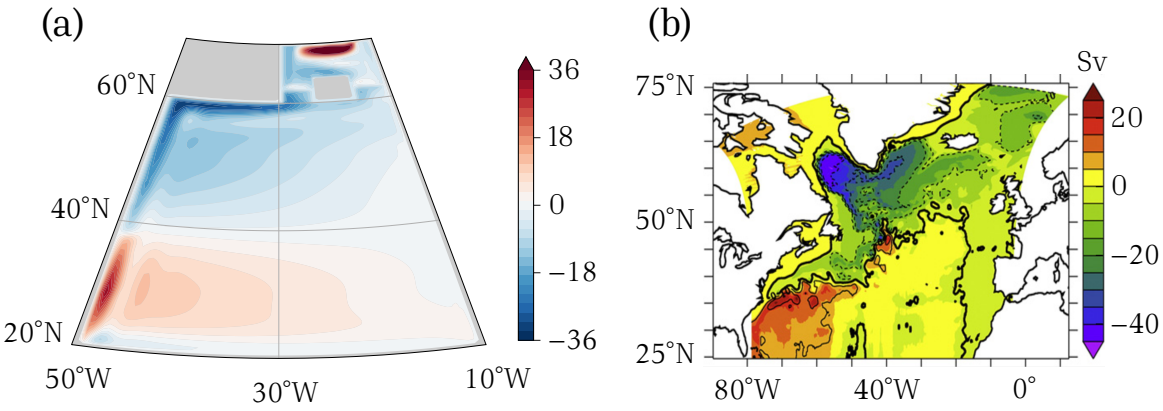


FIGURE 2.5: (a): barotropic streamfunction of the spun-up model control state. Values are indicated by the colormap, and the units are in Sverdrups. (b): figure for comparison taken from Marzocchi et al. (2014). Shows the barotropic streamfunction obtained from an eddying ocean model with realistic wind and buoyancy forcing. Magnitude of the streamfunction is, again, given in Sverdrups and is indicated by the colormap.

Figure 2.5(a) shows the barotropic streamfunction in this equilibrium state. As intended, the circulation comprises two gyres: a subtropical one in the south, and a subpolar one in the north. The separation between the two lies at roughly 40°N. This is as expected, as this is where the wind stress is at its maximum (Figure 2.3(c)). It is therefore the latitude at which the curl of the wind stress changes sign, and hence the depth-integrated flow must also change sign to balance the input of vorticity (see e.g., Vallis 2006).

The shape of the gyres—particularly the subtropical gyre—resembles far more the slightly distorted gyre of Munk (1950), where vorticity is ultimately dissipated by Laplacian viscosity, than that of Stommel (1948), where the balancing sink of vorticity is provided by bottom drag. This is unsurprising as viscosity is present in the model formulation, whereas bottom drag is not. Both gyres are strongly intensified and distorted near the western boundary, with strong recirculations. This, again, is unsurprising as the presence of a sloping sidewall allows for the bottom pressure torque to balance the meridional advection of planetary vorticity (Jackson et al. 2006). With no requirement for friction to close the vorticity balance, the boundary current is less dissipative and more inertial (Hughes and de Cuevas 2001; Jackson et al. 2006), enabling the formation of inertial recirculation gyres (Ierley 1987).

The equilibrated barotropic streamfunction in the control state compares reasonably favorably with more realistic Atlantic simulations. For example, the barotropic streamfunction obtained from an eddying, 1/12° version of the NEMO ocean model (Gurvan et al. 2022) by Marzocchi et al. (2014) is shown in Figure 2.5(b). In both the model control state and the more realistic simulation, the subpolar gyre contorts in such a way that the maximum transport is focussed in the northwest corner, and the barotropic flow is largely blocked by the sills either side of Iceland. These are only broad similarities though, as the model of Marzocchi et al. (2014) explicitly represents eddies—which the idealised model is unable to do—and has realistic topography, as opposed to the regular, rectangular domain geometry of the idealised model.

The meridional overturning circulation of the equilibrated control state is shown in Figure 2.6(a). There is a strong clockwise overturning cell in the upper ocean which extends from the subtropical sponge in the south to the Nordic sponge in the north. There is also a weak counter-clockwise abyssal cell, which is largely restricted to within the subtropical sponge. This abyssal cell results from the formation of the coldest water in the model at depth in the sponge: the coldest temperature in the sponge is 1°C, as opposed to 5°C in the northern sponge—as can be seen from the temperature profiles in Figure 2.4.

The magnitude of the upper cell decreases northwards from its maximum at around ∼ 700 m depth and 35°N. This indicates a gradual sinking across all latitudes north of 35°N. There is strong upwelling near the southern boundary, resulting from the strong relaxation of cold lower limb water to the, warmer, initial stratification. The streamfunction penetrates into the Nordic sponge only fairly weakly, implying that a large fraction of the total downwelling occurs within the main basin.

As with the barotropic streamfunction, the overturning streamfunction obtained from the idealised model control state also compares favorably with more realistic simulations. Again, the analogous overturning streamfunction obtained from the high-resolution model of Marzocchi et al. (2014) is

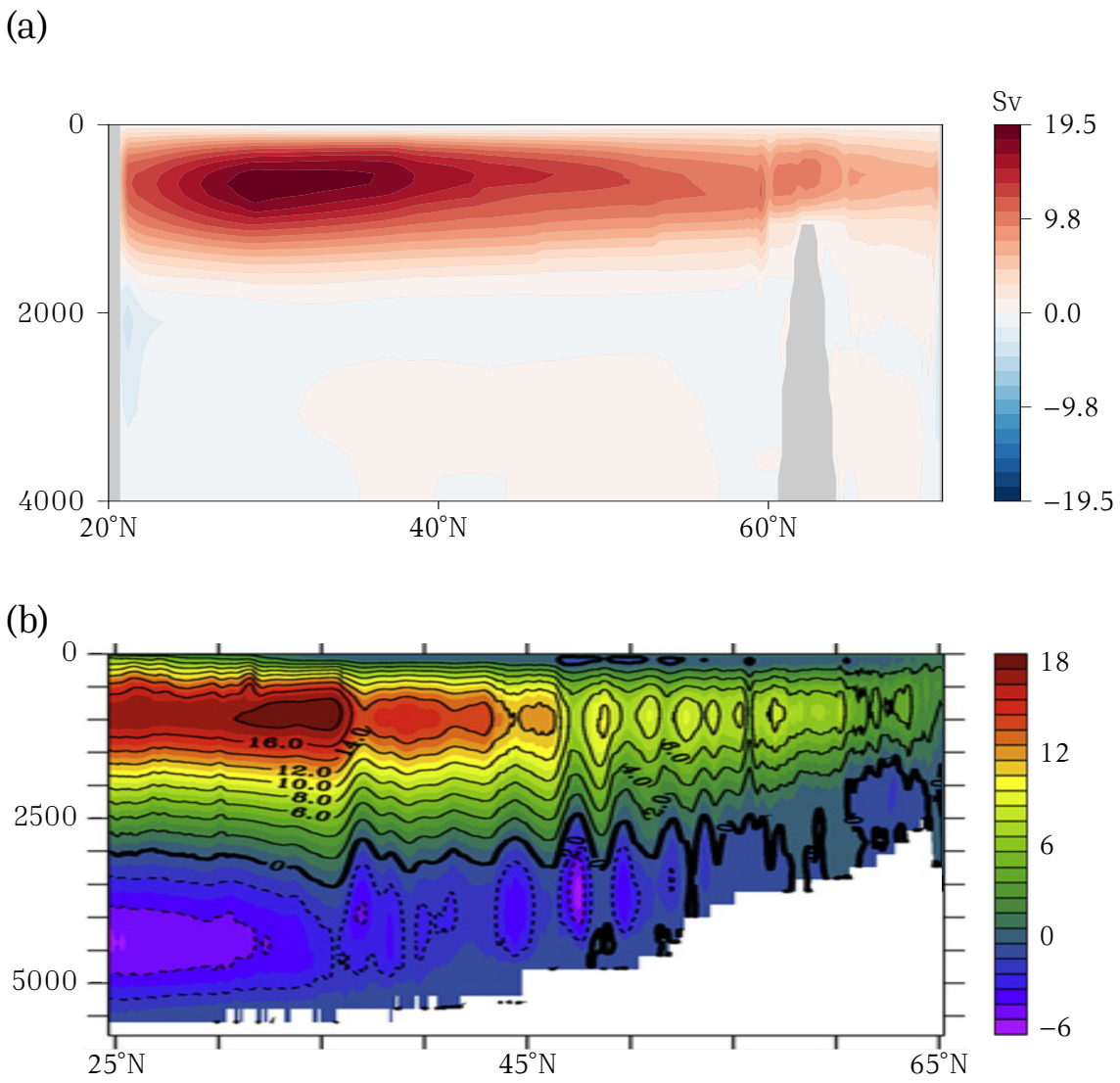


FIGURE 2.6: **(a)** Meridional overturning streamfunction in depth space of the spun-up model control state. The strength of the streamfunction is given in Sverdrups and is shown by the colormap, and depth is in metres. **(b)** Analogous figure for comparison, adapted from Marzocchi et al. (2014), showing the overturning streamfunction in depth space obtained from an eddying ocean model.

shown for comparison in Figure 2.6(b). The maxima of the two upper cells are very similar, both in magnitude, and in location. Further, in both cases, the streamfunction displays a similar gradual diminishing with latitude, and only weakly penetrates into the Nordic Seas. The abyssal cell in Figure 2.6(b), however, is much stronger and extends much further than its counterpart in the idealised model, which suggests that the idealised model representation of bottom water may be deficient.

The upper overturning cell in the idealised model is also restricted to a shallower range of depths than in the more realistic, high-resolution, model. This difference, however, is less pronounced and is less prominent still when the depth is considered as a fraction of the maximum depth, as the idealised model maximum depth is a full 1500 m shallower than in the eddying model of Marzocchi et al. (2014). The difference in depths between the model overturning and that of Marzocchi et al. (2014) is likely in large part a result of the temperature profiles relaxed to in the subtropical and Nordic sponges. From examination of the temperature profile in Figure 2.6, it can be seen that across all depths below ~1700 m in the subtropical sponge, the temperature relaxed to is cooler than any temperature relaxed to at the surface or in the Nordic sponge and this depth is also the approximate depth of the upper overturning cell. This slightly shallow overturning cell is unlikely to be significant as the model is not intended to perfectly resemble the real ocean, only to provide a broadly representative analogue, and the differences between the two overturning circulations in Figure 2.6(b) do not suggest that any key physical processes have been omitted.

The depth-averaged flow fields in the upper and lower limbs of the overturning cell are shown in Figures 2.7(a) and 2.7(b), respectively. These two categories are defined as depths above and below the depth of maximum overturning. Due to the fact that current speeds in the ocean interior are far lower than those in the boundary currents, both the scale of the arrows and the colormap in Figure 2.7 are non-linear to allow simultaneous visualisation of the interior and boundary current velocity fields.

The model appears to do a fairly good job of simulating currents in the model interior: the model analogue of the North Atlantic current follows a similar path to the real world current, separating from the western boundary around 40°N and flowing northeast as a broad, baroclinic current. Flow above the western boundary slope, in both the boundary current itself and the recirculating currents, appears to be barotropic, particularly in the Labrador current in the subpolar gyre.

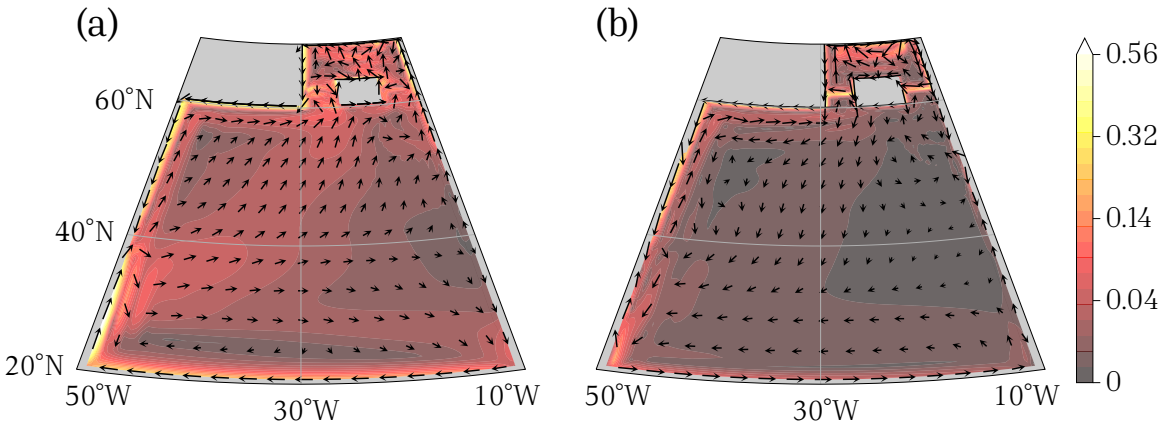


FIGURE 2.7: Depth-averaged flow-fields above, (a), and below, (b), the depth of maximum overturning in depth space in the spun-up model control state. The direction of the flow is shown by the arrows, and the flow speed is indicated by the length of the arrows and the underlying colormap. Speed is given in $\mathrm{m\,s^{-1}}$. Note that the colormap scales logarithmetically, not linearly.

Surface flow through the Nordic basin occurs primarily along the boundaries: flowing in on the eastern boundary and—to a lesser extent—the Icelandic boundaries, and exiting via the western boundary. Deep flow appears to be primarily along isobaths in this region, and so there is little lower flow into or out of the Nordic basin. This pattern is not hugely different from that illustrated in the schematic, taken from Holliday et al. (2018), shown in Figure 1.2. Note that, in any case, this is not a region where the model is expected to perform well, due to the presence of a strong sponge as well as difficulties for coarse-resolution z-coordinate models in representing overflow waters crossing ridges.

The model was constructed with the aim of reproducing the broad features of the large-scale circulation in the subpolar North Atlantic in as simple a model as possible. The motivation behind sacrificing some realism is to expose the physical mechanisms underlying the model response to external forcing, while ensuring results remain applicable to the real ocean. The results shown in this section suggest that the model is able to fairly accurately represent the key features of the circulation in the subpolar North Atlantic, for example, the extent and magnitude of the barotropic and overturning circulations, a southwards-flowing surface current on the western boundary, and a broad baroclinic current flowing northeast across the basin.

2.4 Summary

In this chapter, the general modelling philosophy guiding the design of the experiments in this thesis was introduced, along with the idealised model to be used in those experiments and the MITgcm modelling framework upon which the model is built. The equilibrium state of this model was shown, and compared to that of a high resolution model to demonstrate that it retains a degree of fidelity to the real ocean.

The content set out in this chapter lays the groundwork for interpreting the results of the sensitivity experiments presented in Chapter 3 and Chapter 5, and also defined the discrete notation used to describe the diagnostics used in those chapters. In Chapter 3, the sensivity of the overturning circulation in both depth and density space, as well as of the horizontal gyre circulation, to changes in wind and buoyancy forcing is examined. Chapter 4 then presents the derivation of a novel diagnostic: the rotational momentum balance of the large-scale ocean circulation in the presence of topography. Finally, in Chapter 5 this new diagnostic is then applied to the sensitivity experiments of Chapter 3, to provide an alternative framework for interpreting those results.

3 Decomposing the Subpolar Meridional Overturning Circulation Subject to Different Wind Stress, Buoyancy Forcing, and Topography

3.1 Subpolar Overturning 36
3.1.1 Depth Space vs. Density Space 38
3.1.2 The Importance of Topography 41
3.2 Decomposition of the AMOC 43
3.2.1 Shear Component 45
3.2.2 Ekman Component 47
3.2.3 External Mode Component 47
3.2.4 Numerical Implementation of Decomposition 49
3.3 Numerical Sensitivity Experiments 51
3.3.1 Horizontal Gyre Circulation 52
3.3.2 Overturning in Depth Space 55
3.3.3 Overturning in Density Space 60
3.4 Summary 65

3.1 Subpolar Overturning

As mentioned in Chapter 1, the subpolar North Atlantic is a region of great importance to the Atlantic Meridional Overturning Circulation. Unfortunately,

this region is a particularly challenging one to model. Isopycnals slope strongly across the basin: the broad North Atlantic Current carries warm water polewards near the surface, but the returning upper ocean current on the western boundary—the Labrador Current—carries cold, dense water. This zonal sloping of isopycnals can be easily seen in Figure 3.1. Further, due to a combination of cold ocean temperatures and strong freshwater forcing, salinity plays an important role in controlling ocean density variations at these latitudes. Weak stratification and complex bathymetry mean that topography also plays an important role in this region.

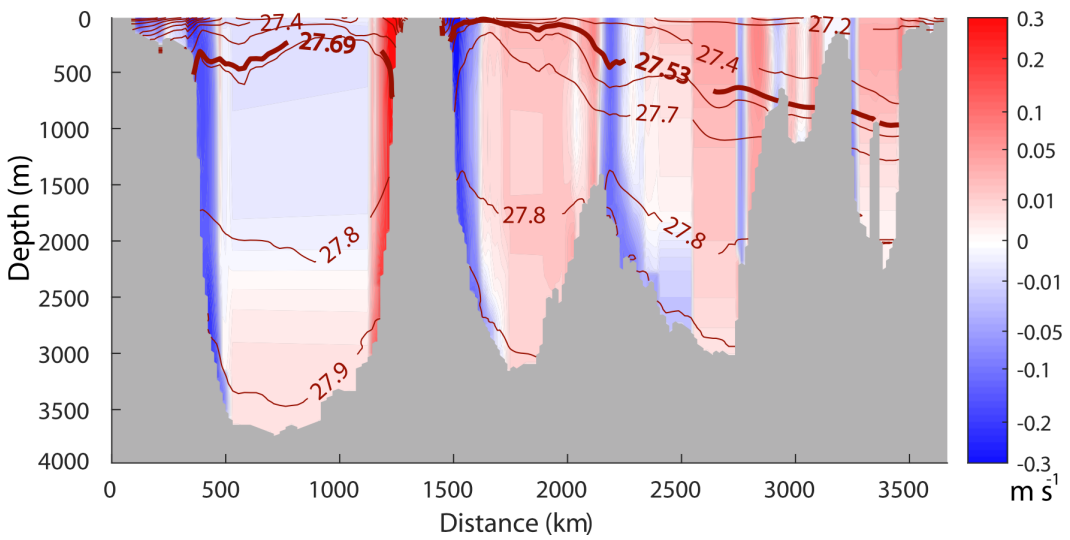


FIGURE 3.1: Mean velocity (colormap, ms^{-1}) and potential density (contours, kg m^{-3}), from observations, across the OSNAP section. The bold isopycnal separates the upper and lower limbs (adapted from Zhang and Thomas 2021)

.

Before the deployment of the OSNAP monitoring program, the paucity of measurements of overturning in the subpolar North Atlantic led to a view of subpolar overturning largely based on model output. The strength of the AMOC in climate models is often linked to densities in the Labrador Sea (e.g., Roberts et al. 2013; Robson et al. 2016). Indeed, the prevailing theory of long-term AMOC variability arising from model studies was that it was driven primarily by the rate of formation of North Atlantic Deep Water in the Labrador Sea (e.g., Bailey et al. 2005; Danabasoglu et al. 2012).

Results from the OSNAP array, and subsequent studies incorporating them, however, have found that overturning in density space across the whole array is dominated by water mass transformation east of Greenland and that transformation in the Labrador Sea plays a much smaller role (Lozier et al. 2019).

The contrasting sensitivity of the AMOC in models and in observations to deep water formation in the Labrador Sea has been addressed by several studies. Zou et al. (2020) explain the surprisingly low overturning in the Labrador Sea in observations as a result of the balancing of changes in density due to cooling by those due to freshening of the boundary current, and suggest that the comparatively large overturning in models may result from inaccurate simulation of the salinity field. In a suite of ocean models with sea ice, Li et al. (2019) find that the local overturning in the Labrador Sea is strongly related to changes in Labrador Sea Water volume across models, but that this relationship degrades quickly along the stream path outside the Labrador Sea. Comparing OSNAP results with a coupled climate model, Menary et al. (2020) find that density variability within the Labrador Sea arises from anomalies due to surface forcing in the Irminger Sea which propagate into the Labrador Sea, and hence that the relationship in models between Labrador Sea density and the AMOC is not necessarily due to overturning within the Labrador Sea.

3.1.1 Choice of Vertical Coordinate: Depth or Density?

Overturning is typically represented mathematically by a zonally-integrated volume transport streamfunction with units of Sverdrups (1 Sv = 10^6 m^3 s^{-1}), and so—in this framework—overturning is a function of both latitude and a vertical coordinate. Given that the overturning has units of volume transport, a natural choice of vertical coordinate is depth. In this case, the overturning streamfunction is given by:

$$\Psi^{(z)}_{\mathrm{MOC}}(y,z) = \int_{-H_{\max}}^{z}\int_{x_{\mathrm{w}}}^{x_{\mathrm{e}}} v(x,y,z')\ \mathrm{d}x\ \mathrm{d}z'\,, \tag{3.1}$$

where z is height (and so is negative below the ocean surface), $H_{\max}$ is the maximum depth along a zonal section, and $x_{\mathrm{w,e}}$ are the western and eastern zonal boundaries at a given latitude and depth. Note that in the case of a zonal section where, for example, the presence of an island means that the trans-basin segment is split into two sub-segments, the zonal integral is simply the sum of the two smaller integrals.

The large-scale ocean is generally stably stratified, and hence vertical density variations tend to be significantly larger than horizontal variations (Li et al. 2020). Density is therefore another potential choice of vertical coordinate, in which case the overturning streamfunction is given by:

$$\Psi^{(\rho)}_{\mathrm{MOC}}(y,\rho) = \int_{\rho_{\max}}^{\rho}\int_{x_{\mathrm{w}}}^{x_{\mathrm{e}}} v(x,y,\rho')\left(\frac{\partial\rho}{\partial z}\right)^{-1} \mathrm{d}x\ \mathrm{d}\rho' \,, \tag{3.2}$$

where ρ is density, $\rho_{\max}$ is the maximum density along the section, and the partial derivative term $(\partial\rho/\partial z)^{-1}$ is included to ensure units of volume transport are preserved.

Having defined an overturning streamfunction Ψ_{MOC}, the strength of the AMOC at a given latitude is then simply the maximum of this streamfunction over the chosen vertical coordinate:

$$\mathrm{MOC}_z(y) = \max_z\{\Psi^{(z)}_{\mathrm{MOC}}(y,z)\}\ ; \qquad \mathrm{MOC}_\rho(y) = \max_\rho\{\Psi^{(\rho)}_{\mathrm{MOC}}(y,\rho)\}\ . \tag{3.3}$$

The choice of vertical coordinate is significant, as the two different overturning streamfunctions $\Psi^{(z)}_{\mathrm{MOC}}$ and $\Psi^{(\rho)}_{\mathrm{MOC}}$ describe different processes. In depth space, the process described is the net Eulerian upwelling/downwelling of water at a given latitude. It therefore does not explicitly tell us anything about the rate of water mass transformation. The overturning in density space, on the other hand, can tell us the rate at which water is being transformed from one density class to another, but not where newly-formed deep water occurs. Although evidently linked, the two processes of water transformation by buoyancy loss and Eulerian downwelling are not generally coincident in the ocean: the transformation of upper limb water to lower limb water occurs

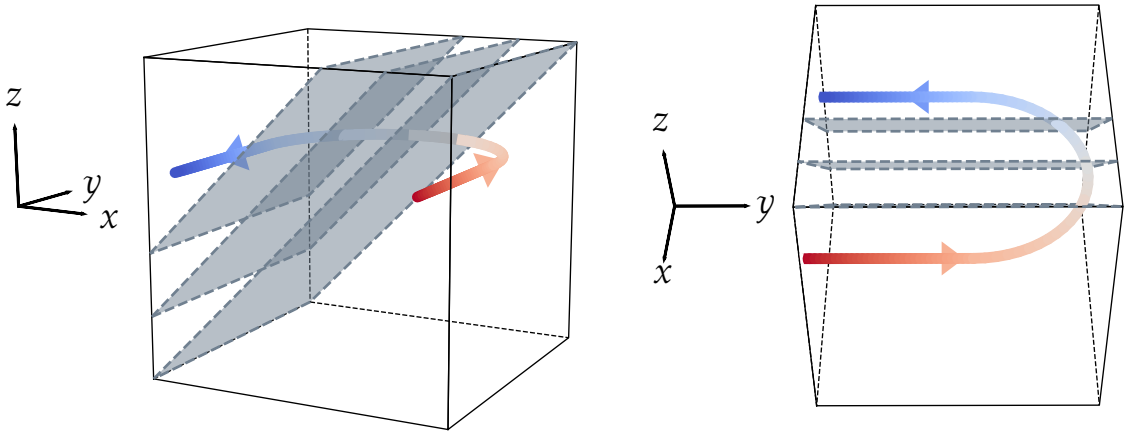


FIGURE 3.2: Schematic showing how horizontal circulation across sloped isopycnals leads to an overturning in density space. The colored line with arrows shows flow at constant depth (color indicates density), and the grey inclined planes are isopycnals. The right hand schematic is the same as the left hand one, but is rotated to a viewing angle parallel to the isopycnal planes to highlight the overturning in density space.

largely in the interior of specific convective regions where there is very little net downwelling (Send and Marshall 1995; Spall and Pickart 2001), whereas downwelling of newly formed lower limb water occurs primarily within the boundary current flowing around these regions (Pedlosky 2003; Spall 2003).

Not only are the two not necessarily coincident, but they may also have different magnitudes. For example, consider an ocean region with isopycnals which slope zonally across the basin, with a current flowing *at a constant depth* northwards on the eastern side of the basin with a return flow southwards on the western boundary (as illustrated in Figure 3.2). In depth space, the northwards flow is balanced exactly in the zonal integral by the return flow on the western boundary, and so there is no overturning in depth space. In density space, however, the water flowing northwards is of a different density to the return flow, and so the two do not cancel, giving a net overturning.

As can be seen from Figure 3.1, isopycnals in the subpolar North Atlantic slope zonally across the basin. The stratification term in definition (3.2) is therefore a function of x, so the overturning calculated in depth space and that calculated in density space would be expected to differ. Indeed, the strength of the overturning measured across the OSNAP array over the period 2014–2016

in density space was significantly larger than that measured in depth space: $MOC_\rho = 14.9 \pm 1.0$ Sv and $MOC_z = 8.0 \pm 0.7$ Sv (Frajka-Williams et al. 2019). This discrepancy is further illustrated by Zhang and Thomas (2021), who find that the contribution of the horizontal gyre circulation to the overturning in density space by carrying water across isopycnals is potentially as much as 40% for the maximum mean overturning.

3.1.2 The Importance of Topography

The weaker stratification in the subpolar region than that in the subtropics leads to subpolar currents generally having a larger barotropic component than their subtropical counterparts (Daniault et al. 2016). This allows for topography to exert a greater influence on the large-scale circulation at subpolar latitudes than in the subtropics. The interior circulation in an ocean basin adjusts via the propagation of Rossby waves of progressively higher baroclinic modes (Young 1981; Killworth et al. 1997). The speed of these waves decreases with higher modes, and so the fastest mode is the barotropic mode, quickly setting up the barotropic circulation in the basin, with subsequent baroclinic modes acting to stratify the flow and restrict it to the surface, effectively shielding it from the effects of topography. As such, topography becomes increasingly important as the flow speed approaches the speed of the first baroclinic Rossby wave (Hughes and de Cuevas 2001). In the subtropics, the wave speed of the first baroclinic Rossby wave is of order $\sim 10\,\mathrm{cm\,s^{-1}}$, whereas at high latitudes this speed drops to around $\sim 1\,\mathrm{cm\,s^{-1}}$. As such, it should be expected that topography would have a greater impact on the circulation in general in the subpolar region than in the subtropics.

For an ocean in Sverdrup balance, fluid can only cross the isolines of potential vorticity (contours of f/H for the depth-integrated circulation) if the resultant change in planetary vorticity is balanced by the input of relative vorticity from the curl of the wind stress (see, e.g., Pedlosky 1987, for a comprehensive overview). Sverdrup balance, however, can generally only satisfy the (no normal

flow) boundary conditions on one of the western and eastern boundaries, and also does not necessarily conserve mass within the basin. The circulation is closed by the presence of a western boundary current, and so if the isolines of potential vorticity impinge on the boundary, there must be significant flow across these f/H contours which cannot be balanced by wind stress curl, and so some other process must provide the required source/sink of relative vorticity.

For a basin with vertical sidewalls, the isolines of potential vorticity are simply lines of latitude, and therefore flow in the western boundary current is necessarily across these isolines, requiring an input of vorticity from some source other than wind stress curl to balance the advection of planetary vorticity. The term providing this balance determines the nature of the boundary current, and can be lateral friction (e.g., Munk 1950), bottom drag (e.g., Stommel 1948), or inertia (e.g., Charney 1955).

The presence of topography in the form of a sloping western boundary deforms f/H contours, such that a meridional flow conserving potential vorticity is possible, as the input of relative vorticity by the bottom pressure torque balances the advection of planetary vorticity by the meridional flow (Holland 1973). As the boundary current returns fluid along the western boundary, it must deflect either up or down the topography to ensure the conservation of potential vorticity. The boundary current is therefore steered by the topography, leading to a distortion of the shape of the gyre (Jackson et al. 2006). As the meridional flow can now be balanced without the explicit need for dissipation, the boundary current becomes progressively more inertial as the width of the topographic slope increases (Hughes and de Cuevas 2001). The barotropic gyre circulation for a given wind stress therefore also increases.

Further, although the ability of the horizontal gyre circulation to drive an overturning in density space has already been demonstrated (Figure 3.2), in the presence of zonally-varying topography the depth-independent flow can induce an overturning even in depth space. This component of the overturning is referred to as the external mode (Lee and Marotzke 1998). Two alternative

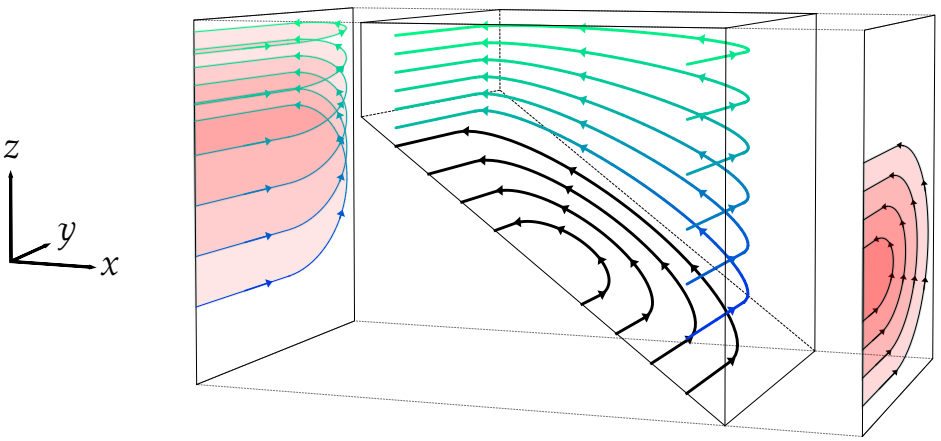


FIGURE 3.3: Schematic showing the possibility of an overturning in depth space arising from depth-independent flow over zonally non-uniform topography, whether the flow considered is taken to be the barotropic circulation (colored lines; color here indicates depth), or the bottom flow (heavy black lines).

ways of conceptualising this overturning are illustrated in Figure 3.3: First, consider a barotropic circulation with a northward flow over a deep region of the domain and a southward return flow over a shallower region. To conserve mass, the transport in each of these currents must be the same. This implies that the southwards-flowing "shallow" current must be more intense than the "deep" northwards-flowing one. At shallow depths, therefore, the zonally-integrated flow will be southward, whereas at depth the shallow current does not contribute and so the zonally-integrated flow will be northward, yielding a net overturning. Alternatively, considering only the bottom flow: flow in one direction at depth and the shallower return flow are connected by flow along the zonal slope which, when zonally-integrated, yields an overturning.

3.2 Decomposition of the AMOC in Density and Depth Space

The decomposition of the overturning in depth space, $\Psi^{(z)}_{\mathrm{MOC}}$, into components which can then be analysed separately is a fairly standard diagnostic tool (e.g., among others, Lee and Marotzke 1998; Sime et al. 2006; Hirschi and Marotzke 2007). Indeed, such a decomposition is fundamental to the design of

the trans-basin mooring array method of measuring overturning employed by the RAPID and OSNAP programs (Baehr et al. 2004; Rayner and Kanzow 2011; Lozier et al. 2017; Li et al. 2017). Similarly, the advantages of using density instead of depth as the vertical coordinate when calculating overturning in regions such as the North Atlantic subpolar gyre—where the isopycnals are sloping—are well known, and use of $\Psi^{(\rho)}_{\mathrm{MOC}}$ is commonplace (Lozier et al. 2019). It is therefore, perhaps, surprising that this decomposition has not been applied (to the best of my knowledge) to the overturning in density space.

In this section, a method of decomposing the AMOC is outlined which allows for the calculation of the various components of the overturning in either density or depth space. The method by which each component is calculated mathematically and the numerical implementation of the decomposition are provided. The application of this diagnostic to a series of model experiments then forms the basis of the following section.

The first step of the decomposition is to split the meridional velocity field into geostrophic and surface Ekman components (nonlinear and other terms are neglected):

$$v = v_g + v_{\mathrm{Ek}} \, . \tag{3.4}$$

The geostrophic component is then further decomposed into a depth-independent component, referred to as the *external mode*, and a *shear velocity* (Lee and Marotzke 1998). This leaves us with a velocity field decomposed into three separate components:

$$v = v_{\mathrm{sh}} + v_{\mathrm{ext}} + v_{\mathrm{Ek}} \, , \tag{3.5}$$

where v_{sh}, v_{ext} and v_{Ek} are the shear, external mode, and Ekman components, respectively. The method for calculating these components are described in the following sections. In this thesis, the shear component of the velocity is defined to be zero at the ocean floor, and so the depth-independent external mode component is simply the bottom velocity. The overturning mediated by each of

these components is then simply obtained by substituting the relevant component of the velocity in place of the full velocity field in equations (3.1) and (3.2).

3.2.1 The Shear Component

The shear velocity is the component of the geostrophic velocity which varies with depth. For a velocity field in geostrophic balance, the variation with depth is given by the thermal wind relation. In a Boussinesq fluid, the thermal wind relation is given by:

$$f\frac{\partial v_g}{\partial z} = f\left(\frac{\partial v_{\text{sh}}}{\partial z} + \frac{\partial v_{\text{ext}}}{\partial z}\right) = -\frac{g}{\rho_0}\frac{\partial \rho}{\partial x}\,, \tag{3.6}$$

but v_{ext} is independent of depth, so

$$f\frac{\partial v_{\text{sh}}}{\partial z} = -\frac{g}{\rho_0}\frac{\partial \rho}{\partial x}\,. \tag{3.7}$$

The shear velocity can then be obtained by integrating (3.7) in the vertical direction and dividing by the Coriolis parameter f. Since the shear velocity is defined such that $v_{\text{sh}} = 0$ at the bottom boundary, we have that:

$$v_{\text{sh}}(x,y,z) = -\int_{-H}^{z}\frac{g}{\rho_0 f}\frac{\partial \rho}{\partial x}(x,y,z')\,\mathrm{d}z'\,. \tag{3.8}$$

To find the contribution of the shear velocity to the overall overturning in depth space, (3.8) can be substituted into (3.1):

$$\Psi^{(z)}_{\text{sh}}(y,z) = -\frac{g}{\rho_0 f}\int_{-H_{\max}}^{z}\int_{x_{\text{w}}}^{x_{\text{e}}}\int_{-H}^{z'}\frac{\partial \rho}{\partial x}(x,y,z'')\,\mathrm{d}z''\,\mathrm{d}x\,\mathrm{d}z'\,, \tag{3.9}$$

where $H_{\max}$ is the zonal maximum depth across a section (that is, $H_{\max}$ is given by $H_{\max}(y) = \max_x(H(x,y))$).

When considering the overturning in depth space, it is possible to exploit the orthogonality of the vertical and zonal coordinates such that the triple integral in equation (3.9) collapses nicely into a single integral over depth via the following procedure. First, Fubini's theorem is used to switch the order of

integration, such that the innermost integral is a zonal integral of a zonal partial derivative:

$$\Psi^{(z)}_{\mathrm{sh}}(y,z) = -\frac{g}{\rho_0 f}\int_{-H_{\max}}^{z}\int_{-H_{\max}}^{z'}\int_{x_{\mathrm{w}}}^{x_{\mathrm{e}}}\frac{\partial\rho}{\partial x}(x,y,z'')\,\mathrm{d}x\,\mathrm{d}z''\,\mathrm{d}z'\,. \tag{3.10}$$

This zonal integral can then be evaluated using the fundamental theorem of calculus, leaving a double integral over depth

$$\Psi^{(z)}_{\mathrm{sh}}(y,z) = -\frac{g}{\rho_0 f}\int_{-H_{\max}}^{z}\int_{-H_{\max}}^{z'}(\rho_{\mathrm{e}}(y,z') - \rho_{\mathrm{w}}(y,z'))\,\mathrm{d}z''\,\mathrm{d}z'\,. \tag{3.11}$$

Now applying Cauchy's rule for repeated integrals leaves a single integral over depth:

$$\Psi^{(z)}_{\mathrm{sh}}(y,z) = -\frac{g}{\rho_0 f}\int_{-H_{\max}}^{z}(z-z')\,(\rho_{\mathrm{e}}(y,z') - \rho_{\mathrm{w}}(y,z'))\,\mathrm{d}z'\,. \tag{3.12}$$

The final expression for $\Psi^{(z)}_{\mathrm{sh}}$ derived in (3.12) depends only on the boundary density profiles ρ_{w} and ρ_{e}, and is therefore independent of conditions in the ocean interior. It is this property of the geostrophic component of the overturning in depth space which makes this decomposition of the overturning so useful in the design of transbasin mooring arrays, as it is possible to deduce the integrated overturning in depth space across an entire section from the two density profiles bounding it (Li et al. 2017; Rayner and Kanzow 2011). Model studies using this decomposition (or a similar one) also exploit this simplification, and so tend to deal primarily with zonally-integrated meridional transports (e.g., Hirschi and Marotzke 2007; Waldman et al. 2021).

Unfortunately, this useful property of the expression for the shear component of the overturning holds only when depth is chosen as the vertical coordinate. When density is chosen as the vertical coordinate, the shear component of the overturning can be obtained by substituting (3.8) into (3.2):

$$\Psi^{(\rho)}_{\mathrm{sh}}(y,\rho) = -\frac{g}{\rho_0 f}\int_{\rho_{\max}}^{\rho}\int_{x_{\mathrm{w}}}^{x_{\mathrm{e}}}\int_{-H}^{z}\frac{\partial\rho}{\partial x}(x,y,z')\left(\frac{\partial\rho}{\partial z}\right)^{-1}(x,y,\rho')\,\mathrm{d}x\;\mathrm{d}\rho'\,\mathrm{d}z'\,. \tag{3.13}$$

The dependence of the $(\partial\rho'/\partial z)^{-1}$ term in (3.13) on x means that the zonal integral can no longer be easily evaluated. The implication of this is that the

overturning due to the geostrophic shear in density space is not set purely by density profiles on the boundaries—local zonal variations are important. It is therefore important to retain the full meridional velocity field as given by equation (3.8) to be able to calculate the overturning in density space.

3.2.2 The Ekman Component

The Ekman contribution to the overturning is estimated from the surface wind stress by calculating the depth-integrated transport from Ekman theory (see, e.g., Vallis 2006), and then uniformly distributing this transport across a surface Ekman layer of a prescribed depth δ_{Ek}. For calculation of v_{Ek}, a value of $\delta_{\mathrm{Ek}} = 52$ m is used (chosen to coincide with a boundary between model levels).

The depth-integrated Ekman velocity is given by

$$V_{\mathrm{Ek}}(x,y) = -\frac{\tau_x(x,y)}{f(y)\rho_0}\,, \tag{3.14}$$

where τ_x is the zonal wind stress. Assuming the Ekman velocity is constant within the Ekman layer and zero below it,

$$v_{\mathrm{Ek}}(x,y,z) = -\frac{\mathbf{1}_{\mathrm{Ek}}(x,y,z)}{\min\{\delta_{\mathrm{Ek}}, H(x,y)\}}\frac{\tau_x(x,y)}{f(y)\rho_0}\,, \tag{3.15}$$

where $\mathbf{1}_{\mathrm{Ek}}(x,y,z)$ is an indicator function for the Ekman layer:

$$\mathbf{1}_{\mathrm{Ek}}(x,y,z) = \begin{cases} 1\,, & \text{if } z \geq -\min\{\delta_{\mathrm{Ek}}, H(x,y)\} \\ 0\,, & \text{otherwise.} \end{cases} \tag{3.16}$$

Having calculated the Ekman velocity, the resulting components of the overturnings in depth and density space are then obtained by substituting (3.15) into equations (3.1) and (3.2) respectively.

3.2.3 The External Mode Component

As previously discussed in Section 3.1, and illustrated by Figure 3.2 and Figure 3.3, a depth-independent flow can mediate an overturning in both depth and density space under certain conditions. The nature of this overturning, however, depends on how this depth-independent velocity is defined.

The first approach is to treat the external mode such that it includes barotropic parts of the other components (Lee and Marotzke 1998; Sime et al. 2006). It is therefore the overturning resulting from the full, depth-averaged, meridional velocity, that is, it is the overturning mediated by the barotropic gyre circulation. This treatment yields closed circulations and illustrates more clearly the effect of each component on the overall overturning, but slightly alters their interpretations. For example, the Ekman component now represents the transport due to flow in the surface Ekman layer plus a barotropic return flow over the full depth.

The other approach is to treat the external mode simply as the transport resulting from the bottom velocity (Jonathan et al. 2021). In this case, the interpretation of the individual terms is clearer, and the decomposition is closer to that used in the arrays deployed to estimate overturning in the ocean. It does not, however, necessarily yield closed circulations for each component, as generally the depth-integrated meridional transport for an individual component will not be zero. This issue, however, can be mitigated by *correcting* the velocities by subtracting from each component its section-averaged velocity, given by

$$v_{\text{correction}}(y) = \frac{\int_{-H_{\max}}^{0}\int_{x_{\text{w}}}^{x_{\text{e}}} v(x,y,z)\,\mathrm{d}x\,\mathrm{d}z}{\int_{-H_{\max}}^{0}\int_{x_{\text{w}}}^{x_{\text{e}}} \mathrm{d}x\,\mathrm{d}z}\,. \tag{3.17}$$

If, instead, the velocities were corrected locally by subtracting their depth average, an alternative correction velocity $\hat{v}_{\text{correction}}$ would be obtained which would be a function of both x and y:

$$\hat{v}_{\text{correction}}(x,y) = \frac{\int_{-H}^{0} v(x,y,z)\,\mathrm{d}z}{H}\,.$$

The zonal dependence of this alternative correction velocity means that a different value for the meridional transport will be obtained. For each component, the total meridional transport from $v_{\text{correction}}(y)$ is simply the area of the section times the correction velocity, whereas calculating the transport

arising from $\hat{v}_{\text{correction}}(x, y)$ requires evaluation of the zonal integral due to the dependence on x.

The depth-independent external mode velocity is defined to be the bottom velocity and can be obtained by considering the depth integral of (3.4).

$$\int_{-H}^{0} v(x, y, z)\ \mathrm{d}z = \int_{-H}^{0} (v_{\text{sh}}(x, y, z) + v_{\text{ext}}(x, y) + v_{\text{Ek}}(x, y, z))\ \mathrm{d}z\,. \tag{3.18}$$

As v_{ext} has no depth dependence, it can be brought outside the integral, and the equation can then be rearranged for v_{ext}:

$$\begin{aligned} v_{\text{ext}} &= \frac{1}{H} \int_{-H}^{0} (v(x, y, z) - v_{\text{sh}}(x, y, z) - v_{\text{Ek}}(x, y, z))\ \mathrm{d}z\,, \\ &= \frac{1}{H} \int_{-H}^{0} (v(x, y, z) - v_{\text{sh}}(x, y, z))\ \mathrm{d}z + \frac{\tau_x(x, y)}{f(y)\rho_0 H}\,. \end{aligned} \tag{3.19}$$

3.2.4 Numerical Implementation of Decomposition

As stated in Section 3.2.1, to be able to apply the decomposition in both depth and density space, the full meridional velocity field for each component is required. The procedure for implementing the decomposition diagnostic for each component can then be summarised as follows. First, calculate the meridional velocity field, ensuring it is defined on the u-point, then calculate the meridional transport in each grid cell, interpolate into density space if necessary, and finally integrate zonally and vertically to obtain the overturning. Note that it is necessary to obtain the values for property fields on the u-point because the thermal wind relation between the geostrophic meridional velocity field and the zonal pressure gradient is derived from the zonal component of the horizontal momentum equation and hence the relations (3.6), (3.7) and (3.8) only hold at the u-point.

The shear velocity is given by (3.8), which—using the notation defined in Section 2.2.4—discretises to:

$$v_{\text{sh}} = -\frac{g}{\rho_0 f} \sum_k \frac{\delta_i \rho}{\Delta x} h \Delta r\,. \tag{3.20}$$

Because the density is defined at the T-point (the cell centre), its zonal derivative is then located at the u-point. Therefore no interpolation is necessary and the shear velocity indexed by (k, j, i) is given by

$$v_{\mathrm{sh},kji} = -\frac{g}{\rho_0 f_j \Delta x^c_j} \sum_{m=1}^{k} \left(\rho_{mj(i+1)} - \rho_{mji}\right) h^{\mathrm{w}}_{mji} \Delta r^f_m \,. \tag{3.21}$$

The zonal wind stress is also defined at the u-point, and therefore all quantities in the equation for the Ekman velocity are defined at the correct location, so (3.15) is discretised as:

$$v_{\mathrm{Ek},kji} = -\frac{\varepsilon^{\mathrm{Ek}}_{kji}}{\min\{\delta_{\mathrm{Ek}}, H^{\mathrm{w}}_{ji}\}} \frac{\tau_{x,ji}}{\rho_0 f_j} \tag{3.22}$$

where $\varepsilon^{\mathrm{Ek}}_{kji}$ is the fraction of the volume of the cell indexed by (k, j, i) which lies within the Ekman layer.

The full meridional velocity field is defined at the v-point, and so needs to be interpolated onto the u-point before the discretised bottom velocity can be obtained from (3.19):

$$v_{\mathrm{ext}} = \frac{1}{H} \sum_k \left[\left(\overline{\overline{v}^{\,i}}^{\,j} - v_{\mathrm{sh}} - v_{\mathrm{Ek}} \right) h \Delta r \right] \,. \tag{3.23}$$

Expanding the average gives the following expression for the external mode velocity in all cells with horizontal indices (j,i).

$$v_{\mathrm{ext},ji} = \frac{1}{H^{\mathrm{w}}_{ji}} \sum_{k=1}^{k_{\max}} \left[\left(\frac{v_{kj(i+1)} + v_{kji} + v_{k(j-1)(i+1)} + v_{k(j-1)i}}{4} - v_{\mathrm{sh},kji} - v_{\mathrm{Ek},kji} \right) h^{\mathrm{w}}_{kji} \Delta r^f_k \right] \,, \tag{3.24}$$

where $v_{\mathrm{sh},kji}$ and $v_{\mathrm{Ek},kji}$ are given by (3.21) and (3.22).

From these velocities, the meridional transport per unit area in each cell is derived simply by multiplying through by the cell thickness, and is therefore given by:

$$\mathcal{T}_{kji} = v_{kji} h^{\mathrm{w}}_{kji} \Delta r^f_k \,. \tag{3.25}$$

To calculate the transport in density space, a vertical grid must first be defined with θ as the coordinate (recall that in the model used in this thesis, buoyancy

is a function of temperature only). The meridional transport in density space in the cell indexed by (l, j, i) where l is the index in the temperature coordinate direction is then calculated from (3.25) and the known temperature field via:

$$\begin{aligned}\mathcal{T}^{(\rho)}_{lji} &= \sum_{k=1}^{k_{\max}} \varepsilon^{(\theta)}_{lkji} \mathcal{T}_{kji} \,, \\ &= \sum_{k=1}^{k_{\max}} \varepsilon^{(\theta)}_{lkji} v_{kji} h^{\mathrm{W}}_{kji} \Delta r^{f}_{k} \,,\end{aligned} \tag{3.26}$$

where $\varepsilon^{(\theta)}_{lkji}$ is a weighting function, given by the fractional overlap between the temperature in the cell in z-space indexed by (k, j, i) and the cell thickness in temperature space indexed by l. This method of interpolating transports effectively bins the meridional transport by its temperature, and ensures that the total transport is conserved, i.e., $\sum_{\{k,j,i\}} \mathcal{T}_{kji} = \sum_{\{l,j,i\}} \mathcal{T}^{(\rho)}_{lji}$.

To obtain the full overturning components, these transports are then integrated zonally and cumulatively summed in the vertical:

$$\Psi^{(z)}_{kj} = \sum_{m=1}^{k} \sum_{i=1}^{i_{\max}} v_{mji} h^{\mathrm{W}}_{mji} \Delta r^{f}_{m} \Delta x^{c}_{ji} \,, \tag{3.27}$$

$$\Psi^{(\rho)}_{lj} = \sum_{m=1}^{l} \sum_{i=1}^{i_{\max}} \sum_{k=1}^{k_{\max}} \varepsilon^{(\theta)}_{mkji} v_{kji} h^{\mathrm{W}}_{kji} \Delta r^{f}_{k} \Delta x^{c}_{ji} \,, \tag{3.28}$$

where v is either the four-point average of the full velocity field $\overline{\overline{v}^{i}}^{j}$, or one of the components defined by (3.21), (3.22), or (3.24).

3.3 Numerical Sensitivity Experiments

The model is spun-up in four different configurations based on the control state described in Section 2.3.2: the control state itself, as well as a configuration with no buoyancy forcing, a configuration with no wind forcing, and a configuration with vertical sidewalls. The no-wind-forcing setup is fairly self-explanatory: the surface zonal wind stress is simply set to zero. In the no-topography configuration, the model wind and buoyancy forcing are unchanged, but the model sidewalls are set to be vertical at every boundary. The sill, however, is retained.

The no-buoyancy forcing configuration is the most difficult to realise, as the state obtained depends strongly on how "no buoyancy forcing" is defined. If all buoyancy forcing is removed, then the initial model stratification will be gradually eroded by diapycnal mixing, finally leaving a barotropic ocean. The definition settled on was that the sponge in the subtropics is left unchanged, whereas the relaxation of ocean temperature in the surface layer and within the Nordic sponge are both set to zero. This choice is somewhat arbitrary, but can be rationalised as allowing the ocean to remain stratified (by relaxation to the initial stratification within the subtropical sponge), while not altering buoyancy by external forcing while a water parcel is within the "subpolar" region of the model.

3.3.1 The Horizontal Gyre Circulation

The resulting barotropic circulations are shown in Figure 3.4. Figure 3.4(a) is a duplicate of Figure 2.5(a) and is reproduced here for comparison. When the model is spun up in the no-buoyancy-forcing configuration, the barotropic circulation again forms two gyres of opposing sign separated at 40°N, as shown in Figure 3.4(b). The pattern of circulation strongly resembles the frictional gyres of Munk (1950), with surprisingly little of the distortion found by Jackson et al. (2006) due to the presence of a sloping western boundary. The major difference between the circulation in the no-buoyancy-forcing and control configurations is the lack of the vigorous recirculations above the topographic slope present in the control state but not in the no-buoyancy-forcing case.

The barotropic streamfunction in the no-wind-forcing configuration (Figure 3.4(d)), on the other hand, has only very weak circulations in the ocean interior. There are, however, intense narrow circulations confined to the regions above the sloping western and northwestern boundaries. These circulations are clockwise and anticlockwise in the subtropical and subpolar regions, with similarly narrow, but far weaker, opposing recirculations to the east. Qualitatively at least, the control state (Figure 3.4(a)) appears almost to

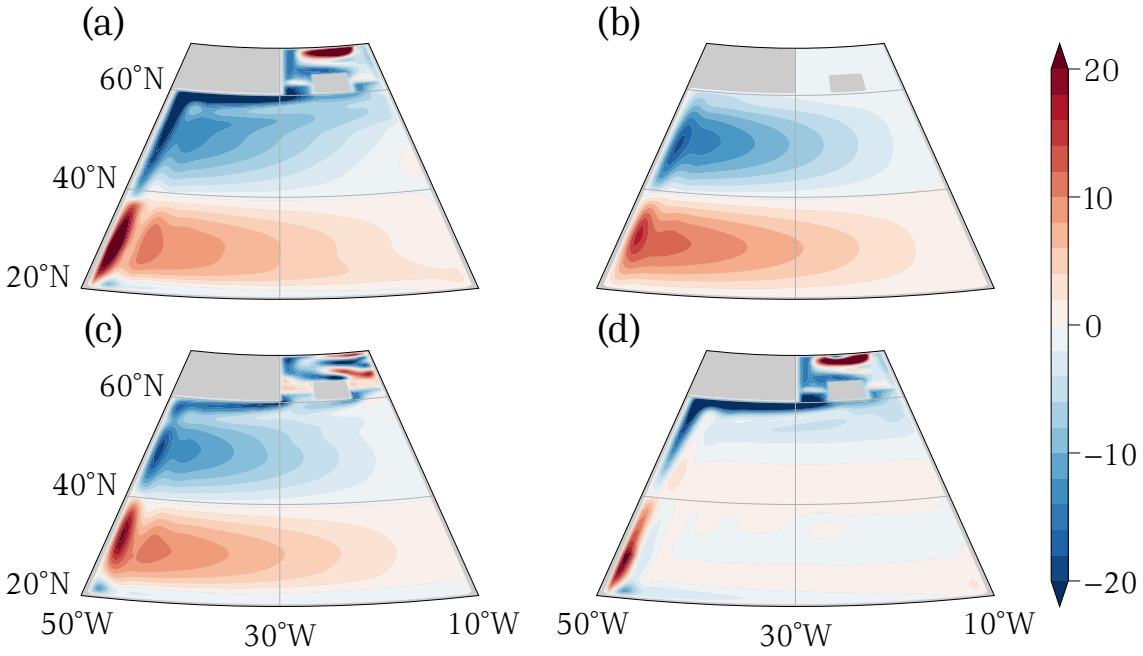


FIGURE 3.4: Barotropic streamfunctions (in Sv) for different model configurations after spin-up: (a) control run, (b) no buoyancy forcing, (c) vertical sidewalls, and (d) no wind forcing.

be a superposition of the equilibrium state in the presence of only buoyancy forcing (Figure 3.4(d)) and the equilibrium state in the presence of only wind forcing (Figure 3.4(b)). Under this premise, the interior barotropic circulation is dominated by the wind-driven circulation, whereas the circulation in proximity to the western boundary is dominated by buoyancy forcing.

Now considering the vertical-sidewalls case (Figure 3.4(c)), the barotropic circulation in the ocean interior is of a similar magnitude to that in the control state, and to that in the no-buoyancy-forcing configuration. The boundary circulation present in the no-wind and control configurations, however, is far weaker than in both the aforementioned cases. In fact, for the vertical-sidewalls case, while the buoyancy forcing is identical to the no-wind and control cases, bears a far stronger relationship to the no-buoyancy configuration than to either of the other two. This is the first hint that there may be some interplay between the buoyancy force and zonally non-uniform topography. This possible interaction will be explored in more detail in Chapters 4 and 5

Figure 3.5 shows the direction and magnitude of the surface flow in each of

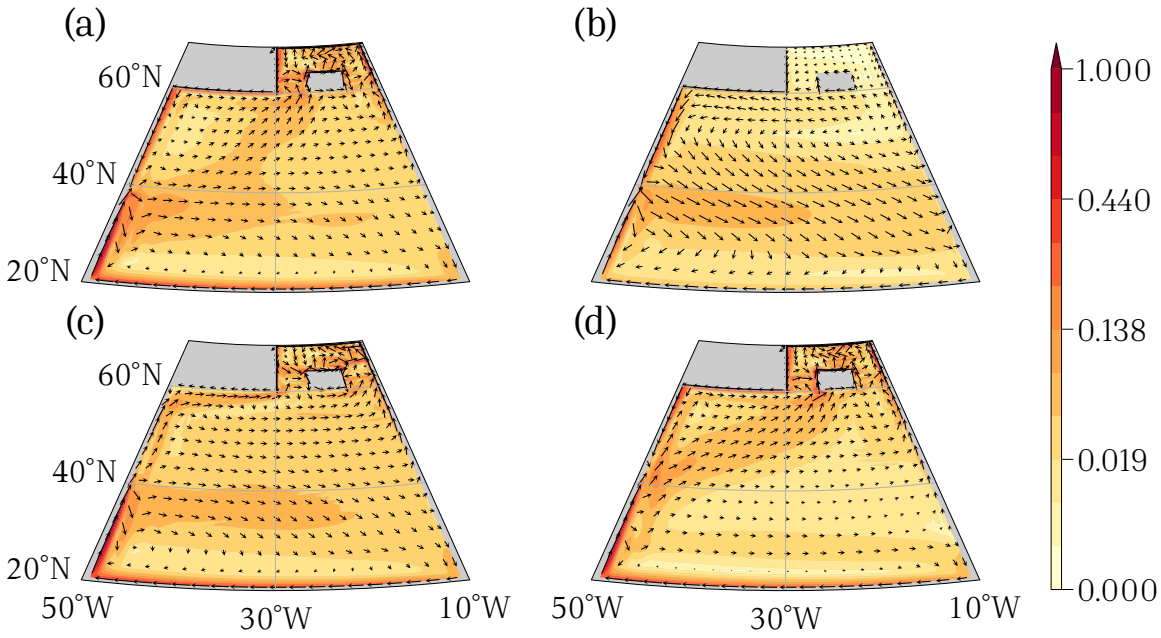


FIGURE 3.5: Surface flow field for different spun-up model configurations: **(a)** control run **(b)** no buoyancy forcing **(c)** vertical sidewalls **(d)** no wind forcing. Arrows indicate direction and speed of flow, and colormap also shows flow speed (in $\mathrm{m\,s^{-1}}$). Note that both the colormap and arrow size scale logarithmically with flow speed.

the four configurations. In all of the plots surface currents along the boundaries—with the exception of the eastern boundary—are far stronger than those in the basin interior. A northeastwards-flowing surface current analogous to the North Atlantic Current, however, is only present in two of the configurations: the control state, and the no-wind-forcing configuration.

In the no-buoyancy-forcing configuration shown in Figure 3.5(b), the pattern of surface flow is largely what would be expected from Ekman theory (e.g., Vallis 2006). The surface flow in the ocean interior is generally south-eastwards and there is divergence of the surface flow field—and hence upwelling—in the subpolar region where the zonal wind stress is decreasing with latitude and convergence (and downwelling) in the subtropics where the wind stress increases with latitude. The northwards-flowing western boundary current separates from the boundary at around 40°N but, away from the boundary, there is no northwards surface flow in the subtropics and therefore no North Atlantic Current.

In the vertical sidewalls case Figure 3.5(c) the interior flow bears a stronger resemblance to the no-buoyancy-forcing configuration than to either the control or no-wind-forcing configurations, particularly in the subtropics. Again, the western boundary current separates from the boundary at around 40°N and is then confined to the subtropics. In this case, however, the separation is only partial and the surface flow along the entire western boundary is northwards. The western boundary current in both the no-wind-forcing and control configurations separates from the boundary around 40°N and continues northeastwards as a broad current, as shown by Figures 3.5(d) and 3.5(a). In the no-wind-forcing case, however, once the northwards boundary current detaches from the western boundary, it splits such that there is still some northwards flow parallel to the boundary, similarly to the vertical sidewalls case. As such the only configuration that gives a "realistic" gyre circulation and pattern of surface currents, with opposing western boundary currents in the subtropics and subpolar region, as well as a North Atlantic Current analog flowing across the basin in the subpolar latitudes, is the control.

3.3.2 The Meridional Overturning Circulation: Depth Space

The total meridional overturning circulation in z-space for each configuration is shown in Figure 3.6. It is immediately obvious that buoyancy forcing is the dominant factor in determining the overall strength of the equilibrated overturning in z-space: the overturning in the no-buoyancy-forcing configuration shown in Figure 3.6(b) is limited to a weak Ekman cell centred at 40°N (the latitude of peak zonal wind stress).

It appears that the wind-stress forcing has the smallest impact on the overturning in depth space. In the no-wind-stress configuration, the overturning stream function, shown in Figure 3.6(d), shares many characteristics with that in the control. The magnitude of maximum overturning is unaffected, and in both cases, the streamfunction penetrates into the Nordic basin only weakly, implying that in both cases a significant proportion of the net Eulerian

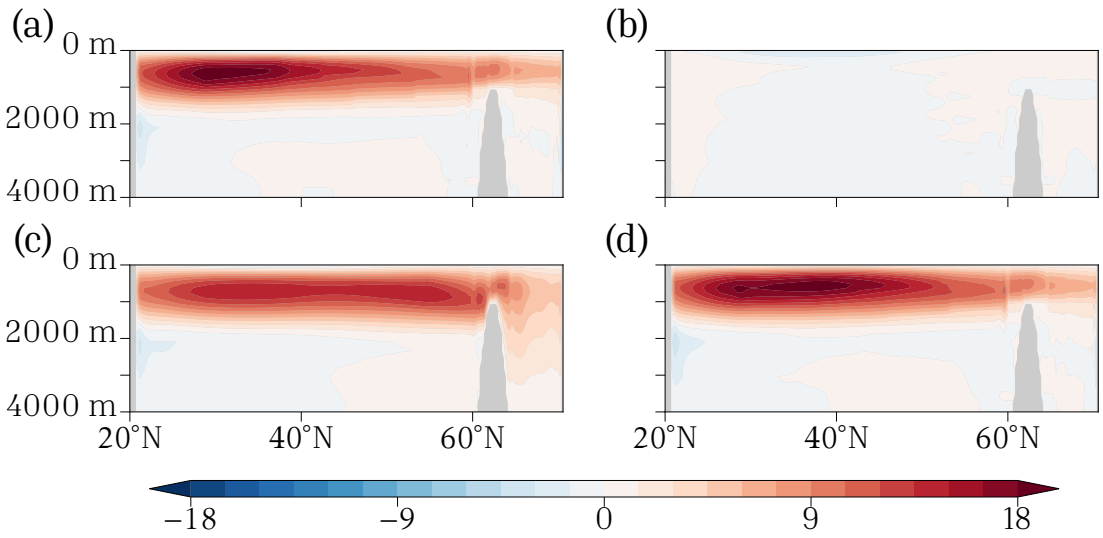


FIGURE 3.6: Total meridional overturning streamfunction in depth space for different model configurations: (a) control run (b) no buoyancy forcing (c) vertical sidewalls (d) no wind forcing. Overturning transport is in Sverdrups.

downwelling occurs in the main basin. The only discernible difference between the two streamfunctions is that the latitude of maximum overturning in the control case is noticeably further south than in the no-wind case.

In the vertical sidewalls case, shown in Figure 3.6(c), there is little attenuation at all of the overturning streamfunction up to the highest latitudes of the main basin. Further, the streamfunction penetrates into the Nordic basin and extends down far deeper than in either the control or the no-wind-stress case. The maximum amplitude of the overturning in the case of vertical sidewalls is also weaker than in both the aforementioned configurations.

Now decomposing the overturning and considering first the geostrophic shear component, the resulting overturnings—corrected to give closed circulations—are shown in Figure 3.7. These overturning transports are calculated from the zonal integral of the thermal wind relation and, in depth space at least, are determined by the difference in density (and hence temperature) profiles between the eastern and western boundaries as demonstrated by equation (3.12).

In the no-buoyancy-forcing case in panel 3.7(b), an overturning arising from the thermal wind shear can evidently only be achieved by the wind-induced heaving of isopycnals. In the subtropics, a weak clockwise cell is driven

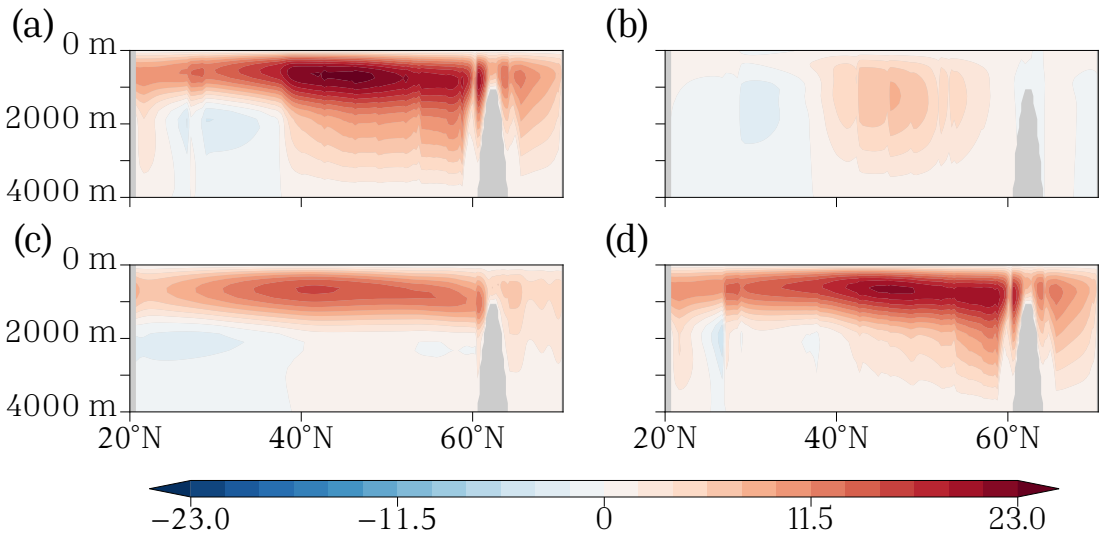


FIGURE 3.7: Geostrophic shear component of the meridional overturning streamfunction in depth space for different model configurations: (a) control run (b) no buoyancy forcing (c) vertical sidewalls (d) no wind forcing. Overturning transport is in Sverdrups.

primarily by temperature differences at the surface. The western boundary density is kept low by the supply of warm water from low latitudes in the boundary current, whereas the water on the eastern boundary is cooler due to the contribution of cooler subpolar surface water. In the subpolar region, the upwelling of deep water via Ekman suction provides a source of cold dense water. This upwelling occurs primarily towards the western boundary, where the gyre is at its strongest (see Figure 3.4(b)).

The shear overturning in the other three cases is significantly stronger; indeed, in each case the maximum of the shear overturning is larger than the maximum total overturning. In both the control and no-wind configurations (Figures 3.7(a) and 3.7(d) respectively), the maximum overturning is to the north of the maximum of the total overturning, and there is an abrupt increase in the magnitude and the depth of the the overturning cell from the subtropics to the subpolar region. This abrupt change is not present in the vertical sidewalls configuration, where the overturning cell is fairly symmetrical about 40°N.

The sudden increase in overturning present in panels 3.7(a) and 3.7(d) occurs in both cases at the same latitude at which the western boundary current separates from the boundary—as can be seen from Figures 3.5(a) and 3.5(d).

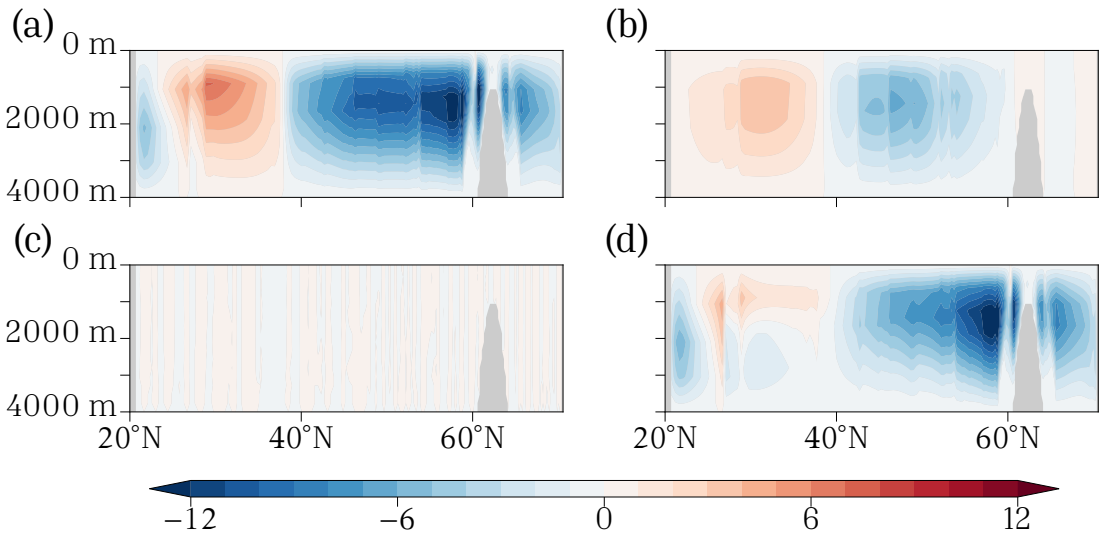


FIGURE 3.8: External mode component of the meridional overturning streamfunction in depth space for different model configurations: (a) control run (b) no buoyancy forcing (c) vertical sidewalls (d) no wind forcing. Overturning transport is in Sverdrups.

Below this latitude, the current on the western boundary is northwards flowing, warm, and stratified. As such, differences in density between the two boundaries are smaller and limited to a narrower range of depths. At higher latitudes, the current on the western boundary is southwards flowing, cold, and comparatively barotropic. This results in a large density difference across a broader range of depths, and so the overturning streamfunction is both stronger and deeper than in the subtropics.

Given that this feature of the shear overturning appears to coincide with the separation of the boundary current from the boundary, and that it has been established (see Figure 3.3) that zonal flow over non-uniform topography can give rise to an overturning in depth space, it might be expected that a similar feature might appear in the external mode component of the overturning. Figures 3.8(a) and 3.8(d) show that this is indeed the case.

Starting at the latitude of separation, there are anticlockwise external mode cells opposing the shear cells from Figure 3.7. These cells balance the deep shear overturning, limiting the net overturning cell to the upper 1500 m or so, and reducing the amplitude of subpolar overturning while slightly amplifying overturning in the subtropics. The net effect is that the maximum

total overturning is slightly smaller, and further south, than the geostrophic shear component alone.

The magnitude and shape of the external mode cells in Figure 3.8 are most easily interpreted with reference to the barotropic streamfunctions given in Figure 3.4. In the no-buoyancy-forcing case (panels 3.8(b) and 3.4(b)), the barotropic circulation either side of the latitude of peak wind stress at 40°N is more-or-less directly offshore and, consequently, downslope. The barotropic flow in the interior is then equatorwards in the subtropical gyre and polewards in the subpolar gyre, but—crucially—does not encroach upon the eastern boundary in either gyre. The return flow along the southern and northern boundaries then impinges on the western boundary, this time flowing up the zonal slope, before returning to 40°N along the slope to close the circulation. The result is two opposing cells of similar magnitude, with steep "downwelling" at 40°N where the zonal barotropic flow is downslope and "upwelling" at the northern and southern boundaries where it is upslope. The flow linking the two is at constant depth, either along the slope in the boundary current, or along the ocean floor in the Sverdrup interior, and so there is neither "upwelling" nor "downwelling".

In the no-wind configuration (panels 3.8(d) and 3.4(d)), although the pattern is very different, its explanation is similar. In this case, there is no symmetry between the subtropical and subpolar external mode cells, because there is no symmetry between the corresponding barotropic circulations. The subpolar "gyre" in the no-wind case is concentrated over the western and northern boundary slopes. The barotropic flow gradually flows up the slope as it moves southwards, leading to a more progressive subpolar "downwelling" than in the no-buoyancy case. A proportion northwards flowing current remains over the topographic slope up to the northern boundary of the main basin before turning sharply away from the western boundary—as can be seen from Figure 3.5(d)—giving a very steep subpolar "downwelling" and, therefore, an overturning cell which is skewed towards the high latitudes. In the subtropics,

while the "gyre" is of similar magnitude to the subpolar one, the overturning cell is both far shallower, and far weaker. This is because the barotropic flow is not directly downslope at any point, so the descent along the topography is gradual, and it never flows fully off the slope, and so the resulting cell is restricted in it depth.

The control configuration (panels 3.8(a) and 3.4(a)) can be explained as a superposition of the no-buoyancy-forcing and no-wind cases: there is a strong, gradually increasing, anticlockwise subpolar cell due to the strong buoyancy-induced circulation over the sloping boundary, as well as the weaker, symmetrical cells extending to the ocean floor arising from the wind-driven gyre circulations. The external mode for the vertical sidewalls configuration is (reassuringly) almost zero, as there is no zonally non-uniform topography in the domain which could give rise to an external mode in depth space.

The final component of the overturning in depth space is also the least interesting: the Ekman component, shown in Figure 3.9(c). In each case its form is essentially prescribed and is independent of the dynamics of the flow: the total transport is calculated as a function of the prescribed wind stress and then distributed throughout an Ekman layer of a prescribed depth, and a barotropic correction is then applied to give a closed circulation. In the vertical sidewalls configuration, however, it is this anticlockwise Ekman cell, centred on 40°N, which counteracts the geostrophic shear cell to give the smoothed out total overturning cell of Figure 3.6(c)

3.3.3 The Meridional Overturning Circulation: Density Space

Now considering the same decomposition of the overturning circulation, but in density space, the full overturning streamfunctions are given in Figure 3.10. The first thing to note is that the streamfunction is only defined between the maximum and minimum temperatures present across the zonal section at each latitude. This is the reason for the differing shapes of the overall streamfunctions between panels. For example, Figure 3.10(b) shows the overturning

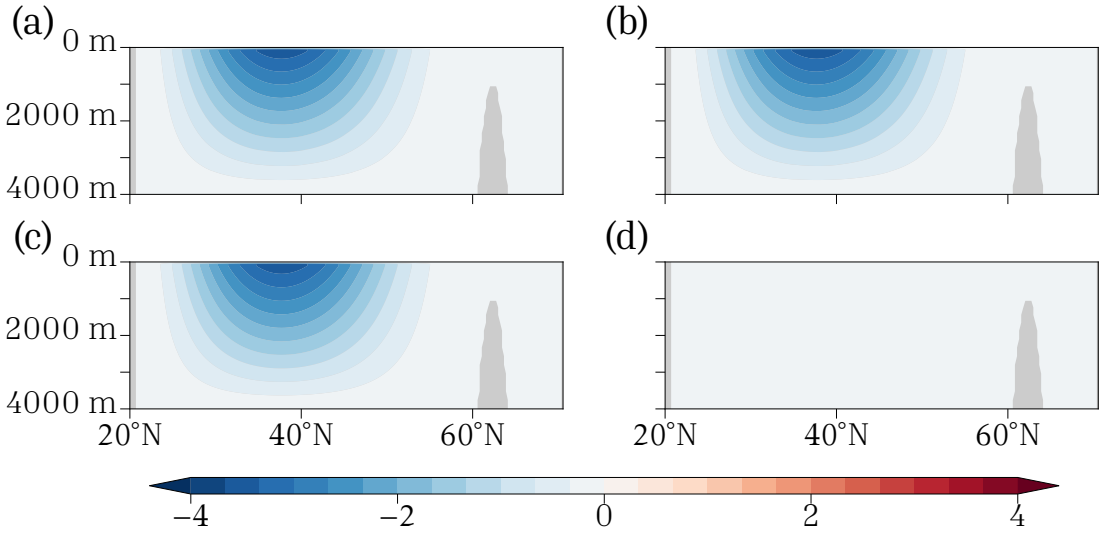


FIGURE 3.9: Ekman component of the meridional overturning streamfunction in depth space for different model configurations: (a) control run (b) no buoyancy forcing (c) vertical sidewalls (d) no wind forcing. Overturning transport is in Sverdrups.

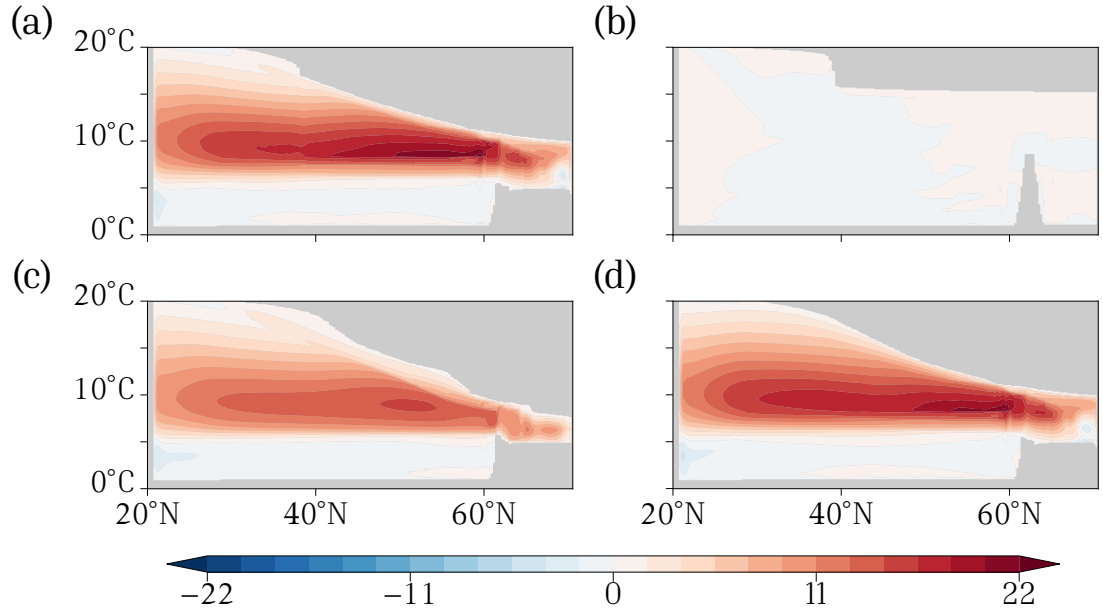


FIGURE 3.10: Total meridional overturning streamfunction in density space for different model configurations: (a) control run (b) no buoyancy forcing (c) vertical sidewalls (d) no wind forcing. Overturning transport is in Sverdrups.

in density space for the no-buoyancy-forcing case. There are two aspects of the shape of this streamfunction which are (at least at first glance) surprising.

First, the steep bump at high temperatures just below 40°N. Due to the strong gradient in temperature near the surface in the profile relaxed to in the subtropical sponge, the warmest water in the model is restricted to a

narrow band of depths near the surface in the subtropics—this can be seen from Figure 2.4(a). In this experiment, subtropical surface waters are quickly carried to near 40°N by the western boundary current, but this current then separates from the boundary and—as shown in Figure 3.5(b)—the warm water then recirculates in the subtropics, never reaching the subpolar gyre. The colder surface water at subpolar latitudes is therefore supplied via Ekman suction from cooler depths and so there is an abrupt decrease in the temperature of warmest water at a given latitude at 40°N.

The other feature is the presence of cold bottom water in the Nordic basin. As there is no Nordic sponge present in this configuration, warm water entering the Nordic basin is not cooled, and so there is no change in surface temperature between the two basins. This also means that the deep water in the Nordic basin, initialised to temperatures colder than the 5°C relaxed to when the sponge is present, is not *warmed* by the sponge. As a result, there are pools of cold water in either basin which are blocked by the sill, leading to the appearance of the sill-like structure in the streamfunction. These features, or similar, are present to varying degrees in the other panels too, but are most evident in panel (b).

Considering now the overturning streamfunctions themselves, one obvious difference which is consistent across all three of the control, no-wind, and vertical sidewalls configurations, is that the overturning cells now continue to increase in magnitude all the way up to the highest latitudes of the main basin. All three also penetrate into the Nordic basin in density space. The surface flow gradually becomes denser along the flow path, losing buoyancy as surface cooling causes the warmest temperature layers to outcrop. The return flow occurs along isopycnals in the ocean interior and there is very little diapycnal mixing.

Similarly to in the depth space framework, the geostrophic shear overturning (Figure 3.11) is the dominant component of the overall overturning circulation. In the no-buoyancy-forcing configuration, the shear component

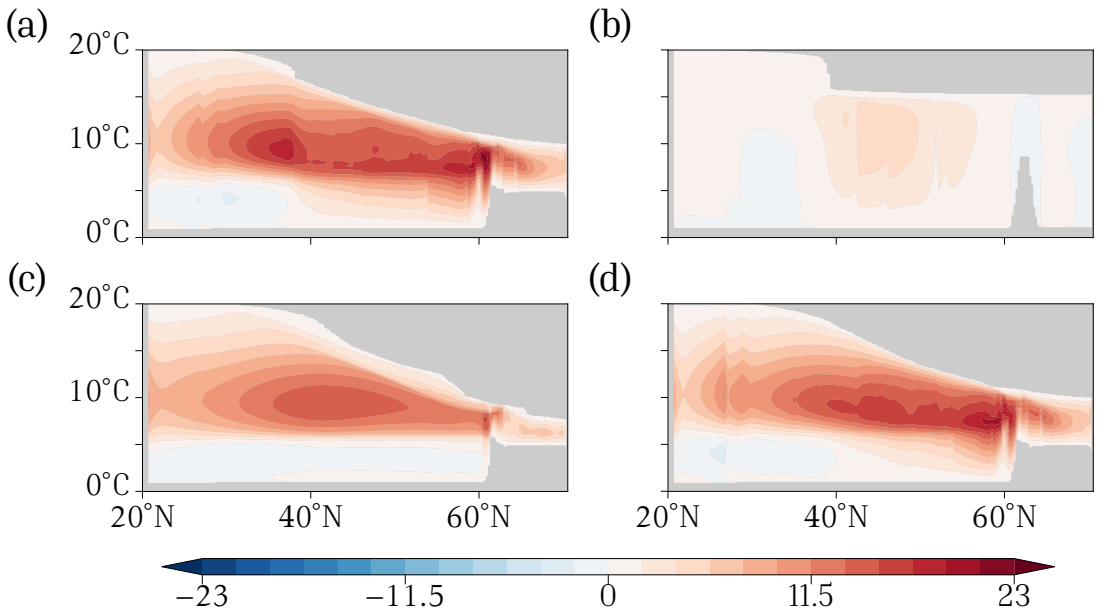


FIGURE 3.11: Geostrophic shear component of the meridional overturning streamfunction in density space for different model configurations: (a) control run (b) no buoyancy forcing (c) vertical sidewalls (d) no wind forcing. Overturning transport is in Sverdrups.

shown in Figure 3.11(b) bears a strong resemblance to the corresponding circulation in depth space. This is unsurprising as, in this configuration, the isopycnals have very little zonal slope across the basin, particularly in the subpolar gyre. As such, the use of density as a vertical coordinate behaves as a rescaled depth. This behaviour is consistent across the external mode component in Figure 3.12(b) and even the Ekman component shown in Figure 3.13(b).

In the control and no-wind configurations (Figures 3.11(a) and 3.11(d) respectively), again the subpolar shear component of the overturning continues to increase with latitude, and extends to the coldest depths. In density space, however, while the amplitude of the overturning at high latitudes no longer differs between the shear component and the full overturning, there is no overturning at depth in the full streamfunction. This implies that the external mode component must also be behaving differently in density space in these configurations.

Examining Figures 3.12(a) and 3.12(d) it can be seen that the external mode component of the overturning for these cases still has a strong anticlockwise cell at subpolar latitudes, but this cell is limited to layers colder than about

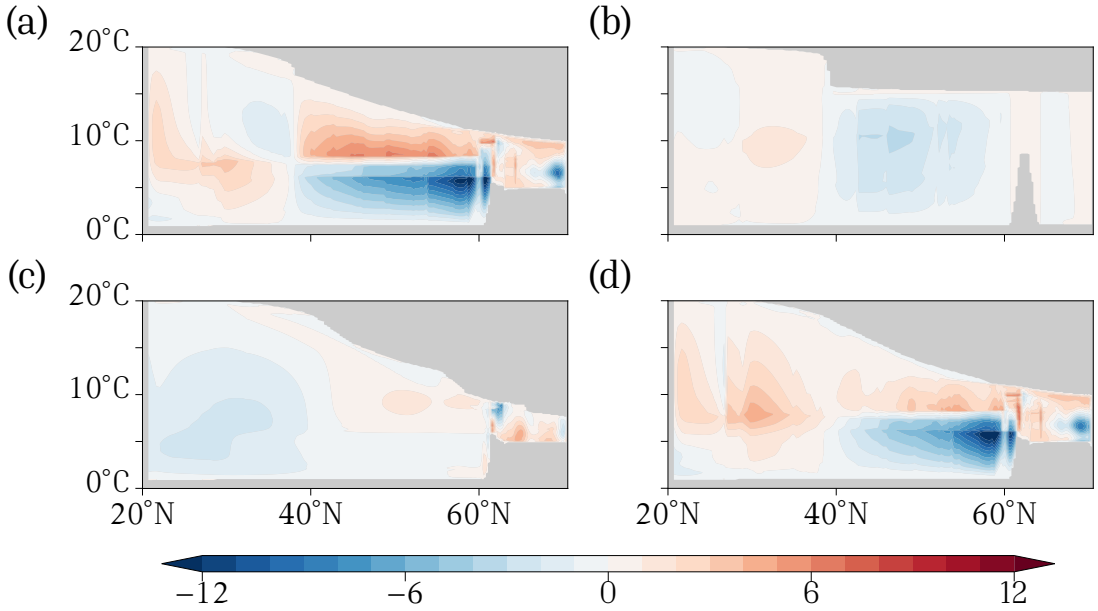


FIGURE 3.12: External mode component of the meridional overturning streamfunction in density space for different model configurations: (a) control run (b) no buoyancy forcing (c) vertical sidewalls (d) no wind forcing. Overturning transport is in Sverdrups.

~ 8°C, and there is in fact a clockwise cell at warmer temperatures. This is best explained referring back to the schematic in Figure 3.2. As shown in the schematic, the external mode in density space is mediated by the transport of water across isopycnals by the barotropic flow. The sign of the overturning cell obtained therefore depends on the sign of the isopycnal gradient, as well as the direction of the flow through the isopycnal. Because the western boundary current is barotropic, and extends down below the depth of the corresponding isopycnal on the eastern boundary, while the temperature increases away from the boundary at the surface, it decreases away from the boundary at depth. There is therefore a sign change in the zonal slope of isopycnals at mid-depth and so, instead of a single subpolar overturning cell (as in depth space), the external mode in density space is a dipole.

Finally, the Ekman component of the overturning in density space, shown in Figure 3.13 is very similar to the corresponding overturning in depth space, but is slanted as a result of surface density levels outcropping, and distorted due to the misalignment between isopycnals and surfaces of constant depth.

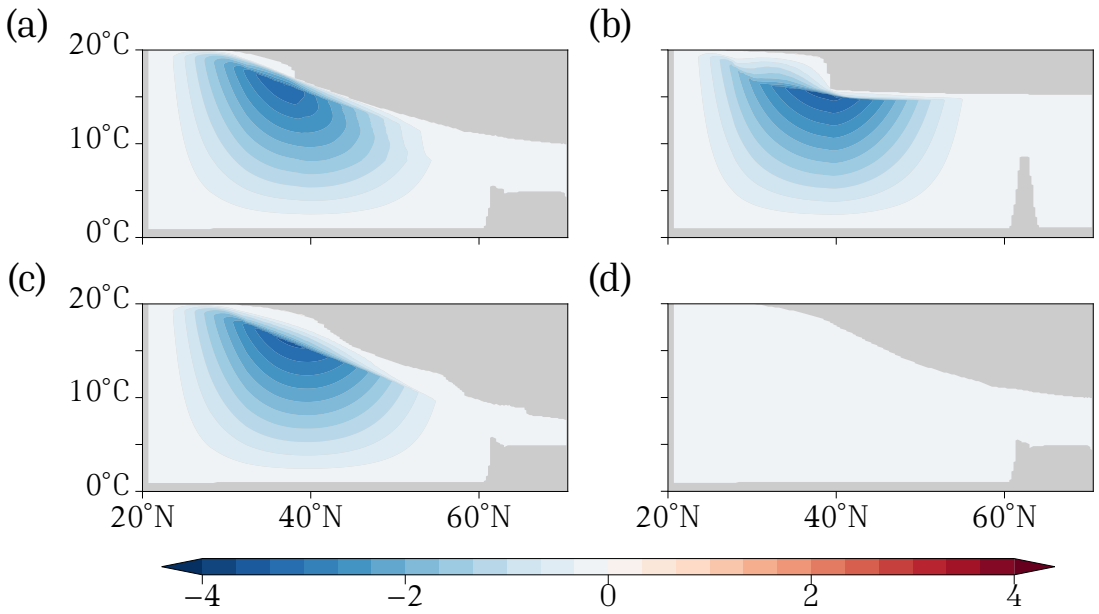


FIGURE 3.13: Ekman component of the meridional overturning streamfunction in density space for different model configurations: (a) control run (b) no buoyancy forcing (c) vertical sidewalls (d) no wind forcing. Overturning transport is in Sverdrups.

3.4 Summary

In this chapter, an introduction to the circulation of the subpolar North Atlantic was given, stressing the contrast between the overturning in depth space and in density space at these latitudes, as well as the importance of topography. A method of decomposing the overturning circulation into components arising from the geostrophic shear, the barotropic flow, and from Ekman flow in depth space was introduced, and subsequently generalised to apply also to the overturning in density space. This decomposition was then applied to a set of numerical experiments to probe the relative impacts of surface buoyancy forcing, wind stress, and topography on the mean circulation in an idealised model of the subpolar North Atlantic. The geostrophic shear component was found to dominate the overall overturning in both frameworks. The external mode component behaves differently in density space at subpolar latitudes, where it forms two opposing cells stacked atop one another, compared to in depth space, where it forms a single overturning cell which opposes the shear cell.

In the next chapter, a novel diagnostic for assessing the rotational momentum balance of the large-scale ocean circulation with non-uniform bathymetry is derived. This diagnostic is then applied in Chapter 5 to the sensitivity experiments presented in this chapter to provide a complementary view of the reasons for differences between simulations.

4 Rotational Momentum Equation Decomposition

4.1 Introduction . . . 67
4.2 The Rotational Momentum Equation . . . 69
4.3 Boundary Conditions . . . 72
4.3.1 Helmholtz Decomposition . . . 73
4.3.2 The Surface & Bottom Boundaries . . . 77
4.4 Overturning and Barotropic Force Functions . . . 78
4.5 Finding the Overturning Force Functions . . . 80
4.6 Finding the Barotropic Force Function . . . 81
4.7 Simplifying the Forcing Terms . . . 87
4.7.1 Eliminating 3-D Differential Operators . . . 87
4.7.2 Horizontal and Vertical Forces . . . 90
4.8 Boundary Condition on Barotropic Force Function . . . 92
4.9 Relating Force Functions to Transport Streamfunctions . . . 96
4.9.1 Overturning Circulation . . . 96
4.9.2 Barotropic Circulation . . . 98
4.9.3 Barotropic Potential Vorticity Equation and JEBAR . . . 99
4.10 Summary . . . 100

4.1 Introduction

In the large-scale ocean, the vertical momentum equation is dominated by hydrostatic balance, where the acceleration due to gravity is balanced by

the pressure gradient force. The corresponding balance in the horizontal is geostrophic balance between the Coriolis force and the pressure gradient force. As the gradient of a scalar field, the pressure gradient force is necessarily conservative. Due to the non-divergence of an incompressible fluid, however, the net acceleration due to an applied force must be solenoidal. As such, the evolution of the ocean circulation is determined by small departures from the dominant force balances.

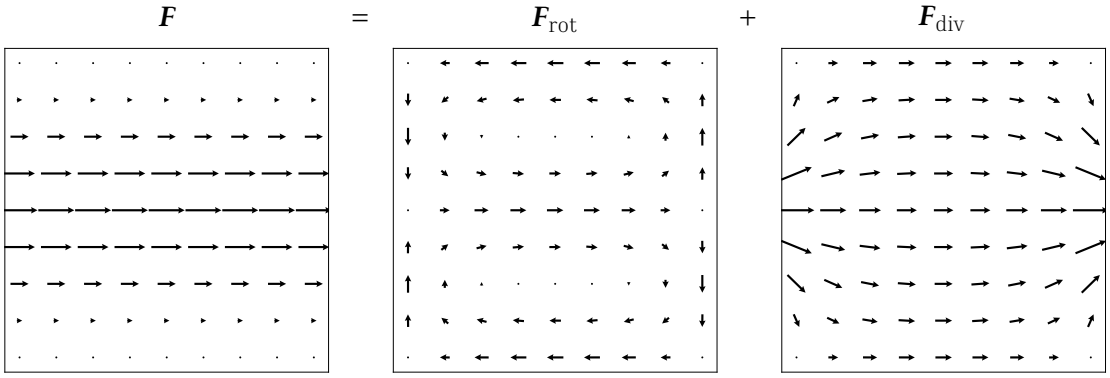


FIGURE 4.1: Schematic illustrating decomposition of an applied force (F) into rotational (F_{rot}) and divergent (F_{div}) parts subject to the boundary condition that F_{rot} be parallel to the boundary.

The terms in the momentum equation governing this evolution can therefore be isolated by removing divergent terms such as the pressure gradient. This is typically achieved by taking the curl to form the vorticity equation (see, e.g., Pedlosky 1987). Marshall and Pillar (2011) take a different approach: using Helmholtz's theorem (Helmholtz 1858) to decompose the force terms in the momentum equation into rotational and divergent parts, as illustrated in Figure 4.1. The rotational force acts to accelerate the flow, with the divergent components acting to balance the pressure gradient established to maintain non-divergence of the flow and satisfy any boundary conditions imposed.

By expressing the 'rotational force' as the curl of a vector potential, Marshall and Pillar (2011) show that, in the hydrostatic limit, this vector potential can be further decomposed into three 'force functions': a depth-integrated one

that projects onto the barotropic circulation, and two overturning ones which project onto the meridional and zonal overturning circulations.

Their derivation of the force functions, however, uses a scaling argument to neglect a term which, while small at any given depth, is non-negligible when integrated over the full fluid depth. The outcome of neglecting this term is that the resulting force functions erroneously ignore the effect of variations in topography on the barotropic circulation. While the force functions derived in Marshall and Pillar (2011) remain valid for the flat-bottomed case, the missing terms are non-negligible in the presence of topography—as will be demonstrated in Chapter 5.

The following section introduces the rotational momentum equation framework of Marshall and Pillar (2011). The chapter then continues with a derivation of the overturning and barotropic force functions in which the mistakes present in the previous derivation are corrected, generalising the rotational momentum equation approach to allow for variable topography. A simplification to the expression for the barotropic force function allowing for its calculation without the need for three-dimensional differential operators is also provided, and finally the relationship between the force functions and the barotropic and overturning circulations is made explicit.

Some of the material in this chapter follows Marshall and Pillar (2011) closely. Specifically, much of Sections 4.2, 4.3.2, 4.5 and (to a lesser extent) Section 4.4 either reproduce, or expand on, steps taken in the derivation of Marshall and Pillar (2011).

4.2 The Rotational Momentum Equation

The momentum and continuity equations for a Boussinesq fluid can be expressed as:

$$\frac{\partial \boldsymbol{u}}{\partial t} + \frac{\boldsymbol{\nabla} p}{\rho_0} = \sum_{\boldsymbol{F}} \frac{\boldsymbol{F}}{\rho_0} \,, \tag{4.1}$$

$$\boldsymbol{\nabla} \cdot \boldsymbol{u} = 0 \,, \tag{4.2}$$

where all terms other than the pressure gradient force and the Eulerian component of acceleration have been brought across to the right hand side as individual 'force' terms. From this point on, unless specified otherwise, $\partial \boldsymbol{u}/\partial t$ and $\boldsymbol{\nabla} p/\rho_0$ are used to refer to the acceleration and pressure gradient due to individual force term $\boldsymbol{F}$, i.e.:

$$\frac{\partial \boldsymbol{u}}{\partial t} \equiv \left(\frac{\partial \boldsymbol{u}}{\partial t}\right)_{\boldsymbol{F}}, \tag{4.3}$$

$$\frac{\boldsymbol{\nabla} p}{\rho_0} \equiv \left(\frac{\boldsymbol{\nabla} p}{\rho_0}\right)_{\boldsymbol{F}}. \tag{4.4}$$

The acceleration and pressure gradient due to a force $\boldsymbol{F}$ can then be written as the superposition of the rotational and divergent components of the force using Helmholtz's theorem:

$$\frac{\partial \boldsymbol{u}}{\partial t} + \frac{\boldsymbol{\nabla} p}{\rho_0} = \frac{\boldsymbol{F}_{\text{rot}}}{\rho_0} + \frac{\boldsymbol{F}_{\text{div}}}{\rho_0}, \tag{4.5}$$

where

$$\boldsymbol{\nabla} \cdot \boldsymbol{F}_{\text{rot}} = 0, \quad \boldsymbol{\nabla} \times \boldsymbol{F}_{\text{div}} = 0. \tag{4.6}$$

Equations (4.6), together with (4.2), imply that only the rotational component of force $\boldsymbol{F}$ can act to accelerate the flow, and we therefore have that:

$$\frac{\partial \boldsymbol{u}}{\partial t} = \frac{\boldsymbol{F}_{\text{rot}}}{\rho_0}. \tag{4.7}$$

Because $\boldsymbol{F}_{\text{rot}}$ is purely rotational, it can be written as the curl of a vector potential $\boldsymbol{A}$:

$$\frac{\boldsymbol{F}_{\text{rot}}}{\rho_0} = \boldsymbol{\nabla} \times \boldsymbol{A}. \tag{4.8}$$

Similarly, the divergent component of $\boldsymbol{F}$ projects onto the pressure gradient and because it is—by definition—conservative, it can be written as the gradient of a scalar potential ϕ:

$$\begin{aligned} \boldsymbol{\nabla} p &= \boldsymbol{F}_{\text{div}}, \\ \frac{\boldsymbol{F}_{\text{div}}}{\rho_0} &= \boldsymbol{\nabla} \phi. \end{aligned} \tag{4.9}$$

Therefore, combined with (4.8), the full force can be written as a superposition of the gradient of a scalar potential and the curl of a vector potential:

$$\frac{\boldsymbol{F}}{\rho_0} = \boldsymbol{\nabla}\phi + \boldsymbol{\nabla} \times \boldsymbol{A} \,. \tag{4.10}$$

This is the Helmholtz decomposition. It is then possible to find expressions for the potentials $\boldsymbol{A}$ and ϕ, by taking the curl and divergence of (4.10). Taking the curl of $\boldsymbol{F}$ eliminates the ϕ term, giving an expression solely in terms of $\boldsymbol{A}$:

$$\begin{aligned} \frac{\boldsymbol{\nabla} \times \boldsymbol{F}}{\rho_0} &= \frac{\boldsymbol{\nabla} \times \boldsymbol{F}_{\text{div}} + \boldsymbol{\nabla} \times \boldsymbol{F}_{\text{rot}}}{\rho_0} \\ &= \frac{\boldsymbol{\nabla} \times \boldsymbol{F}_{\text{rot}}}{\rho_0} \\ &= \boldsymbol{\nabla} \times \boldsymbol{\nabla} \times \boldsymbol{A} \\ &= \boldsymbol{\nabla} (\boldsymbol{\nabla} \cdot \boldsymbol{A}) - \nabla^2 \boldsymbol{A} \,. \end{aligned} \tag{4.11}$$

In the present definition of the vector potential $\boldsymbol{A}$, (4.8), there is a redundant degree of freedom: if we write $\boldsymbol{A}$ as

$$\boldsymbol{A} = \boldsymbol{A}_{\text{rot}} + \boldsymbol{A}_{\text{div}} \,, \tag{4.12}$$

where

$$\boldsymbol{\nabla} \cdot \boldsymbol{A}_{\text{rot}} = 0 \,; \quad \boldsymbol{\nabla} \times \boldsymbol{A}_{\text{div}} = 0 \,,$$

then any (zero-curl) value of $\boldsymbol{A}_{\text{div}}$ will satisfy (4.8). We can obtain a unique definition of $\boldsymbol{A}$ by imposing a gauge condition on $\boldsymbol{A}_{\text{div}}$. Looking back at (4.11), a sensible choice is the Coulomb gauge,

$$\boldsymbol{\nabla} \cdot \boldsymbol{A}_{\text{div}} = 0 \,, \tag{4.13}$$

$$\text{and so} \qquad \boldsymbol{\nabla} \cdot \boldsymbol{A} = 0 \,. \tag{4.14}$$

Equation (4.11) therefore simplifies to a three-dimensional Poisson equation relating the vector potential to the curl of the force:

$$\frac{\boldsymbol{\nabla} \times \boldsymbol{F}}{\rho_0} = -\nabla^2 \boldsymbol{A} \,. \tag{4.15}$$

Taking the divergence of (4.10) yields an analogous expression for the scalar potential:

$$\begin{aligned}\frac{\boldsymbol{\nabla}\cdot\boldsymbol{F}}{\rho_0} &= \boldsymbol{\nabla}\cdot\boldsymbol{\nabla}\phi + \boldsymbol{\nabla}\cdot\boldsymbol{\nabla}\times\boldsymbol{A} \\ &= \nabla^2\phi\,. \end{aligned} \tag{4.16}$$

In this section, the Helmholtz decomposition of the full force into its rotational and divergent components has been introduced, along with expressions for both the scalar potential ϕ and vector potential $\boldsymbol{A}$. To be able to find the rotational and divergent components of the force using this decomposition, however, first the correct boundary conditions must be established.

4.3 Boundary Conditions

The boundary conditions on the elliptic equation (4.15) come from the kinematic boundary condition on the velocity, in combination with the imposed gauge condition. The kinematic boundary condition—that there must be no normal flow at the boundary—implies that

$$\hat{\boldsymbol{n}}\cdot\boldsymbol{u} = 0\,, \tag{4.17}$$

where $\boldsymbol{n}$ is the unit normal to the boundary. From (4.7) and (4.8) it therefore follows that

$$\hat{\boldsymbol{n}}\cdot\frac{\partial\boldsymbol{u}}{\partial t} = \hat{\boldsymbol{n}}\cdot\boldsymbol{F}_{\text{rot}} = \hat{\boldsymbol{n}}\cdot(\boldsymbol{\nabla}\times\boldsymbol{A}) = 0\,. \tag{4.18}$$

The Helmholtz decomposition introduced in the previous section is unique in any unbounded domain where the force $\boldsymbol{F}(r)$ vanishes as $r\to\infty$. In a bounded domain, it is the boundary condition which allows for a unique decomposition into rotational and divergent components. This is hinted at by the schematic in Figure 4.1: both the flows in the first and second panels are non-divergent, but once the boundary condition that $\boldsymbol{F}_{\text{rot}}$ be parallel to the boundary has been imposed only the second panel is a valid rotational component. As the large-scale ocean is a bounded domain, and forces do not generally vanish at the boundary, it is worth showing that the decomposition given in (4.10) *is* unique.

4.3.1 The Helmholtz Decomposition: Existence and Uniqueness

The existence and uniqueness of the decomposition as given in (4.10) is briefly demonstrated below (this proof is adapted from Denaro (2003) which, along with Bhatia et al. (2012), provides a more general and detailed discussion of the Helmholtz decomposition).

Equation (4.16) states that

$$\nabla^2 \phi = \frac{\boldsymbol{\nabla} \cdot \boldsymbol{F}}{\rho_0} \tag{4.19}$$

within a bounded domain, denoted as V, with bounding surface S. This is a Poisson equation, to which a solution (unique up to an additive constant) exists if and only if the following constraint on the integral of (4.19) over domain V is satisfied (e.g. Courant and Hilbert 1989):

$$\int_V \nabla^2 \phi \, \mathrm{d}V = \int_V \frac{\boldsymbol{\nabla} \cdot \boldsymbol{F}}{\rho_0} \, \mathrm{d}V \, . \tag{4.20}$$

Applying the divergence theorem to compatibility condition (4.20) gives

$$\int_V \nabla^2 \phi \, \mathrm{d}V = \oint_S \frac{\boldsymbol{F}}{\rho_0} \cdot \hat{\boldsymbol{n}} \, \mathrm{d}S \, , \tag{4.21}$$

where $\hat{\boldsymbol{n}}$ is the unit vector normal to S, and $\mathrm{d}S$ is the surface area element on S.

From the kinematic boundary condition (4.18), we have the following boundary conditions on the vector and scalar potentials:

$$(\boldsymbol{\nabla} \times \boldsymbol{A}) \cdot \hat{\boldsymbol{n}} = 0 \, , \tag{4.22}$$

$$\boldsymbol{\nabla} \phi \cdot \hat{\boldsymbol{n}} = \frac{\boldsymbol{F}}{\rho_0} \cdot \hat{\boldsymbol{n}} \, . \tag{4.23}$$

Substituting (4.23) into (4.21) yields

$$\int_V \nabla^2 \phi \, \mathrm{d}V = \oint_S \boldsymbol{\nabla} \phi \cdot \hat{\boldsymbol{n}} \, \mathrm{d}S \, , \tag{4.24}$$

which is the divergence theorem, and hence (4.20) is satisfied and so a solution exists for the scalar potential ϕ, and the rotational component can then obtained by

$$\boldsymbol{\nabla} \times \boldsymbol{A} = \frac{\boldsymbol{F}}{\rho_0} - \boldsymbol{\nabla} \phi \, .$$

To verify that the decomposition is unique, first assume that the converse is true, and that two different decompositions with the aforementioned properties exist:

$$\frac{\boldsymbol{F}}{\rho_0} = \boldsymbol{\nabla}\phi_1 + \boldsymbol{\nabla}\times\boldsymbol{A}_1 = \boldsymbol{\nabla}\phi_2 + \boldsymbol{\nabla}\times\boldsymbol{A}_2\,, \tag{4.25}$$

and therefore the two decompositions are related by:

$$\boldsymbol{\nabla}(\phi_1 - \phi_2) + \boldsymbol{\nabla}\times(\boldsymbol{A}_1 - \boldsymbol{A}_2) = 0\,. \tag{4.26}$$

Then taking the inner product (defined as $\langle \boldsymbol{u}, \boldsymbol{v}\rangle = \int_V \boldsymbol{u}\cdot\boldsymbol{v}\,\mathrm{d}V$) of (4.26) with $\boldsymbol{\nabla}\times(\boldsymbol{A}_1 - \boldsymbol{A}_2)$ gives:

$$\left\langle \boldsymbol{\nabla}\times(\boldsymbol{A}_1 - \boldsymbol{A}_2)\,,\, \boldsymbol{\nabla}(\phi_1 - \phi_2) + \boldsymbol{\nabla}\times(\boldsymbol{A}_1 - \boldsymbol{A}_2)\right\rangle = 0\,, \tag{4.27}$$

$$\begin{aligned}\left\langle \boldsymbol{\nabla}\times(\boldsymbol{A}_1 - \boldsymbol{A}_2)\,,\, \boldsymbol{\nabla}\times(\boldsymbol{A}_1 - \boldsymbol{A}_2)\right\rangle + \left\langle \boldsymbol{\nabla}\times\boldsymbol{A}_1,\, \boldsymbol{\nabla}\phi_1\right\rangle \\ + \left\langle \boldsymbol{\nabla}\times\boldsymbol{A}_2,\, \boldsymbol{\nabla}\phi_2\right\rangle - \left\langle \boldsymbol{\nabla}\times\boldsymbol{A}_2,\, \boldsymbol{\nabla}\phi_1\right\rangle - \left\langle \boldsymbol{\nabla}\times\boldsymbol{A}_1,\, \boldsymbol{\nabla}\phi_2\right\rangle = 0\,.\end{aligned} \tag{4.28}$$

The final four terms in Equation (4.28) can be shown to vanish as follows:

$$\left\langle \boldsymbol{\nabla}\times\boldsymbol{A}_i,\, \boldsymbol{\nabla}\phi_j\right\rangle = \int_V (\boldsymbol{\nabla}\times\boldsymbol{A}_i)\cdot\boldsymbol{\nabla}\phi_j\,\mathrm{d}V \qquad i,j\in\{1,2\}\,, \tag{4.29}$$

which, using the product rule and the fact that the divergence of a curl is zero, is given by

$$\left\langle \boldsymbol{\nabla}\times\boldsymbol{A}_i,\, \boldsymbol{\nabla}\phi_j\right\rangle = \int_V \boldsymbol{\nabla}\cdot\phi_j\,(\boldsymbol{\nabla}\times\boldsymbol{A}_i)\,\mathrm{d}V\,. \tag{4.30}$$

First converting to a surface integral using the divergence theorem, and then applying the boundary condition (4.22) gives the desired result:

$$\left\langle \boldsymbol{\nabla}\times\boldsymbol{A}_i,\, \boldsymbol{\nabla}\phi_j\right\rangle = \oint_S \phi_j\,(\boldsymbol{\nabla}\times\boldsymbol{A}_i)\cdot\hat{\boldsymbol{n}}\,\mathrm{d}S = 0\,. \tag{4.31}$$

Equation (4.28) therefore simplifies to

$$\left\langle \boldsymbol{\nabla}\times(\boldsymbol{A}_1 - \boldsymbol{A}_2)\,,\, \boldsymbol{\nabla}\times(\boldsymbol{A}_1 - \boldsymbol{A}_2)\right\rangle = \int_V \left|\boldsymbol{\nabla}\times(\boldsymbol{A}_1 - \boldsymbol{A}_2)\right|^2\mathrm{d}V = 0\,, \tag{4.32}$$

$$\implies \boldsymbol{\nabla}\times\boldsymbol{A}_1 = \boldsymbol{\nabla}\times\boldsymbol{A}_2 \implies \boldsymbol{\nabla}\phi_1 = \boldsymbol{\nabla}\phi_2\,. \tag{4.33}$$

The two decompositions are therefore identical, so the decomposition

$$\frac{\boldsymbol{F}}{\rho_0} = \frac{\boldsymbol{F}_{\text{rot}}}{\rho_0} + \frac{\boldsymbol{F}_{\text{div}}}{\rho_0} = \boldsymbol{\nabla}\phi + \boldsymbol{\nabla}\times\boldsymbol{A} \tag{4.34}$$

is unique.

While the boundary condition (4.18) and gauge condition (4.14) are sufficient to uniquely specify the rotational force $\boldsymbol{\nabla}\times\boldsymbol{A}$, the vector potential itself is still not unique. To see this, consider a second vector potential $\boldsymbol{A}'$, defined by

$$\boldsymbol{A}' = \boldsymbol{A} + \boldsymbol{\nabla}\eta\,, \tag{4.35}$$

where η is a harmonic function and $\boldsymbol{A}$ is a solution to (4.15) subject to (4.18) and (4.14). Now, because the curl of a gradient is zero and η is harmonic, we have that $\boldsymbol{\nabla}\times\boldsymbol{A}' = \boldsymbol{\nabla}\times\boldsymbol{A}$ and $\boldsymbol{\nabla}\cdot\boldsymbol{A}' = \boldsymbol{\nabla}\cdot\boldsymbol{A}$, and so $\boldsymbol{A}'$ is also a solution.

This ambiguity in $\boldsymbol{A}$ allows us to impose an additional boundary condition, provided this condition is compatible with the kinematic boundary condition and the gauge condition evaluated on the bounding surface S. A particularly convenient choice is to require that

$$\hat{\boldsymbol{n}}\times\boldsymbol{A} = 0\,, \tag{4.36}$$

on the boundary. To show that (4.36) with (4.18) and (4.14), consider the local basis consisting of $\hat{\boldsymbol{n}}$ and two orthogonal basis vectors tangent to bounding surface S. Equation (4.36) implies that the components of $\boldsymbol{A}$ along the two tangent directions, denoted $\boldsymbol{A}^t$, vanish when evaluated on S.

Using (4.36), the kinematic boundary condition (4.18) can be written as

$$\begin{aligned}
\hat{\boldsymbol{n}}\cdot(\boldsymbol{\nabla}\times\boldsymbol{A}) &= 0\,,\\
\boldsymbol{A}\cdot(\boldsymbol{\nabla}\times\hat{\boldsymbol{n}}) - \boldsymbol{\nabla}\cdot(\hat{\boldsymbol{n}}\times\boldsymbol{A}) &= 0\,,\\
\boldsymbol{A}\cdot(\boldsymbol{\nabla}\times\hat{\boldsymbol{n}}) &= 0\,,
\end{aligned} \tag{4.37}$$

but $\boldsymbol{A}^t = 0$, so

$$(\hat{\boldsymbol{n}}\cdot\boldsymbol{A})\,(\hat{\boldsymbol{n}}\cdot\boldsymbol{\nabla}\times\hat{\boldsymbol{n}}) = 0\,. \tag{4.38}$$

Surface S can be described implicitly as the set of points satisfying the equation

$$f(\boldsymbol{x}) = 0\,. \tag{4.39}$$

The unit vector normal to S is therefore given by

$$\hat{\boldsymbol{n}} = \frac{\boldsymbol{\nabla} f}{|\boldsymbol{\nabla} f|}\,, \tag{4.40}$$

and so, using the product rule and the fact that the curl of a gradient is zero, (4.38) becomes

$$(\boldsymbol{\nabla} f \cdot \boldsymbol{A})\left(\boldsymbol{\nabla} f \cdot \left(\frac{1}{|\boldsymbol{\nabla} f|}\right) \times \boldsymbol{\nabla} f\right) = 0\,. \tag{4.41}$$

The cyclic property of the scalar triple product means that (4.41)—and hence the kinematic boundary condition—is automatically satisfied for any differentiable f.

To show that (4.36) is also compatible with the gauge condition, consider the divergence of $\boldsymbol{A}$ evaluated on S in the local basis:

$$(\boldsymbol{\nabla} \cdot \boldsymbol{A})_S = \frac{1}{\sqrt{|g|}} \partial_i \left(\sqrt{|g|} A^i\right)\Big|_S = 0\,, \tag{4.42}$$

where g is the metric tensor. Now, given that $\boldsymbol{A}^t = 0$, (4.43) becomes

$$\frac{\partial \sqrt{|g|} A^n}{\partial n}\Big|_S = 0\,. \tag{4.43}$$

The imposition of (4.36) is therefore consistent with any $\boldsymbol{F}$, while not contradicting the gauge condition. Further, (4.15) is a system of three equations in three unknowns and we now have three boundary conditions on $\boldsymbol{A}$—two Dirichlet conditions on the tangential components, and one Neumann condition on the normal component—the solutions for both the rotational component of the force and the vector potential itself (given by $\boldsymbol{\nabla} \times \boldsymbol{A}$ and $\boldsymbol{A}$ respectively) are unique.

Having established the uniqueness of the Helmholtz decomposition and of the vector potential $\boldsymbol{A}$ for the large-scale ocean subject to the no-normal flow boundary condition in this section, the following sections return to the problem of finding the vector potential $\boldsymbol{A}$. In the next section, the specific forms of the boundary conditions on the expression for $\boldsymbol{A}$ given in (4.15) are found.

4.3.2 The Surface & Bottom Boundaries

Rewritten as a linear superposition of its vertical and horizontal components the vector potential $\boldsymbol{A}$ is given by:

$$\boldsymbol{A}(x,y,z) = \boldsymbol{A}^h(x,y,z) + A^z(x,y,z)\hat{\boldsymbol{e}}_z \,, \tag{4.44}$$

where $\hat{\boldsymbol{e}}_z$ is the unit vector in the z-direction.

Assuming a rigid lid, the surface boundary condition on $\boldsymbol{A}^h$ is obtained by considering the surface defined by the equation $z = 0$, with unit normal $\hat{\boldsymbol{n}} = \hat{\boldsymbol{e}}_z$. It follows trivially from (4.36) that the surface boundary condition on the horizontal component of the vector potential is:

$$\boldsymbol{A}^h_{\text{surf}}(x,y) = 0 \,. \tag{4.45}$$

The bottom bounding surface—the ocean floor—is defined implicitly as the set of points satisfying the equation $z + H(x,y) = 0$, and so a vector normal to the bottom surface can be obtained by taking the gradient of this function:

$$\boldsymbol{n} = -\boldsymbol{\nabla}\left(z + H(x,y)\right) \,, \tag{4.46}$$

$$\boldsymbol{n} = -\left(\hat{\boldsymbol{e}}_z + \boldsymbol{\nabla}H\right) \,, \tag{4.47}$$

where the normal vector is oriented such that it points out of domain V. The associated unit normal is then given by:

$$\hat{\boldsymbol{n}} = -\frac{\hat{\boldsymbol{e}}_z + \boldsymbol{\nabla}H}{\sqrt{1 + |\boldsymbol{\nabla}H|^2}} \,. \tag{4.48}$$

At every point on the bottom surface, we can further define two orthogonal vectors tangential to the bounding surface—an isobathic vector $\boldsymbol{t}$, and a downslope vector $\boldsymbol{s}$:

$$\boldsymbol{t} = \boldsymbol{\nabla}H \times \hat{\boldsymbol{e}}_z \,, \tag{4.49}$$

$$\boldsymbol{s} = \boldsymbol{t} \times \boldsymbol{n} = \boldsymbol{\nabla}H - |\boldsymbol{\nabla}H|^2 \hat{\boldsymbol{e}}_z \,, \tag{4.50}$$

with associated unit vectors

$$\hat{\boldsymbol{t}} = \frac{\boldsymbol{t}}{|\boldsymbol{\nabla} H|} \,, \tag{4.51}$$

$$\hat{\boldsymbol{s}} = \frac{\boldsymbol{s}}{|\boldsymbol{\nabla} H| \sqrt{1 + |\boldsymbol{\nabla} H|^2}} \,. \tag{4.52}$$

The bottom boundary condition on $\boldsymbol{A}^h$ can now be obtained by substituting (4.48) into (4.36), then taking the cross product with $\hat{\boldsymbol{e}}_z$, then simplifying using Lagrange's formula for the vector triple product:

$$\begin{aligned}
& -\frac{\hat{\boldsymbol{e}}_z + \boldsymbol{\nabla} H}{\sqrt{1 + |\boldsymbol{\nabla} H|^2}} \times \boldsymbol{A}_{\text{bot}} = 0 \\
\implies \quad & \hat{\boldsymbol{e}}_z \times \hat{\boldsymbol{e}}_z \times \boldsymbol{A}_{\text{bot}} + \hat{\boldsymbol{e}}_z \times \boldsymbol{\nabla} H \times \boldsymbol{A}_{\text{bot}} = 0 \\
\implies \quad & A^z_{\text{bot}} \left(\hat{\boldsymbol{e}}_z + \boldsymbol{\nabla}_h H \right) - \left(A^z_{\text{bot}} \hat{\boldsymbol{e}}_z + \boldsymbol{A}^h_{\text{bot}} \right) = 0 \\
\implies \quad & \boldsymbol{A}^h_{\text{bot}} = A^z_{\text{bot}} \boldsymbol{\nabla}_h H \,.
\end{aligned} \tag{4.53}$$

Now that the boundary conditions have been determined, equation (4.15) can be solved for $\boldsymbol{A}$. The problem is still a formidable one, however, consisting of a three-dimensional elliptic equation for $\boldsymbol{A}$. Fortunately, the problem can be simplified greatly by recasting the vector potential in terms of force functions, as shown in the following section.

4.4 The Overturning and Barotropic Force Functions

The horizontal component of the vector potential is now written in terms of *overturning force functions* $\boldsymbol{A}^{\text{OT}}$, which are defined to vanish at the top and bottom boundaries such that the meridional and zonal overturning force functions (the components of $\boldsymbol{A}^{\text{OT}}$ in the x and y-directions: $A^{\text{OT}x}$ and $A^{\text{OT}y}$) force closed circulations in their respective planes, giving

$$\boldsymbol{A}^h(x, y, z) = \boldsymbol{A}^{\text{OT}}(x, y, z) + \left(\boldsymbol{A}^h(x, y, z) - \boldsymbol{A}^{\text{OT}}(x, y, z) \right) \,, \tag{4.54}$$

where

$$\boldsymbol{A}^{\text{OT}}_{surf}(x, y) = \boldsymbol{A}^{\text{OT}}_{bot}(x, y) = 0 \,. \tag{4.55}$$

The vertical component is decomposed into *barotropic* (depth-averaged) and *baroclinic* (depth-dependent) force functions:

$$A^z(x,y,z) = A^{\mathrm{BT}}(x,y) + A^{\mathrm{BC}}(x,y,z)\,, \tag{4.56}$$

where

$$A^{\mathrm{BT}} = \frac{1}{H}\int_{-H}^{0} A^z \,\mathrm{d}z\,, \tag{4.57}$$

$$A^{\mathrm{BC}} = A^z - A^{\mathrm{BT}}\,. \tag{4.58}$$

Substituting (4.54) and (4.56) into (4.44) gives us an expression for $\boldsymbol{A}$ in terms of these newly defined force functions:

$$\boldsymbol{A} = \boldsymbol{A}^{\mathrm{OT}} + \left(\boldsymbol{A}^h - \boldsymbol{A}^{\mathrm{OT}}\right) + \left(A^{\mathrm{BT}} + A^{\mathrm{BC}}\right)\hat{\boldsymbol{e}}_z\,. \tag{4.59}$$

To capture the depth variation in $\boldsymbol{A}^h$ and eliminate it from (4.59), the difference between $\boldsymbol{A}^h$ and $\boldsymbol{A}^{\mathrm{OT}}$ is set to vary linearly with depth. The choice of a linear variation with depth is arbitrary, but intuitive, as any nonlinear variation would imply a vertical shear in the horizontal rotational force. This can be seen by writing $\boldsymbol{A}^h$ as

$$\boldsymbol{A}^h(x,y,z) = \boldsymbol{A}^{\mathrm{OT}}(x,y,z) + \boldsymbol{c}(x,y)z + \boldsymbol{c}_0(x,y)\,,$$

where any constant or linear variation with depth in $\boldsymbol{A}^h$ is captured in the two purely horizontal vectors $\boldsymbol{c}$ and $\boldsymbol{c}_0$. Recalling that the horizontal rotational force is given by the horizontal components of the curl of $\boldsymbol{A}$, the horizontal force arising from $\boldsymbol{A}^h$ is therefore given by:

$$\left(\boldsymbol{\nabla}\times\boldsymbol{A}^h\right)^h = \left(\boldsymbol{\nabla}\times\boldsymbol{A}^{\mathrm{OT}}\right)^h + \hat{\boldsymbol{e}}_z\times\boldsymbol{c}\,. \tag{4.60}$$

The only remaining term in (4.60) containing $\boldsymbol{c}$ or $\boldsymbol{c}_0$ has no dependence on z, and so any vertical shear in the horizontal rotational force mediated by $\boldsymbol{A}^h$ must be encapsulated within $\boldsymbol{A}^{\mathrm{OT}}$.

From the surface boundary conditions on $\boldsymbol{A}^h$ and $\boldsymbol{A}^{\mathrm{OT}}$ (equations 4.45 and 4.55), the two terms are both zero at the surface, and so the difference between the two as a function of depth can be written:

$$\boldsymbol{A}^h - \boldsymbol{A}^{\mathrm{OT}} = \boldsymbol{c}z \,. \tag{4.61}$$

The value of the constant of linearity, $\boldsymbol{c}$, is found by substituting the bottom boundary conditions on $\boldsymbol{A}^h$ and $\boldsymbol{A}^{\mathrm{OT}}$ (equations 4.53 and 4.55) into (4.61):

$$\begin{aligned} \boldsymbol{A}^h_{\mathrm{bot}} - \boldsymbol{A}^{\mathrm{OT}}_{\mathrm{bot}} &= -\boldsymbol{c}H \,, \\ A^z_{\mathrm{bot}}\boldsymbol{\nabla}H - 0 &= -\boldsymbol{c}H \,, \\ \boldsymbol{c} &= -\frac{A^z_{\mathrm{bot}}\boldsymbol{\nabla}H}{H} \,. \end{aligned} \tag{4.62}$$

Substituting (4.62) into (4.59) eliminates the A^h term from the right hand side:

$$\boldsymbol{A} = \boldsymbol{A}^{\mathrm{OT}} - \frac{z}{H}A^z_{\mathrm{bot}}\boldsymbol{\nabla}_h H + \left(A^{\mathrm{BT}} + A^{\mathrm{BC}}\right)\hat{\boldsymbol{e}}_z \,, \tag{4.63}$$

or, recombining the barotropic and baroclinic force functions:

$$\boldsymbol{A} = \boldsymbol{A}^{\mathrm{OT}} - \frac{z}{H}A^z_{\mathrm{bot}}\boldsymbol{\nabla}_h H + A^z\hat{\boldsymbol{e}}_z \,. \tag{4.64}$$

Having re-expressed the problem in terms of overturning, barotropic, and baroclinic force functions in this section, the next section derives expressions for the overturning force functions in particular.

4.5 Finding the Overturning Force Functions

In a hydrostatic ocean, it is possible to solve for the overturning force functions $\boldsymbol{A}^{\mathrm{OT}}$ by first considering the horizontal components of (4.15):

$$\nabla^2\boldsymbol{A}^h = -\frac{(\boldsymbol{\nabla}\times\boldsymbol{F})^h}{\rho_0} \,, \tag{4.65}$$

which can be written

$$\nabla_h^2\boldsymbol{A}^h + \frac{\partial^2\boldsymbol{A}^h}{\partial z^2} = -\frac{(\boldsymbol{\nabla}\times\boldsymbol{F})^h}{\rho_0} \,. \tag{4.66}$$

The two derivative terms on the left hand side of (4.64) scale as:

$$\left|\nabla_h^2 \boldsymbol{A}^h\right| \sim \frac{\left|\boldsymbol{A}^h\right|}{L_h^2} \qquad \text{and} \qquad \left|\frac{\partial^2 \boldsymbol{A}^h}{\partial z^2}\right| \sim \frac{\left|\boldsymbol{A}^h\right|}{L_z^2}\,, \tag{4.67}$$

where L_h and L_z are characteristic horizontal and vertical length scales respectively. For an ocean in hydrostatic balance, $L_h \gg L_z$, and therefore the vertical derivative in (4.66) dominates:

$$\nabla^2 \boldsymbol{A}^h \approx \left(1 + O\left(\frac{L_z^2}{L_h^2}\right)\right) \frac{\partial^2 \boldsymbol{A}^h}{\partial z^2}\,, \tag{4.68}$$

$$\approx \frac{\partial^2 \boldsymbol{A}^h}{\partial z^2}\,, \tag{4.69}$$

and hence from (4.65):

$$\frac{\partial^2 \boldsymbol{A}^h}{\partial z^2} \approx -\frac{(\boldsymbol{\nabla} \times \boldsymbol{F})^h}{\rho_0}\,. \tag{4.70}$$

Differentiating the horizontal component of (4.64) twice in the vertical to find $\partial^2 \boldsymbol{A}^h / \partial z^2$ in terms of the overturning force function and then substituting into (4.70) yields two second order uncoupled differential equations for the zonal and meridional overturning force functions:

$$\boldsymbol{A}^h = \boldsymbol{A}^{\mathrm{OT}} - \frac{z}{H} A^z_{\mathrm{bot}} \boldsymbol{\nabla} H\,, \tag{4.71}$$

$$\frac{\partial^2 \boldsymbol{A}^h}{\partial z^2} = \frac{\partial^2 \boldsymbol{A}^{\mathrm{OT}}}{\partial z^2}\,, \tag{4.72}$$

$$\frac{\partial^2 \boldsymbol{A}^{\mathrm{OT}}}{\partial z^2} \approx -\frac{(\boldsymbol{\nabla} \times \boldsymbol{F})^h}{\rho_0}\,. \tag{4.73}$$

This section has shown how, in the hydrostatic limit, the equations for the overturning force functions reduce to a pair of second order differential equations. In the following section, an analogous expression for the barotropic force function is derived.

4.6 Finding the Barotropic Force Function

Finding an expression for the barotropic force function is slightly more involved, particularly in the presence of varying topography. The first step, however, is to depth-integrate the vertical component of (4.15):

$$\int_{-H}^{0} \hat{\boldsymbol{e}}_z \cdot \frac{\boldsymbol{\nabla} \times \boldsymbol{F}}{\rho_0} \, \mathrm{d}z = -\int_{-H}^{0} \nabla^2 A^z \, \mathrm{d}z \,, \tag{4.74}$$

$$= -\int_{-H}^{0} \left(\nabla_h^2 A^z + \frac{\partial^2 A^z}{\partial z^2} \right) \mathrm{d}z \,. \tag{4.75}$$

It is the second term in the above integral that is neglected by Marshall and Pillar (2011), who argue that due to the baroclinic component of A^z being much smaller than the barotropic component (a fact that will be used later), this second term can be dropped. In fact, as will become evident, when integrated vertically over the full ocean depth, this term is not negligible at all in the presence of topography.

Using the gauge condition on $\boldsymbol{A}$ (4.14), the vertical second derivative in (4.75) can be written as

$$\frac{\partial^2 A^z}{\partial z^2} = -\frac{\partial}{\partial z} \left(\boldsymbol{\nabla}_h \cdot \boldsymbol{A}^h \right) = -\boldsymbol{\nabla}_h \cdot \left(\frac{\partial \boldsymbol{A}^h}{\partial z} \right) . \tag{4.76}$$

Then, substituting back into (4.75):

$$\int_{-H}^{0} \hat{\boldsymbol{e}}_z \cdot \frac{\boldsymbol{\nabla} \times \boldsymbol{F}}{\rho_0} \, \mathrm{d}z = -\int_{-H}^{0} \boldsymbol{\nabla}_h \cdot \left(\boldsymbol{\nabla}_h A^z - \frac{\partial \boldsymbol{A}^h}{\partial z} \right) \mathrm{d}z \,. \tag{4.77}$$

To evaluate this integral, the differential operators must be pulled outside the depth integral. Using the Leibniz integral rule to move the divergence operator outside the integral gives:

$$\begin{aligned} \int_{-H(x,y)}^{0} \hat{\boldsymbol{e}}_z \cdot \frac{\boldsymbol{\nabla} \times \boldsymbol{F}}{\rho_0} \, \mathrm{d}z = -\boldsymbol{\nabla} \cdot \int_{-H(x,y)}^{0} \left(\boldsymbol{\nabla}_h A^z - \frac{\partial \boldsymbol{A}^h}{\partial z} \right) \mathrm{d}z \\ + \left(\boldsymbol{\nabla}_h A^z \right)_{\mathrm{bot}} \cdot \boldsymbol{\nabla} H - \left(\frac{\partial \boldsymbol{A}^h}{\partial z} \right)_{\mathrm{bot}} \cdot \boldsymbol{\nabla} H \,, \end{aligned} \tag{4.78}$$

where the first term on the right hand side is due to the curl of the depth-integrated force, and the second is due to the interaction between the rotational component of the bottom force and the non-uniform topography.

Applying the Leibniz integral rule again to the remaining horizontal gradient term within the integral and using the fundamental theorem of calculus to

integrate the vertical derivative yields an expression for the curl of the forcing with no differential operators under the integral sign:

$$\int_{-H(x,y)}^{0} \hat{\boldsymbol{e}}_z \cdot \frac{\boldsymbol{\nabla} \times \boldsymbol{F}}{\rho_0} \, \mathrm{d}z = -\nabla^2 \int_{-H}^{0} A^z \, \mathrm{d}z + \boldsymbol{\nabla} \cdot (A^z_{\mathrm{bot}} \boldsymbol{\nabla} H) + \boldsymbol{\nabla} \cdot \boldsymbol{A}^h_{\mathrm{surf}} - \boldsymbol{\nabla} \cdot \boldsymbol{A}^h_{\mathrm{bot}} + (\boldsymbol{\nabla}_h A^z)_{\mathrm{bot}} \cdot \boldsymbol{\nabla} H - \left(\frac{\partial \boldsymbol{A}^h}{\partial z} \right)_{\mathrm{bot}} \cdot \boldsymbol{\nabla} H \, . \tag{4.79}$$

The integral in (4.79) can now be evaluated using the definition of the barotropic force function (4.57), and the expression can be further simplified using the surface and bottom boundary conditions on $\boldsymbol{A}^h$ (4.45,4.53) to eliminate the divergence terms arising from taking the curl of the depth-integrated force:

$$\hat{\boldsymbol{e}}_z \cdot \int_{-H}^{0} \frac{\boldsymbol{\nabla} \times \boldsymbol{F}}{\rho_0} \, \mathrm{d}z = -\nabla^2 (H A^{\mathrm{BT}}) + (\boldsymbol{\nabla}_h A^z)_{\mathrm{bot}} \cdot \boldsymbol{\nabla} H - \left(\frac{\partial \boldsymbol{A}^h}{\partial z} \right)_{\mathrm{bot}} \cdot \boldsymbol{\nabla} H \, . \tag{4.80}$$

There are several relations which will be used to help convert (4.80) into a more tractable form. First, the chain rule can be used to express bottom derivatives of 3-D fields (e.g., $(\boldsymbol{\nabla}_h A^z)_{\mathrm{bot}}$) in terms of derivatives of the associated 2-D bottom fields ($\boldsymbol{\nabla} A^z_{\mathrm{bot}}$):

$$\begin{aligned} (\boldsymbol{\nabla}_h A^z)_{\mathrm{bot}} &= \boldsymbol{\nabla} A^z_{\mathrm{bot}} + \left(\frac{\partial A^z}{\partial z} \right)_{\mathrm{bot}} \boldsymbol{\nabla} H \, , \\ (\boldsymbol{\nabla} \cdot \boldsymbol{A}^h)_{\mathrm{bot}} &= \boldsymbol{\nabla} \cdot \boldsymbol{A}^h_{\mathrm{bot}} + \left(\frac{\partial \boldsymbol{A}^h}{\partial z} \right)_{\mathrm{bot}} \cdot \boldsymbol{\nabla} H \, . \end{aligned} \tag{4.81}$$

It is also useful to derive several scaling relations. First, it is required from the gauge condition (4.14) that

$$\boldsymbol{\nabla}_h \cdot \boldsymbol{A}^h = -\frac{\partial A^{\mathrm{BC}}}{\partial z}$$

holds everywhere, yielding a scaling relation between $\boldsymbol{A}^h$ and A^{BC}:

$$A^{\mathrm{BC}} \sim \frac{L_z}{L_h} \left| \boldsymbol{A}^h \right| \, . \tag{4.82}$$

Another scaling relation is obtained by considering the bottom boundary condition on $\boldsymbol{A}^h$ (4.53):

$$\boldsymbol{A}^h_{\mathrm{bot}} = A^{\mathrm{BT}} \boldsymbol{\nabla}_h H + A^{\mathrm{BC}}_{\mathrm{bot}} \boldsymbol{\nabla}_h H \, . \tag{4.83}$$

Using 4.82, the terms in (4.83) scale as:

$$\begin{aligned} \left|\boldsymbol{A}^h_{\text{bot}}\right| &\sim \frac{L_h}{L_z} A^{\text{BC}}_{\text{bot}} \,, \\ \left|A^{\text{BT}} \boldsymbol{\nabla}_h H\right| &\sim \frac{H}{\delta} A^{\text{BT}} \,, \\ \text{and} \qquad \left|A^{\text{BC}}_{\text{bot}} \boldsymbol{\nabla}_h H\right| &\sim \frac{H}{\delta} A^{\text{BC}}_{\text{bot}} \,, \end{aligned} \tag{4.84}$$

where δ is the slope width of the sloping sidewall.

The continental slope in the North Atlantic was measured to have a mean width of 63.6 ± 0.8 km by Harris et al. (2014). This value ignores the continental shelf (mean width 115.7 ± 1.6 km), and further the authors note that subpolar slope widths are wider than those at lower latitudes in the North Atlantic, so this value of δ seems a fairly conservative one (although this argument, based on mean slope widths, neglects extreme values and so should be considered rudimentary). It is therefore reasonable to assume that δ is at least an order of magnitude larger than H. The scalings in (4.84) therefore provide the following scaling relation between A^{BT} and $A^{\text{BC}}_{\text{bot}}$:

$$A^{\text{BC}}_{\text{bot}} \sim \frac{L_z H}{L_h \delta} A^{\text{BT}} \,, \tag{4.85}$$

where $L_z \ll L_h$, and $H < \delta$, so for an ocean in hydrostatic balance,

$$A^{\text{BC}}_{\text{bot}} \ll A^{\text{BT}} \,, \tag{4.86}$$

and, therefore,

$$A^z_{\text{bot}} \approx A^{\text{BT}} \,. \tag{4.87}$$

Further, we approximate the z-component of the full vector potential as $A^{\text{BT}}\, \hat{\boldsymbol{e}}_z$ at all depths. The rationale behind this is that the effect of the z-component of the vector potential on the rotational force (through the curl of $\boldsymbol{A}$) is limited to the horizontal components:

$$\boldsymbol{F}^h_{\text{rot}} = -\hat{\boldsymbol{e}}_z \times \left(\boldsymbol{\nabla}_h A^{\text{BT}} + \boldsymbol{\nabla}_h A^{\text{BC}} - \frac{\partial \boldsymbol{A}^h}{\partial z} \right) . \tag{4.88}$$

Note that scaling relation (4.82) implies that the $\boldsymbol{\nabla}_h A^{\mathrm{BC}}$ term in (4.88) is dominated by the $\partial_z \boldsymbol{A}^h$ term, and hence the dynamical effect of A^{BC} is negligible. We therefore have that

$$\boldsymbol{A} = \boldsymbol{A}^{\mathrm{OT}} - \frac{z}{H} A^{\mathrm{BT}} \boldsymbol{\nabla} H + A^{\mathrm{BT}} \hat{\boldsymbol{e}}_z \,. \tag{4.89}$$

Returning now to Equation (4.80), and rewriting $(\boldsymbol{\nabla} A^z)_{\mathrm{bot}}$ using (4.81) (4.87):

$$\begin{aligned} \hat{\boldsymbol{e}}_z \cdot \int_{-H}^{0} \frac{\boldsymbol{\nabla} \times \boldsymbol{F}}{\rho_0} \,\mathrm{d}z \\ = -\nabla^2 (H A^{\mathrm{BT}}) + \boldsymbol{\nabla} A^{\mathrm{BT}} \cdot \boldsymbol{\nabla} H + \left(\frac{\partial A^z}{\partial z} \right)_{\mathrm{bot}} |\boldsymbol{\nabla} H|^2 - \left(\frac{\partial \boldsymbol{A}^h}{\partial z} \right)_{\mathrm{bot}} \cdot \boldsymbol{\nabla} H \,, \end{aligned} \tag{4.90}$$

Note that in Equation (4.90) and all subsequent equations, (4.87) has been used to replace A^z_{bot} with A^{BT}. Now using the gauge condition (4.14) to eliminate $(\partial A^z / \partial z)_{\mathrm{bot}}$:

$$\begin{aligned} \hat{\boldsymbol{e}}_z \cdot \int_{-H}^{0} \frac{\boldsymbol{\nabla} \times \boldsymbol{F}}{\rho_0} \,\mathrm{d}z = -\nabla^2 (H A^{\mathrm{BT}}) + \boldsymbol{\nabla}_h A^{\mathrm{BT}} \cdot \boldsymbol{\nabla} H \\ - \left(\boldsymbol{\nabla} \cdot \boldsymbol{A}^h \right)_{\mathrm{bot}} |\boldsymbol{\nabla} H|^2 - \left(\frac{\partial \boldsymbol{A}^h}{\partial z} \right)_{\mathrm{bot}} \cdot \boldsymbol{\nabla} H \,. \end{aligned} \tag{4.91}$$

Using (4.81) to rewrite the horizontal divergence term and then substituting in the bottom boundary condition (4.53):

$$\begin{aligned} \hat{\boldsymbol{e}}_z \cdot \int_{-H}^{0} \frac{\boldsymbol{\nabla} \times \boldsymbol{F}}{\rho_0} \,\mathrm{d}z &= -\nabla^2 (H A^{\mathrm{BT}}) + \boldsymbol{\nabla}_h A^{\mathrm{BT}} \cdot \boldsymbol{\nabla} H - \left(\boldsymbol{\nabla} \cdot \boldsymbol{A}^h_{\mathrm{bot}} \right) |\boldsymbol{\nabla} H|^2 \\ &\quad - \left(1 + |\boldsymbol{\nabla} H|^2 \right) \left(\frac{\partial \boldsymbol{A}^h}{\partial z} \right)_{\mathrm{bot}} \cdot \boldsymbol{\nabla} H \,. \\ &= -\nabla^2 (H A^{\mathrm{BT}}) + \boldsymbol{\nabla}_h A^{\mathrm{BT}} \cdot \boldsymbol{\nabla} H - \left(\boldsymbol{\nabla} \cdot A^{\mathrm{BT}} \boldsymbol{\nabla} H \right) |\boldsymbol{\nabla} H|^2 \\ &\quad - \left(1 + |\boldsymbol{\nabla} H|^2 \right) \left(\frac{\partial \boldsymbol{A}^h}{\partial z} \right)_{\mathrm{bot}} \cdot \boldsymbol{\nabla} H \,. \end{aligned} \tag{4.92}$$

As previously discussed, the magnitude of the topographic slope $|\boldsymbol{\nabla} H|$ scales as $\frac{H}{\delta}$ where δ is at least an order of magnitude larger than H. This implies that $|\boldsymbol{\nabla} H|^3 \ll 1$ and so, neglecting terms $\mathcal{O}(|\boldsymbol{\nabla} H|^3)$, (4.92) becomes:

$$\hat{\boldsymbol{e}}_z \cdot \int_{-H}^{0} \frac{\boldsymbol{\nabla} \times \boldsymbol{F}}{\rho_0} \,\mathrm{d}z = -\nabla^2 \left(H A^{\mathrm{BT}} \right) + \boldsymbol{\nabla} A^{\mathrm{BT}} \cdot \boldsymbol{\nabla} H - \left(\frac{\partial \boldsymbol{A}^h}{\partial z} \right)_{\mathrm{bot}} \cdot \boldsymbol{\nabla} H \,, \tag{4.93}$$

Then re-expressing $\boldsymbol{A}^h$ in terms of $\boldsymbol{A}^{\mathrm{OT}}$ and A^{BT} using (4.71) and simplifying,

$$\begin{aligned}\hat{\boldsymbol{e}}_z \cdot \int_{-H}^{0} \frac{\boldsymbol{\nabla}\times\boldsymbol{F}}{\rho_0}\,\mathrm{d}z &= -\nabla^2\left(HA^{\mathrm{BT}}\right) + \boldsymbol{\nabla}A^{\mathrm{BT}}\cdot\boldsymbol{\nabla}H + \frac{A^{\mathrm{BT}}|\boldsymbol{\nabla}H|^2}{H} - \left(\frac{\partial \boldsymbol{A}^{\mathrm{OT}}}{\partial z}\right)_{\mathrm{bot}}\cdot\boldsymbol{\nabla}H\,,\\ &= -\nabla^2\left(HA^{\mathrm{BT}}\right) + \frac{\boldsymbol{\nabla}\left(HA^{\mathrm{BT}}\right)\cdot\boldsymbol{\nabla}H}{H} - \left(\frac{\partial \boldsymbol{A}^{\mathrm{OT}}}{\partial z}\right)_{\mathrm{bot}}\cdot\boldsymbol{\nabla}H\,,\\ &= -H\boldsymbol{\nabla}\cdot\left(\frac{\boldsymbol{\nabla}\left(HA^{\mathrm{BT}}\right)}{H}\right) - \left(\frac{\partial \boldsymbol{A}^{\mathrm{OT}}}{\partial z}\right)_{\mathrm{bot}}\cdot\boldsymbol{\nabla}H\,,\end{aligned} \tag{4.94}$$

Taking the coupling term in Equation (4.94) across to the other side leaves the following elliptic equation for A^{BT}:

$$-H\boldsymbol{\nabla}\cdot\left(\frac{\boldsymbol{\nabla}\left(HA^{\mathrm{BT}}\right)}{H}\right) = \hat{\boldsymbol{e}}_z\cdot\int_{-H}^{0}\frac{\boldsymbol{\nabla}\times\boldsymbol{F}}{\rho_0}\,\mathrm{d}z + \left(\frac{\partial \boldsymbol{A}^{\mathrm{OT}}}{\partial z}\right)_{\mathrm{bot}}\cdot\boldsymbol{\nabla}H\,. \tag{4.95}$$

Finally, the $\left(\partial \boldsymbol{A}^{\mathrm{OT}}/\partial z\right)_{\mathrm{bot}}$ coupling term can be evaluated by integrating (4.70) twice in the vertical:

$$\frac{\partial \boldsymbol{A}^{\mathrm{OT}}}{\partial z} = -\int_{-H}^{z}\frac{(\boldsymbol{\nabla}\times\boldsymbol{F})^h}{\rho_0}dz' + \left(\frac{\partial \boldsymbol{A}^{\mathrm{OT}}}{\partial z}\right)_{\mathrm{bot}}\,, \tag{4.96}$$

$$\boldsymbol{A}^{\mathrm{OT}}(z) = -\int_{-H}^{z}\int_{-H}^{z'}\frac{(\boldsymbol{\nabla}\times\boldsymbol{F})^h}{\rho_0}dz''dz' + (z+H)\left(\frac{\partial \boldsymbol{A}^{\mathrm{OT}}}{\partial z}\right)_{\mathrm{bot}} + \boldsymbol{A}^{\mathrm{OT}}_{\mathrm{bot}}\,. \tag{4.97}$$

The two integration constants are fixed by the surface and bottom boundary conditions on $\boldsymbol{A}^{\mathrm{OT}}$ (4.55). Substituting the bottom boundary condition into (4.97) and equating the resulting expression to the surface boundary condition gives:

$$\left(\frac{\partial \boldsymbol{A}^{\mathrm{OT}}}{\partial z}\right)_{\mathrm{bot}} = \frac{1}{H}\int_{-H}^{0}\int_{-H}^{z}\frac{(\boldsymbol{\nabla}\times\boldsymbol{F})^h}{\rho_0}dz'dz\,. \tag{4.98}$$

Then, using the Cauchy formula for repeated integration to convert the double integral and taking the dot product with $\boldsymbol{\nabla}H$:

$$\left(\frac{\partial \boldsymbol{A}^{\mathrm{OT}}}{\partial z}\right)_{\mathrm{bot}}\cdot\boldsymbol{\nabla}H = -\int_{-H}^{0}\frac{z}{H}\boldsymbol{\nabla}H\cdot\frac{(\boldsymbol{\nabla}\times\boldsymbol{F})^h}{\rho_0}dz\,. \tag{4.99}$$

Finally, substituting (4.99) into (4.95) yields a two-dimensional, uncoupled, elliptic equation for A^{BT}, in terms only of known terms:

$$\boxed{-H\boldsymbol{\nabla}\cdot\left(\frac{\boldsymbol{\nabla}\left(HA^{\mathrm{BT}}\right)}{H}\right) = \int_{-H}^{0}\left(\hat{\boldsymbol{e}}_z - \frac{z\boldsymbol{\nabla}H}{H}\right)\cdot\frac{\boldsymbol{\nabla}\times\boldsymbol{F}}{\rho_0}\,\mathrm{d}z\,.} \tag{4.100}$$

Equation (4.100) is a linear steady-state diffusion equation with a source term which is a function of a known force. The three-dimensional curl term in the integrand, however, can still pose numerical issues. The following section presents two simplifications to (4.100) in the hydrostatic limit which make finding solutions a far more straightforward proposition.

4.7 Simplifying the Forcing Terms

While equation (4.100) is uncoupled and two-dimensional and is therefore a vast improvement on the original three-dimensional Poisson equation (4.15), it is still challenging to solve numerically. The main difficulty arises from the calculation of horizontal components of the curl of the forcing, where the large aspect ratio can cause problems accurately evaluating the three-dimensional differential operators inside the integral. Fortunately, it is possible to simplify the integral and circumvent these issues.

4.7.1 Eliminating 3-D Differential Operators

Considering first the first term in the integrand in Equation (4.100), the differential operator can be pulled outside the integral using the Leibniz integral rule:

$$\int_{-H}^{0} \hat{\boldsymbol{e}}_z \cdot \frac{\boldsymbol{\nabla} \times \boldsymbol{F}}{\rho_0} \, \mathrm{d}z = \hat{\boldsymbol{e}}_z \cdot \left(\boldsymbol{\nabla} \times \int_{-H}^{0} \frac{\boldsymbol{F}}{\rho_0} \, \mathrm{d}z + \frac{\boldsymbol{F}_{\mathrm{bot}} \times \boldsymbol{\nabla} H}{\rho_0} \right) . \tag{4.101}$$

Using the cyclic property of the scalar triple product to rewrite the second term, and then substituting in for the isobathic vector $\boldsymbol{t}$ using (4.49):

$$\begin{aligned} \int_{-H}^{0} \hat{\boldsymbol{e}}_z \cdot \frac{\boldsymbol{\nabla} \times \boldsymbol{F}}{\rho_0} \, \mathrm{d}z &= \hat{\boldsymbol{e}}_z \cdot \boldsymbol{\nabla} \times \int_{-H}^{0} \frac{\boldsymbol{F}}{\rho_0} \, \mathrm{d}z + \frac{\boldsymbol{F}_{\mathrm{bot}} \cdot \boldsymbol{\nabla} H \times \hat{\boldsymbol{e}}_z}{\rho_0} , \\ &= \hat{\boldsymbol{e}}_z \cdot \boldsymbol{\nabla} \times \int_{-H}^{0} \frac{\boldsymbol{F}}{\rho_0} \, \mathrm{d}z + \frac{\boldsymbol{F}_{\mathrm{bot}} \cdot \boldsymbol{t}}{\rho_0} . \end{aligned} \tag{4.102}$$

Now considering the second term in the integrand in (4.100), the product rule can be used to convert the dot product into a divergence (recalling that

the curl of a gradient is zero):

$$-\int_{-H}^{0} \frac{z\boldsymbol{\nabla}H}{H} \cdot \frac{\boldsymbol{\nabla}\times\boldsymbol{F}}{\rho_0}\,\mathrm{d}z = -\frac{1}{H}\int_{-H}^{0} z\left(\boldsymbol{\nabla}\cdot\frac{\boldsymbol{F}\times\boldsymbol{\nabla}H}{\rho_0} + \frac{\boldsymbol{F}\cdot\boldsymbol{\nabla}\times\boldsymbol{\nabla}H}{\rho_0}\right)\mathrm{d}z\,,$$
$$= -\frac{1}{H}\int_{-H}^{0} z\boldsymbol{\nabla}\cdot\frac{\boldsymbol{F}\times\boldsymbol{\nabla}H}{\rho_0}\,\mathrm{d}z\,. \tag{4.103}$$

To evaluate the integral in (4.103), the divergence operator needs to be split into horizontal and vertical components:

$$-\int_{-H}^{0} \frac{z\boldsymbol{\nabla}H}{H} \cdot \frac{\boldsymbol{\nabla}\times\boldsymbol{F}}{\rho_0}\,\mathrm{d}z = -\frac{1}{H}\int_{-H}^{0} z\boldsymbol{\nabla}_h\cdot\frac{\boldsymbol{F}\times\boldsymbol{\nabla}H}{\rho_0} + z\frac{\partial}{\partial z}\frac{\hat{\boldsymbol{e}}_z\cdot\boldsymbol{F}\times\boldsymbol{\nabla}H}{\rho_0}\,\mathrm{d}z\,. \tag{4.104}$$

Now writing

$$(\boldsymbol{F}\times\boldsymbol{\nabla}H)^h = F^z\hat{\boldsymbol{e}}_z\times\boldsymbol{\nabla}H$$
$$\text{and}\qquad \hat{\boldsymbol{e}}_z\cdot\boldsymbol{F}\times\boldsymbol{\nabla}H = \boldsymbol{F}\cdot\boldsymbol{\nabla}H\times\hat{\boldsymbol{e}}_z = \boldsymbol{F}\cdot\boldsymbol{t}\,,$$

and re-expressing Equation (4.104) as the sum of two separate integrals:

$$-\int_{-H}^{0} \frac{z\boldsymbol{\nabla}H}{H} \cdot \frac{\boldsymbol{\nabla}\times\boldsymbol{F}}{\rho_0}\,\mathrm{d}z = -\frac{1}{H}\int_{-H}^{0} \boldsymbol{\nabla}_h\cdot\frac{zF^z\hat{\boldsymbol{e}}_z\times\boldsymbol{\nabla}H}{\rho_0}\,\mathrm{d}z - \frac{1}{H}\int_{-H}^{0} z\frac{\partial}{\partial z}\frac{\boldsymbol{F}\cdot\boldsymbol{t}}{\rho_0}\,\mathrm{d}z\,. \tag{4.105}$$

The first integral on the right-hand side of (4.105) can be simplified first by noting that:

$$\boldsymbol{\nabla}_h\cdot\frac{zF^z\hat{\boldsymbol{e}}_z\times\boldsymbol{\nabla}H}{\rho_0} = \hat{\boldsymbol{e}}_z\times\boldsymbol{\nabla}H\cdot\frac{\boldsymbol{\nabla}_h(zF^z)}{\rho_0} + \frac{zF^z\boldsymbol{\nabla}_h\cdot\hat{\boldsymbol{e}}_z\times\boldsymbol{\nabla}H}{\rho_0}\,, \tag{4.106}$$

where the second term vanishes after application of the identity

$$\boldsymbol{\nabla}_h\cdot\hat{\boldsymbol{e}}_z\times\boldsymbol{\nabla}H = \boldsymbol{\nabla}H\cdot(\boldsymbol{\nabla}_h\times\hat{\boldsymbol{e}}_z) - \hat{\boldsymbol{e}}_z\cdot(\boldsymbol{\nabla}_h\times\boldsymbol{\nabla}H) = 0\,. \tag{4.107}$$

Pulling the cross product outside the integral and substituting in the isobathic vector $\boldsymbol{t}$, the integral becomes

$$-\frac{1}{H}\int_{-H}^{0} \boldsymbol{\nabla}_h\cdot\frac{zF^z\hat{\boldsymbol{e}}_z\times\boldsymbol{\nabla}H}{\rho_0}\,\mathrm{d}z = \frac{\boldsymbol{t}}{H}\cdot\int_{-H}^{0}\frac{\boldsymbol{\nabla}_h(zF^z)}{\rho_0}\,\mathrm{d}z\,,$$
$$= \frac{\boldsymbol{t}}{H}\cdot\left(\boldsymbol{\nabla}_h\int_{-H}^{0}\frac{(zF^z)}{\rho_0}\,\mathrm{d}z - [zF^z\boldsymbol{\nabla}H]_{z=-H}^{z=0}\right),$$
$$= \frac{\boldsymbol{t}}{H}\cdot\boldsymbol{\nabla}_h\int_{-H}^{0}\frac{zF^z}{\rho_0}\,\mathrm{d}z\,. \tag{4.108}$$

The final two steps in arriving at (4.108) involve using the Leibniz integral rule to pull the gradient operator out of the integral, and then noticing that $\boldsymbol{t} \cdot \boldsymbol{\nabla} H = 0$ ($\boldsymbol{t}$ is the isobathic vector, and so is evidently orthogonal to the depth gradient).

The second integral on the right-hand side of (4.105) can be evaluated using integration by parts:

$$\begin{aligned} -\frac{1}{H}\int_{-H}^{0} z\frac{\partial}{\partial z}\frac{\boldsymbol{F}\cdot\boldsymbol{t}}{\rho_0}\,\mathrm{d}z &= -\frac{\boldsymbol{t}}{H}\cdot\left(\left[\frac{z\boldsymbol{F}}{\rho_0}\right]_{z=-H}^{z=0} - \int_{-H}^{0}\frac{\boldsymbol{F}}{\rho_0}\,\mathrm{d}z\right), \\ &= \frac{\boldsymbol{t}}{H}\cdot\int_{-H}^{0}\frac{\boldsymbol{F}}{\rho_0}\,\mathrm{d}z - \frac{\boldsymbol{t}\cdot\boldsymbol{F}_{\mathrm{bot}}}{\rho_0}. \end{aligned} \tag{4.109}$$

Substituting (4.108) and (4.109) into (4.105) gives

$$-\int_{-H}^{0}\frac{z\boldsymbol{\nabla}H}{H}\cdot\frac{\boldsymbol{\nabla}\times\boldsymbol{F}}{\rho_0}\,\mathrm{d}z = \boldsymbol{t}\cdot\left(\frac{1}{H}\boldsymbol{\nabla}_h\int_{-H}^{0}\frac{zF^z}{\rho_0}\,\mathrm{d}z + \frac{1}{H}\int_{-H}^{0}\frac{\boldsymbol{F}}{\rho_0}\,\mathrm{d}z - \frac{\boldsymbol{F}_{\mathrm{bot}}}{\rho_0}\right). \tag{4.110}$$

Introducing the notation $\overline{\alpha}$ to denote the depth average of α (with the consequence that the depth integral of α can be written $H\overline{\alpha}$ as a convenient shorthand), such that

$$\overline{\alpha} = \frac{1}{H}\int_{-H}^{0}\alpha\,\mathrm{d}z,$$

and substituting (4.110) and (4.102) into (4.100) yields a more numerically tractable elliptic equation for A^{BT} where the right-hand side contains no three-dimensional differential operators and the bottom force terms cancel:

$$-H\boldsymbol{\nabla}\cdot\left(\frac{\boldsymbol{\nabla}\left(HA^{\mathrm{BT}}\right)}{H}\right) = \hat{\boldsymbol{e}}_z\cdot\boldsymbol{\nabla}\times\frac{H\overline{\boldsymbol{F}}}{\rho_0} + \frac{\boldsymbol{t}}{H}\cdot\boldsymbol{\nabla}\frac{H\overline{zF^z}}{\rho_0} + \frac{\boldsymbol{t}\cdot\overline{\boldsymbol{F}}}{\rho_0}. \tag{4.111}$$

The first two terms on the right-hand side of (4.111) can both be expanded using the product rule:

$$\begin{aligned} \hat{\boldsymbol{e}}_z\cdot\boldsymbol{\nabla}\times\frac{H\overline{\boldsymbol{F}}}{\rho_0} &= H\hat{\boldsymbol{e}}_z\cdot\boldsymbol{\nabla}\times\frac{\overline{\boldsymbol{F}}}{\rho_0} - \hat{\boldsymbol{e}}_z\cdot\frac{\overline{\boldsymbol{F}}}{\rho_0}\times\boldsymbol{\nabla}H, \\ &= H\hat{\boldsymbol{e}}_z\cdot\boldsymbol{\nabla}\times\frac{\overline{\boldsymbol{F}}}{\rho_0} - \boldsymbol{t}\cdot\frac{\overline{\boldsymbol{F}}}{\rho_0}, \end{aligned} \tag{4.112}$$

and

$$\begin{aligned}\frac{\boldsymbol{t}}{H}\cdot\boldsymbol{\nabla}_h\frac{H\overline{zF^z}}{\rho_0} &= \frac{\overline{zF^z}}{\rho_0 H}\,\boldsymbol{t}\cdot\boldsymbol{\nabla}H + \boldsymbol{t}\cdot\frac{\boldsymbol{\nabla}\overline{zF^z}}{\rho_0}\,,\\ &= \boldsymbol{t}\cdot\frac{\boldsymbol{\nabla}\overline{zF^z}}{\rho_0}\,.\end{aligned} \tag{4.113}$$

Hence, substituting (4.112) and (4.113) into (4.111), dividing through by H, and cancelling terms, the following expression is obtained:

$$-\boldsymbol{\nabla}\cdot\left(\frac{\boldsymbol{\nabla}\left(HA^{\mathrm{BT}}\right)}{H}\right) = \hat{\boldsymbol{e}}_z\cdot\frac{\boldsymbol{\nabla}\times\overline{\boldsymbol{F}}}{\rho_0} + |\boldsymbol{\nabla}H|\;\hat{\boldsymbol{t}}\cdot\frac{\boldsymbol{\nabla}\overline{zF^z}}{H\rho_0}\,, \tag{4.114}$$

or, equivalently,

$$-\boldsymbol{\nabla}\cdot\left(\frac{\boldsymbol{\nabla}\left(HA^{\mathrm{BT}}\right)}{H}\right) = \hat{\boldsymbol{e}}_z\cdot\left(\frac{\boldsymbol{\nabla}\times\overline{\boldsymbol{F}}}{\rho_0} + \frac{\boldsymbol{\nabla}\overline{zF^z}\times\boldsymbol{\nabla}H}{H\rho_0}\right). \tag{4.115}$$

4.7.2 Horizontal and Vertical Forces: Exploiting Hydrostatic Balance

Examining the two force terms on the right-hand side of Equation (4.115), it is clear that they neatly separate the effects of the horizontal and vertical components of an applied force. The effects of the horizontal components of the force are confined to the curl term (no vertical components appear in the z-component of the curl), and the Jacobian term encapsulates the effects of the vertical component of the force.

This equation also provides an early hint about the importance of topography: in a basin with vertical sidewalls—i.e., when $|\boldsymbol{\nabla}H| = 0$—the vertical force term vanishes, and so A^{BT} depends only on the horizontal force. As the magnitude of the topographic gradient increases, so does the ability of vertical forces to affect A^{BT}.

For an ocean in hydrostatic balance, the dominant forcing term in the vertical is the buoyancy force, and all other forces are assumed to be purely horizontal. There is therefore only one vertical force to be considered. Further, it can be shown that the rotational buoyancy force can be calculated from the

horizontal pressure gradient, and so there is no need to consider vertical forces at all to calculate all the rotational forces acting on the flow.

The buoyancy force is obtained from hydrostatic balance:

$$\boldsymbol{F}^{(\text{buoy})} = \boldsymbol{F}^{(\text{buoy})}_{\text{rot}} + \boldsymbol{F}^{(\text{buoy})}_{\text{div}} = \rho g \hat{\boldsymbol{e}}_z = \frac{\partial p}{\partial z}\hat{\boldsymbol{e}}_z \,, \tag{4.116}$$

and we define the horizontal pressure gradient force as

$$\boldsymbol{F}^{(\nabla_h p)} = \boldsymbol{F}^{(\nabla_h p)}_{\text{rot}} + \boldsymbol{F}^{(\nabla_h p)}_{\text{div}} = -\nabla_h p \,. \tag{4.117}$$

It is important to note at this stage that, although $\boldsymbol{F}^{(\text{buoy})}$ and $\boldsymbol{F}^{(\nabla_h p)}$ are both components of the gradient of scalar field p, this scalar field is a function of both horizontal and vertical position (i.e., $p = p(x, y, z)$). Therefore neither force can, in general, be written as the full three-dimensional gradient of a scalar field, and so they can not be considered to be conservative forces. This means that the curl of each force individually does not generally vanish, and so both may have a non-zero rotational component. The full pressure gradient can now be expressed in terms of the two forces as

$$-\nabla p = \boldsymbol{F}^{(\nabla_h p)} - \boldsymbol{F}^{(\text{buoy})} \,. \tag{4.118}$$

The gradient in (4.118) is a full three-dimensional gradient, and so when taking the curl of (4.118) the left-hand side vanishes, leaving:

$$0 = \nabla \times \boldsymbol{F}^{(\nabla_h p)} - \nabla \times \boldsymbol{F}^{(\text{buoy})} \,, \tag{4.119}$$

$$0 = \nabla \times \boldsymbol{F}^{(\nabla_h p)}_{\text{rot}} - \nabla \times \boldsymbol{F}^{(\text{buoy})}_{\text{rot}} \,. \tag{4.120}$$

$$\nabla \times \boldsymbol{F}^{(\nabla_h p)}_{\text{rot}} = \nabla \times \boldsymbol{F}^{(\text{buoy})}_{\text{rot}} \tag{4.121}$$

From definition (4.8), $\boldsymbol{F}_{\text{rot}}$ has no divergent component and, as discussed in Section 4.3.1, the requisite boundary condition on $\boldsymbol{F}_{\text{rot}}$ means that it can have no harmonic component either. Equation (4.121) therefore implies that

$$\boldsymbol{F}^{(\nabla_h p)}_{\text{rot}} = \boldsymbol{F}^{(\text{buoy})}_{\text{rot}} \,. \tag{4.122}$$

By using Equation (4.122) to find the vector potential for the buoyancy force indirectly by instead solving for the horizontal pressure force, there is no longer any need to consider any vertical forces to find the full rotational momentum balance. This is particularly useful when determining the boundary condition on the barotropic force function, as will be demonstrated in the following section.

4.8 Boundary Condition on the Barotropic Force Function

Before Equation (4.115) can be solved, the correct boundary condition on the depth-integrated force function HA^{BT} must be imposed. Note that, because it is related to the streamfunction for horizontal flow, HA^{BT} should be expected to remain finite as H tends to zero, and so it is not sufficient to simply assume $HA^{\mathrm{BT}} = 0$ on all boundaries. The obvious approach is to use the kinematic boundary condition of no rotational forcing through the boundary (4.18). As it turns out, this is a necessary, but not sufficient condition to allow solution of the elliptic problem in a multiply connected domain.

The relevant boundary for the two-dimensional equation (4.115) is the boundary between the land and the ocean. This boundary is defined mathematically as the intersection of the upper bounding surface (given by the plane $z = 0$) with the bottom bounding surface (defined in Section 4.3.2 as the surface $z + H = 0$). The boundary is therefore defined by the set of points satisfying the equation $H(x, y) = 0$, with an associated normal vector given by $\boldsymbol{n}_{2\mathrm{D}} = -\boldsymbol{\nabla} H$. The kinematic boundary condition for the depth-integrated problem is therefore:

$$\boldsymbol{n}_{2\mathrm{D}} \cdot \int_{-H}^{0} \boldsymbol{\nabla} \times \boldsymbol{A} \, \mathrm{d}z = 0 \,. \tag{4.123}$$

To obtain a boundary condition on the depth-integrated barotropic force function, first we write the horizontal component of the curl in (4.123) as

$$(\boldsymbol{\nabla} \times \boldsymbol{A})^h = \hat{\boldsymbol{e}}_z \times \left(\frac{\partial \boldsymbol{A}^h}{\partial z} - \boldsymbol{\nabla}_h A^z \right) ,$$

so we have that

$$\boldsymbol{n}_{2\mathrm{D}} \cdot \int_{-H}^{0} \boldsymbol{\nabla} \times \boldsymbol{A} \, \mathrm{d}z = -\boldsymbol{\nabla} H \cdot \hat{\boldsymbol{e}}_z \times \int_{-H}^{0} \frac{\partial \boldsymbol{A}^h}{\partial z} - \boldsymbol{\nabla}_h A^z \, \mathrm{d}z \,. \tag{4.124}$$

Evaluating the integral on the right hand side then substituting in for the top and bottom boundary conditions on A^h (4.45, 4.53) gives

$$\begin{aligned} \boldsymbol{n}_{2\mathrm{D}} \cdot \int_{-H}^{0} \boldsymbol{\nabla} \times \boldsymbol{A} \, \mathrm{d}z &= -\boldsymbol{\nabla} H \cdot \hat{\boldsymbol{e}}_z \times \left([\boldsymbol{A}^h]_{z=-H}^{z=0} - \boldsymbol{\nabla} \left(H A^{\mathrm{BT}} \right) + A^z_{\mathrm{bot}} \boldsymbol{\nabla} H \right) , \\ &= -\boldsymbol{\nabla} H \cdot \hat{\boldsymbol{e}}_z \times -\boldsymbol{\nabla} \left(H A^{\mathrm{BT}} \right) . \end{aligned} \tag{4.125}$$

Substituting back into (4.123) gives the required boundary condition on HA^{BT}:

$$\boldsymbol{\nabla} H \cdot \hat{\boldsymbol{e}}_z \times \boldsymbol{\nabla} \left(H A^{\mathrm{BT}} \right) = 0 \,, \tag{4.126}$$

or equivalently, using the cyclic property of the cross product,

$$\boldsymbol{\nabla} \left(H A^{\mathrm{BT}} \right) \cdot \boldsymbol{t} = 0 \,. \tag{4.127}$$

Recalling from (4.49) that $\mathbf{t}$ is oriented along isobaths, the constraint arising from imposing the kinematic boundary condition is that the depth-integrated force function HA^{BT} must be constant along the boundary. This constraint, however, tells us nothing about the value HA^{BT} assumes on the boundary. In a domain where the boundary comprises n continuous curves, the value of HA^{BT} on any one of these curves can be specified without loss of generality, but specifying the value on one curve fixes HA^{BT} on the others to unknown values. Applying the kinematic boundary condition, then, yields one Dirichlet boundary condition, leaving $(n-1)$ further Dirichlet boundary conditions to be determined via a different approach.

The method used to calculate these additional boundary conditions is based on that used in Pillar (2013) but corrects two minor errors, one which is shown to have no effect, whereas the other is highly significant in the presence of non-uniform topography.

The depth integral of the horizontal component of the full force in terms of the force functions $\boldsymbol{A}$ and the scalar potential $\boldsymbol{\phi}$ is given by:

$$\int_{-H}^{0} \frac{\boldsymbol{F}^h}{\rho_0} \,\mathrm{d}z = \int_{-H}^{0} (\boldsymbol{\nabla} \times \boldsymbol{A})^h + \boldsymbol{\nabla}_h \phi \,\mathrm{d}z \tag{4.128}$$

$$= \int_{-H}^{0} \hat{\boldsymbol{e}}_z \times \frac{\partial \boldsymbol{A}^h}{\partial z} - \hat{\boldsymbol{e}}_z \times \boldsymbol{\nabla}_h A^{\mathrm{BT}} + \boldsymbol{\nabla}_h \phi \,\mathrm{d}z \tag{4.129}$$

$$= \hat{\boldsymbol{e}}_z \times \left([\boldsymbol{A}^h]_{z=-H}^{z=0} - H \boldsymbol{\nabla}_h A^{\mathrm{BT}} \right) + \boldsymbol{\nabla}_h \int_{-H}^{0} \phi \,\mathrm{d}z - \phi_{\mathrm{bot}} \boldsymbol{\nabla}_h H \tag{4.130}$$

$$= -\hat{\boldsymbol{e}}_z \times \boldsymbol{\nabla}_h \left(H A^{\mathrm{BT}} \right) + \boldsymbol{\nabla}_h \int_{-H}^{0} \phi \,\mathrm{d}z - \phi_{\mathrm{bot}} \boldsymbol{\nabla}_h H \,. \tag{4.131}$$

Equation (4.131) can be integrated along lines of latitude or longitude connecting boundary segments where the value of $H A^{\mathrm{BT}}$ is known to ones where it is not. This process can be repeated until each of the unknown Dirichlet boundary conditions has been obtained. To be able to apply this approach, however, the scalar potential must first be solved for.

The approach to obtaining the scalar potential is similar to the one used to obtain the barotropic force function, and exploits the hydrostatic nature of the problem. First, the scalar potential is split into barotropic and baroclinic parts (plus an additive constant, which, because we are concerned only with gradients of the scalar potential, is arbitratily set to zero):

$$\phi(x, y, z) = \phi^{\mathrm{BT}}(x, y) + \phi^{\mathrm{BC}}(x, y, z) \,, \tag{4.132}$$

where

$$\phi^{\mathrm{BT}} = \frac{1}{H} \int_{-H}^{0} \phi \,\mathrm{d}z \,, \tag{4.133}$$

$$\phi^{\mathrm{BC}} = \phi - \phi^{\mathrm{BT}} \,. \tag{4.134}$$

Substituting (4.133) and (4.134) back into (4.131) gives the expression

$$\int_{-H}^{0} \frac{\boldsymbol{F}^h}{\rho_0} \,\mathrm{d}z = -\hat{\boldsymbol{e}}_z \times \boldsymbol{\nabla}_h \left(H A^{\mathrm{BT}} \right) + H \boldsymbol{\nabla}_h \phi^{\mathrm{BT}} - \phi^{\mathrm{BC}}_{\mathrm{bot}} \boldsymbol{\nabla}_h H \,. \tag{4.135}$$

Now considering only purely horizontal forces—which is not restrictive, courtesy of the trick for replacing the vertical buoyancy force with the horizontal pressure gradient force outlined in Section 4.7.2—the unwanted $\phi^{\mathrm{BC}}_{\mathrm{bot}}$ can be

addressed. Pillar (2013) asserts that for a purely horizontal force, $\partial\phi/\partial z = 0$ and hence that $\phi^{\mathrm{BC}} = 0$. This, however, is not the case: although the net vertical force is zero, the only constraint that this places on the baroclinic scalar potential is that it must balance the vertical component of the rotational force. The baroclinic scalar potential is therefore related to the vector potential by:

$$\frac{\partial \phi^{\mathrm{BC}}}{\partial z} = -\hat{\boldsymbol{e}}_z \cdot \boldsymbol{\nabla} \times \boldsymbol{A}^h \,. \tag{4.136}$$

A quick scaling argument is sufficient to show that while not necessarily zero for horizontal forces, ϕ^{BC} is small enough to be neglected in Equation (4.135). The terms in (4.136) scale as:

$$\frac{\phi^{\mathrm{BC}}}{L_z} \sim \frac{\left|\boldsymbol{A}^h\right|}{L_h} \,, \tag{4.137}$$

which, when combined with scaling relation (4.82) arising from the gauge condition, gives

$$\phi^{\mathrm{BC}} \sim A^{\mathrm{BC}} \ll A^{\mathrm{BT}} \,. \tag{4.138}$$

The baroclinic scalar potential term in (4.135) can therefore safely be neglected, and so the equation used to determine the additional boundary conditions can be rewritten

$$\int_{-H}^{0} \frac{\boldsymbol{F}^h}{\rho_0} \,\mathrm{d}z = -\hat{\boldsymbol{e}}_z \times \boldsymbol{\nabla}_h \left(H A^{\mathrm{BT}}\right) + H \boldsymbol{\nabla}_h \phi^{\mathrm{BT}} \,, \tag{4.139}$$

such that now only the two-dimensional barotropic scalar potential is required, as opposed to the full three-dimensional field.

To find the barotropic scalar potential, take the divergence of (4.139). This eliminates the barotropic force function and leaves another two-dimensional elliptic equation, this time for ϕ^{BT}:

$$\boldsymbol{\nabla} \cdot \int_{-H}^{0} \frac{\boldsymbol{F}^h}{\rho_0} \,\mathrm{d}z = \boldsymbol{\nabla} \cdot \left(H \boldsymbol{\nabla}_h \phi^{\mathrm{BT}}\right) \,. \tag{4.140}$$

The boundary condition on this problem can be obtained by taking the dot product of (4.139) with the normal vector $\boldsymbol{n}_{2\mathrm{D}} = -\boldsymbol{\nabla} H$ and then substituting the

depth-integrated kinematic boundary condition (4.126) into (4.139). This yields a Neumann boundary condition on each boundary:

$$\boldsymbol{n}_{2\mathrm{D}} \cdot \int_{-H}^{0} \frac{\boldsymbol{F}^{h}}{\rho_0} \, \mathrm{d}z = \boldsymbol{n}_{2\mathrm{D}} \cdot H \boldsymbol{\nabla}_h \phi^{\mathrm{BT}} \, . \tag{4.141}$$

Inverting (4.140) subject to (4.141) gives the barotropic scalar potential, and so the components (4.139) now give the partial derivatives $\partial/\partial x$ and $\partial/\partial y$ of HA^{BT}, which can be integrated along lines of latitude and longitude to obtain any unknown boundary values.

Now that a complete set of equations for the overturning and barotropic force functions has been derived, along with accompanying boundary conditions, the full vector potential can be calculated. The following section relates this vector potential to the barotropic and meridional overturning streamfunctions.

4.9 Relating the Force Functions to the Barotropic and Overturning Circulations

4.9.1 The Overturning Circulation

To relate the vector potential $\boldsymbol{A}$ to the overturning circulation, recall the definition of the MOC:

$$\Psi^{(z)}_{\mathrm{MOC}} = - \int_{-H_{\max}}^{z} \int_{x_{\mathrm{w}}}^{x_{\mathrm{e}}} v \, \mathrm{d}x \, \mathrm{d}z' \, . \tag{4.142}$$

Differentiating with respect to time to obtain an equation for the rate of change of the overturning streamfunction, and then considering only the rate of change due to a single force, gives an expression relating this rate of change to the rotational component of the force (recalling that only the rotational force acts to accelerate the flow).

$$- \frac{\partial \Psi^{(z)}_{\mathrm{MOC}}}{\partial t} = \int_{-H_{\max}}^{z} \int_{x_{\mathrm{w}}}^{x_{\mathrm{e}}} \hat{\boldsymbol{e}}_y \cdot \frac{\boldsymbol{F}_{\mathrm{rot}}}{\rho_0} \, \mathrm{d}x \, \mathrm{d}z' \, . \tag{4.143}$$

Substituting in the definition of the rotational force yields an expression for the tendency in the overturning streamfunction in terms of the vector potential.

$$\begin{aligned} -\frac{\partial \Psi^{(z)}_{\mathrm{MOC}}}{\partial t} &= \int_{-H_{\max}}^{z} \int_{x_w}^{x_e} \hat{\boldsymbol{e}}_y \cdot (\boldsymbol{\nabla} \times \boldsymbol{A}) \, \mathrm{d}x \, \mathrm{d}z' \,, \\ &= \int_{-H_{\max}}^{z} \int_{x_w}^{x_e} \frac{\partial A^x}{\partial z} - \frac{\partial A^{\mathrm{BT}}}{\partial x} \, \mathrm{d}x \, \mathrm{d}z' \,. \end{aligned} \tag{4.144}$$

Next, using (4.71) to write A^x in terms of overturning and barotropic force functions

$$\begin{aligned} -\frac{\partial \Psi^{(z)}_{\mathrm{MOC}}}{\partial t} &= \int_{-H_{\max}}^{z} \int_{x_w}^{x_e} \frac{\partial A^{\mathrm{OT}x}}{\partial z} - \frac{A^{\mathrm{BT}}}{H} \frac{\partial H}{\partial x} - \frac{\partial A^{\mathrm{BT}}}{\partial x} \, \mathrm{d}x \, \mathrm{d}z' \,, \\ &= \int_{-H_{\max}}^{z} \int_{x_w}^{x_e} \frac{\partial A^{\mathrm{OT}x}}{\partial z} - \frac{1}{H} \frac{\partial (H A^{\mathrm{BT}})}{\partial x} \, \mathrm{d}x \, \mathrm{d}z' \,. \end{aligned} \tag{4.145}$$

Then, using Fubini's theorem to switch the order of integration and integrate first over depth, as well as the fact that $A^{\mathrm{OT}x}$ vanishes on the bottom boundary:

$$-\frac{\partial \Psi^{(z)}_{\mathrm{MOC}}}{\partial t} = \int_{x_w}^{x_e} A^{\mathrm{OT}x} - \left(1 + \frac{z}{H}\right) \frac{\partial (H A^{\mathrm{BT}})}{\partial x} \, \mathrm{d}x \,, \tag{4.146}$$

Note that as the integrand in (4.145) is simply the rotational acceleration (i.e., no vertical integration has occurred yet), it can be simply adapted to relate the rate of change of the overturning streamfunction in density space to the overturning and barotropic force functions:

$$-\frac{\partial \Psi^{(\rho)}_{\mathrm{MOC}}}{\partial t} = \int_{\rho_{\max}}^{\rho} \int_{x_w}^{x_e} \left(\frac{\partial A^{\mathrm{OT}x}}{\partial z} - \frac{1}{H} \frac{\partial (H A^{\mathrm{BT}})}{\partial x} \right) \left(\frac{\partial \rho}{\partial z} \right)^{-1} \mathrm{d}x \, \mathrm{d}\rho' \,. \tag{4.147}$$

Note that in both (4.146) and (4.147), the integral can be cleanly split into two components: one containing only the overturning force function $A^{\mathrm{OT}x}$—which drives closed circulations in the zy-plane, projecting onto the shear component of the overturning—and the other containing only the barotropic force function A^{BT}—which will be shown in the next section to drive the barotropic circulation, projecting onto the external mode. In this way the effect of a force on the shear and external mode components of the overturning circulation can be easily extracted from the vector potential $\boldsymbol{A}$.

4.9.2 The Barotropic Gyre Circulation

The non-divergence of the flow, as stated in the continuity equation (4.2), means that the barotropic flow can be represented by a volume transport streamfunction Ψ_{BT}, defined by

$$\hat{\boldsymbol{e}}_z \times \boldsymbol{\nabla} \Psi_{\mathrm{BT}} = \int_{-H}^{0} \boldsymbol{u}^h \, \mathrm{d}z \, . \tag{4.148}$$

Taking the time derivative of (4.148), and again considering only the acceleration due to a single force, gives an expression relating Ψ_{BT} to the vector potential $\boldsymbol{A}$:

$$\begin{aligned} \hat{\boldsymbol{e}}_z \times \boldsymbol{\nabla} \frac{\partial \Psi_{\mathrm{BT}}}{\partial t} &= \int_{-H}^{0} \frac{\boldsymbol{F}_{\mathrm{rot}}}{\rho_0} \, \mathrm{d}z \, , \\ &= \int_{-H}^{0} (\boldsymbol{\nabla} \times \boldsymbol{A})^h \, \mathrm{d}z \, , \\ &= - \int_{-H}^{0} \hat{\boldsymbol{e}}_z \times \left(\frac{\partial \boldsymbol{A}^h}{\partial z} - \boldsymbol{\nabla} A^{\mathrm{BT}} \right) \mathrm{d}z \, , \end{aligned} \tag{4.149}$$

integrating, applying the boundary conditions on $\boldsymbol{A}^h$, and collecting terms gives

$$\hat{\boldsymbol{e}}_z \times \boldsymbol{\nabla} \frac{\partial \Psi_{\mathrm{BT}}}{\partial t} = - \hat{\boldsymbol{e}}_z \times \boldsymbol{\nabla} \left(H A^{\mathrm{BT}} \right) \, , \tag{4.150}$$

$$\implies \quad \boldsymbol{\nabla} \frac{\partial \Psi_{\mathrm{BT}}}{\partial t} = - \boldsymbol{\nabla} \left(H A^{\mathrm{BT}} \right) \, . \tag{4.151}$$

Equation (4.151) implies that $\partial_t \Psi_{\mathrm{BT}}$ and $H A^{\mathrm{BT}}$ are equal up to a spatially-constant term. As with the boundary condition on $H A^{\mathrm{BT}}$, however, it is possible to choose any arbitrary value for $\partial_t \Psi_{\mathrm{BT}}$ on a single bounding curve without loss of generality. Therefore, by choosing the same value as $H A^{\mathrm{BT}}$ at a specific point on the boundary, the equation relating the volume transport streamfunction to the barotropic force function becomes:

$$H A^{\mathrm{BT}} = - \frac{\partial \Psi_{\mathrm{BT}}}{\partial t} \, . \tag{4.152}$$

This equation demonstrates, unsurprisingly, that the barotropic force function is responsible for driving the barotropic gyre circulation. This is unsurprising as the elliptic equation for the barotropic force function strongly resembles the barotropic potential vorticity equation for depth-integrated flow (e.g., Hughes and Killworth 1995; Hughes 2008).

4.9.3 The Barotropic Potential Vorticity Equation and JEBAR

Displayed below is the form of the barotropic potential vorticity equation given by Equation 8 from Hughes (2008). The notation is adapted to match that used in this chapter in that all horizontal forces are bundled into a sum and the Jacobian pressure term is expanded into a cross product.

$$-\boldsymbol{\nabla}\cdot\left(\frac{\boldsymbol{\nabla}(\partial_t \Psi_{\mathrm{BT}})}{H}\right) = \hat{\boldsymbol{e}}_z\cdot\left(\sum_{\boldsymbol{F}^h}\frac{\boldsymbol{\nabla}\times\overline{\boldsymbol{F}^h}}{\rho_0} - \frac{\boldsymbol{\nabla}(H\overline{\rho g z})\times\boldsymbol{\nabla}H}{H^2\rho_0}\right). \tag{4.153}$$

Note that in the above equation, Ψ_{BT} is the net rate of change in the volume transport streamfunction, not that due to a single force as previously. As such, the terms on the right-hand side represent the curl of the depth-averaged horizontal forces acting on the flow, and a term accounting for the effects of baroclinicity in the presence of non-uniform topography, generally referred to as the JEBAR (Joint Effect of Baroclinicity And Relief; introduced by Sarkisyan and Ivanov 1971—see Sarkisyan 2006 for an English-language overview).

In Hughes (2008), this term arises from the curl of the depth-averaged horizontal pressure gradient. From the discussion in Section 4.7.2, however, it would be expected that the barotropic rotational acceleration calculated from the horizontal pressure gradient should be identical to that determined from the buoyancy force. The form of the cross product in (4.153) suggests that this is the case. Considering only the JEBAR term, and using the product rule to expand the gradient term:

$$\begin{aligned}\hat{\boldsymbol{e}}_z\cdot\frac{\boldsymbol{\nabla}(H\overline{\rho g z})\times\boldsymbol{\nabla}H}{H^2\rho_0} &= \hat{\boldsymbol{e}}_z\cdot\frac{\boldsymbol{\nabla}(\overline{\rho g z})\times\boldsymbol{\nabla}H}{H\rho_0} + \hat{\boldsymbol{e}}_z\cdot\frac{\overline{\rho g z}\boldsymbol{\nabla}H\times\boldsymbol{\nabla}H}{H^2\rho_0},\\ &= \hat{\boldsymbol{e}}_z\cdot\frac{\boldsymbol{\nabla}(\overline{\rho g z})\times\boldsymbol{\nabla}H}{H\rho_0}.\end{aligned} \tag{4.154}$$

From hydrostatic balance, we have that $\boldsymbol{F}_{\mathrm{buoy}} = -\rho g\,\hat{\boldsymbol{e}}_z$, and substituting this into the above equation gives

$$\begin{aligned}\hat{\boldsymbol{e}}_z\cdot\frac{\boldsymbol{\nabla}(H\overline{\rho g z})\times\boldsymbol{\nabla}H}{H^2\rho_0} &= -\,\hat{\boldsymbol{e}}_z\cdot\frac{\boldsymbol{\nabla}(\overline{zF^z_{\mathrm{buoy}}})\times\boldsymbol{\nabla}H}{H\rho_0},\\ &= -\,\hat{\boldsymbol{e}}_z\cdot\left(\frac{\boldsymbol{\nabla}\times\overline{\boldsymbol{F}_{\mathrm{buoy}}}}{\rho_0} + \frac{\boldsymbol{\nabla}(\overline{zF^z_{\mathrm{buoy}}})\times\boldsymbol{\nabla}H}{H\rho_0}\right),\end{aligned} \tag{4.155}$$

where the curl term is zero due to the purely vertical nature of the buoyancy force. Now, substituting in using (4.115), the JEBAR term is related to the barotropic buoyancy force function by:

$$\hat{\boldsymbol{e}}_z \cdot \frac{\boldsymbol{\nabla}(H\overline{\rho g z}) \times \boldsymbol{\nabla} H}{H^2 \rho_0} = \boldsymbol{\nabla} \cdot \left(\frac{\boldsymbol{\nabla}(H A^{\mathrm{BT}}_{\mathrm{buoy}})}{H} \right) . \tag{4.156}$$

The JEBAR term therefore represents the effect of the buoyancy force on the evolution of the flow.

Similarly, because the vertical component of every other force is zero, for all forces that are not buoyancy:

$$\hat{\boldsymbol{e}}_z \cdot \frac{\boldsymbol{\nabla} \times \overline{\boldsymbol{F}^h}}{\rho_0} = -\boldsymbol{\nabla} \cdot \left(\frac{\boldsymbol{\nabla}(H A^{\mathrm{BT}})}{H} \right) . \tag{4.157}$$

Substituting (4.156) and (4.157) into (4.153) then gives the expected result:

$$\boldsymbol{\nabla} \cdot \left(\frac{\boldsymbol{\nabla}(\partial_t \Psi_{\mathrm{BT}})}{H} \right) = \sum_{\boldsymbol{F}} \boldsymbol{\nabla} \cdot \left(\frac{\boldsymbol{\nabla}(H A^{\mathrm{BT}}_{\boldsymbol{F}})}{H} \right) , \tag{4.158}$$

Where the subscript $\boldsymbol{F}$ indicates that the sum on the right hand side is taken over the force functions arising from each force acting on the circulation.

4.10 Summary

This chapter introduced a decomposition of the momentum equation, where it is split into its rotational and divergent components through the application of the Helmholtz decomposition to the force terms. The divergent component was shown to project solely onto the pressure gradient, whereas the rotational component determines the evolution of the flow. The rotational equation therefore is an alternative formulation of the vorticity equation, though the former is expressed more intuitively in terms of force balances, as opposed to sources and sinks of vorticity as in the latter.

The force functions used to describe the rotational force balance were then derived. The calculation initially followed that used by Marshall and Pillar (2011). Their derivation, however, contained an error. This error meant, first, that the

resulting force functions incorrectly ignored the effects of topography, and also led to an inability to correctly determine the lateral boundary conditions.

The correct form of the force functions and accompanying boundary conditions were therefore derived, and it was shown that the equations for the barotropic and overturning force functions could still be decoupled even in the presence of topography. Further simplifications to the elliptic equation for the barotropic force function arising from hydrostatic balance were then presented. Finally, the connection between the force functions and the barotropic and overturning circulations, and the relationship between the rotational buoyancy force and the JEBAR term in the barotropic potential vorticity equation, were made explicit. A summary of the important equations from this chapter is given in Table 4.1.

In the following chapter, a numerical implementation of the rotational momentum equation decomposition is introduced. The decomposition is then applied to the experiments presented in Chapter 3 and the resulting force functions are used to diagnose the rotational force balances underlying the circulation in each case.

Helmholtz decomposition of applied force (4.10)	$\frac{\boldsymbol{F}}{\rho_0} = \boldsymbol{\nabla}\phi + \boldsymbol{\nabla} \times \boldsymbol{A}$
Poisson equation for the vector potential (4.15)	$-\nabla^2 \boldsymbol{A} = \frac{\boldsymbol{\nabla} \times \boldsymbol{F}}{\rho_0}$
Gauge condition on the vector potential (4.14)	$\boldsymbol{\nabla} \cdot \boldsymbol{A} = 0$
Boundary condition on the vector potential (4.36)	$\hat{\boldsymbol{n}} \times \boldsymbol{A} = 0$
Vector potential in terms of barotropic and overturning force functions (4.89)	$\boldsymbol{A} = \boldsymbol{A}^{\mathrm{OT}} - \frac{z}{H} A^{\mathrm{BT}} \boldsymbol{\nabla} H + A^{\mathrm{BT}} \hat{\boldsymbol{e}}_z$
ODEs for the overturning force functions (4.73)	$\frac{\partial^2 \boldsymbol{A}^{\mathrm{OT}}}{\partial z^2} = -\frac{(\boldsymbol{\nabla} \times \boldsymbol{F})^h}{\rho_0}$
Boundary conditions on the overturning force functions (4.55)	$\boldsymbol{A}^{\mathrm{OT}}_{surf} = \boldsymbol{A}^{\mathrm{OT}}_{bot} = 0$
Elliptic equation for the barotropic force function (4.100)	$-H\boldsymbol{\nabla} \cdot \left(\frac{\boldsymbol{\nabla}\left(H A^{\mathrm{BT}}\right)}{H} \right) = \int_{-H}^{0} \left(\hat{\boldsymbol{e}}_z - \frac{z \boldsymbol{\nabla} H}{H} \right) \cdot \frac{\boldsymbol{\nabla} \times \boldsymbol{F}}{\rho_0} \, \mathrm{d}z$
As above, but with simplified right hand side (4.115)	$-\boldsymbol{\nabla} \cdot \left(\frac{\boldsymbol{\nabla}\left(H A^{\mathrm{BT}}\right)}{H} \right) = \hat{\boldsymbol{e}}_z \cdot \left(\frac{\boldsymbol{\nabla} \times \overline{\boldsymbol{F}}}{\rho_0} + \frac{\boldsymbol{\nabla} \overline{z F^z} \times \boldsymbol{\nabla} H}{H \rho_0} \right)$
Boundary conditions on the barotropic force function	See Section 4.8

TABLE 4.1: Summary of important equations from Chapter 4

5 Application of Decomposition to Sensitivity Experiments

5.1 Introduction . . . 103
5.2 Numerical Implementation . . . 104
5.2.1 Solving for the Overturning Force Functions . . . 104
5.2.2 Solving for the Depth-Integrated Force Function . . . 105
5.2.3 Further Decomposition of the Barotropic Rotational Momentum Equation . . . 109
5.3 Rotational Momentum Balance of the Barotropic Circulation 114
5.4 Rotational Momentum Balance of the Overturning Circulation 120
5.4.1 The Overturning Force Function . . . 120
5.4.2 The Overturning Circulation in Depth Space . . . 128
5.4.3 The Overturning Circulation in Density Space . . . 136
5.4.4 Shear and External Mode Components . . . 144
5.5 Summary . . . 148

5.1 Introduction

The full rotational momentum equation relates the acceleration of the flow to the net rotational force acting on it, written as the curl of a vector potential $\boldsymbol{A}$:

$$\frac{\partial \boldsymbol{u}}{\partial t} = \sum_{\boldsymbol{F}} \boldsymbol{\nabla} \times \boldsymbol{A}_{\boldsymbol{F}} \,, \tag{5.1}$$

where vector potential $\boldsymbol{A}$ can be expressed in terms of barotropic and overturning force functions (A^{BT} and $\boldsymbol{A}^{\mathrm{OT}}$):

$$\boldsymbol{A} = \boldsymbol{A}^{\mathrm{OT}} - \frac{z}{H} A^{\mathrm{BT}} \boldsymbol{\nabla}_h H + A^{\mathrm{BT}} \hat{\boldsymbol{e}}_z \ . \tag{5.2}$$

These force functions encapsulate the effect of the relevant force on the evolution of the barotropic and overturning circulations, as demonstrated in Section 4.9.

Calculating the barotropic and overturning force functions requires solving equations (4.73) and (4.115) respectively.

In this section, the numerical method by which these equations are solved for the model output is presented, and the force functions derived by applying the decomposition to the experiments from Chapter 3 are then analysed. Finally, the calculated depth-integrated and meridional overturning force functions are used in conjunction with equations (4.146) and (4.147) to determine the torque applied by each force to the meridional overturning circulation in both depth space and density space.

5.2 Numerical Implementation of Rotational Momentum Decomposition

5.2.1 Solving for the Overturning Force Functions

Finding the meridional and zonal overturning force functions, $A^{\mathrm{OT}x}$ and $A^{\mathrm{OT}y}$, requires solving the two uncoupled second order differential equations given by (4.73), reproduced below:

$$\frac{\partial^2 \boldsymbol{A}^{\mathrm{OT}}}{\partial z^2} = -\frac{(\boldsymbol{\nabla} \times \boldsymbol{F})^h}{\rho_0} \ . \tag{5.3}$$

The boundary conditions on $\boldsymbol{A}^{\mathrm{OT}}$ are that it is zero at the bottom and at the surface.

The right hand side of (5.3) contains the horizontal components of the curl of the applied force. As discussed in the previous chapter, this poses problems

from a numerical perspective due to both the large aspect ratio of the grid cells, and to potential ambiguities arising from the treatment of partial cells near the boundaries. Fortunately, due to the hydrostatic nature of the model, all forces asides from the purely vertical buoyancy force, are purely horizontal. This means that the horizontal components of the curl reduce to first order derivatives for each individual force, simplifying the calculation greatly.

Therefore, the discretised equation for the meridional overturning force function, using the notation introduced in Section 2.2.4, is:

$$\frac{1}{\overline{h^{\mathrm{S}}}^{k}\Delta r^{c}}\delta_{k}\left(\frac{\delta_{k}A^{\mathrm{OT}x}}{h^{\mathrm{S}}\Delta r^{f}}\right)=-\left(\frac{\delta_{j}F^{z}}{\rho_{0}\Delta y^{c}}+\frac{\delta_{k}F^{y}}{\rho_{0}\overline{h^{\mathrm{S}}}^{k}\Delta r^{c}}\right)\,. \tag{5.4}$$

Note that the vertical index k increases in the downwards direction, hence the sign change between (5.4) and (5.3).

Similarly, the discretised equation for the zonal overturning force function is given by:

$$\frac{1}{\overline{h^{\mathrm{W}}}^{k}\Delta r^{c}}\delta_{k}\left(\frac{\delta_{k}A^{\mathrm{OT}y}}{h^{\mathrm{W}}\Delta r^{f}}\right)=\frac{\delta_{i}F^{z}}{\rho_{0}\Delta x^{c}}+\frac{\delta_{k}F^{x}}{\rho_{0}\overline{h^{\mathrm{W}}}^{k}\Delta r^{c}}\,. \tag{5.5}$$

The discrete form of the Dirichlet boundary conditions on $\boldsymbol{A}^{\mathrm{OT}}$ is

$$\begin{aligned} A^{\mathrm{OT}x}_{ij0}&=A^{\mathrm{OT}y}_{ij0}=0\\ A^{\mathrm{OT}x}_{ijk}&=A^{\mathrm{OT}y}_{ijk}=0 \qquad \forall\ \ k\geq k_{\mathrm{bot}}\,, \end{aligned} \tag{5.6}$$

where k_{bot} is the vertical index of the ocean floor at a horizontal grid point. Equations (5.4) and (5.5) form a set of $(k_{\mathrm{bot}}-1)$ equations for $(k_{\mathrm{bot}}-1)$ unknowns at each horizontal grid point, which can be solved to find $A^{\mathrm{OT}x}$ and $A^{\mathrm{OT}y}$.

5.2.2 Solving for the Depth-Integrated Force Function

Finding the depth-integrated force function HA^{BT} involves inverting the linear elliptic equation (4.115), reproduced below:

$$-\boldsymbol{\nabla}\cdot\left(\frac{\boldsymbol{\nabla}\left(HA^{\mathrm{BT}}\right)}{H}\right)=\hat{\boldsymbol{e}}_{z}\cdot\left(\frac{\boldsymbol{\nabla}\times\overline{\boldsymbol{F}}}{\rho_{0}}+\frac{\boldsymbol{\nabla}\overline{zF^{z}}\times\boldsymbol{\nabla}H}{H\rho_{0}}\right)\,. \tag{5.7}$$

The domain, S, of the depth-integrated problem is not simply connected (i.e., there are one or more islands within the domain). To solve (5.7) in a domain which is not simply connected, the Dirichlet boundary condition on each boundary $C_i = \partial S$ must be found. Only one of these boundary conditions can be specified without loss of generality. For the purposes of this thesis, S has two bounding curves: the outer boundary C_{out}, and the boundary around Iceland C_{Ice}. The value on C_{out} can freely be set to zero, leaving the boundary condition on C_{Ice} to be determined. The method for doing this is described in Section 4.8, but involves finding the divergent component of the force, subtracting it from the total force to isolate the rotational component, and then integrating this from a point on C_{out} to one on C_{Ice} to find the unknown condition.

The equations integrated in the x and y directions to find the unknown boundary condition are given by equation (4.139), and rearranging for $\boldsymbol{\nabla} H A^{\text{BT}}$ yields:

$$\hat{\boldsymbol{e}}_z \times \boldsymbol{\nabla}_h \left(H A^{\text{BT}} \right) = - \int_{-H}^{0} \frac{\boldsymbol{F}^h}{\rho_0} \, \mathrm{d}z + H \boldsymbol{\nabla}_h \phi^{\text{BT}} \, . \tag{5.8}$$

To be able to solve this equation, ϕ^{BT} must first be determined from equation (4.140):

$$\boldsymbol{\nabla} \cdot \left(H \boldsymbol{\nabla}_h \phi^{\text{BT}} \right) = \boldsymbol{\nabla} \cdot \int_{-H}^{0} \frac{\boldsymbol{F}^h}{\rho_0} \, \mathrm{d}z \, . \tag{5.9}$$

Equation (5.9) discretises to:

$$\begin{aligned} \delta_i \left(\frac{H^{\text{W}} \Delta y^g \delta_i \phi^{\text{BT}}}{\Delta x^c} \right) + \delta_j \left(\frac{H^{\text{S}} \Delta x^g \delta_j \phi^{\text{BT}}}{\Delta y^c} \right) \\ = \frac{\delta_i \left(\sum_k F^x h^{\text{W}} \Delta r^f \Delta y^g \right)}{\rho_0} + \frac{\delta_j \left(\sum_k F^y h^{\text{S}} \Delta r^f \Delta x^g \right)}{\rho_0} \, . \end{aligned} \tag{5.10}$$

The kinematic boundary condition of no rotational force through the boundary gives the following discrete Neumann boundary conditions on (5.10):

$$\begin{aligned} \frac{H^{\text{W}} \delta_i \phi^{\text{BT}}}{\Delta x^c} - \frac{\sum_k F^x h^{\text{W}} \Delta r^f}{\rho_0} = 0 \qquad & \text{on meridional boundaries,} \\ \frac{H^{\text{S}} \delta_j \phi^{\text{BT}}}{\Delta y^c} - \frac{\sum_k F^y h^{\text{S}} \Delta r^f}{\rho_0} = 0 \qquad & \text{on zonal boundaries.} \end{aligned} \tag{5.11}$$

Together, (5.10) and (5.11) form a linear system of equations which can be solved for ϕ^{BT}.

With ϕ^{BT} now known, any unknown Dirichlet boundary conditions on HA^{BT} can be calculated from the discrete form of (5.8):

$$\begin{aligned}\frac{\delta_j\left(HA^{\mathrm{BT}}\right)}{\Delta y^c} &= -\frac{H^{\mathrm{W}}\delta_i\phi^{\mathrm{BT}}}{\Delta x^c} + \frac{\sum_k F^x h^{\mathrm{W}}\Delta r^f}{\rho_0}\,,\\ \frac{\delta_i\left(HA^{\mathrm{BT}}\right)}{\Delta x^c} &= \frac{H^{\mathrm{S}}\delta_j\phi^{\mathrm{BT}}}{\Delta y^c} - \frac{\sum_k F^y h^{\mathrm{S}}\Delta r^f}{\rho_0}\,.\end{aligned} \tag{5.12}$$

Now all boundary values have been found, the following system of equations comprising the discretised form of (5.7) can be solved to obtain HA^{BT}:

$$\begin{aligned}&-\delta_i\left(\frac{\Delta y^c\delta_i\left(HA^{\mathrm{BT}}\right)}{H^{\mathrm{S}}\Delta x^g}\right) - \delta_j\left(\frac{\Delta x^c\delta_j\left(HA^{\mathrm{BT}}\right)}{H^{\mathrm{W}}\Delta y^g}\right)\\ &\quad= \frac{1}{\mathcal{A}^\zeta\rho_0}\left[\delta_j\left(\Delta x^c\left(\frac{\sum_k(F^x h^{\mathrm{W}}\Delta r^f)}{H^{\mathrm{W}}} - H^{\mathrm{W}}\delta_i\frac{\sum_k(z^f F^z\overline{h^c}^k\Delta r^c)}{H^{c\,2}}\right)\right)\right.\\ &\qquad\left.-\delta_i\left(\Delta y^c\left(\frac{\sum_k(F^y h^{\mathrm{S}}\Delta r^f)}{H^{\mathrm{S}}} - H^{\mathrm{S}}\delta_j\frac{\sum_k(z^f F^z\overline{h^c}^k\Delta r^c)}{H^{c\,2}}\right)\right)\right]\,.\end{aligned} \tag{5.13}$$

The method of determining unknown boundary conditions outlined above also suggests an alternative method of obtaining HA^{BT}. As the divergent component of the depth-integrated force has to be subtracted off before integrating to find the value on the boundary, the residual force is necessarily non-divergent, and so it should be possible to find the value of the force function at all points by integrating one of (5.12). Reassuringly, the force functions obtained by the direct solution of (5.13) and those obtained by this residual method are effectively identical (differences between the two force functions have a magnitude $\mathcal{O}(10^{-12})$ smaller than that of the force functions themselves, approaching machine precision). This is illustrated in Figure 5.1, which compares the two methods for obtaining the depth-integrated force function for the Coriolis force in the control configuration.

Although (5.13) holds for all forces, in practice, using it to calculate the depth-integrated force function for the buoyancy force can lead to numerical

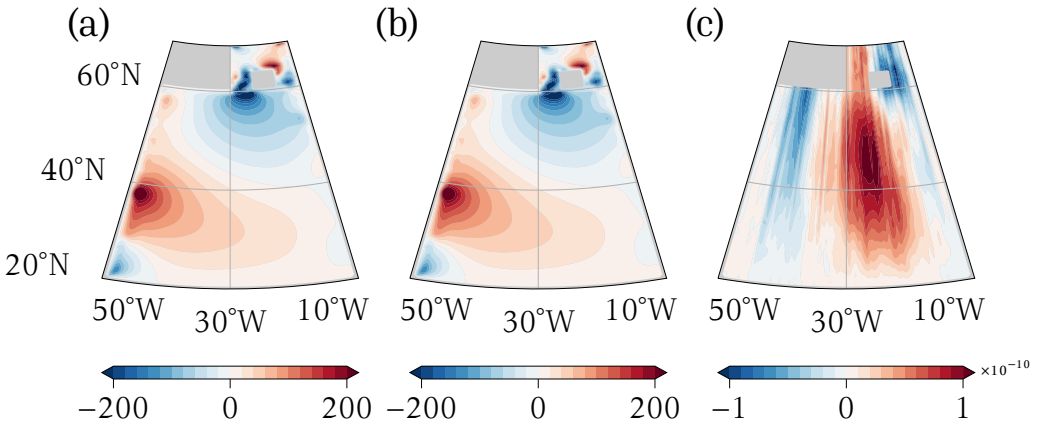


FIGURE 5.1: The two equivalent ways of calculating the depth-integrated force function, shown for the Coriolis force in the control configuration. (a) direct method, derived in Chapter 4 (b) residual method: divergent component subtracted off, then integrated from the southern boundary northwards. (c) difference between the two. Note the different scales on the colorbars. Depth-integrated force functions are given in $m^3\ s^{-2}$.

errors. These errors arise from difficulties in calculating vertical derivatives at the ocean floor near the boundary slope. This problem can be circumvented by instead calculating HA^{BT} for the buoyancy force indirectly from the horizontal pressure gradient force, exploiting hydrostatic balance as shown in Section 4.7.2. The issues in using the vertical buoyancy force are illustrated in Figure 5.2, where it can be seen that errors near the boundary are diffused into the ocean interior. As such, in the remainder of this thesis, the force functions for the buoyancy force are calculated using the horizontal pressure gradient force, rather than the buoyancy force itself.

With the numerical method outlined above, it is now possible to generate force functions for the forcing terms driving the evolution of the flow in the model. The forcing is split into five terms: the Coriolis force, the buoyancy force, external wind-stress forcing, inertia, and dissipation. If this is a valid decomposition of the net force acting on the flow, then we would expect the rotational momentum balance obtained by summing the individual force functions for each force to match the force function obtained from the net force inferred from the model velocity tendencies. The force functions obtained in the control case are shown, along with their sum and the net force function, in

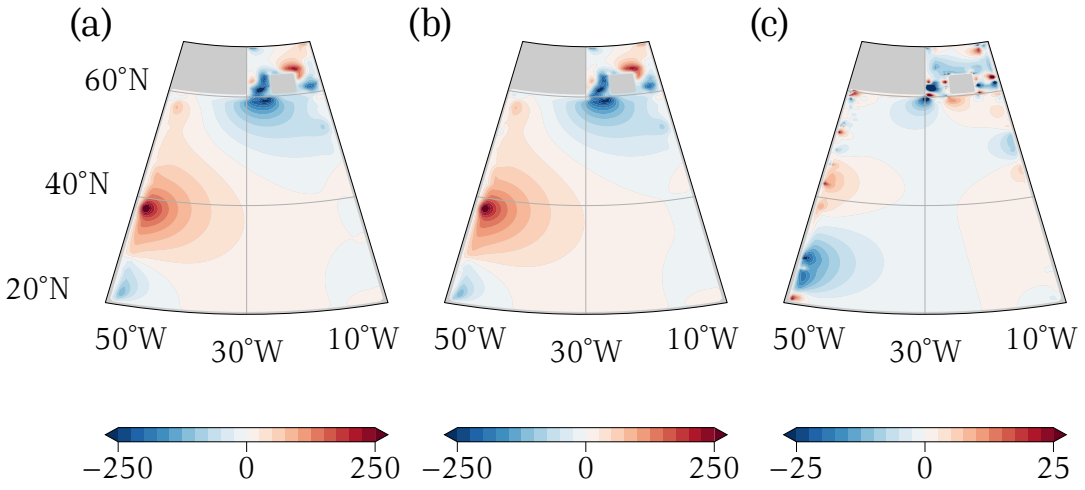


FIGURE 5.2: Illustration of the difficulty in directly calculating the depth-integrated force function directly from the buoyancy force. **(a)** shows HA^{BT} calculated indirectly from the horizontal pressure gradient force. **(b)** shows HA^{BT} calculated directly from the (vertical) buoyancy force. **(c)** shows the difference between the two force functions. Depth-integrated force functions are given in $\mathrm{m}^3\,\mathrm{s}^{-2}$.

Figure 5.3. The sum of the individual force functions does match very closely the inferred net force function, confirming the closure of the momentum balance.

5.2.3 Further Decomposition of the Barotropic Rotational Momentum Equation

Before moving on, it will prove helpful to first explore further decomposing the barotropic force function to attempt to isolate the effects of topography on the force function.

Considering only horizontal forces—the term in F^z can safely be discarded now buoyancy is calculated via the horizontal pressure gradient—and expanding the curl term on the right-hand side, (5.7) can be rewritten as:

$$-\boldsymbol{\nabla}\cdot\left(\frac{\boldsymbol{\nabla}\left(HA^{\mathrm{BT}}\right)}{H}\right)=\hat{\boldsymbol{e}}_z\cdot\left(\frac{\boldsymbol{\nabla}\times H\overline{\boldsymbol{F}}}{H\rho_0}+\frac{\overline{\boldsymbol{F}}\times\boldsymbol{\nabla}H}{H\rho_0}\right). \tag{5.14}$$

This equation is a steady-state, forced, diffusion equation with a "diffusion coefficient" of $1/H$. This "diffusion coefficient" is obviously independent of HA^{BT}, and so the equation is linear. As a consequence of this, the solution

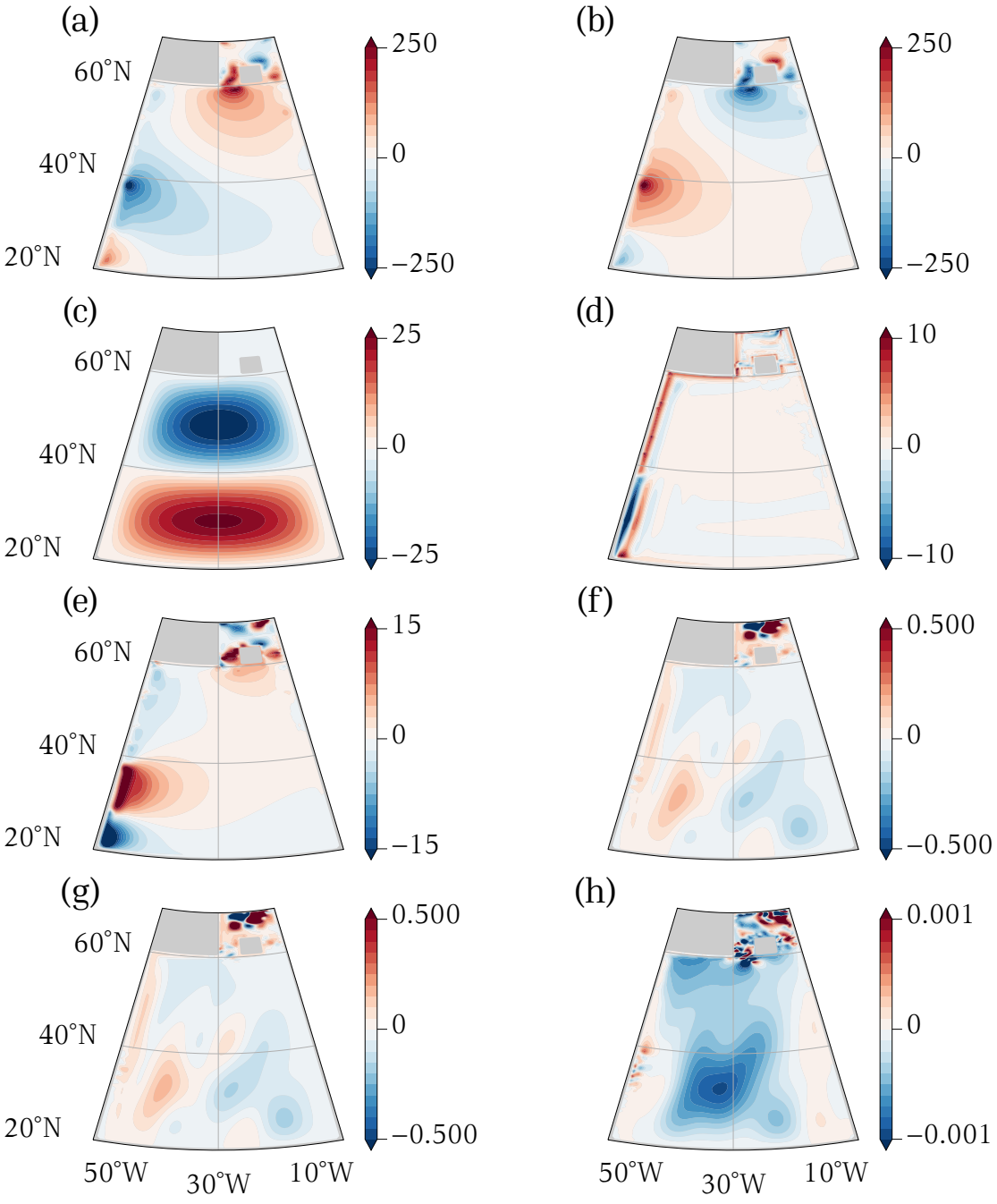


FIGURE 5.3: The depth-integrated force functions in the control state due to **(a)** the Coriolis force, **(b)** the buoyancy force, **(c)** the wind-stress, **(d)** viscous forces, **(e)** inertial forces, **(f)** the sum of force functions *(a)–(e)*, **(g)** net force function deduced from model momentum tendencies, **(h)** the difference between *(f)* and *(g)*. All depth-integrated force functions are given in $m^3\,s^{-2}$.

HA^{BT} can be written as a linear sum of auxiliary force functions:

$$HA^{\mathrm{BT}} = HA_1^{\mathrm{BT}} + HA_2^{\mathrm{BT}} + HA_3^{\mathrm{BT}} \,. \tag{5.15}$$

These auxiliary force functions are the solutions to the three sub-problems:

$$-H\boldsymbol{\nabla}\cdot\left(\frac{\boldsymbol{\nabla}\left(HA_1^{\mathrm{BT}}\right)}{H}\right) = \hat{\boldsymbol{e}}_z\cdot\frac{\boldsymbol{\nabla}\times H\overline{\boldsymbol{F}}}{\rho_0}\,, \tag{5.16}$$

$$-H\boldsymbol{\nabla}\cdot\left(\frac{\boldsymbol{\nabla}\left(HA_2^{\mathrm{BT}}\right)}{H}\right) = \hat{\boldsymbol{e}}_z\cdot\frac{\overline{\boldsymbol{F}}\times\boldsymbol{\nabla}H}{\rho_0}\,, \tag{5.17}$$

$$-H\boldsymbol{\nabla}\cdot\left(\frac{\boldsymbol{\nabla}\left(HA_3^{\mathrm{BT}}\right)}{H}\right) = 0\,, \tag{5.18}$$

subject to boundary conditions:

$$HA_1^{\mathrm{BT}} = 0 \qquad \text{on } C_{\mathrm{out}} \text{ and } C_{\mathrm{Ice}}\,; \tag{5.19}$$

$$HA_2^{\mathrm{BT}} = 0 \qquad \text{on } C_{\mathrm{out}} \text{ and } C_{\mathrm{Ice}}\,; \tag{5.20}$$

$$HA_3^{\mathrm{BT}} = \begin{cases} 0 & \text{on } C_{\mathrm{out}}\,, \\ HA^{\mathrm{BT}} & \text{on } C_{\mathrm{Ice}}\,. \end{cases} \tag{5.21}$$

In this way, the force function is split into three components: one arising from the curl of the depth-integrated force, one due to the projection of the depth-averaged force along isobaths, and one from the boundary condition on the Icelandic boundary. The first of these is present even when there is no variation in topography, and if H is taken to be constant, it simplifies to the equation derived by Marshall and Pillar (2011). The second component, on the other hand, is only non-zero in the presence of a topographic gradient and is perhaps best regarded as a correction to the force function to account for the presence of topography.

The precise interpretation of these components, however, is not trivial. The right-hand side of (5.16) is the torque of the full depth-integrated force, which is just the depth-integrated torque, less the bottom torque:

$$\hat{\boldsymbol{e}}_z\cdot\boldsymbol{\nabla}\times\int_{-H}^{0}\frac{\boldsymbol{F}}{\rho_0}\,\mathrm{d}z = \hat{\boldsymbol{e}}_z\cdot\left[\int_{-H}^{0}\frac{\boldsymbol{\nabla}\times\boldsymbol{F}}{\rho_0}\,\mathrm{d}z - \frac{\boldsymbol{F}_{\mathrm{bot}}\times\boldsymbol{\nabla}H}{\rho_0}\right]. \tag{5.22}$$

The right-hand side of (5.17), on the other hand, is the projection of the depth-averaged force along isobaths—in other words the torque arising from the depth-averaged force. It can also be thought of as the sum of the bottom torque and an additional term accounting for baroclinicity of the force:

$$\hat{\boldsymbol{e}}_z \cdot \int_{-H}^{0} \frac{\boldsymbol{F} \times \boldsymbol{\nabla} H}{H \rho_0} \, \mathrm{d}z = \hat{\boldsymbol{e}}_z \cdot \left[\frac{\boldsymbol{F}_{\mathrm{bot}} \times \boldsymbol{\nabla} H}{\rho_0} - \int_{-H}^{0} \frac{z}{H \rho_0} \frac{\partial \boldsymbol{F}}{\partial z} \times \boldsymbol{\nabla} H \, \mathrm{d}z \right] . \tag{5.23}$$

The additional term on the right-hand side of (5.23) is therefore the difference between the torque calculated from the force at the ocean floor, and that calculated from the depth-averaged force. This term therefore bears an extremely strong resemblance to the interpretation of JEBAR by Mertz and Wright (1992)—as well as Cane et al. (1998)—as a correction to the vortex stretching term in the barotropic potential vorticity equation arising from its calculation from the depth-averaged velocity in place of the bottom velocity. In fact, substituting the horizontal pressure gradient force into the integral in (5.23) and then using hydrostatic balance to substitute in for $\partial p / \partial z$ yields, as expected, the exact expression for JEBAR.

The decomposition into auxiliary force functions therefore splits the depth-integrated force function into a component arising from the barotropic torque, and one due to the effects of non-uniform topography and baroclinicity. This is illustrated for the Coriolis force in the control configuration in Figure 5.4, which also further demonstrates the linearity of equation (5.7). The difference between the sum of the three components and the total force function is of order $\sim \mathcal{O}(10^{-15})$ (close to machine precision) the magnitude of the force functions themselves, and is therefore entirely negligible.

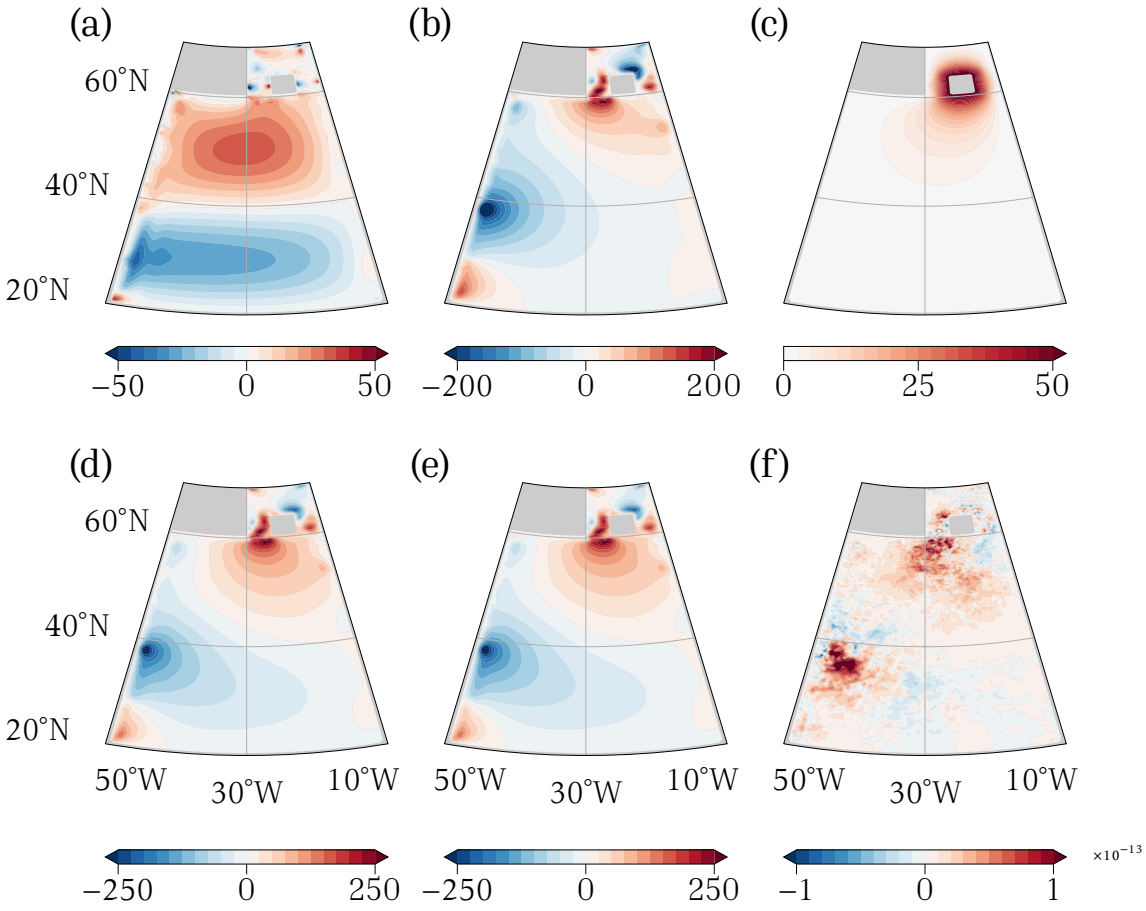


FIGURE 5.4: The decomposition of the depth-integrated force function for the Coriolis force in the control configuration into contributions from: (a) the curl of the depth-integrated force, (b) the projection of the depth-averaged force along isobaths, (c) a component arising from the boundary condition along the Iceland boundary. (d) The sum of the above components. (e) The full depth-integrated force function. (f) The difference between *(d)* and *(e)*. Depth-integrated force functions are given in $m^3\,s^{-2}$.

5.3 Rotational Momentum Balance of the Barotropic Circulation

Having established the numerics underlying the computation of the depth-integrated force functions, they can now be calculated for the configurations presented in Chapter 3. Recalling the result from Section 4.9.2 that the depth-integrated force function is simply the rate of change of the depth-integrated transport streamfunction (equation 4.152), comparison of the depth-integrated force functions for each force immediately reveals the rotational momentum balance of the barotropic gyre circulation.

It is perhaps most logical to begin with the simplest configuration—the vertical sidewalls case—instead of the control, in which topography, wind-stress and surface buoyancy forcing, are all present. The depth-integrated force functions in this case are shown in Figure 5.5 and hold few surprises. The primary rotational force balance supporting the horizontal gyre circulation in the basin interior is between the Coriolis force and the external wind stress. This is simply the manifestation of Sverdrup balance in the rotational momentum equation and results in the familiar double-gyre shape of the interior circulation in Figure 3.4(c), as the input of vorticity from the wind-stress curl is balanced by the meridional advection of planetary vorticity in the basin interior.

The effect of the buoyancy force on the barotropic circulation is restricted to small regions in close proximity to the sill, which is the only non-vertical topography present in this configuration. In a hint of the results to come when topography is included, the magnitude of the rotational force exerted on the flow in these regions by the buoyancy force is larger than that exerted by the wind stress anywhere in the ocean interior. The two strong, linked, cells are the result of the barotropic flow moving up the centre of the sill leading to vortex compression—or equivalently, a bottom pressure torque—balanced by the rotational Coriolis force.

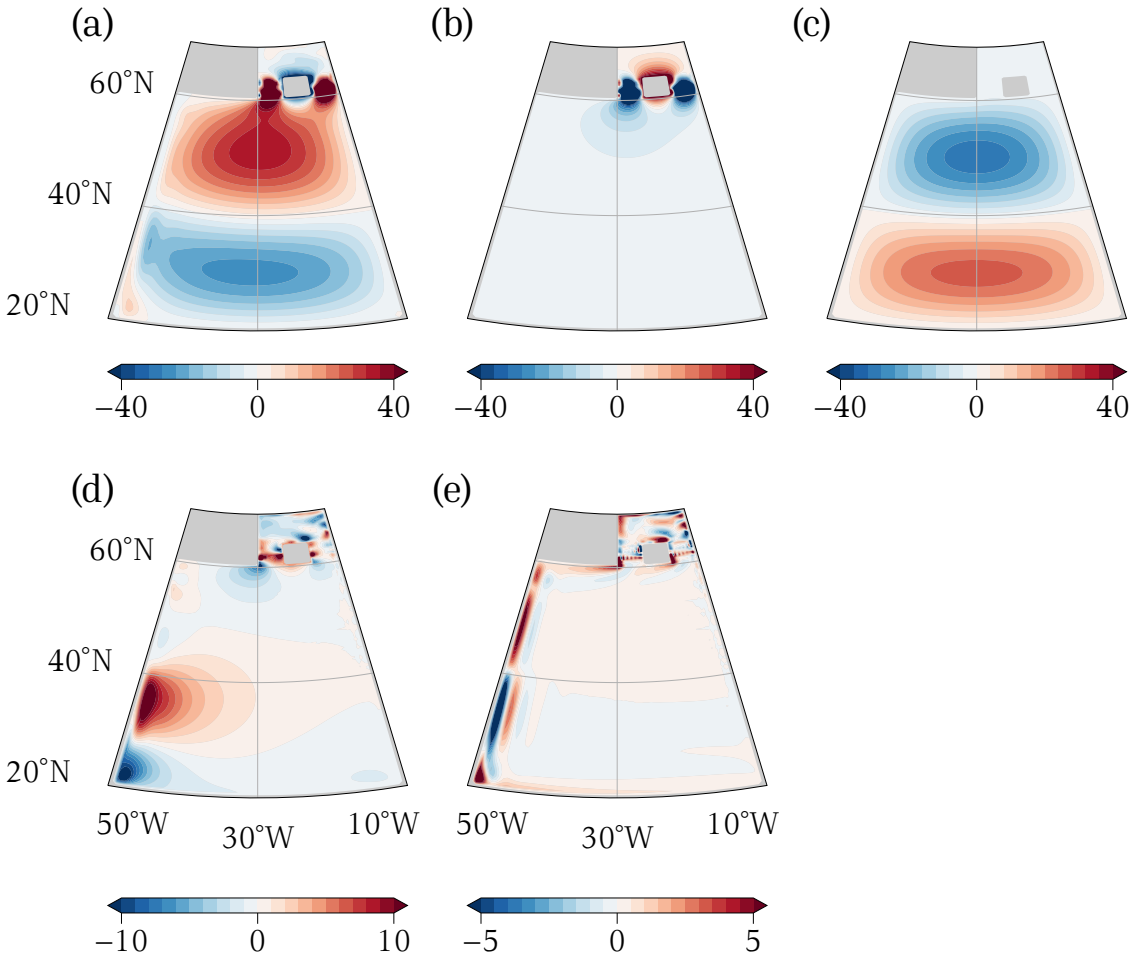


FIGURE 5.5: The depth-integrated force functions for the vertical sidewall configuration due to: (a) the Coriolis force, (b) the buoyancy force, (c) the wind-stress, (d) inertial forces, (e) viscous forces. Depth-integrated force functions are given in $m^3\,s^{-2}$—cf. the barotropic streamfunction shown in Figure 3.4(c).

Inertia and viscous dissipation have weaker effects. The rotational viscous force is limited to a narrow band of longitudes near the western sidewall, where it provides the sink of vorticity required by the classical theories of Stommel (1948) and Munk (1950) to permit meridional flow in the western boundary current and balance the net input of vorticity from the wind-stress. It is aligned along streamlines and is strongest by far in the western boundary current where velocities are highest, and therefore acts to decelerate the circulation. Inertia acts to oppose the Coriolis force within the subtropical gyre western boundary current, as would be expected for what is a reasonably inertial boundary current. Inertia supports the small recirculation subgyre

in the subtropics, as the dipole feature acts to confine the recirculating cell towards the west and also accelerates it northwards. It is therefore "trying" to form the subtropical recirculation gyre in the northwest corner of Cessi et al. (1987) and Ierley and Young (1988).

Now consider the case with sloping sidewalls, but no buoyancy forcing other than a relaxation to the initial temperature profile in the subtropical sponge to maintain a stratification, i.e., the no-buoyancy forcing configuration. The depth-integrated force functions in this case are given in Figure 5.6. The wind forcing in the ocean interior is still balanced by the rotational Coriolis force; however, the dominant force balance is now between the Coriolis and buoyancy forces.

The reason the rotational buoyancy force has such a large effect on the flow even in the absence of external buoyancy forcing is that it is dominated here by the contribution of the bottom pressure torque. As the barotropic circulation is strikingly similar to the double wind-driven gyre of Munk (1950), there is a large barotropic flow perpendicular to the sidewall slope around the latitude of zero wind-stress curl at 40°N. This results in a large vortex stretching term which must then be balanced by the Coriolis force. Notably, this vortex stretching would still occur in a homogeneous ocean, and so the rotational balance between the Coriolis and buoyancy forces would still be the dominant balance even with no stratification. This is because the contribution to the rotational momentum balance of the bottom pressure torque is contained within the buoyancy force term, and hence this term also includes topographic effects.

The rotational viscous force in the no-buoyancy configuration has a similar form to that in the vertical sidewalls configuration (Figure 5.5(e)), in that again it opposes the barotropic circulation and is strongest in the western boundary current, where flow speeds are highest. It is, however, smaller in magnitude, due to the weaker barotropic flow near the western boundary than in the vertical sidewalls case, as can be seen from Figure 3.4(b). The rotational force due to inertia is also smaller than in the vertical sidewalls case, and has a different form. In the no-buoyancy forcing case, while inertia still opposes the

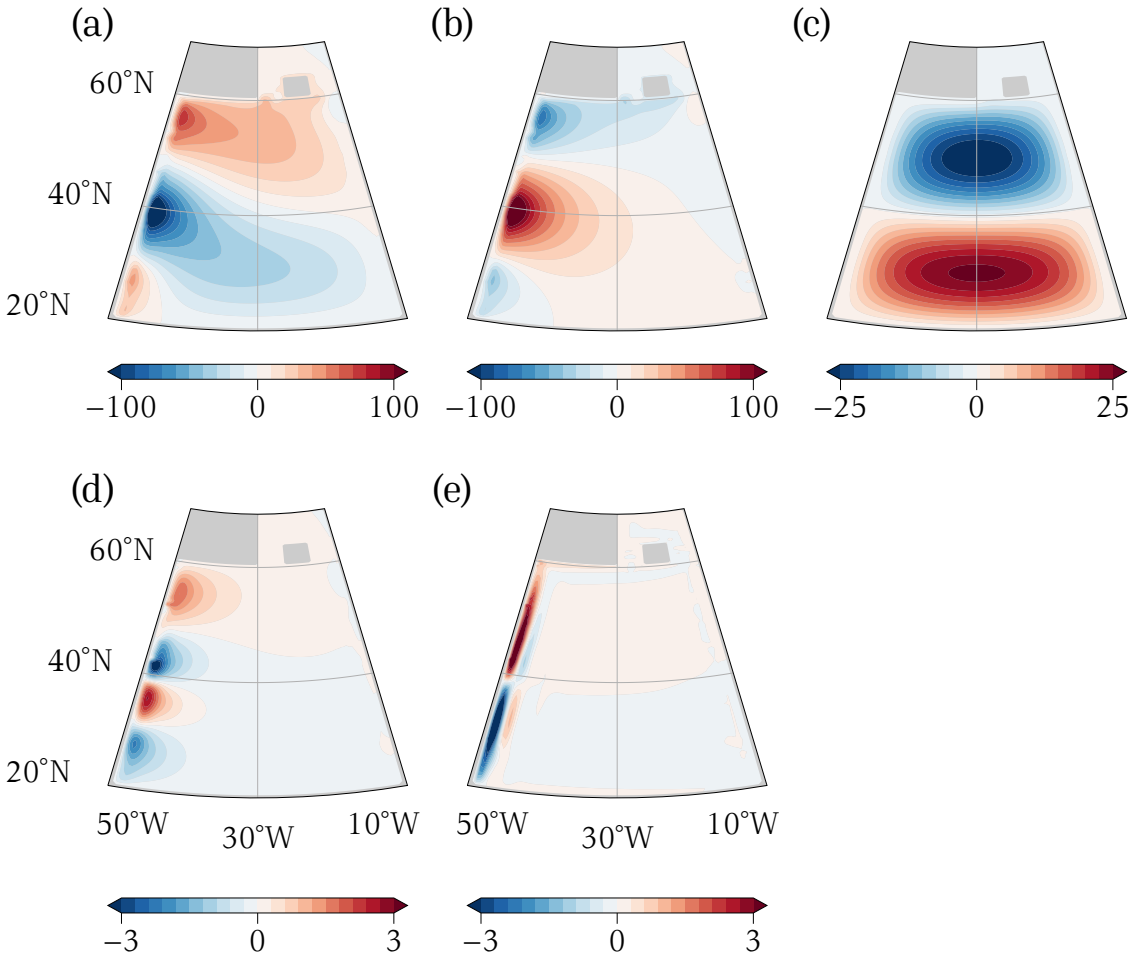


FIGURE 5.6: The depth-integrated force functions for the no-buoyancy-forcing configuration due to: **(a)** the Coriolis force, **(b)** the buoyancy force, **(c)** the wind-stress, **(d)** inertial forces, **(e)** viscous forces, Depth-integrated force functions are given in $m^3\,s^{-2}$—cf. the barotropic streamfunction shown in Figure 3.4(b).

rotational Coriolis force in the subtropical gyre, in the subpolar gyre they act in the same direction. This is because the boundary current in the subpolar gyre flows southwards (see Figure 3.4(b)), and hence the advection of vorticity in the subpolar gyre is the opposite of that in the subtropical gyre.

In the case with sloping sidewalls and external buoyancy forcing, but no wind-stress forcing, the force balance looks quite different, as illustrated in Figure 5.7. First, there is obviously no rotational wind-stress force. More interestingly, while the dominant rotational force balance is still between the Coriolis and buoyancy forces, the magnitude of the rotational buoyancy force is now significantly lower than in the no-buoyancy forcing case.

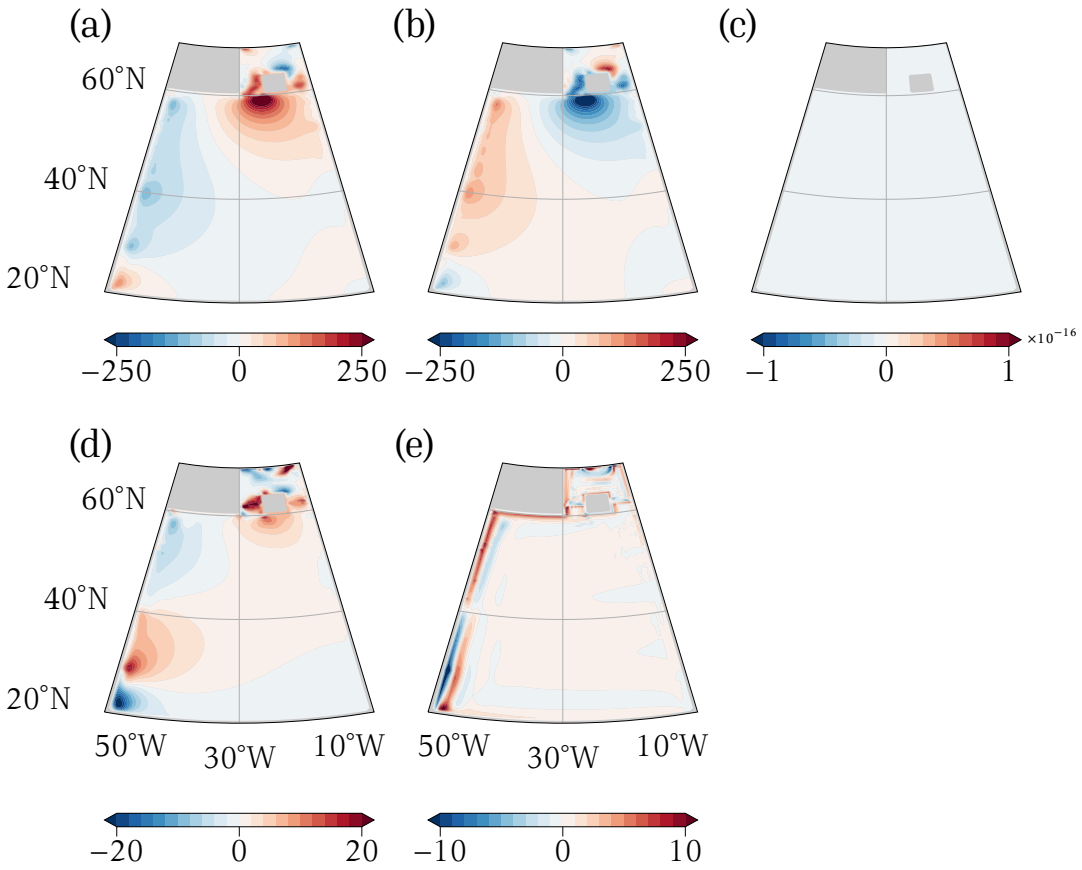


FIGURE 5.7: The depth-integrated force functions for the no-wind-stress configuration due to: (a) the Coriolis force, (b) the buoyancy force, (c) the wind-stress, (d) inertial forces, (e) viscous forces, Depth-integrated force functions are given in $m^3\ s^{-2}$—cf. the barotropic streamfunction shown in Figure 3.4(d).

The underlying explanation, however, is similar: in this case (with no wind-stress forcing), the barotropic circulation—while intense—is confined over the boundary slope (Figure 3.4(d)). Whereas in the wind-driven case, the barotropic circulation flows roughly perpendicular to the isobaths, leading to large vortex stretching terms, in the buoyancy-driven case the barotropic flow moves roughly along isobaths, only slowly descending down-slope as it progresses northwards. As such, the topographic stretching of vortices occurs more slowly, and to a lesser degree, so the rotational force exerted on the fluid is lower.

The explanation for the structure of the rotational viscous and inertial forces is as in previous experiments, although the viscous force function illustrates that in the no-wind forcing case, unlike in either previous case,

there is a significant barotropic flow that penetrates into the Nordic basin. In the previous two cases, the barotropic flow is either largely blocked by the sill (the vertical sidewalls case) or is not driven into the channels at all (the no-buoyancy forcing case). This also explains the larger peak in the buoyancy force function around the sill relative to that in the vertical sidewalls case, as a weaker barotropic flow over the sill necessarily leads to a smaller torque acting on the flow.

Finally considering the control case, which combines wind-stress forcing, surface buoyancy forcing, and topography, the resulting depth-integrated force functions are given in Figure 5.8. The presence of wind-stress forcing again leads to the re-emergence of the strong peak in the buoyancy force function on the western boundary situated at 40°N, which was absent in the no-wind configuration. Similarly, the presence of surface buoyancy forcing gives a barotropic circulation which now penetrates into the Nordic basin, resulting in the other peak in magnitude of the buoyancy force function at the mouth of the channel to the west of Iceland, whereas this feature was absent from the no-buoyancy-forcing case.

These plots demonstrate that the introduction of topography radically changes the nature of the rotational momentum balance of the barotropic circulation. Non-uniform topography allows the buoyancy force to project onto the horizontal gyre circulation. The effects of both surface wind-stress and buoyancy forcing on the force balance are altered in different ways. The driving of the barotropic circulation off the sloping western sidewall leads to a strong torque, which must be balanced by the Coriolis force. Similarly, as surface buoyancy forcing mediates a flow up the sill in the Nordic basin, another large torque term arises there which must also be balanced by the Coriolis force.

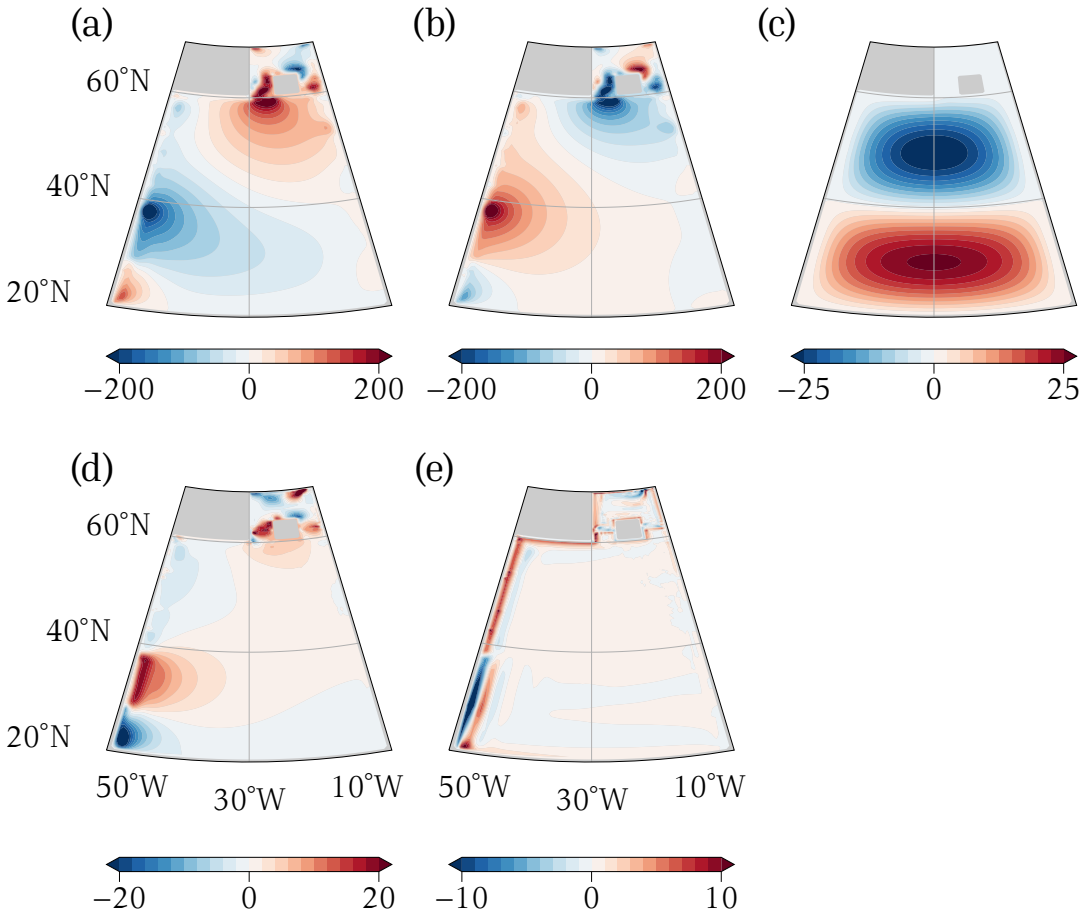


FIGURE 5.8: The depth-integrated force functions for the control state due to: (a) the Coriolis force, (b) the buoyancy force, (c) the wind-stress, (d) inertial forces, (e) viscous forces, Depth-integrated force functions are given in $m^3\ s^{-2}$—cf. the barotropic streamfunction shown in Figure 3.4(a).

5.4 Rotational Momentum Balance of the Overturning Circulation

5.4.1 The Overturning Force Function

Whereas the depth-integrated force function is a two-dimensional field, the meridional overturning force function $\boldsymbol{A}^{\mathrm{OT}x}$ is three-dimensional, and so cannot be as simply illustrated. Figures 5.9, 5.10, 5.11, and, 5.12 therefore show only three meridional sections at different longitudes of the meridional overturning force functions for the control, no-wind-forcing, no-buoyancy-forcing, and vertical sidewalls configurations respectively. The first section (at 47°W) is

just off the western boundary slope, the final section (at 27°W) bisects the channel to the west of Iceland, and the middle section (at 37°W) lies in the ocean interior, halfway between the other two. The interpretation of these sections is that they are the contribution of the meridional component of the torque at the given longitude to the overall baroclinic component of the overturning circulation (i.e., not the external mode).

The main feature which is consistent across all four model configurations is that the primary rotational force balance in the overturning is between the buoyancy force and the Coriolis force. This is exactly the expected result, and is simply the manifestation of thermal wind balance, i.e., the baroclinic production of vorticity is balanced by the tilting of planetary vortex tubes. It is therefore expected that the sign and magnitude of the buoyancy force function should vary with those of the zonal density gradient at a given point. As noted, the buoyancy force term also includes topographic effects, and so we would also expect to see an intensified signal in this term where there is a zonal barotropic flow over zonally-varying topography, due to the resulting stretching of vortex tubes. This is precisely what is seen from the figures.

Considering the control case, Figures 5.9(d–f), near the western boundary the broad, baroclinic, North Atlantic Current analogue has yet to fully separate and so crosses the 47°W section south of 40°N. Where this current crosses the section is where the largest density gradients and, hence, the largest contribution to the overturning from that longitude, are located. This manifests as a round peak in the overturning force function at the latitude at which the current crosses the relevant section, and at a depth of roughly 500 m. As the current crosses the basin, it moves northwards and becomes broader, leading to diminished density gradients and causing this peak to also shift northwards and weaken.

A similar effect is seen in Figures 5.10(d–f), but in this case, the western boundary current only separates from the boundary very close to the northern boundary. This results in the westernmost section not having such a clearly

defined maximum, and in the torque due to the buoyancy force being restricted largely to higher latitudes.

The opposite is true for the no-buoyancy-forcing case in Figures 5.11(d–f): not only is the magnitude of the torque from the buoyancy force weaker, but the latitude of the peak in the force function is unchanging, as there is no northwards flowing North Atlantic Current analogue in this case. The vertical sidewalls case appears similar, in that the latitude of the central peak in the force function remains somewhat stationary. With vertical sidewalls, however, this behaviour is due to the fact that the northwards-flowing warm current in the subpolar region does not separate from the boundary, rather than arising from the lack of such a current.

In all cases, the meridional torque due to the buoyancy force is balanced almost exactly by that due to the Coriolis force (shown by panels (a–c) in Figures 5.9, 5.10, 5.11, and 5.12). For inertia (panels (g–i)) and viscosity (panels (j–l)), the torques near the western boundary—where meridional flow speeds are significantly larger than in the interior—are orders of magnitude larger than they are in the basin interiors in all cases. Further, in each case—with the obvious exception of the no-wind-stress configuration—there is a clockwise viscous torque concentrated near the surface (the top ~ 50 m) highlighting the presence of an Ekman cell. The magnitude of this torque does not diminish away from the western boundary because the underlying zonal wind-stress is constant with longitude.

As pointed out by Marshall and Pillar (2011), on the western boundary itself, the picture painted by Figures 5.9, 5.10, 5.11, and 5.12 (i.e., of a meridional rotational force balance dominated by thermal wind balance) must break down. This is because the kinematic boundary condition precludes any zonal flow on the western boundary, and hence the Coriolis force cannot counteract the rotational buoyancy force. This breakdown of thermal wind balance is not observed in the force functions generated in any of these experiments. The reason for this is that the model used in this thesis is discretised on a C

grid, and the meridional overturning force function is located (horizontally) at the v-point, so is not calculated actually *on* the western boundary. Marshall and Pillar (2011) use a C-D grid (Adcroft et al. 1999) to obtain their results for precisely this reason.

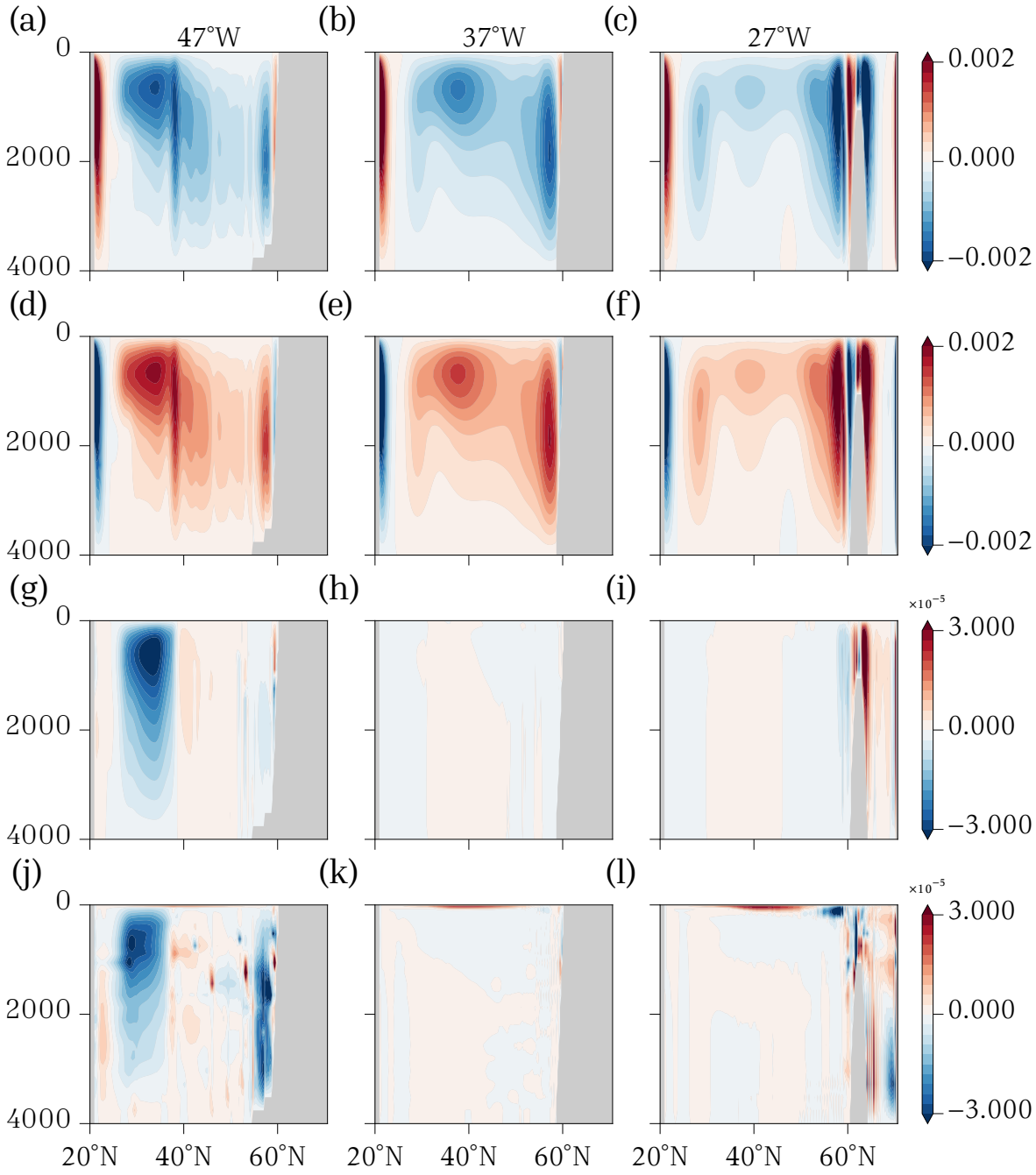


FIGURE 5.9: Meridional sections of the meridional overturning force function for the control experiment. The longitude of the section is constant for each column and is indicated atop the uppermost panels. Each row depicts a different force: panels (a)–(c) show the force function due to the Coriolis force, (d)–(f) that due to the buoyancy force, (g)–(i) that due to inertial forces, and (j)–(l) that due to viscous forces. The zonal overturning force functions are given in $m^2\ s^{-2}$. Note that the scales differ between panels (a)–(f) and panels (g)–(l).

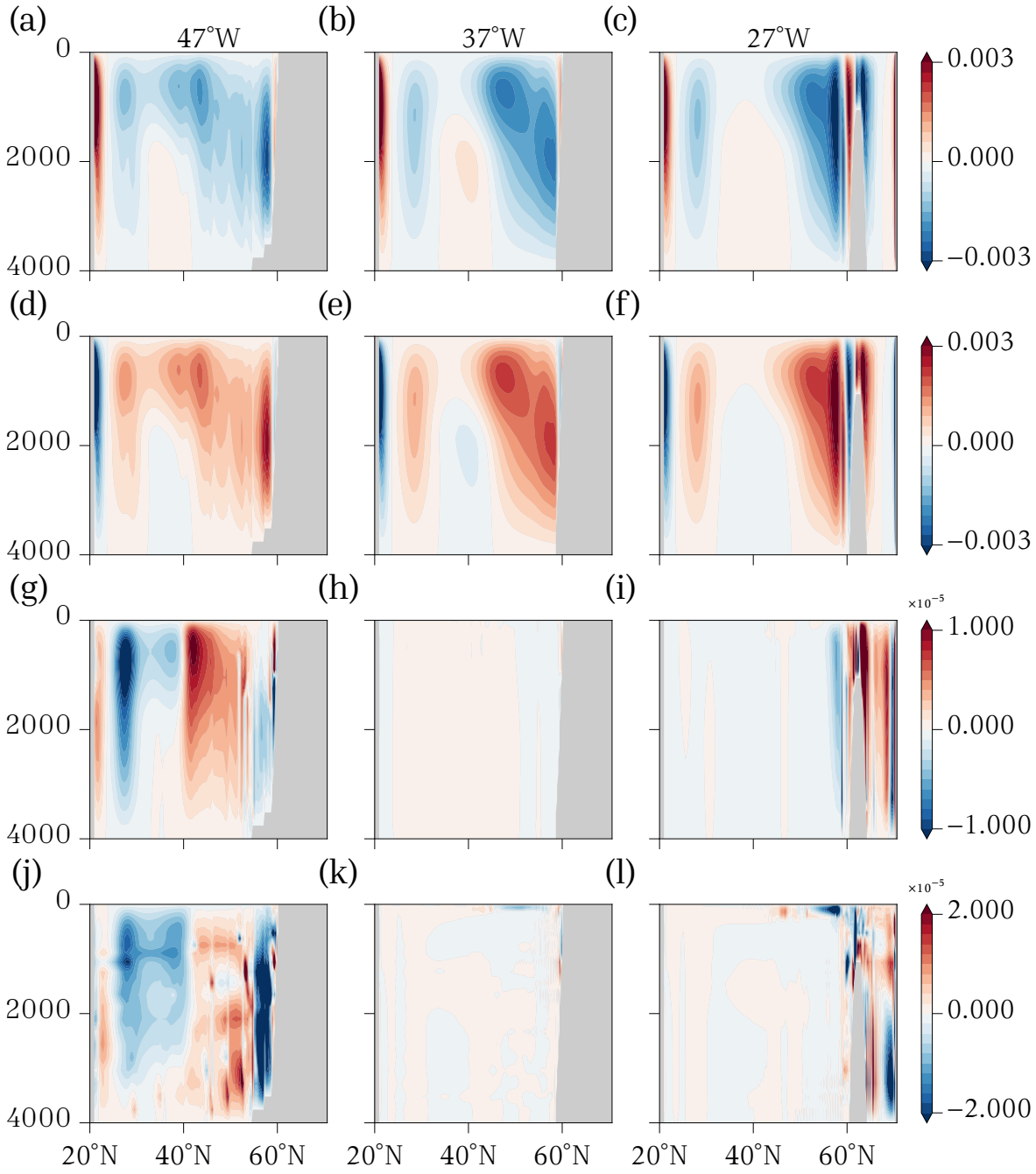


FIGURE 5.10: Meridional sections of the meridional overturning force function for the no-wind-stress configuration for: (a)–(c) the Coriolis force, (d)–(f) the buoyancy force, (g)–(i) inertial forces, (j)–(l) viscous forces. The zonal overturning force functions are given in $m^2\ s^{-2}$. Note that the scales differ between panels (a)–(f) and panels (g)–(l).

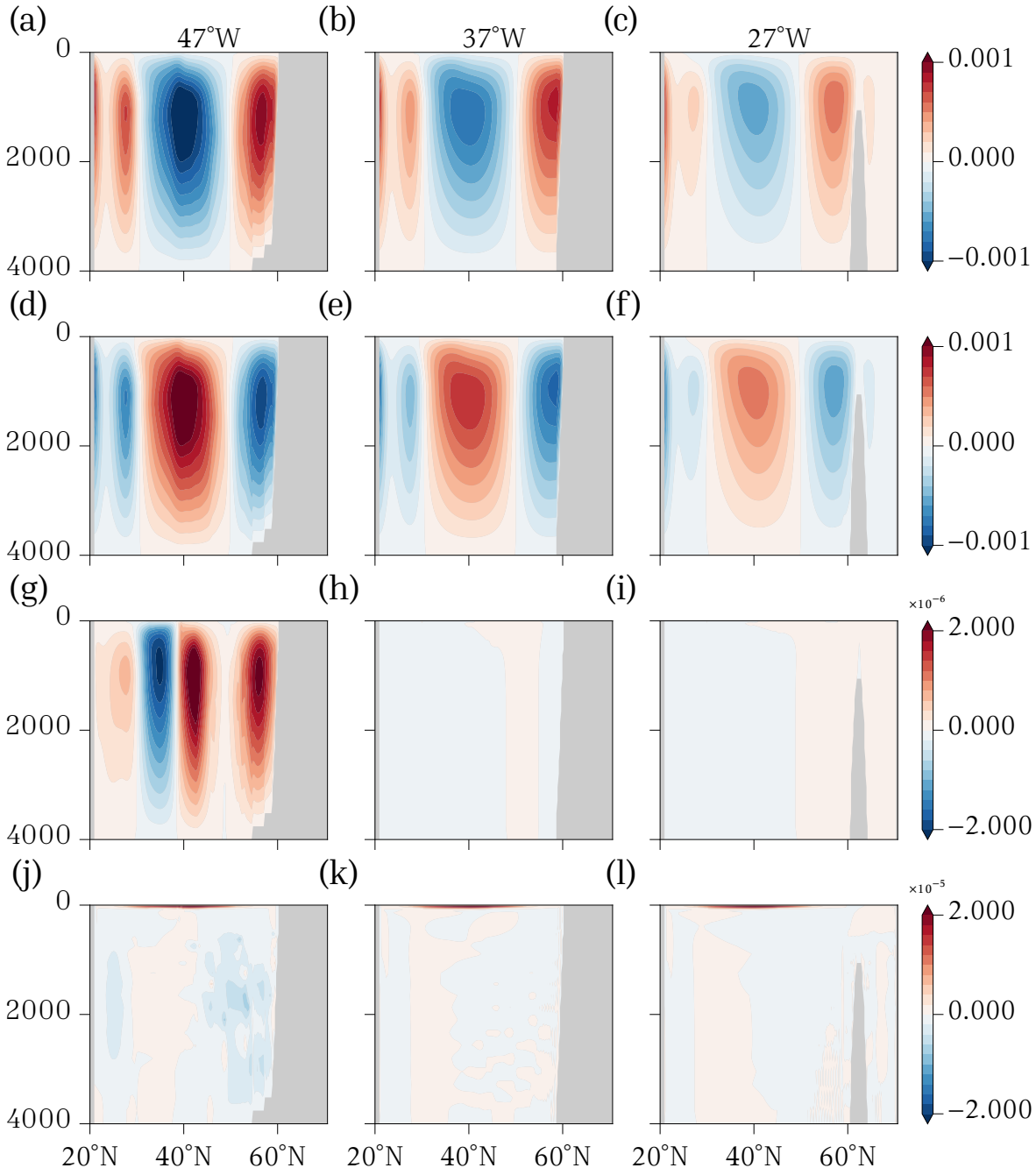


FIGURE 5.11: Meridional sections of the meridional overturning force function for the no-buoyancy-forcing configuration for: (a)–(c) the Coriolis force, (d)–(f) the buoyancy force, (g)–(i) inertial forces, (j)–(l) viscous forces. The zonal overturning force functions are given in $m^2\ s^{-2}$. Note that the scales differ between panels (a)–(f) and panels (g)–(l).

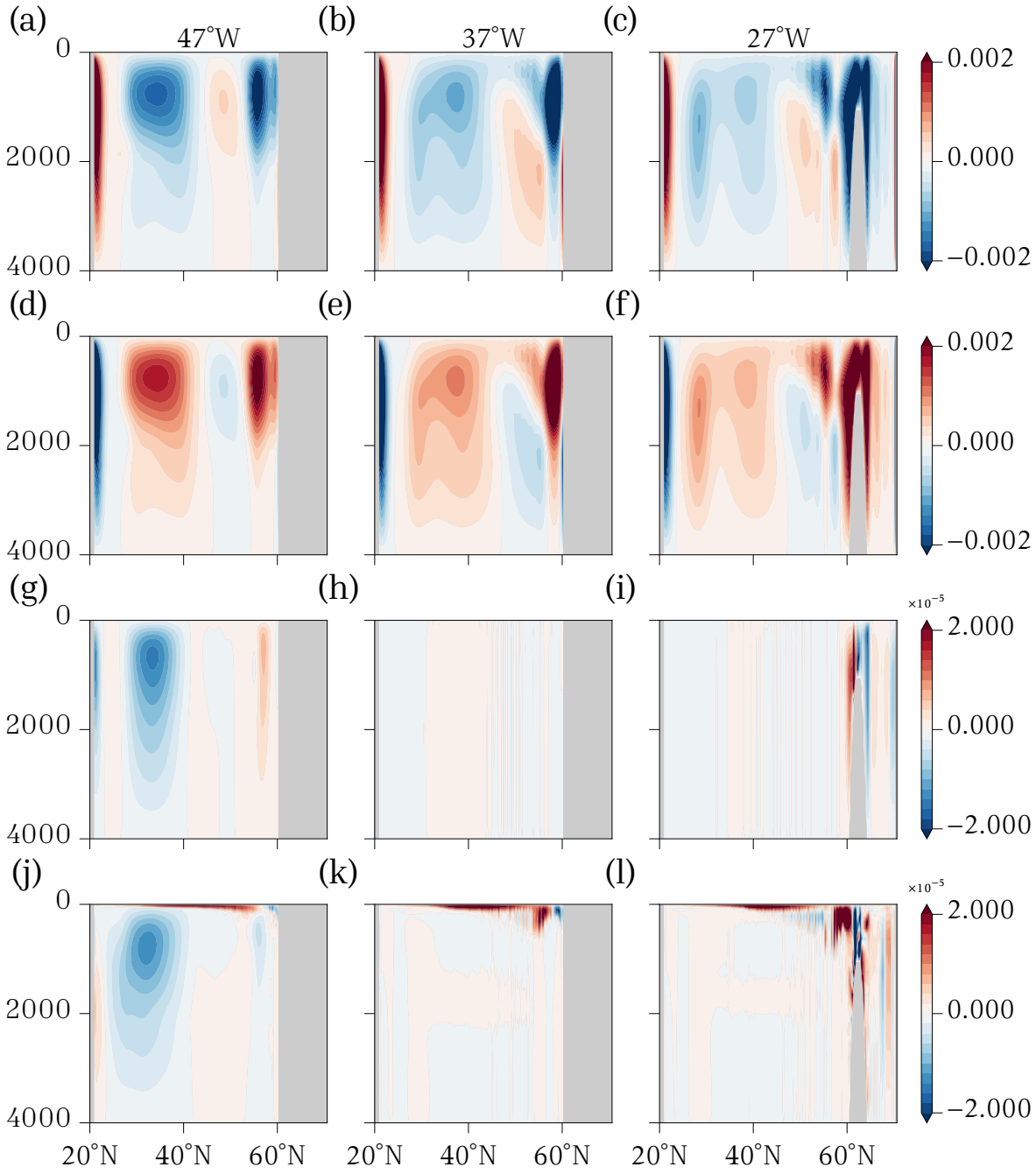


FIGURE 5.12: Meridional sections of the meridional overturning force function for the vertical sidewalls configuration for: (a)–(c) the Coriolis force, (d)–(f) the buoyancy force, (g)–(i) inertial forces, (j)–(l) viscous forces. The zonal overturning force functions are given in $m^2\ s^{-2}$. Note that the scales differ between panels (a)–(f) and panels (g)–(l).

5.4.2 The Overturning Circulation in Depth Space

Although the meridional overturning force function is a three-dimensional function, Section 4.9.1 demonstrated that, together with the depth-integrated force function, it can be used to derive an expression—given in equation (4.146)—for the rate of change of the overturning circulation. Equipped with this expression, it is possible to obtain the rotational momentum balance of the overturning circulation as a whole. Similar to the analysis of the rotational momentum balance of the barotropic circulation presented in Section 5.3, the analogous balance for the overturning circulation is easiest to interpret by starting with the vertical sidewalls case and concluding with the full control configuration.

Figure 5.13 shows the rotational momentum balance of the meridional overturning circulation in depth space for the vertical sidewalls case. As in the case of the three-dimensional overturning force functions presented in Figure 5.12, the primary balance is between the Coriolis force and buoyancy force. As previously stated, this is just thermal wind balance, and dominates the momentum balance of the meridional overturning circulation across all four configurations. The extent to which the balance between the Coriolis and buoyancy forces dominates the overall balance is a reasonable indicator of the extent to which the basin can be expected to be in thermal wind balance. Its dominance is therefore reassuring, as the decomposition of the meridional overturning circulation in Chapter 3 depends on the assumption that the ocean interior is largely in geostrophic balance.

The zonally-integrated torques in Figure 5.13 arising from the Coriolis and buoyancy forces strongly resemble the force functions in Figure 5.12. This is because there is comparatively little longitudinal variation in the force functions and there is no barotropic component. The latter is evident from consideration of the second term in the integral in (4.146): the lack of variation in depth reduces the term to one proportional to the difference between the values of HA^{BT} on the eastern and western boundaries, but the kinematic

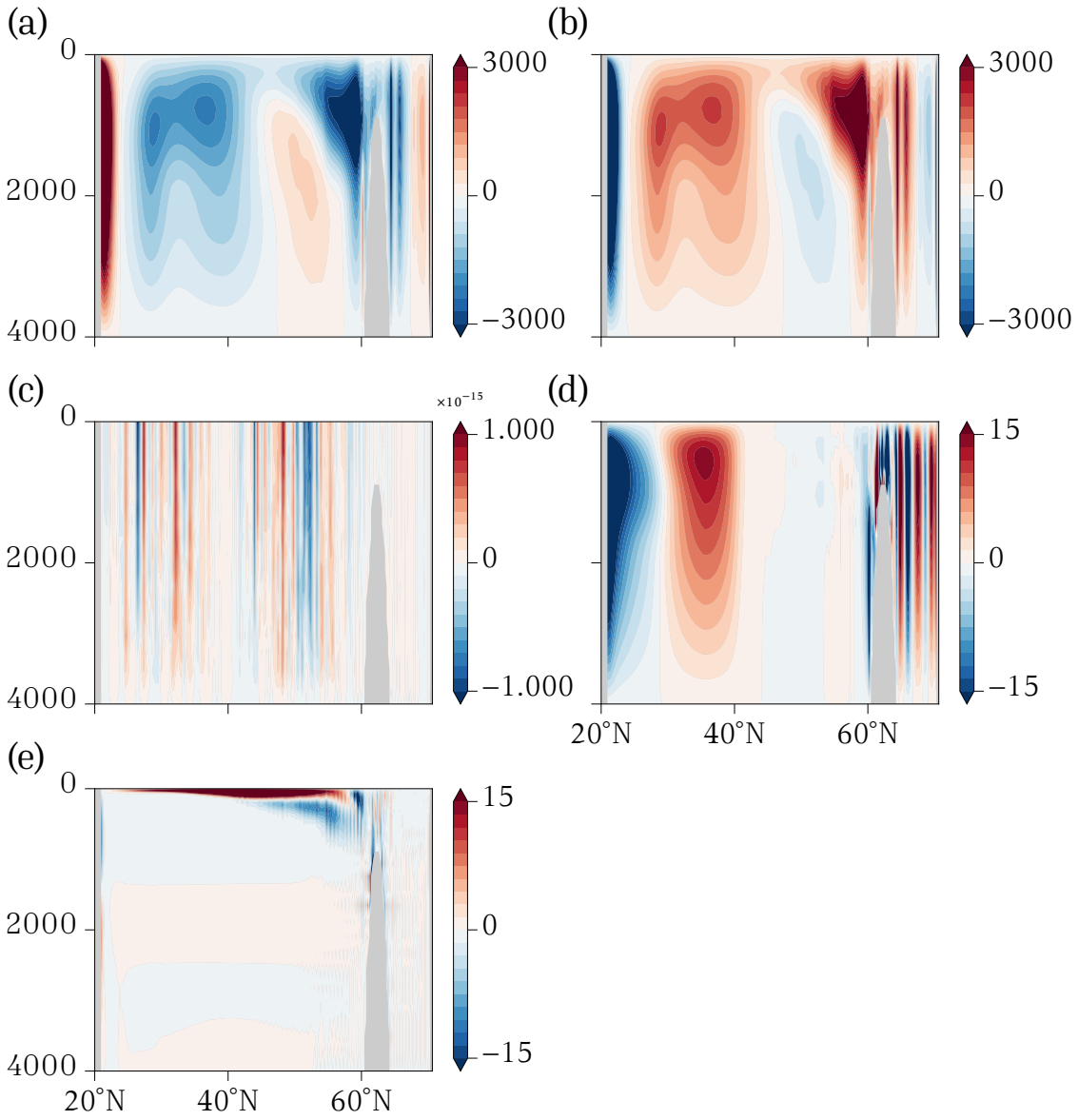


FIGURE 5.13: The rates of change of the meridional overturning streamfunction in depth space in the vertical sidewalls configuration due to: (a) the Coriolis force, (b) the buoyancy force, (c) the wind-stress, (d) inertial forces, (e) viscous forces, each given in $m^3\ s^{-2}$—cf. the overturning streamfunction in Figure 3.6(c). Note that the scales differ between panels.

boundary condition requires that the two values are identical and hence the barotropic contribution is zero.

Similarly, there is no barotopic contribution to the wind, inertial, or viscous torques in Figures 5.13(c), 5.13(d), and 5.13(e) respectively. As such, effect of a

given force on the overturning circulation in the vertical sidewalls case is

$$-\frac{\partial \Psi^{(z)}_{\mathrm{MOC}}}{\partial t} = \int_{x_\mathrm{w}}^{x_\mathrm{e}} A^{\mathrm{OT}x}\,\mathrm{d}x\,, \tag{5.24}$$

where

$$\frac{\partial^2 A^{\mathrm{OT}x}}{\partial z^2} = -\hat{\boldsymbol{e}}_x \cdot \left(\frac{\boldsymbol{\nabla}\times\boldsymbol{F}}{\rho_0}\right). \tag{5.25}$$

The zonally-integrated torque on the overturning circulation applied by the wind is therefore zero, as the wind-stress is purely zonal, hence the meridional force function is zero everywhere. The viscous torque is limited to a shallow Ekman cell centred on 40°N, with an additional signal at high latitudes in the main basin arising from surface-forced convection in the northeast corner of the basin (similar patterns of convection are found in Gjermundsen and LaCasce 2017). The inertial torque can be thought of as the tilting of columns of relative vorticity from the horizontal plane into the meridional plane by vertical shear in the zonal velocity. Anticyclonic relative vorticity in the subtropical gyre is carried northwards in the western boundary current and is then advected offshore when the current separates from the boundary, but the surface-intensified nature of the current deforms columns of vorticity, tilting them to give a clockwise torque in the meridional plane.

Consider next the no-buoyancy forcing configuration shown in Figure 5.14. Again the zonally-integrated torques due to the buoyancy and Coriolis forces which dominate the meridional rotational momentum balance bear a strong resemblance to the analogous force functions in Figure 5.11. This is in spite of the fact that there are now sloping sidewalls, and therefore the barotropic component is not necessarily zero, and implies that the net torque exerted by these forces is dominated by the respective meridional overturning force functions, and not the corresponding depth-integrated ones.

The form of the torque due to the external wind stress in Figure 5.14(c) appears initially unintuitive. It is non-zero, but is by far the smallest of the five forces, and is concentrated at latitudes where the wind stress is weak.

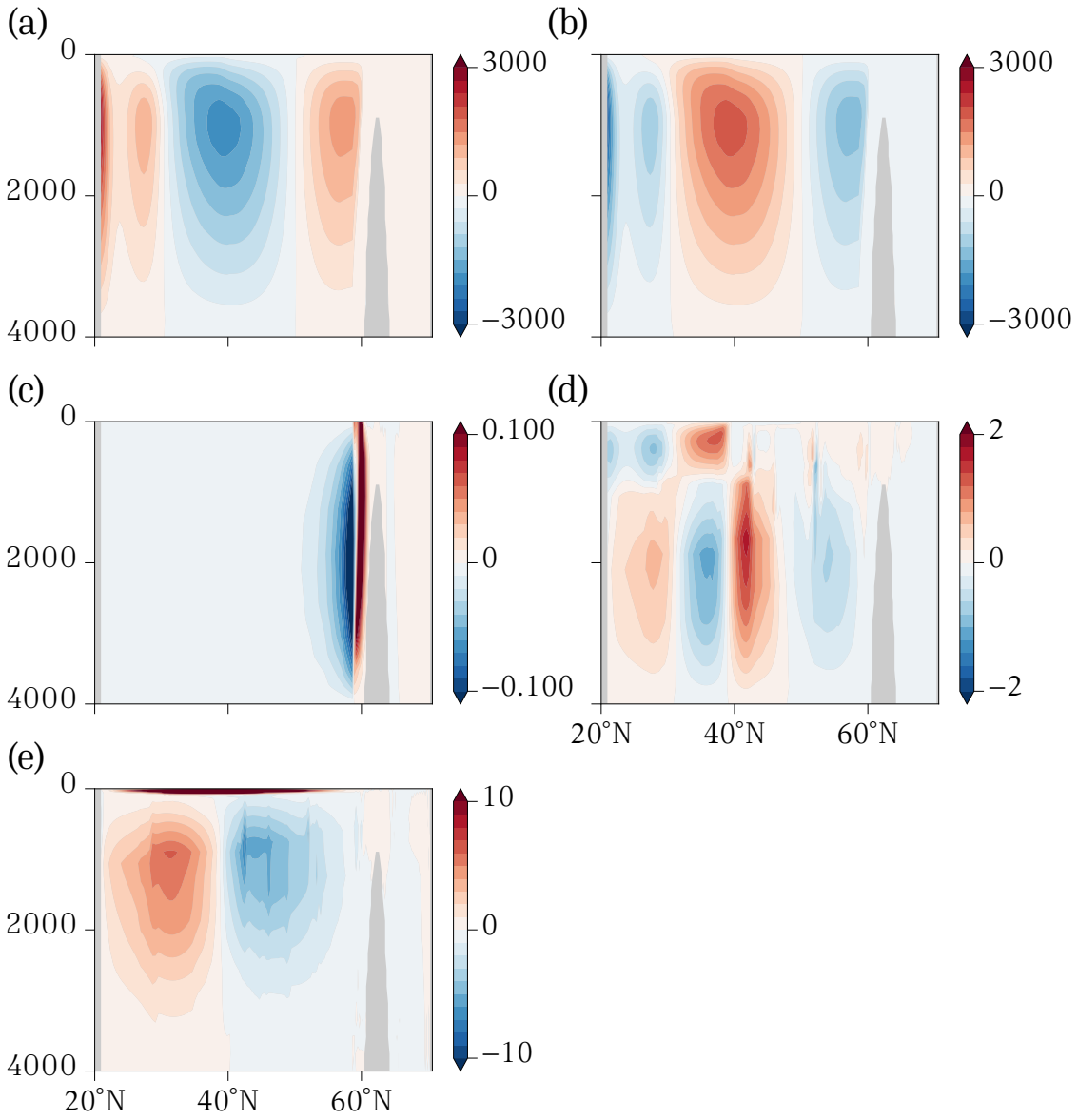


FIGURE 5.14: The rates of change of the meridional overturning streamfunction in depth space in the no-buoyancy-forcing configuration due to: (a) the Coriolis force, (b) the buoyancy force, (c) the wind-stress, (d) inertial forces, (e) viscous forces, each given in $m^3\ s^{-2}$—cf. the overturning streamfunction in Figure 3.6(b). Note that the scales differ between panels.

Considering the form of the depth-integrated force function in Figure 5.6(c) (which, as previously explained, is the only way wind stress can directly affect the overturning circulation), the reason for this form quickly becomes apparent. As this depth-integrated force function is zonally symmetric, and the same is *almost* true of the topography in the main basin where the wind stress is non-

zero, any contribution from the coupling of the zonal gradients in HA^{BT} and H in the western half of the basin will be cancelled by an equal, but opposite, contribution in the eastern half of the basin. The only place where this is not true is in the vicinity of the two channels, and so this is the only latitude at which a non-zero net torque appears. This torque, however, is weak as zonal gradients in HA^{BT} are particularly small at these latitudes.

The inertial torque on the overturning circulation shown by Figure 5.14(d) is noticeably different from the vertical sidewalls case. First, there is a sign change in the torque with depth. This arises from the competing effects of the overturning and depth-integrated components: while the component from the overturning force function (via the mechanism described in the vertical sidewalls case above) is still the larger of the two, it is restricted tightly to the region near the western boundary, above the upper slope. This means that this component is only significant at shallow depths, and allows the depth-integrated component to dominate at deeper depths, leading to a sign change at approximately 800m. Secondly, there is a larger (relatively speaking) subpolar inertial torque. This is due to the greater subtropical-subpolar symmetry in the flow in the no-buoyancy-forcing case relative to the others (see Figure 3.4). Offshore zonal flow just to the north of 40°N, however, is weaker than the corresponding flow to the south, and so the shear component of the torque balances the barotropic component at shallow depths rather than outcompete it (as is the case in the subtropical gyre).

Comparing the viscous torque in the no-buoyancy-forcing case in Figure 5.14(e) with that in the vertical sidewalls case in Figure 5.13(e): the Ekman cell remains, but the feature at high latitudes arising from surface-forced convection is no longer present—as would intuitively be expected. There is an additional dipole feature present at depth, which is broadly symmetric about 40°N. Again, inspection of the depth-integrated force function in Figure 5.6(e) reveals the origin of this feature: it arises from the coupling between the depth-integrated force function and the topographic slope on the western boundary.

Moving on now to the no-wind-stress configuration, the zonally-integrated torques for the five forces are shown in Figure 5.15. As in the previous cases, the torques from the buoyancy and Coriolis forces are dominated by the respective meridional overturning force functions. The "central" peak in the torque is located at relatively high latitudes. This is because this peak is associated with the baroclinic North Atlantic Current analogue, particularly where it separates from the western boundary and, in the no-wind-stress configuration, this separation occurs at higher latitudes.

The torque from the wind stress is obviously zero, and those due to inertia and dissipation are simply explained using the interpretations given for the previous two configurations. In the case of inertia, in the subtropical gyre there is again a sign change with depth resulting from the competing effects of the shear and barotropic components, with the shear dominating at the shallow depths where the intense western boundary current flows above the shallow boundary slope, and the barotropic component dominating at greater depths. In the viscous torque shown in Figure 5.15(e), the shallow Ekman cell present in both previous cases is now (reassuringly) absent, but the dipole from the barotropic component remains from Figure 5.14(e) and the feature arising from surface-forced convection present in Figure 5.13(e) has also returned.

Finally, Figure 5.16 shows the rotational momentum balance of the meridional overturning circulation in the control case. The torques from the buoyancy and Coriolis forces are still dominated by the respective meridional overturning force functions, and have a "central" peak around 40°N where the boundary current separates from the western sidewall. The zonally-integrated torque due to wind is identical to that in the no-buoyancy-forcing case, shown in Figure 5.14(c). This is because the applied wind stress and the bathymetry are identical in the two cases. The torque due to inertia is very similar to that in the no-wind-stress case, but is slightly stronger. This increase in strength is due to the presence of larger zonal velocities, and hence stronger vortex tilting, in the control case, resulting from the presence of wind stress forcing

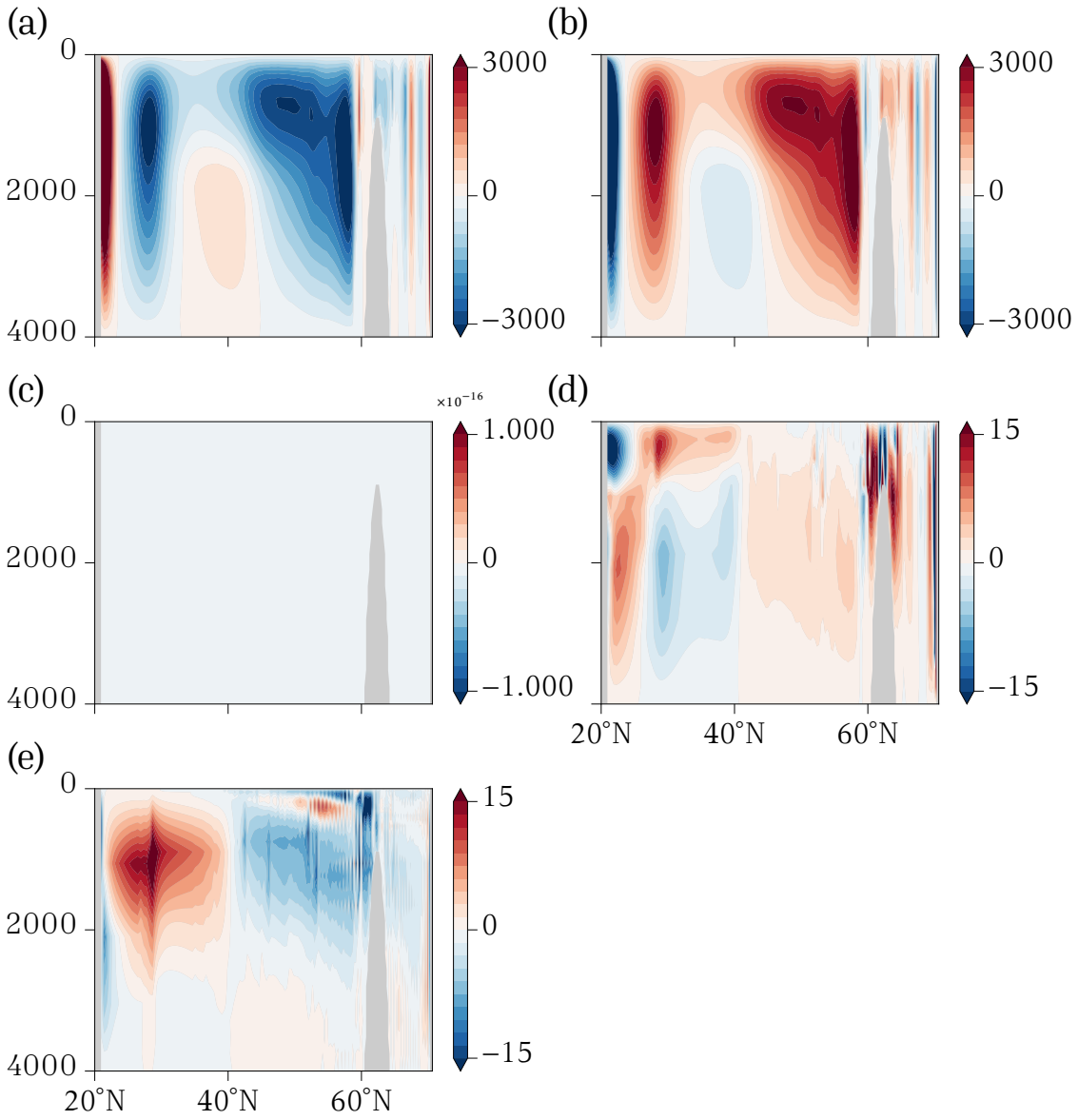


FIGURE 5.15: The rates of change of the meridional overturning streamfunction in depth space in the no-wind-stress configuration due to: (a) the Coriolis force, (b) the buoyancy force, (c) the wind-stress, (d) inertial forces, (e) viscous forces, each given in $m^3\ s^{-2}$—cf. the overturning streamfunction in Figure 3.6(d). Note that the scales differ between panels.

in the control case. The viscous torque is simply a combination of the three features previously discussed: an Ekman cell, a feature arising from convection at high latitudes, and a dipole caused by dissipation in the western boundary current above the boundary slope.

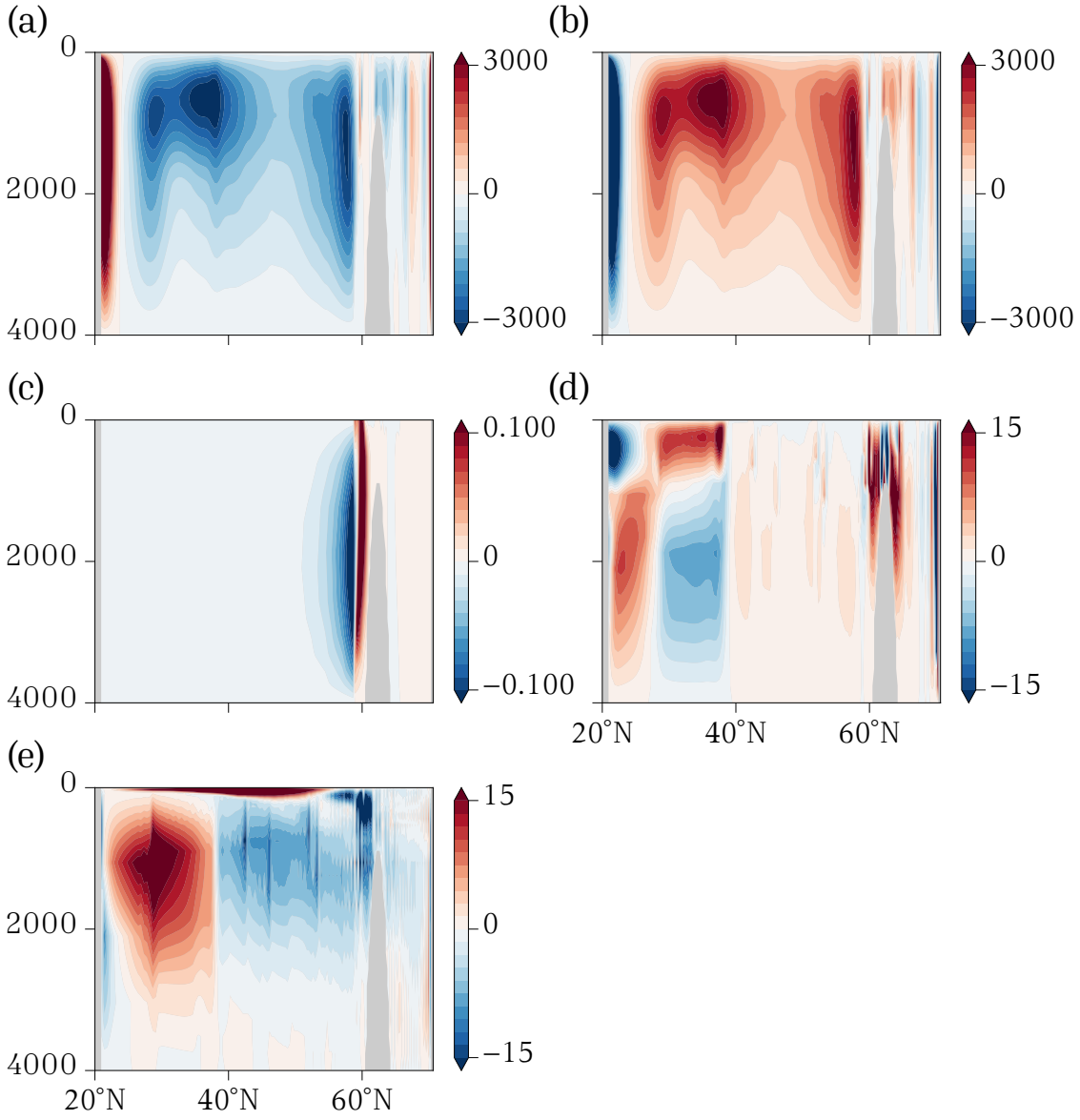


FIGURE 5.16: The rates of change of the meridional overturning streamfunction in depth space in the control configuration due to: (a) the Coriolis force, (b) the buoyancy force, (c) the wind-stress, (d) inertial forces, (e) viscous forces, each given in $m^3\ s^{-2}$—cf. the overturning streamfunction in Figure 3.6(a). Note that the scales differ between panels.

5.4.3 The Overturning Circulation in Density Space

While the results presented in the previous section give the rate of change of the meridional overturning circulation in depth space for each force, calculated using (4.146), it is also possible to derive the corresponding torques in density space, using equation (4.147). The zonally-integrated torques in density space for the vertical sidewalls configuration are shown in Figure 5.17. The torques due to the Coriolis, buoyancy and inertial forces appear similar to the analogous torques in depth space, just with a re-scaled vertical coordinate.

The most pronounced difference is to the torque exerted by the zonal wind stress. This was zero in depth space, but in density space this is no longer the case. The reason for this is that the stratification term in the integral in (4.147) allows the depth-integrated force function to contribute to the torque even in the absence of zonal variations in topography. This is analogous to the possibility of a non-zero external mode in the decomposition of the meridional overturning streamfunction in density space, sketched out in Figure 3.2.

The changes in sign with decreasing temperature can be interpreted by dividing the water column into distinct water masses. Considering the subpolar gyre (latitudes between 40°N and 60°N), the warmest water mass is surface water which has been carried northwards in the western boundary current. The next warmest water mass is water with a temperature above that relaxed to in the Nordic sponge (5°C), but cooler than the surface water in the boundary current. The third water mass is water cooler than this relaxation temperature, and the final water mass is the coolest water in the model, which is formed only at the very bottom of the subtropical sponge. The reason for the sign changes between each water mass is that the zonal slope of the isotherms at these latitudes changes sign. On the western boundary, the very surface waters are still northwards-flowing water in the warmest class, and so isopycnals slope upwards away from the boundary as they outcrop—this class is only present close to the boundary. The slope in the other classes is explained by the fact that the boundary current below the surface layer is the southwards-flowing, highly

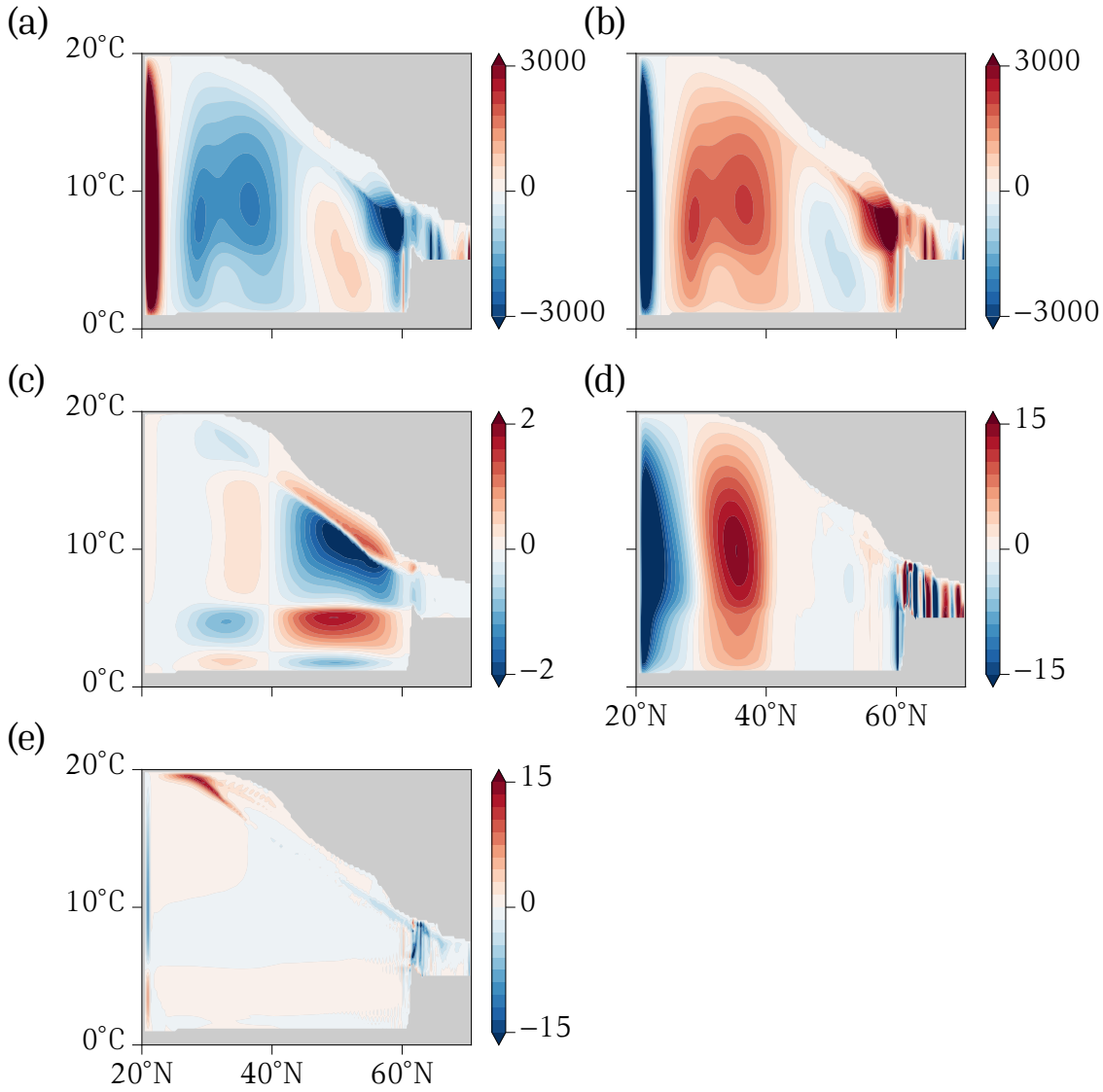


FIGURE 5.17: The rate of change of the meridional overturning streamfunction in density space in the vertical sidewalls configuration due to: (a) the Coriolis force, (b) the buoyancy force, (c) the wind-stress, (d) inertial forces, (e) viscous forces, each given in $m^3\ s^{-2}$. Note that the scales differ between panels.

barotropic, return current. As such, isopycnals above the coolest buoyancy-forced relaxation temperature 5°C slope downwards, and isopycnals below this temperature slope upwards, between the barotropic western boundary, and the stratified eastern boundary. This results in the "external mode" component switching signs between water masses.

The viscous torque also differs by more than just a vertical re-scaling, with the Ekman cell which was present across the entire basin in Figure 5.13(e) now

restricted to a narrow band of latitudes in the subtropics. This is a result of the deepening of the mixed layer in the model with increasing latitude: the Ekman cell acts to "stir" water across a shallow range of depths at all latitudes, but at high latitudes these depths are all within the mixed layer. This means that the water being "stirred" is all in the same density class, and so there is no signal in density space outside of the highly-stratified subtropics.

In the no-buoyancy-forcing configuration, shown in Figure 5.18, again the torques arising from the Coriolis, buoyancy and inertial forces appear to simply be re-scalings of the corresponding torques in depth space from Figure 5.14. The torque arising from the wind stress has a different form to that in the vertical sidewalls case. First, it is weaker: this is because the lack of buoyancy forcing means that the zonal gradient of isopycnals across the basin is weaker and hence the ability of the depth-integrated force function to project onto the meridional overturning torque is degraded. Secondly, there are no changes of sign with temperature within the subpolar gyre. The lack of a narrow clockwise cell at the warmest temperatures results from the fact the northwards-flowing western boundary current carrying warm subtropical water no longer penetrates into the subpolar gyre. In the absence of buoyancy forcing, the density structure of the subpolar gyre is set by the gradual upwelling of cold water by Ekman suction. This upwelled water then flows southwards in the western boundary current before being exported to the subtropical gyre. Because this cold boundary current extends from the bottom up to the surface in this configuration, isopycnals slope downwards to the east across all depths in the subpolar gyre, resulting in a unipolar torque.

The viscous torque in Figure 5.18(e) again has an Ekman cell which is restricted to within the subtropical sponge. This implies that the mixing by wind alone is sufficient to create a mixed layer at least as deep as the Ekman layer, as even with no surface buoyancy forcing, there is still no mixing across isopycnals within the Ekman cell. The dipole from the barotropic component, on the other hand, appears to simply be re-scaled from the same feature in depth space.

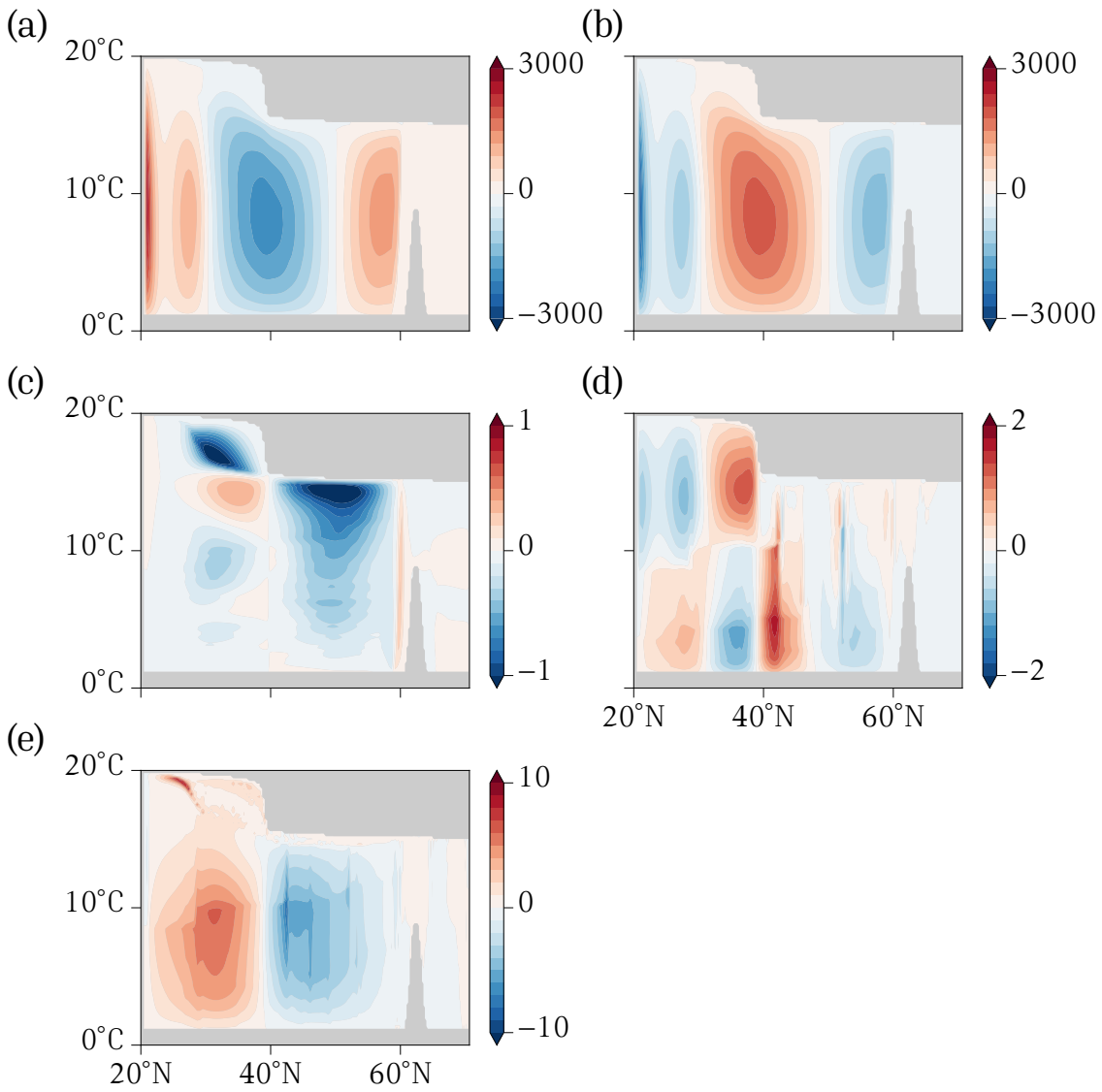


FIGURE 5.18: The rate of change of the meridional overturning streamfunction in density space in the no-buoyancy-forcing configuration due to: (a) the Coriolis force, (b) the buoyancy force, (c) the wind-stress, (d) inertial forces, (e) viscous forces, each given in $m^3\ s^{-2}$. Note that the scales differ between panels.

This is somewhat surprising, as this is the external mode component and would be expected to be affected more than the shear component. This might suggest that this dipole has its origins in the overturning force function, and not the depth-integrated force function. It may also, however, be explained by the fact that—with no buoyancy forcing—zonal density gradients are very weak, and so the distortion of the barotropic component of the torque is minimal.

This second explanation appears somewhat justified when the no-wind-

stress configuration shown in Figure 5.19 is considered. In this case, the viscous torque is distorted from the analogous torque in depth space. While a proportion of the dipole feature remains across all densities, it is largely focused on a narrow band of densities around a temperature slightly above 5°C. This is because the effects of viscosity are most prominent by far within the western boundary current. In the subpolar region, this current is largely barotropic, with a temperature range focused just above 5°C by exposure to buoyancy forcing either at the surface or in the Nordic sponge. This barotropic current continues into the subtropics, subducting under the warm northwards-flowing surface current. The presence of the warm boundary current in the subtropics and its absence in the subpolar gyre also explains why the subpolar cell has been more restricted than the subtropical one.

There is obviously no torque from the wind stress in this configuration, and the Coriolis and buoyancy torques are still simply re-scalings of the same torques in depth space. There is, however, one subtle change in the torque due to inertia. The subtropical torque is simply a re-scaling where the sign change now occurs at the temperature separating the northwards-flowing surface boundary current from the southwards-flowing deep return current, instead of the corresponding depth. The weak subpolar torque, however, is now restricted entirely to lower temperatures, implying that inertial torque in the subpolar gyre is dominated by the external mode.

Finally, considering the zonally-integrated torques on the meridional overturning circulation in density space for the full control configuration given in Figure 5.20, those arising from the Coriolis, buoyancy, and inertial forces are similar to those in the no-wind-stress case. As in depth space, the viscous torque in density space appears largely to be a combination of the no-wind-stress and no-buoyancy-forcing cases. The Ekman cell, however, extends across a larger range of latitudes in the control than in the no-buoyancy forcing case. This would suggest that the surface buoyancy forcing in the control maintains a surface stratification which is sufficiently strong that the depth of the Ekman

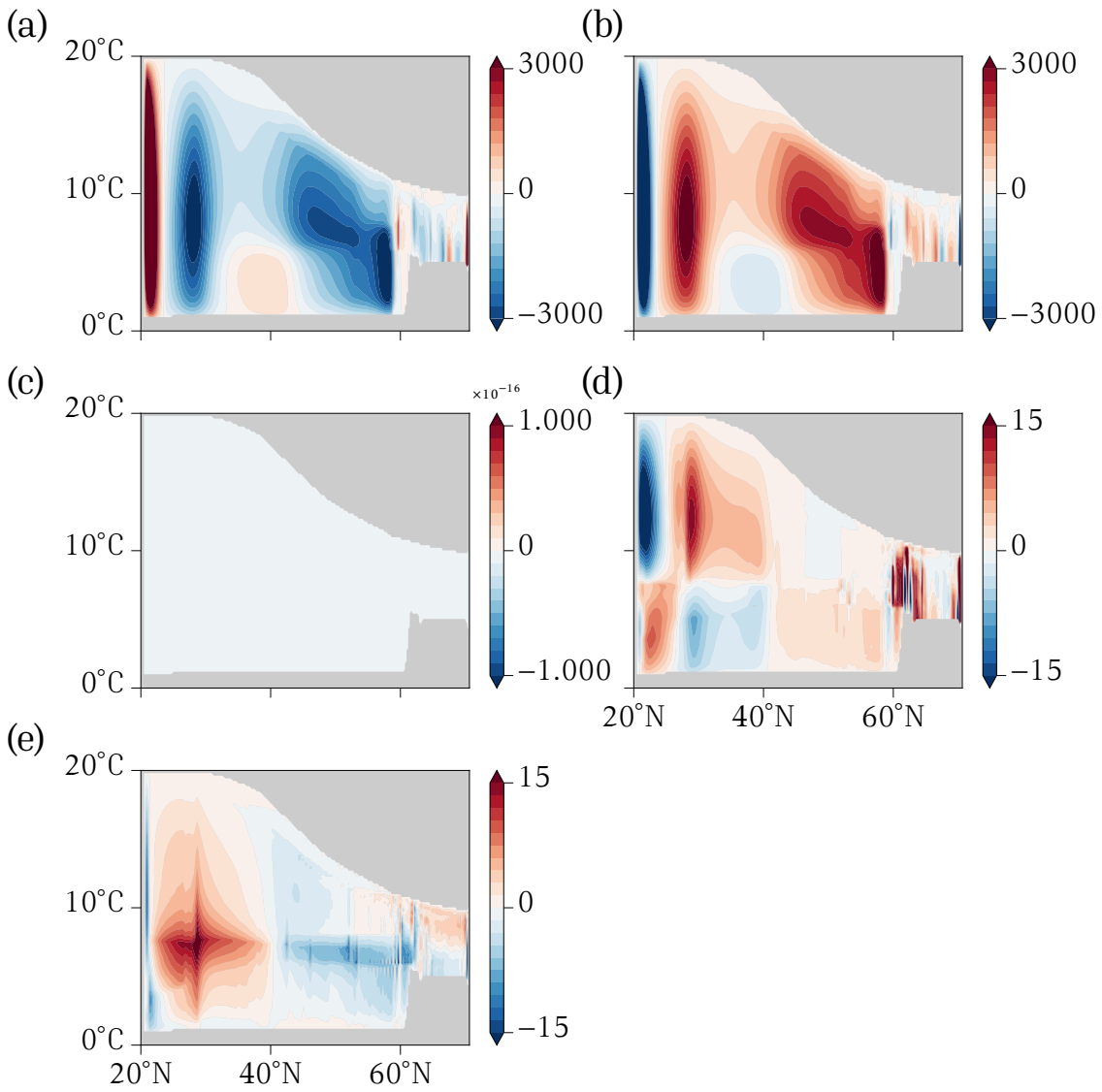


FIGURE 5.19: The rate of change of the meridional overturning streamfunction in density space in the no-wind-stress configuration due to: (a) the Coriolis force, (b) the buoyancy force, (c) the wind-stress, (d) inertial forces, (e) viscous forces, each given in $m^3\ s^{-2}$. Note that the scales differ between panels.

cell is deeper than the mixed layer, and so the "stirring" of the Ekman cell can act across isopycnals over a wider range of latitudes than with no buoyancy forcing.

The torque due to the wind stress, however, is significantly different from any other configuration. While it still has a similar multi-polar appearance to the torque in the vertical sidewalls case shown in Figure 5.17, there is no boundary current cell, the warm cell in the subpolar gyre dominates and the maximum torque is much stronger than in any other configuration. All

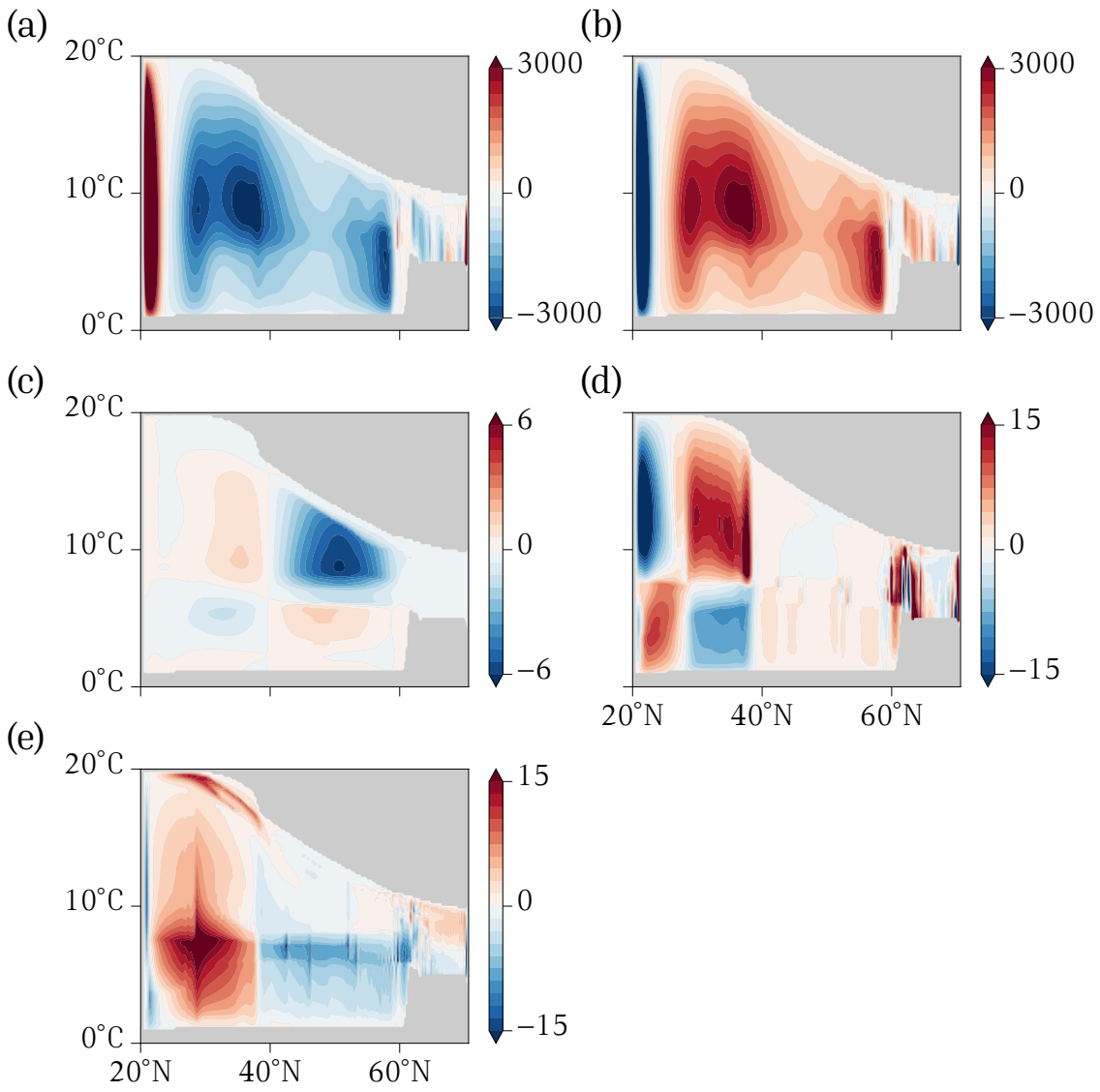


FIGURE 5.20: The rate of change of the meridional overturning streamfunction in density space in the control configuration due to: (a) the Coriolis force, (b) the buoyancy force, (c) the wind-stress, (d) inertial forces, (e) viscous forces, each given in $m^3\ s^{-2}$. Note that the scales differ between panels.

three of these differences are linked, and result from the fact that the warm, northwards-flowing, western boundary current separates from the boundary in the control case, whereas it does not in the vertical sidewalls configuration. This separation immediately explains the lack of a warm boundary current cell, as there is no warm boundary current. The separated boundary current becomes a model analogue of the North Atlantic Current, flowing northeast as a warm, baroclinic current. This leads to isopycnals sloping strongly downwards

zonally across the basin in the warmer density classes, in a similar fashion to in the real-world subpolar North Atlantic—see Figure 3.1. These strongly sloping warm isopycnals lead to the depth-integrated force function projecting strongly onto the zonally-integrated torque at these densities, although the resulting torque is still far weaker than that of the thermal wind component.

5.4.4 Separating the Shear and External Mode Components

Examining equations (4.146) and (4.147), it is obvious that the integral can be split into two separate integrals: one containing only the overturning force function, and another containing only the contribution of the depth-integrated force function. These are the projections of the torque due to a specific force onto the shear and external mode components of the overturning circulation presented in Chapter 3. By considering these integrals individually, it is possible to isolate the effects of a force on a single component of the overturning.

This decomposition can be used to test the validity of the explanations for the form of the torques given in the previous section, particularly the relative importance of the shear and external mode torques. Figure 5.21 shows the decomposition applied to the zonally-integrated torque arising due to the Coriolis force in both depth and density space. The first thing to note is that, as predicted in Sections 5.4.2 and 5.4.3, the shear component is an order of magnitude larger than the external mode component irrespective of the vertical coordinate chosen.

Further, as expected, the external mode component is dominated by a peak just south of 40°N, corresponding to the peak at the same latitude on the western boundary in the depth-integrated force function from Figure 5.8(a), and is positive—as HA^{BT} is increasing to the east. The torque from the external mode component in density space is also confined largely to cooler temperatures, supporting the reasoning in the previous section: the external mode is dominated by the contribution from the (cold) deep western boundary current, and so the external mode is largely confined to temperatures below that of the current.

As a sanity check, the decomposition can be applied to the wind stress. In this case, the shear component would be expected to be zero in both depth space and density space, and the full torque should therefore be equal to the external mode. Reassuringly, this is precisely what is seen in Figure 5.22.

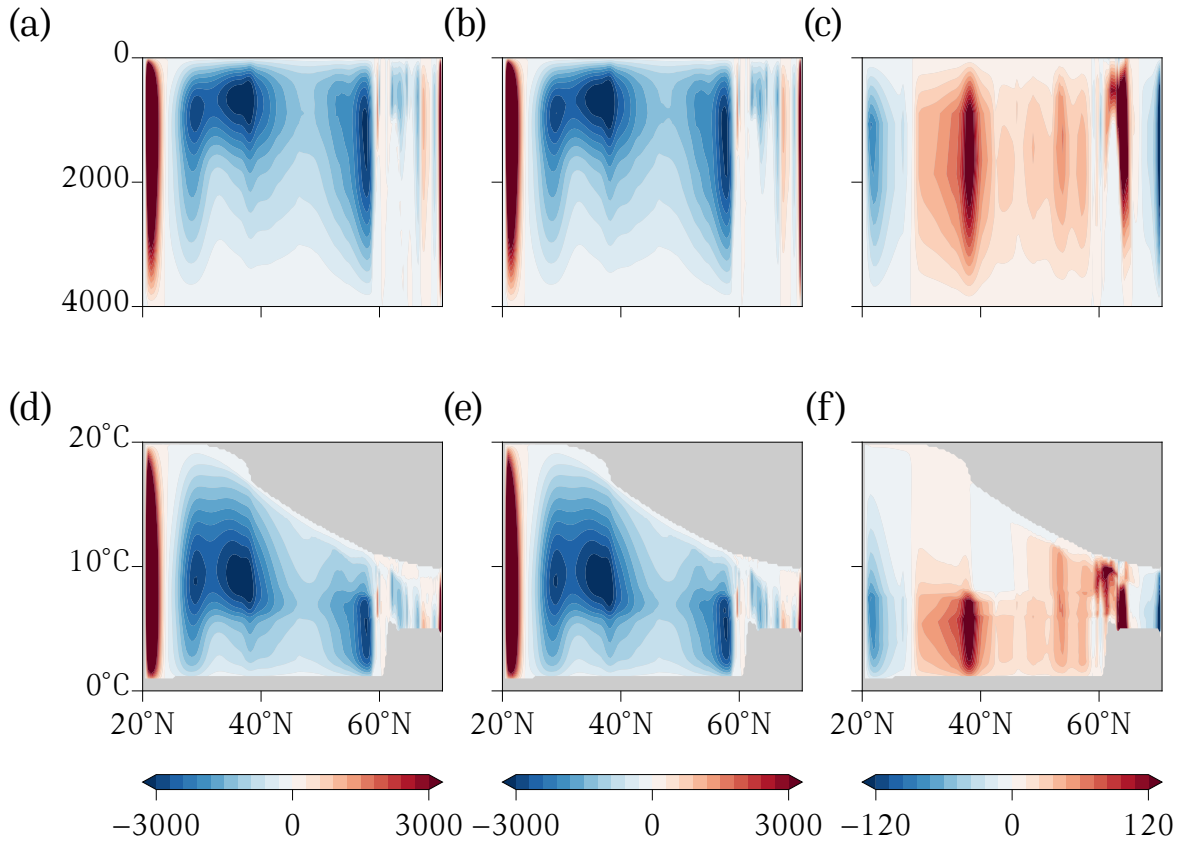


FIGURE 5.21: Decomposition of the rate of change of the overturning circulation in the control state due to the Coriolis force. Panels (a)–(c) show the rate of change in depth space due to the full force, the shear component, and the external mode component respectively. Panels (d)–(f) show the same components, but in density space. All values are in $m^3\ s^{-2}$. Note that the scales differ between panels.

More interesting is to decompose the torque from viscosity, and the resulting components are shown in Figure 5.23. As expected, the Ekman cell and the convective feature are contained within the shear component of the torque in both frameworks. Surprisingly, however, the dipole feature—which was hypothesised to simply be the external mode—appears to be partitioned almost equally between the shear and external mode components of the torque. Further, the shear component in density space is distorted in much the same way as the external mode component. This is perhaps unsurprising as the effects of viscosity are most pronounced where the shear in flow speed is largest—i.e., in the boundary current. The same argument for why the external mode is restricted to cooler temperatures would therefore apply to

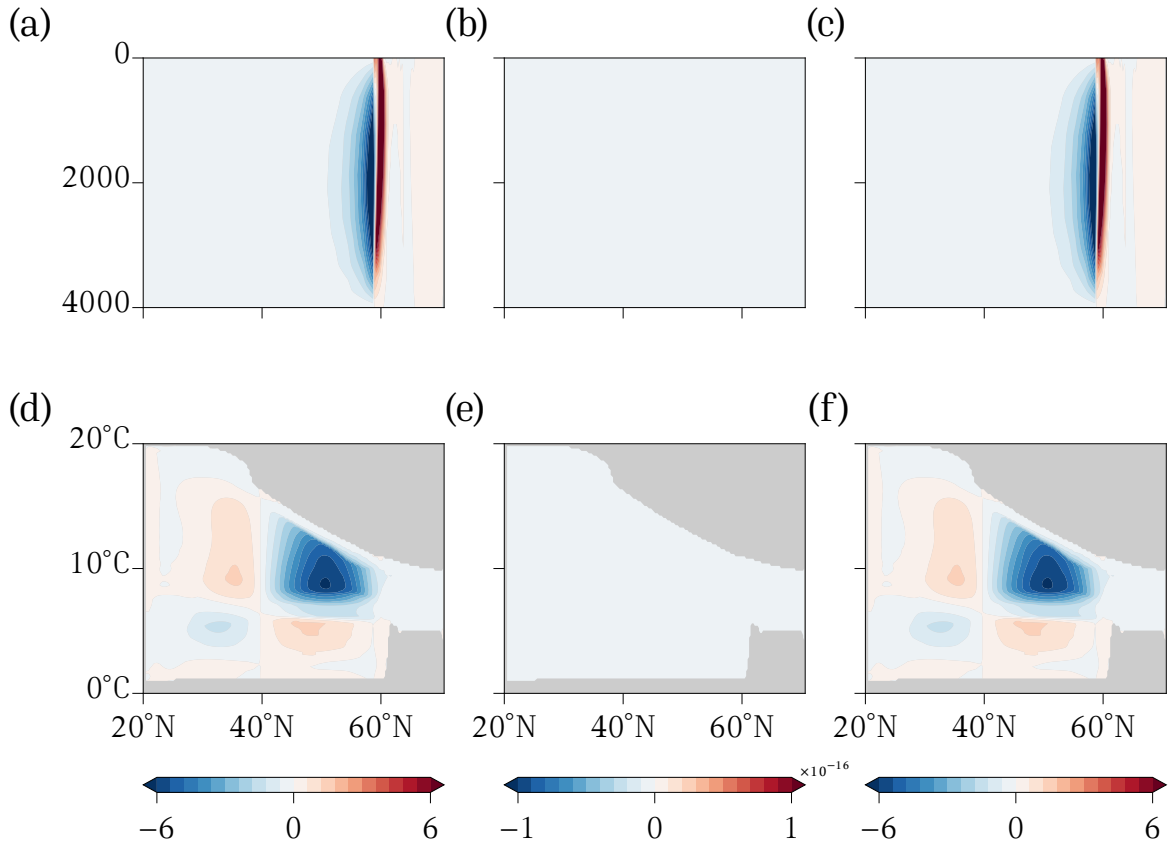


FIGURE 5.22: Decomposition of the rate of change of the overturning circulation in the control state due to the wind stress. Panels (a)–(c) show the rate of change in depth space due to the full force, the shear component, and the external mode component respectively. Panels (d)–(f) show the same components, but in density space. All values are in $m^3\ s^{-2}$. Note that the scales differ between panels.

the shear component.

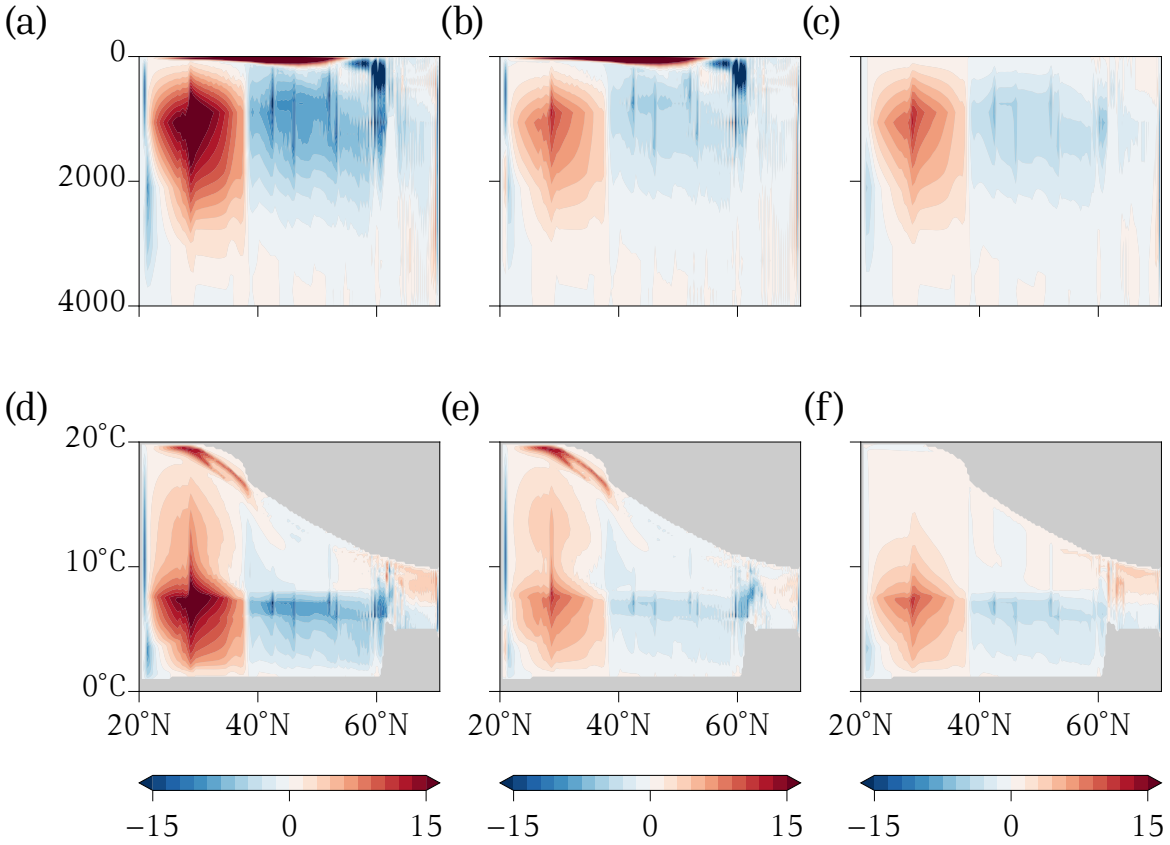


FIGURE 5.23: Decomposition of the rate of change of the overturning circulation in the control state due to viscous effects. Panels (a)–(c) show the rate of change in depth space due to the full force, the shear component, and the external mode component respectively. Panels (d)–(f) show the same components, but in density space. All values are in $m^3\,s^{-2}$.

5.5 Summary

In this section, first the precise numerical method by which the decomposition of the rotational momentum balance derived in the previous chapter can be applied to the model was presented in Section 5.2. The depth-integrated force functions for each of the Coriolis, buoyancy, wind stress, inertial, and viscous forces were then calculated for each of the configurations introduced in the experiments in Chapter 3. This yielded the surprising result that, in the presence of sloping sidewalls, the dominant force balance in the rotational momentum equation is between the Coriolis force and the joint effects of topography and the buoyancy force, and not between the Coriolis force and the wind stress as is the case with vertical sidewalls. While this coupling between topography, wind-stress and surface buoyancy forcing holds for all three experiments with sloping sidewalls, it is most pronounced in the control configuration, where all three are present.

The meridional overturning force functions for the four configurations were then calculated, and used to determine the zonally-integrated torques on the meridional overturning circulation in both depth space and density space. Here, the dominant force balance was found to be largely unaffected by the introduction of sloping sidewalls: in every configuration the opposing torques due to the Coriolis and buoyancy forces were larger than any other torque by a factor of $\mathcal{O}(100)$. This dominance of geostrophic terms is to be expected: for a midlatitude basin-scale oceanic flow with a characteristic flow speed of order $U \sim 10\,\mathrm{cm\,s^{-1}}$ varying over length scales of order $L \sim 10^5\,\mathrm{m}$, the Rossby number is of order $\mathrm{Ro} \sim 10^{-2}$, and we would therefore expect inertial effects to be roughly a hundred times smaller than those due to the Coriolis force. The main differences were in the torques due to the wind stress, inertia, and viscosity, but due to them being comparatively tiny, this had little effect on the overall momentum balance.

Finally, it was shown that the zonally-integrated torques associated with each force could be decomposed into their projections onto the shear and external mode components of the meridional overturning circulation. Applying this decomposition to the Coriolis force showed that its projection onto the shear component dominates the projection onto the external mode. The opposite was found for the wind stress, which has no projection onto the shear component, and the projections of the viscous torque onto the shear and external mode components were shown to be of similar magnitude.

6 Conclusions

6.1 Summary 151
6.2 Future Work 157
6.3 Concluding Remarks 159

This thesis has explored the roles played by wind-stress, surface buoyancy forcing, and topography, in driving the barotropic and overturning circulations in an idealised model of the subpolar North Atlantic. First, the mean-state overturning circulation arising in a set of experiments with different combinations of wind-stress, buoyancy forcing, and topography was decomposed in both depth space and density space to highlight the effects of each on the different components of the overturning. A corrected version of the rotational momentum equation framework introduced by Marshall and Pillar (2011) was then derived. Finally, this novel diagnostic was applied to the aforementioned experiments to expose the force balances regulating the ocean circulation in each case.

A detailed summary of the contents of Chapters 2, 3, 4, and 5 is provided at the end of each chapter. This final chapter briefly outlines the preceding ones, bringing attention to any key results and limitations therein, and suggests potential areas for future research.

6.1 Summary

The purpose of Chapter 2 was to introduce the idealised model used throughout the following chapters. The precise configuration of the model was specified, and the various approximations and parametrisations used were explained. The notation used in the discrete equations appearing in later chapters was also introduced, as well as the discrete form of the relevant differential operators. Finally, the equilibrated state of the spun-up control configuration was presented. While it was neither expected, nor intended, to *precisely* replicate the circulation of more realistic models, both the barotropic and overturning circulations were shown to compare favourably to the analogous circulations in more realistic high-resolution simulations.

Chapter 3 presented a decomposition of the overturning circulation in depth space into components arising from the geostrophic shear, the barotropic flow, and from Ekman flow. This decomposition, introduced by Lee and Marotzke (1998), forms the basis of the methods used by the RAPID and OSNAP programs (McCarthy et al. 2015 and Lozier et al. 2017 respectively) to infer the overturning circulation in the subtropical and subpolar North Atlantic, respectively. The calculation of the geostrophic shear component in this decomposition exploits the orthogonality of the vertical and zonal components to reduce the zonal integral of the thermal wind balance relation into the difference between the boundary densities. This simplification is no longer possible in density space, but a method of generalising the decomposition to apply to density space was introduced and subsequently applied to a series of numerical experiments with different combinations of wind-stress, buoyancy forcing, and topography.

The effects of wind-stress and surface buoyancy forcing on the barotropic circulation were shown to be somewhat independent of one another. The double gyre system driven by the wind-stress bears a strong resemblance to the depth-integrated circulation derived by Munk (1950), where the Sverdrup interior is closed by Laplacian dissipation. The circulation pattern arising from

surface buoyancy forcing, however, is a more intense double cell, confined to the regions close to the western and northern boundaries. The sloping topography itself had a weaker effect than expected on the wind-driven circulation, with only a small amount of the kind of distortion found by Jackson et al. (2006). This may be due to the use of a comparatively steep slope limiting the impact of the topography on the circulation, else may be a result of the coarse model resolution, particularly at low latitudes, not sufficiently resolving flow above the western boundary slope.

In both depth and density space, the geostrophic shear component of the overturning was found to dominate the external mode and Ekman components. The presence of sloping sidewalls generally intensifies the overturning circulation, and permits an external mode in depth space. In density space, while there is an external mode component of the overturning in the vertical sidewalls configuration, it is an order of magnitude weaker than the external mode in the control case (which has sloping sidewalls). At subpolar latitudes, the external mode in density space forms a dipole, with the two cells sharply separated at a critical density—slightly warmer than the temperature relaxed to in the sponge in the Nordic basin 5°C. This is due to a sign change in the zonal temperature gradient across the basin with depth, arising from temperature differences between the barotropic western boundary current and the baroclinic interior. With no surface buoyancy forcing, no meridional overturning circulation forms in the model. The decomposition of the overturning circulation reveals that this is due to a cancellation between the geostrophic shear component, and the external mode, suggesting that the heaving of isopycnals is counteracted by the barotropic flow over sloping topography.

Chapter 4 introduced the rotational momentum balance framework of Marshall and Pillar (2011), whereby the dynamically relevant component of an applied force can be extracted in the form of *force functions*. These force functions, which are the components of a vector potential, immediately reveal the force balances controlling the barotropic and overturning circulations. The

fundamental motivation behind reformulation of the momentum equation in terms of rotational forces is the same as that guiding its reformulation in terms of vorticity: elimination of the components of each force projecting onto the pressure gradient.

The advantages of the rotational momentum equation framework are primarily to do with interpretation, as it is easier to visualise a rotational force balance than the corresponding balance in the vorticity equation, and force balances themselves seem more intuitively appealing than balancing sources and sinks of vorticity. If two terms in the vorticity equation balance each other at any point in the domain, then the same balance exists at that point between the two analogous terms in the rotational momentum equation. The two equations describe the same physics, but the rotational momentum framework is a complementary view which can provide additional insight. For example, the fact that the introduction of topography alters the force balance of the barotropic circulation is well known (e.g., Jackson et al. 2006; Hughes and de Cuevas 2001), but the extent of this alteration is not immediately obvious from examination of the vorticity equation. Inspection of the force functions in Figure 5.8, however, immediately reveals the drastic nature of this change. A further advantage of the rotational momentum framework over the vorticity formulation is that the effects of the boundary conditions on the resulting flow is explicitly included, whereas these effects are harder to deduce from consideration of the vorticity balance.

Marshall and Pillar (2011) find, however, that their framework is of limited scope. While useful in diagnosing force balances in simply-connected, flat-bottomed basins, the approach fails when applied to a domain with topography and multiple boundaries. It is shown in Chapter 4 that these limitations arise from a subtle error in their derivation. A correct derivation is then presented, along with a method of obtaining the required Dirichlet boundary conditions in a multiply-connected domain. The final result is not as clean as that of Marshall and Pillar (2011), as the barotropic and overturning force functions

are implicitly coupled in the presence of sloping topography. The result is shown to be analogous to the barotropic potential vorticity equation for each individual force. The effect of a force can be represented by the sum of the curl of the depth integrated force and a JEBAR-like term (in the case of the buoyancy force, this term is precisely JEBAR) arising from the coupling due to topography.

Finally, in Chapter 5, the rotational momentum balance framework is applied to the experiments presented in Chapter 3. The two methods of obtaining the force functions (either directly, or as a residual after subtracting off the divergent component) are compared and shown to yield identical solutions, demonstrating the robustness of the approximations made in deriving the direct method.

The key result from the application of the new diagnostic is that the dominant rotational force balance in the barotropic circulation in the presence of sloping topography is not between the wind-stress and the Coriolis force, as in the vertical sidewalls case, but is between the buoyancy force and the Coriolis force. Notably, this result holds even in the case of no surface buoyancy forcing.

Several papers have taken similar approaches to diagnosing the dominant balances governing the barotropic circulation, but using a vorticity-based approach. Schoonover et al. (2016) take the terms in the barotropic vorticity equation, and integrate them first over the subtropical gyre, and then over a region encompassing the Gulf Stream. In the former case they find that the net input of vorticity from the wind stress curl is primarily balanced by the bottom pressure torque, and in the latter that the advection of planetary vorticity in the Gulf Stream is balanced by the bottom pressure torque. They apply this approach across a range of models and resolutions to demonstrate the robustness of the results. Yeager (2015) also plot the terms in the vertically-integrated barotropic vorticity balance to show the dominant vorticity balance in the North Atlantic. Plotting smoothed fields, they find that the primary balance is between the Coriolis force and the bottom pressure torque.

Le Corre et al. (2020) apply a similar methodology to the subpolar gyre, but use a single, high-resolution, model to allow for a good representation of both eddies and flow-topography interactions. Integrating the barotropic vorticity balance over parts of the gyre boundary slope, they find that the dominant balance depends on the region. Over western boundaries, the dominant balance is between the bottom pressure torque and the Coriolis force. Over eastern boundaries, on the other hand, the dominant balance is between the bottom pressure torque and nonlinear terms. Finally, in regions with particularly strong bottom currents, the bottom drag dominates, and is balanced by some combination of the Coriolis force, bottom pressure torque, and nonlinear terms.

These studies show broad agreement with the results obtained in this thesis via the rotational momentum equation framework. The major differences, particularly in the case of Le Corre et al. (2020), can be readily explained by the differences in model setup. For example, they find that nonlinear terms are at least as important as the bottom pressure torque and the Coriolis force, whereas this is not the case in the results from Chapter 5. This discrepancy, however, is most likely the result of the large difference in resolutions between the two models: the model of Le Corre et al. (2020) resolves eddies, whereas the idealised model used in this thesis is not capable of doing so. Further, Le Corre et al. (2020) also find the bottom drag curl to be an important effect, whereas bottom drag features only implicitly in the rotational momentum decomposition presented in Chapter 5. This is due to the combination of a terrain-following vertical coordinate and higher resolution allowing for an accurate representation of bottom flow over topography.

One significant advantage, however, of the rotational momentum balance framework over the methods employed in the aforementioned studies is the inclusion of the non-local impacts of each force. While plotting the terms in the barotropic vorticity equation reveals the local vorticity balance, to determine the basin-scale balances, all of the above studies either integrate over an arbitrary area or apply some form of smoothing to give readily-interpretable results,

neither of which are necessary in the rotational momentum balance framework.

Further, both Yeager (2015) and Le Corre et al. (2020) highlight that the magnitude of the JEBAR term is of a similar magnitude to—and in some places is larger than—the bottom pressure torque, and hence that the bottom flow is to some extent decoupled from the barotropic flow. The rotational momemtum balance framework also provides a natural way of probing the differences between the projections of a force onto JEBAR, and onto the bottom pressure torque. Equation (4.115) is essentially the contribution of a single force to the barotropic potential vorticity equation, and the second term on the right hand side is the projection of the force onto JEBAR. A similar expression for the contribution of a force to the barotropic vorticity equation is:

$$-\nabla^2 \left(H A^{\mathrm{BT}} \right) = \hat{\boldsymbol{e}}_z \cdot \left(\frac{\boldsymbol{\nabla} \times H \overline{\boldsymbol{F}}}{\rho_0} + \boldsymbol{\nabla} \times \phi_{\mathrm{bot}} \boldsymbol{\nabla} H \right) , \tag{6.1}$$

where the second term on the right hand side describes the projection of the force onto the bottom pressure torque.

Whereas the force balance underlying the barotropic circulation is altered significantly by the introduction of topography, the force balance governing the overturning circulation is largely unaffected. The dominant force balance in this case is between the buoyancy force and Coriolis force in all experiments in both depth space and density space with only minor variations in the form of the torques exerted on the overturning circulation by these forces. This is simply thermal wind balance, and the extent to which it dominates confirms that the circulation is overwhelmingly geostrophic.

Yeager (2015) use the various terms in the barotropic vorticity equation to decompose the overturning streamfunction in depth space, finding that there is an abrupt change in character of the overturning circulation at around 37°N, as the Gulf Stream separates from the western boundary. This transition is also immediately apparent from the results of Chapter 5, and while the decomposition in Chapter 5 is of the torque on the overturning and not the

overturning itself, it seems more natural as it is derived from the full three-dimensional forces, as opposed to the depth-integrated vorticity balance.

6.2 Future Work

There are, however, limitations with the force function approach as it stands. First, a source of numerical difficulty in calculating the force functions in a z-coordinate model is that values for depth on the boundaries between grid cells are required. The depth on these boundaries, however, is not uniquely defined (see Figure 2.2(b)). This is particularly problematic for the direct calculation of the rotational buoyancy force—as illustrated by Figure 5.2. Whether this difficulty would be eased or exacerbated by increasing the resolution of the model remains to be seen, but would be comparatively simple to test. More interesting, perhaps, would be to apply the approach to either a σ-coordinate (terrain-following) or isopycnal-coordinate model.

Schoonover et al. (2016) find that, while the balance between bottom pressure torque and the Coriolis force is the dominant net vorticity balance in the Gulf Stream across all models and resolutions, the magnitude of the signal does vary. In z-coordinate models, the bottom pressure torque signal is far larger at low resolutions, and tends to that of the σ-coordinate models as the resolution increases. This would imply that, perhaps, increasing the resolution would lead to improvements in accuracy in representing the effects of topography, although use of a terrain-following vertical coordinate would be preferable.

A second major limitation of the rotational momentum framework—as derived in Chapter 4—is the approximation of the ocean surface as a rigid lid. This assumption was made to simplify the treatment of the surface boundary condition: the presence of a rigid horizontal lid gives the straightforward condition that the vertical component of the rotational force at the surface is zero. With a free surface, a rotational force through the boundary is now evidently permitted, as the boundary is free to move. This problem is alluded to

in an appendix by Marshall and Pillar (2011), who suggest the alternative boundary condition—arising from taking pressure to be constant at the surface—that the component of the rotational force tangential to the free surface is equal to the corresponding component of the full force. Due to the fact that generally $\nabla\eta \ll 1$ (where η is sea surface elevation) in the large-scale ocean, the surface normal at the free surface could be expected to be approximately vertical. Instinctively, therefore, I would not expect the introduction of a free surface to significantly alter the dominant force balances. An important piece of future work therefore, would be to adapt the derivation of the rotational momentum framework presented in this thesis to admit a free surface to test this hypothesis, and allow for the application of the framework to models with a free surface.

Having generalised the rotational momentum balance approach to allow for non-uniform topography, one particularly obvious avenue for further work would be to apply it to a realistic, global, model geometry. Potential difficulties may arise from other assumptions made in the derivation presented in this thesis. The assumption of a shallow topographic slope, in particular, may cause issues in a realistic domain. Some terms discarded in the derivation of the direct approach may turn out to be non-negligible in a global geometry. Should this be the case, one potential solution would be to instead obtain the force functions via the residual method (where the divergent force is calculated instead, and the rotational component is inferred as a residual), as this method makes no such assumption.

A further issue with the application of the rotational momentum balance framework in a global geometry is presented by the Southern Ocean, in particular the treatment of eddies. One potential means of handling eddies would be that suggested by Gent et al. (1995), where the largest eddy fluxes are left in the buoyancy equation as an "eddy-induced transport velocity". An alternative approach would be to adopt a residual-mean formulation of the momentum equation (e.g., Young 2012), in which case the eddy forcing is present in the

momentum equation as the divergence of a stress tensor. The use of force functions to represent the dynamical impact of eddy fluxes has been explored by Maddison et al. (2015), but the full incorporation of the effects of eddies into the rotational momentum framework is very much an open question.

Another natural continuation of the work presented in this thesis would be to extend the experiments and analysis in Chapters 3 and 5 to examine the transient response of the overturning circulation to changes in wind stress and surface buoyancy forcing. This would allow for the determination of not just how the response is partitioned among the three components of the overturning, but also how the rotational force balance adjusts to mediate that response. Further, through a judicious choice of averaging period, the rotational momemtum balance framework could also be used to determine the forces underlying the dominant modes of temporal variability.

Finally, considerable effort has been expended to estimate the zonally-integrated overturning in density space at OSNAP, and the programme is now probing the individual array measurements to understand what causes variations in this overturning. The tools presented in Chapters 3 and 4 of this thesis, particularly when formulated in density space, could provide a conceptual framework to aid the interpretation of these results. Further, SNAP-DRAGON, a major new project building on OSNAP, was recently launched with one of its stated goals being to "*Expose the time-dependent causal relationships governing variability in the subpolar ocean*". The ability to diagnose the force balances underlying the subpolar circulation means that the rotational momentum framework presented in this thesis could prove to be a useful tool in achieving this goal.

6.3 Concluding Remarks

The rotational momentum balance approach presents a powerful new method for probing the mechanisms determining the large-scale ocean circulation.

Particular advantages of this approach are that the three-dimensional nature of the overturning force functions allows for a more detailed interrogation of the structure of the overturning circulation than the traditional two-dimensional zonally-integrated streamfunction. Also, as shown, both the barotropic and overturning force functions themselves can be further decomposed. The barotropic force function can be split into the component due to the depth-integrated torque, and the JEBAR-like term arising from the presence of topography, whereas the overturning force functions can be split into its shear and external mode components. Together with the potential improvements outlined in the previous section, these advantages demonstrate that the rotational momentum framework can provide a potent diagnostic framework for addressing large-scale problems in physical oceanography.

References

Adcroft, A., C. Hill, J.-M. Campin, J. Marshall, and P. Heimbach. 2004. "Overview of the Formulation and Numerics of the MIT GCM." *Proceedings of the ECMWF Seminar Series on Numerical Methods, Recent Developments in Numerical Methods for Atmosphere and Ocean Modeling* (January 1, 2004).

Adcroft, A., C. Hill, and J. Marshall. 1997. "Representation of Topography by Shaved Cells in a Height Coordinate Ocean Model," https://doi.org/10.1175/1520-0493(1997)125<2293:ROTBSC>2.0.CO;2.

———. 1999. "A New Treatment of the Coriolis Terms in C-Grid Models at Both High and Low Resolutions." *Monthly Weather Review - MON WEATHER REV* 127 (August 1, 1999). https://doi.org/10.1175/1520-0493(1999)127<1928:ANTOTC>2.0.CO;2.

Arakawa, A. 2000. "Chapter 1 - A Personal Perspective on the Early Years of General Circulation Modeling at UCLA." In *International Geophysics,* edited by D. A. Randall, 70:1–65. General Circulation Model Development. Academic Press, January 1, 2000. https://doi.org/10.1016/S0074-6142(00)80049-2. https://www.sciencedirect.com/science/article/pii/S0074614200800492.

Arakawa, A., and V. R. Lamb. 1977. "Computational Design of the Basic Dynamical Processes of the UCLA General Circulation Model." In *Methods in Computational Physics: Advances in Research and Applications,* edited by J. Chang, 17:173–265. General Circulation Models of the Atmosphere. Elsevier, January 1, 1977. https://doi.org/10.1016/B978-0-12-460817-7.50009-4. https://www.sciencedirect.com/science/article/pii/B9780124608177500094.

Baehr, J., J. Hirschi, J. O. Beismann, and J. Marotzke. 2004. "Monitoring the Meridional Overturning Circulation in the North Atlantic: A Model-Based Array Design Study." In collaboration with J. Baehr, J. Hirschi, J. O. Beismann, and J. Marotzke. *Journal of Marine Research* 62, no. 3 (3): 283–312. ISSN: 0022-2402. https://doi.org/10.1357/0022240041446191. https://eprints.soton.ac.uk/9694/.

Bailey, D., P. Rhines, and S. Häkkinen. 2005. "Formation and Pathways of North Atlantic Deep Water in a Coupled Ice–Ocean Model of the Arctic–North Atlantic Oceans." *Climate Dynamics* 25 (October 1, 2005): 497–516. https://doi.org/10.1007/s00382-005-0050-3.

Baringer, M. O., and J. C. Larsen. 2001. "Sixteen Years of Florida Current Transport at 27° N." *Geophysical Research Letters* 28 (16): 3179–3182. ISSN: 1944-8007. https://doi.org/10.1029/2001GL013246. https://onlinelibrary.wiley.com/doi/abs/10.1029/2001GL013246.

Bhatia, H., G. Norgard, V. Pascucci, and P.-T. Bremer. 2012. "The Helmholtz-Hodge Decomposition-A Survey." *IEEE Transactions on Visualization and Computer Graphics* 19 (November 29, 2012): 1386. https://doi.org/10.1109/TVCG.2012.316.

Born, A., and T. F. Stocker. 2014. "Two Stable Equilibria of the Atlantic Subpolar Gyre." *Journal of Physical Oceanography* 44, no. 1 (January 1, 2014): 246–264. ISSN: 0022-3670, 1520-0485. https://doi.org/10.1175/JPO-D-13-073.1. https://journals.ametsoc.org/jpo/article/44/1/246/12245/Two-Stable-Equilibria-of-the-Atlantic-Subpolar.

Bower, A., S. Lozier, A. Biastoch, K. Drouin, N. Foukal, H. Furey, M. Lankhorst, S. Rühs, and S. Zou. 2019. "Lagrangian Views of the Pathways of the Atlantic Meridional Overturning Circulation." *Journal of Geophysical Research: Oceans* 124 (8): 5313–5335. ISSN: 2169-9291. https://doi.org/10.1029/2019JC015014. https://agupubs.onlinelibrary.wiley.com/doi/abs/10.1029/2019JC015014.

Bower, A. S., M. S. Lozier, and S. Gary. 2011. "Export of Labrador Sea Water from the Subpolar North Atlantic: A Lagrangian Perspective." *Deep Sea Research Part II: Topical Studies in Oceanography,* ISSN: 0967-0645. https://doi.org/10.1016/j.dsr2.2010.10.060. https://pure.uhi.ac.uk/en/publications/export-of-labrador-sea-water-from-the-subpolar-north-atlantic-a-l.

Bryan, K. 1969. "A Numerical Method for the Study of the Circulation of the World Ocean." *Journal of Computational Physics* 4, no. 3 (October 1, 1969): 347–376. ISSN: 0021-9991. https://doi.org/10.1016/0021-9991(69)90004-7. https://www.sciencedirect.com/science/article/pii/0021999169900047.

Bryan, K., S. Manabe, and R. C. Pacanowski. 1975. "A Global Ocean-Atmosphere Climate Model. Part II. The Oceanic Circulation." *Journal of Physical Oceanography* 5, no. 1 (January 1, 1975): 30–46. ISSN: 0022-3670, 1520-0485. https://doi.org/10.1175/1520-0485(1975)005<0030:AGOACM>2.0.CO;2. https://journals.ametsoc.org/view/journals/phoc/5/1/1520-0485_1975_005_0030_agoacm_2_0_co_2.xml.

Buckley, M. W., and J. Marshall. 2016. "Observations, Inferences, and Mechanisms of the Atlantic Meridional Overturning Circulation: A Review." *Reviews of Geophysics* 54 (1): 5–63. ISSN: 1944-9208. https://doi.org/10.1002/2015RG000493. https://agupubs.onlinelibrary.wiley.com/doi/abs/10.1002/2015RG000493.

Campin, J.-M., P. Heimbach, M. Losch, et al. 2021. "MITgcm/MITgcm: Checkpoint67z," June 16, 2021. https://doi.org/10.5281/zenodo.4968496. https://zenodo.org/record/4968496.

Cane, M. A., V. M. Kamenkovich, and A. Krupitsky. 1998. "On the Utility and Disutility of JEBAR." *Journal of Physical Oceanography* 28, no. 3 (March 1, 1998): 519–526. ISSN: 0022-3670, 1520-0485. https://doi.org/10.1175/1520-0485(1998)028<0519:OTUADO>2.0.CO;2. https://journals.ametsoc.org/view/journals/phoc/28/3/1520-0485_1998_028_0519_otuado_2.0.co_2.xml.

Cessi, P., G. Ierley, and W. Young. 1987. "A Model of the Inertial Recirculation Driven by Potential Vorticity Anomalies." *Journal of Physical Oceanography* 17, no. 10 (October 1, 1987): 1640–1652. ISSN: 0022-3670, 1520-0485. https://doi.org/10.1175/1520-0485(1987)017<1640:AMOTIR>2.0.CO;2. https://journals.ametsoc.org/view/journals/phoc/17/10/1520-0485_1987_017_1640_amotir_2_0_co_2.xml.

Charney, J. 1955. "The Gulf Stream as an Inertial Boundary Layer." *Proceedings of the National Academy of Sciences of the United States of America,* https://doi.org/10.1073/PNAS.41.10.731.

Chassignet, E., and X. Xu. 2021. "On the Importance of High-Resolution in Large-Scale Ocean Models." *Advances in Atmospheric Sciences* 38 (July 31, 2021). https://doi.org/10.1007/s00376-021-0385-7.

Chassignet, E. P., and X. Xu. 2017. "Impact of Horizontal Resolution (1/12° to 1/50°) on Gulf Stream Separation, Penetration, and Variability." *Journal of Physical Oceanography* 47, no. 8 (August 1, 2017): 1999–2021. ISSN: 0022-3670, 1520-0485. https://doi.org/10.1175/JPO-D-17-0031.1. https://journals.ametsoc.org/view/journals/phoc/47/8/jpo-d-17-0031.1.xml.

Cimoli, L., A. Mashayek, H. Johnson, et al. 2022. "Significance of Diapycnal Mixing within the Atlantic Meridional Overturning Circulation." *ESS Open Archive* (August 29, 2022). https://doi.org/10.1002/essoar.10512257.1.

Courant, R., and D. Hilbert. 1989. *Methods of Mathematical Physics*. 1st ed. John Wiley & Sons, Ltd. https://doi.org/10.1002/9783527617210. https://onlinelibrary.wiley.com/doi/10.1002/9783527617210.

Danabasoglu, G., S. G. Yeager, Y.-O. Kwon, J. J. Tribbia, A. S. Phillips, and J. W. Hurrell. 2012. "Variability of the Atlantic Meridional Overturning Circulation in CCSM4." *Journal of Climate* 25, no. 15 (August 1, 2012): 5153–5172. ISSN: 0894-8755, 1520-0442. https://doi.org/10.1175/JCLI-D-11-00463.1. https://journals.ametsoc.org/view/journals/clim/25/15/jcli-d-11-00463.1.xml.

Daniault, N., H. Mercier, P. Lherminier, et al. 2016. "The Northern North Atlantic Ocean Mean Circulation in the Early 21st Century." *Progress in Oceanography* 146 (August 1, 2016): 142–158. ISSN: 0079-6611. https://doi.org/10.1016/j.pocean.2016.06.007. https://www.sciencedirect.com/science/article/pii/S0079661116300659.

Denaro, F. M. 2003. "On the Application of the Helmholtz–Hodge Decomposition in Projection Methods for Incompressible Flows with General Boundary Conditions." *International Journal for Numerical Methods in Fluids* 43 (1): 43–69. ISSN: 1097-0363. https://doi.org/10.1002/fld.598. https://onlinelibrary.wiley.com/doi/abs/10.1002/fld.598.

Desbruyères, D. G., S. G. Purkey, E. L. McDonagh, G. C. Johnson, and B. A. King. 2016. "Deep and Abyssal Ocean Warming from 35 Years of Repeat Hydrography." *Geophysical Research Letters* 43 (19): 10, 356–10, 365. ISSN: 1944-8007. https://doi.org/10.1002/2016GL070413. https://agupubs.onlinelibrary.wiley.com/doi/abs/10.1002/2016GL070413.

Duchez, A., E. Frajka-Williams, S. A. Josey, D. G. Evans, J. P. Grist, R. Marsh, G. D. McCarthy, B. Sinha, D. I. Berry, and J. J.-M. Hirschi. 2016. "Drivers of Exceptionally Cold North Atlantic Ocean Temperatures and Their Link to the 2015 European Heat Wave." *Environmental Research Letters* 11, no. 7 (July): 074004. ISSN: 1748-9326. https://doi.org/10.1088/1748-9326/11/7/074004. https://dx.doi.org/10.1088/1748-9326/11/7/074004.

Dunstone, N., D. Smith, A. Scaife, et al. 2018. "Skilful Seasonal Predictions of Summer European Rainfall." *Geophysical Research Letters* 45 (7): 3246–3254. ISSN: 1944-8007. https://doi.org/10.1002/2017GL076337. https://onlinelibrary.wiley.com/doi/abs/10.1002/2017GL076337.

Feulner, G., S. Rahmstorf, A. Levermann, and S. Volkwardt. 2013. "On the Origin of the Surface Air Temperature Difference between the Hemispheres in Earth's Present-Day Climate." *Journal of Climate* 26, no. 18 (September 15, 2013): 7136–7150. ISSN: 0894-8755, 1520-0442. https://doi.org/10.1175/JCLI-D-12-00636.1. https://journals.ametsoc.org/view/journals/clim/26/18/jcli-d-12-00636.1.xml.

Fox-Kemper, B., A. Adcroft, C. W. Böning, et al. 2019. "Challenges and Prospects in Ocean Circulation Models." *Frontiers in Marine Science* 6. ISSN: 2296-7745. https://www.frontiersin.org/articles/10.3389/fmars.2019.00065.

Frajka-Williams, E., I. J. Ansorge, J. Baehr, et al. 2019. "Atlantic Meridional Overturning Circulation: Observed Transport and Variability." *Frontiers in Marine Science* 6. ISSN: 2296-7745. https://doi.org/10.3389/fmars.2019.00260. https://www.frontiersin.org/articles/10.3389/fmars.2019.00260/full.

Gary, S. F., M. S. Lozier, C. W. Böning, and A. Biastoch. 2011. "Deciphering the Pathways for the Deep Limb of the Meridional Overturning Circulation." *Deep Sea Research Part II: Topical Studies in Oceanography,* Climate and the Atlantic Meridional Overturning Circulation, 58, no. 17 (September 1, 2011): 1781–1797. ISSN: 0967-0645. https://doi.org/10.1016/j.dsr2.2010.10.059. http://www.sciencedirect.com/science/article/pii/S0967064511000221.

Garzoli, S. L., and R. Matano. 2011. "The South Atlantic and the Atlantic Meridional Overturning Circulation." *Deep Sea Research Part II: Topical Studies in Oceanography,* Climate and the Atlantic Meridional Overturning Circulation, 58, no. 17 (September 1, 2011): 1837–1847. ISSN: 0967-0645. https://doi.org/10.1016/j.dsr2.2010.10.063. http://www.sciencedirect.com/science/article/pii/S0967064511000464.

Gent, P., and J. C. McWilliams. 1990. "Isopycnal Mixing in Ocean Circulation Models." *Journal of Physical Oceanography* 20 (January 1, 1990): 150–155. https://doi.org/10.1175/1520-0485(1990)020<0150:IMIOCM>2.0.CO;2.

Gent, P. R., J. Willebrand, T. J. McDougall, and J. C. McWilliams. 1995. "Parameterizing Eddy-Induced Tracer Transports in Ocean Circulation Models." *Journal of Physical Oceanography* 25, no. 4 (April 1, 1995): 463–474. ISSN: 0022-3670, 1520-0485. https://doi.org/10.1175/1520-0485(1995)025<0463:PEITTI>2.0.CO;2. https://journals.ametsoc.org/view/journals/phoc/25/4/1520-0485_1995_025_0463_peitti_2_0_co_2.xml.

Gibson, A. H., A. M. Hogg, A. E. Kiss, C. J. Shakespeare, and A. Adcroft. 2017. "Attribution of Horizontal and Vertical Contributions to Spurious Mixing in an Arbitrary Lagrangian–Eulerian Ocean Model." *Ocean Modelling* 119 (November 1, 2017): 45–56. ISSN: 1463-5003. https://doi.org/10.1016/j.ocemod.2017.09.008. https://www.sciencedirect.com/science/article/pii/S1463500317301440.

Gjermundsen, A., and J. H. LaCasce. 2017. "Comparing the Linear and Nonlinear Buoyancy-Driven Circulation." *Tellus A: Dynamic Meteorology and Oceanography* 69, no. 1 (January 1, 2017): 1299282. ISSN: 1600-0870. https://doi.org/10.1080/16000870.2017.1299282. https://www.tandfonline.com/doi/full/10.1080/16000870.2017.1299282.

Gjermundsen, A., J. H. LaCasce, and L. Denstad. 2018. "The Thermally Driven Ocean Circulation with Realistic Bathymetry." *Journal of Physical Oceanography* 48, no. 3 (March 1, 2018): 647–665. ISSN: 0022-3670, 1520-0485. https://doi.org/10.1175/JPO-D-17-0147.1. https://journals.ametsoc.org/view/journals/phoc/48/3/jpo-d-17-0147.1.xml.

Griffies, S., C. Böning, F. Bryan, E. Chassignet, R. Gerdes, H. Hasumi, A. Hirst, A.-M. Treguier, and D. Webb. 2000. "Developments in Ocean Climate Modelling." *Ocean Modelling* 2 (December 4, 2000): 123–192. https://doi.org/10.1016/S1463-5003(00)00014-7.

Griffies, S. M. 1998. "The Gent–McWilliams Skew Flux." *Journal of Physical Oceanography,* 831–841. https://doi.org/10.1175/1520-0485(1998)028<0831:TGMSF>2.0.CO;2.

———. 2004. *Fundamentals of Ocean Climate Models.* May 9, 2004. ISBN: 978-0-691-11892-5.

Griffies, S. M., and A. M. Treguier. 2013. "Chapter 20 - Ocean Circulation Models and Modeling." In *International Geophysics,* edited by G. Siedler, S. M. Griffies, J. Gould, and J. A. Church, 103:521–551. Ocean Circulation and Climate. Academic Press, January 1, 2013. https://doi.org/10.1016/B978-0-12-391851-2.00020-9. https://www.sciencedirect.com/science/article/pii/B9780123918512000209.

Gulev, S., and L. Hasse. 1998. "North Atlantic Wind Waves and Wind Stress Fields from Voluntary Observing Ship Data." *Journal of Physical Oceanography - J PHYS OCEANOGR* 28 (June 1, 1998): 1107–1130. https://doi.org/10.1175/1520-0485(1998)028<1107:NAWWAW>2.0.CO;2.

Gurvan, M., R. Bourdallé-Badie, J. Chanut, et al. 2022. *NEMO Ocean Engine.* Scientific Notes of Climate Modelling Center 27. Zenodo / Institut Pierre-Simon Laplace (IPSL), March 7, 2022. https://doi.org/10.5281/zenodo.1464816.

Harris, P. T., M. Macmillan-Lawler, J. Rupp, and E. K. Baker. 2014. "Geomorphology of the Oceans." *Marine Geology,* 50th Anniversary Special Issue, 352 (June 1, 2014): 4–24. ISSN: 0025-3227. https://doi.org/10.1016/j.margeo.2014.01.011. https://www.sciencedirect.com/science/article/pii/S0025322714000310.

Helmholtz, H. 1858. "Über Integrale Der Hydrodynamischen Gleichungen, Welche Den Wirbelbewegungen Entsprechen." *Journal für die reine und angewandte Mathematik* 1858, no. 55 (January 1, 1858): 25–55. ISSN: 0075-4102, 1435-5345. https://doi.org/10.1515/crll.1858.55.25. https://www.degruyter.com/document/doi/10.1515/crll.1858.55.25/html.

———. 1867. "On Integrals of the Hydrodynamical Equations, Which Express Vortex-Motion." *The London, Edinburgh, and Dublin Philosophical Magazine and Journal of Science* 33, no. 226 (January 1, 1867): 485–512. ISSN: 1941-5982. https://doi.org/10.1080/14786446708639824. https://doi.org/10.1080/14786446708639824.

Hirschi, J., and J. Marotzke. 2007. "Reconstructing the Meridional Overturning Circulation from Boundary Densities and the Zonal Wind Stress." *Journal of Physical Oceanography* 37, no. 3 (March 1, 2007): 743–763. ISSN: 0022-3670. https://doi.org/10.1175/JPO3019.1. https://journals.ametsoc.org/jpo/article/37/3/743/10811/Reconstructing-the-Meridional-Overturning.

Holland, W. R. 1973. "Baroclinic and Topographic Influences on the Transport in Western Boundary Currents." *Geophysical Fluid Dynamics* 4, no. 3 (January 1, 1973): 187–210. ISSN: 0016-7991. https://doi.org/10.1080/03091927208236095. https://doi.org/10.1080/03091927208236095.

Holliday, N. P., S. Bacon, S. A. Cunningham, S. F. Gary, J. Karstensen, B. A. King, F. Li, and E. L. Mcdonagh. 2018. "Subpolar North Atlantic Overturning and Gyre-Scale Circulation in the Summers of 2014 and 2016." *Journal of Geophysical Research: Oceans* 123 (7): 4538–4559. ISSN: 2169-9291. https://doi.org/10.1029/2018JC013841. https://onlinelibrary.wiley.com/doi/abs/10.1029/2018JC013841.

Hughes, C. W. 2008. "A Form of Potential Vorticity Equation for Depth-Integrated Flow with a Free Surface." *Journal of Physical Oceanography* 38, no. 5 (May 1, 2008): 1131–1136. ISSN: 0022-3670, 1520-0485. https://doi.org/10.1175/2007JPO3809.1. https://journals.ametsoc.org/view/journals/phoc/38/5/2007jpo3809.1.xml.

Hughes, C. W., and B. de Cuevas. 2001. "Why Western Boundary Currents in Realistic Oceans Are Inviscid: A Link between Form Stress and Bottom Pressure Torques." *Journal of Physical Oceanography* 31:15.

Hughes, C. W., and P. D. Killworth. 1995. "Effects of Bottom Topography in the Large-Scale Circulation of the Southern Ocean." *Journal of Physical Oceanography* 25, no. 11 (November 1, 1995): 2485–2497. ISSN: 0022-3670, 1520-0485. https://doi.org/10.1175/1520-0485(1995)025<2485:EOBTIT>2.0.CO;2. https://journals.ametsoc.org/view/journals/phoc/25/11/1520-0485_1995_025_2485_eobtit_2_0_co_2.xml.

Ierley, G. R. 1987. "On the Onset of Inertial Recirculation in Barotropic General Circulation Models." *Journal of Physical Oceanography* 17, no. 12 (December 1, 1987): 2366–2374. ISSN: 0022-3670, 1520-0485. https://doi.org/10.1175/1520-0485(1987)017<2366:OTOOIR>2.0.CO;2. https://journals.ametsoc.org/view/journals/phoc/17/12/1520-0485_1987_017_2366_otooir_2_0_co_2.xml.

Ierley, G. R., and W. R. Young. 1988. "Inertial Recirculation in a □-Plane Corner." *Journal of Physical Oceanography* 18, no. 4 (April 1, 1988): 683–689. ISSN: 0022-3670, 1520-0485. https://doi.org/10.1175/1520-0485(1988)018<0683:IRIAPC>2.0.CO;2. https://journals.ametsoc.org/view/journals/phoc/18/4/1520-0485_1988_018_0683_iriapc_2_0_co_2.xml.

Ilıcak, M., A. J. Adcroft, S. M. Griffies, and R. W. Hallberg. 2012. "Spurious Dianeutral Mixing and the Role of Momentum Closure." *Ocean Modelling* 45–46 (January 1, 2012): 37–58. ISSN: 1463-5003. https://doi.org/10.1016/j.ocemod.2011.10.003. https://www.sciencedirect.com/science/article/pii/S1463500311001685.

Jackson, L., C. W. Hughes, and R. G. Williams. 2006. "Topographic Control of Basin and Channel Flows: The Role of Bottom Pressure Torques and Friction." *Journal of Physical Oceanography* 36, no. 9 (September 1, 2006): 1786–1805. ISSN: 1520-0485, 0022-3670. https://doi.org/10.1175/JPO2936.1. https://journals.ametsoc.org/jpo/article/36/9/1786/10597/Topographic-Control-of-Basin-and-Channel-Flows-The.

Jackson, L. C., K. A. Peterson, C. D. Roberts, and R. A. Wood. 2016. "Recent Slowing of Atlantic Overturning Circulation as a Recovery from Earlier Strengthening." *Nature Geoscience* 9, no. 7 (July): 518–522. ISSN: 1752-0894, 1752-0908. https://doi.org/10.1038/ngeo2715. http://www.nature.com/articles/ngeo2715.

Jonathan, T., M. Bell, H. Johnson, and D. Marshall. 2021. "Decomposing the Time-Mean Atlantic Meridional Overturning Circulation and Its Variability with Latitude." (April 1, 2021): EGU21–1164. https://ui.adsabs.harvard.edu/abs/2021EGUGA..23.1164J.

Jong, M. F. de, S. S. Drijfhout, W. Hazeleger, H. M. van Aken, and C. A. Severijns. 2009. "Simulations of Hydrographic Properties in the Northwestern North Atlantic Ocean in Coupled Climate Models." *Journal of Climate* 22, no. 7 (April 1, 2009): 1767–1786. ISSN: 0894-8755, 1520-0442. https://doi.org/10.1175/2008JCLI2448.1. https://journals.ametsoc.org/view/journals/clim/22/7/2008jcli2448.1.xml.

Josey, S. A., J. J.-M. Hirschi, B. Sinha, A. Duchez, J. P. Grist, and R. Marsh. 2018. "The Recent Atlantic Cold Anomaly: Causes, Consequences, and Related Phenomena." *Annual Review of Marine Science* 10, no. 1 (January 3, 2018): 475–501. ISSN: 1941-1405, 1941-0611. https://doi.org/10.1146/annurev-marine-121916-063102. https://www.annualreviews.org/doi/10.1146/annurev-marine-121916-063102.

Killworth, P. D., D. B. Chelton, and R. A. de Szoeke. 1997. "The Speed of Observed and Theoretical Long Extratropical Planetary Waves." *Journal of Physical Oceanography* 27, no. 9 (September 1, 1997): 1946–1966. ISSN: 0022-3670, 1520-0485. https://doi.org/10.1175/1520-0485(1997)027<1946:TSOOAT>2.0.CO;2. https://journals.ametsoc.org/view/journals/phoc/27/9/1520-0485_1997_027_1946_tsooat_2.0.co_2.xml.

Klotzbach, P., W. Gray, and C. Fogarty. 2015. "Active Atlantic Hurricane Era at Its End?" *Nature Geoscience* 8, no. 10 (10): 737–738. ISSN: 1752-0908. https://doi.org/10.1038/ngeo2529. https://www.nature.com/articles/ngeo2529.

Kostov, Y., H. L. Johnson, D. P. Marshall, P. Heimbach, G. Forget, N. P. Holliday, M. S. Lozier, F. Li, H. R. Pillar, and T. Smith. 2021. "Distinct Sources of Interannual Subtropical and Subpolar Atlantic Overturning Variability." *Nature Geoscience* 14, no. 7 (7): 491–495. ISSN: 1752-0908. https://doi.org/10.1038/s41561-021-00759-4. https://www.nature.com/articles/s41561-021-00759-4.

Large, W. G., G. Danabasoglu, S. C. Doney, and J. C. McWilliams. 1997. "Sensitivity to Surface Forcing and Boundary Layer Mixing in a Global Ocean Model: Annual-Mean Climatology." *Journal of Physical Oceanography* 27, no. 11 (November 1, 1997): 2418–2447. ISSN: 0022-3670, 1520-0485. https://doi.org/10.1175/1520-0485(1997)027<2418:STSFAB>2.0.CO;2. https://journals.ametsoc.org/view/journals/phoc/27/11/1520-0485_1997_027_2418_stsfab_2.0.co_2.xml.

Large, W. G., J. C. McWilliams, and S. C. Doney. 1994. "Oceanic Vertical Mixing: A Review and a Model with a Nonlocal Boundary Layer Parameterization." *Reviews of Geophysics* 32 (4): 363–403. ISSN: 1944-9208. https://doi.org/10.1029/94RG01872. https://agupubs.onlinelibrary.wiley.com/doi/abs/10.1029/94RG01872.

Le Bras, I. A.-A., F. Straneo, J. Holte, M. F. de Jong, and N. P. Holliday. 2020. "Rapid Export of Waters Formed by Convection Near the Irminger Sea's Western Boundary." *Geophysical Research Letters* 47 (3): e2019GL085989. ISSN: 1944-8007. https://doi.org/10.1029/2019GL085989. https://onlinelibrary.wiley.com/doi/abs/10.1029/2019GL085989.

Le Corre, M., J. Gula, and A.-M. Tréguier. 2020. "Barotropic Vorticity Balance of the North Atlantic Subpolar Gyre in an Eddy-Resolving Model." *Ocean Science* 16, no. 2 (April 20, 2020): 451–468. ISSN: 1812-0784. https://doi.org/10.5194/os-16-451-2020. https://os.copernicus.org/articles/16/451/2020/.

Le Sommer, J., E. Chassignet, and A. Wallcraft. 2018. "Ocean Circulation Modeling for Operational Oceanography: Current Status and Future Challenges." August 11, 2018. ISBN: 978-1-72054-997-0. https://doi.org/10.17125/gov2018.ch12.

Ledwell, J. R., A. J. Watson, and C. S. Law. 1993. "Evidence for Slow Mixing across the Pycnocline from an Open-Ocean Tracer-Release Experiment." *Nature* 364, no. 6439 (6439): 701–703. ISSN: 1476-4687. https://doi.org/10.1038/364701a0. https://www.nature.com/articles/364701a0.

Lee, T., and J. Marotzke. 1998. "Seasonal Cycles of Meridional Overturning and Heat Transport of the Indian Ocean." *Journal of Physical Oceanography* 28, no. 5 (May 1, 1998): 923–943. ISSN: 0022-3670, 1520-0485. https://doi.org/10.1175/1520-0485(1998)028<0923:SCOMOA>2.0.CO;2. https://journals.ametsoc.org/view/journals/phoc/28/5/1520-0485_1998_028_0923_scomoa_2.0.co_2.xml.

Li, L. Cheng, J. Zhu, K. E. Trenberth, M. E. Mann, and J. P. Abraham. 2020. "Increasing Ocean Stratification over the Past Half-Century." *Nature Climate Change* 10, no. 12 (12): 1116–1123. ISSN: 1758-6798. https://doi.org/10.1038/s41558-020-00918-2. https://www.nature.com/articles/s41558-020-00918-2.

Li, F., M. S. Lozier, S. Bacon, et al. 2021. "Subpolar North Atlantic Western Boundary Density Anomalies and the Meridional Overturning Circulation." *Nature Communications* 12, no. 1 (1 2021): 3002. ISSN: 2041-1723. https://doi.org/10.1038/s41467-021-23350-2. https://www.nature.com/articles/s41467-021-23350-2.

Li, F., M. S. Lozier, G. Danabasoglu, N. P. Holliday, Y.-O. Kwon, A. Romanou, S. G. Yeager, and R. Zhang. 2019. "Local and Downstream Relationships between Labrador Sea Water Volume and North Atlantic Meridional Overturning Circulation Variability." *Journal of Climate* 32, no. 13 (July 1, 2019): 3883–3898. ISSN: 0894-8755, 1520-0442. https://doi.org/10.1175/JCLI-D-18-0735.1. https://journals.ametsoc.org/jcli/article/32/13/3883/343947/Local-and-Downstream-Relationships-between.

Li, F., M. S. Lozier, and W. Johns. 2017. "Calculating the Meridional Volume, Heat, and Freshwater Transports from an Observing System in the Subpolar North Atlantic: Observing System Simulation Experiment." *Journal of Atmospheric and Oceanic Technology* 34, no. 7 (July 1, 2017): 1483–1500. ISSN: 0739-0572, 1520-0426. https://doi.org/10.1175/JTECH-D-16-0247.1. https://journals.ametsoc.org/view/journals/atot/34/7/jtech-d-16-0247.1.xml.

Lindzen, R. S., and M. Fox-Rabinovitz. 1989. "Consistent Vertical and Horizontal Resolution." *Monthly Weather Review* 117, no. 11 (November 1, 1989): 2575–2583. ISSN: 1520-0493, 0027-0644. https://doi.org/10.1175/1520-0493(1989)117<2575:CVAHR>2.0.CO;2. https://journals.ametsoc.org/view/journals/mwre/117/11/1520-0493_1989_117_2575_cvahr_2_0_co_2.xml.

Little, C. M., A. Hu, C. W. Hughes, G. D. McCarthy, C. G. Piecuch, R. M. Ponte, and M. D. Thomas. 2019. "The Relationship Between U.S. East Coast Sea Level and the Atlantic Meridional Overturning Circulation: A Review." *Journal of Geophysical Research: Oceans* 124 (9): 6435–6458. ISSN: 2169-9291. https://doi.org/10.1029/2019JC015152. https://agupubs.onlinelibrary.wiley.com/doi/abs/10.1029/2019JC015152.

Lozier, M. S., S. Bacon, A. S. Bower, et al. 2017. "Overturning in the Subpolar North Atlantic Program: A New International Ocean Observing System." *Bulletin of the American Meteorological Society* 98, no. 4 (April 1, 2017): 737–752. ISSN: 0003-0007. https://doi.org/10.1175/BAMS-D-16-0057.1. https://journals.ametsoc.org/bams/article/98/4/737/216042/Overturning-in-the-Subpolar-North-Atlantic-Program.

Lozier, M. S., A. S. Bower, H. H. Furey, K. L. Drouin, X. Xu, and S. Zou. 2022. "Overflow Water Pathways in the North Atlantic." *Progress in Oceanography* 208 (November 1, 2022): 102874. ISSN: 0079-6611. https://doi.org/10.1016/j.pocean.2022.102874. https://www.sciencedirect.com/science/article/pii/S0079661122001331.

Lozier, M. S., S. F. Gary, and A. S. Bower. 2013. "Simulated Pathways of the Overflow Waters in the North Atlantic: Subpolar to Subtropical Export." *Deep Sea Research Part II: Topical Studies in Oceanography,* Modern Physical Oceanography and Professor H.T. Rossby, 85 (January 1, 2013): 147–153. ISSN: 0967-0645. https://doi.org/10.1016/j.dsr2.2012.07.037. http://www.sciencedirect.com/science/article/pii/S0967064512001233.

Lozier, M. S., F. Li, S. Bacon, et al. 2019. "A Sea Change in Our View of Overturning in the Subpolar North Atlantic." *Science* 363, no. 6426 (February 1, 2019): 516–521. ISSN: 0036-8075, 1095-9203. https://doi.org/10.1126/science.aau6592. https://www.sciencemag.org/lookup/doi/10.1126/science.aau6592.

MacGilchrist, G. A., H. L. Johnson, D. P. Marshall, C. Lique, M. Thomas, L. C. Jackson, and R. A. Wood. 2020. "Locations and Mechanisms of Ocean Ventilation in the High-Latitude North Atlantic in an Eddy-Permitting Ocean Model." *Journal of Climate* 33, no. 23 (December 1, 2020): 10113–10131. ISSN: 0894-8755, 1520-0442. https://doi.org/10.1175/JCLI-D-20-0191.1. https://journals.ametsoc.org/view/journals/clim/33/23/jcliD200191.xml.

Maddison, J. R., D. P. Marshall, and J. Shipton. 2015. "On the Dynamical Influence of Ocean Eddy Potential Vorticity Fluxes." *Ocean Modelling* 92 (August 1, 2015): 169–182. ISSN: 1463-5003. https://doi.org/10.1016/j.ocemod.2015.06.003. https://www.sciencedirect.com/science/article/pii/S146350031500102X.

Marshall, D. P., and H. R. Pillar. 2011. "Momentum Balance of the Wind-Driven and Meridional Overturning Circulation." *Journal of Physical Oceanography* 41, no. 5 (May 1, 2011): 960–978. ISSN: 0022-3670, 1520-0485. https://doi.org/10.1175/2011JPO4528.1. https://journals.ametsoc.org/view/journals/phoc/41/5/2011jpo4528.1.xml.

Marshall, J., A. Adcroft, J.-M. Campin, C. Hill, and A. White. 2004. "Atmosphere–Ocean Modeling Exploiting Fluid Isomorphisms." *Monthly Weather Review* 132, no. 12 (December 1, 2004): 2882–2894. ISSN: 1520-0493, 0027-0644. https://doi.org/10.1175/MWR2835.1. https://journals.ametsoc.org/view/journals/mwre/132/12/mwr2835.1.xml.

Marshall, J., A. Adcroft, C. Hill, L. Perelman, and C. Heisey. 1997. "A Finite-Volume, Incompressible Navier Stokes Model for Studies of the Ocean on Parallel Computers." *Journal of Geophysical Research: Oceans* 102 (C3): 5753–5766. ISSN: 2156-2202. https://doi.org/10.1029/96JC02775. https://agupubs.onlinelibrary.wiley.com/doi/abs/10.1029/96JC02775.

Marshall, J., A. Donohoe, D. Ferreira, and D. McGee. 2013. "The Ocean's Role in Setting the Mean Position of the Inter-Tropical Convergence Zone." *Climate Dynamics* (May). ISSN: 0930-7575. https://dspace.mit.edu/handle/1721.1/85592.

Marshall, J., and F. Schott. 1999. "Open-Ocean Convection: Observations, Theory, and Models." *Reviews of Geophysics* 37 (1): 1–64. ISSN: 1944-9208. https://doi.org/10.1029/98RG02739. https://agupubs.onlinelibrary.wiley.com/doi/abs/10.1029/98RG02739.

Marshall, J., and K. Speer. 2012. "Closure of the Meridional Overturning Circulation through Southern Ocean Upwelling." *Nature Geoscience* 5, no. 3 (3): 171–180. ISSN: 1752-0908. https://doi.org/10.1038/ngeo1391. https://www.nature.com/articles/ngeo1391.

Marzocchi, A., J. Hirschi, N. Holliday, S. Cunningham, A. Blaker, and A. Coward. 2014. "The North Atlantic Subpolar Circulation in an Eddy-Resolving Global Ocean Model." *Journal of Marine Systems* (October 30, 2014): 2818. https://doi.org/10.1016/j.jmarsys.2014.10.007.

McCarthy, G., P. J. Brown, C. N. Flagg, et al. 2020. "Sustainable Observations of the AMOC: Methodology and Technology." *Reviews of Geophysics* 58 (1): e2019RG000654. ISSN: 1944-9208. https://doi.org/10.1029/2019RG000654. https://agupubs.onlinelibrary.wiley.com/doi/abs/10.1029/2019RG000654.

McCarthy, G. D., D. A. Smeed, W. E. Johns, E. Frajka-Williams, B. I. Moat, D. Rayner, M. O. Baringer, C. S. Meinen, J. Collins, and H. L. Bryden. 2015. "Measuring the Atlantic Meridional Overturning Circulation at 26°N." *Progress in Oceanography* 130 (January 1, 2015): 91–111. ISSN: 0079-6611. https://doi.org/10.1016/j.pocean.2014.10.006. https://www.sciencedirect.com/science/article/pii/S0079661114001694.

McKinley, G. A., A. R. Fay, N. S. Lovenduski, and D. J. Pilcher. 2017. "Natural Variability and Anthropogenic Trends in the Ocean Carbon Sink." *Annual Review of Marine Science* 9, no. 1 (January 3, 2017): 125–150. ISSN: 1941-1405, 1941-0611. https://doi.org/10.1146/annurev-marine-010816-060529. http://www.annualreviews.org/doi/10.1146/annurev-marine-010816-060529.

McWilliams, J. C. 2000. "Chapter 14 - Formulation of Oceanic General Circulation Models." In *International Geophysics,* edited by D. A. Randall, 70:421–456. General Circulation Model Development. Academic Press, January 1, 2000. https://doi.org/10.1016/S0074-6142(00)80062-5. https://www.sciencedirect.com/science/article/pii/S0074614200800625.

Menary, M. B., L. Hermanson, and N. J. Dunstone. 2016. "The Impact of Labrador Sea Temperature and Salinity Variability on Density and the Subpolar AMOC in a Decadal Prediction System." *Geophysical Research Letters* 43 (23): 12, 217–12, 227. ISSN: 1944-8007. https://doi.org/10.1002/2016GL070906. https://agupubs.onlinelibrary.wiley.com/doi/abs/10.1002/2016GL070906.

Menary, M. B., L. C. Jackson, and M. S. Lozier. 2020. "Reconciling the Relationship Between the AMOC and Labrador Sea in OSNAP Observations and Climate Models." *Geophysical Research Letters* 47 (18): e2020GL089793. ISSN: 1944-8007. https://doi.org/10.1029/2020GL089793. https://agupubs.onlinelibrary.wiley.com/doi/abs/10.1029/2020GL089793.

Mertz, G., and D. G. Wright. 1992. "Interpretations of the JEBAR Term." *Journal of Physical Oceanography* 22, no. 3 (March 1, 1992): 301–305. ISSN: 0022-3670, 1520-0485. https://doi.org/10.1175/1520-0485(1992)022<0301:IOTJT>2.0.CO;2. https://journals.ametsoc.org/view/journals/phoc/22/3/1520-0485_1992_022_0301_iotjt_2_0_co_2.xml.

Monin, A., and A. Obukhov. 1954. "Basic Laws of Turbulent Mixing in the Atmosphere near the Ground." *Trudy geofiz. inst. AN SSSR* 24 (151): 163–187.

Munk, W. H. 1950. "On the Wind-Driven Ocean Circulation." *Journal of Meteorology* 7, no. 2 (April 1, 1950): 80–93. ISSN: 0095-9634. https://doi.org/10.1175/1520-0469(1950)007<0080:OTWDOC>2.0.CO;2. https://journals.ametsoc.org/jas/article/7/2/80/37839/ON-THE-WIND-DRIVEN-OCEAN-CIRCULATION.

Pedlosky, J. 1987. *Geophysical Fluid Dynamics*. New York, NY: Springer New York. ISBN: 978-1-4612-4650-3. https://doi.org/10.1007/978-1-4612-4650-3. http://link.springer.com/10.1007/978-1-4612-4650-3.

———. 2003. "Thermally Driven Circulations in Small Oceanic Basins." *Journal of Physical Oceanography* 33, no. 11 (November 1, 2003): 2333–2340. ISSN: 0022-3670, 1520-0485. https://doi.org/10.1175/1520-0485(2003)033<2333:TDCISO>2.0.CO;2. https://journals.ametsoc.org/view/journals/phoc/33/11/1520-0485_2003_033_2333_tdciso_2.0.co_2.xml.

Petit, T., M. S. Lozier, S. A. Josey, and S. A. Cunningham. 2020. "Atlantic Deep Water Formation Occurs Primarily in the Iceland Basin and Irminger Sea by Local Buoyancy Forcing." *Geophysical Research Letters* 47 (22): e2020GL091028. ISSN: 1944-8007. https://doi.org/10.1029/2020GL091028. https://agupubs.onlinelibrary.wiley.com/doi/abs/10.1029/2020GL091028.

———. 2021. "Role of Air–Sea Fluxes and Ocean Surface Density in the Production of Deep Waters in the Eastern Subpolar Gyre of the North Atlantic." *Ocean Science* 17, no. 5 (October 5, 2021): 1353–1365. ISSN: 1812-0784. https://doi.org/10.5194/os-17-1353-2021. https://os.copernicus.org/articles/17/1353/2021/.

Pickart, R. S., M. A. Spall, M. H. Ribergaard, G. W. K. Moore, and R. F. Milliff. 2003. "Deep Convection in the Irminger Sea Forced by the Greenland Tip Jet." *Nature* 424, no. 6945 (6945): 152–156. ISSN: 1476-4687. https://doi.org/10.1038/nature01729. https://www.nature.com/articles/nature01729.

Pillar, H. 2013. "Sensitivity of the Atlantic Meridional Overturning Circulation to Surface Forcing," Oxford University, UK. https://ora.ox.ac.uk/objects/uuid:42366dc7-e699-4349-95d2-89a97033d957.

Pillar, H. R., P. Heimbach, H. L. Johnson, and D. P. Marshall. 2016. "Dynamical Attribution of Recent Variability in Atlantic Overturning." *Journal of Climate* 29, no. 9 (May 1, 2016): 3339–3352. ISSN: 0894-8755, 1520-0442. https://doi.org/10.1175/JCLI-D-15-0727.1. https://journals.ametsoc.org/jcli/article/29/9/3339/342694/Dynamical-Attribution-of-Recent-Variability-in.

Quadfasel, D., and R. Käse. 2007. "Present-Day Manifestation of the Nordic Seas Overflows." In *Ocean Circulation: Mechanisms and Impacts, Geophys. Monogr. Ser.* 173:75–89. January 1, 2007. ISBN: 978-0-87590-438-2. https://doi.org/10.1029/173GM07.

Rayner, D., and T. Kanzow. 2011. "The Design Strategy and Methodology of the RAPID-MOC Project Moorings." *Underwater Technology* 29 (March 1, 2011): 159–171. https://doi.org/10.3723/ut.29.159.

Redi, M. H. 1982. "Oceanic Isopycnal Mixing by Coordinate Rotation." *Journal of Physical Oceanography* 12, no. 10 (10): 1154–1158. ISSN: 15200485. https://www.mendeley.com/catalogue/ccdc81e4-916d-3a85-bf0a-864907087456/.

Rhein, M., D. Kieke, and R. Steinfeldt. 2015. "Advection of North Atlantic Deep Water from the Labrador Sea to the Southern Hemisphere." *Journal of Geophysical Research: Oceans* 120 (4): 2471–2487. ISSN: 2169-9291. https://doi.org/10.1002/2014JC010605. https://agupubs.onlinelibrary.wiley.com/doi/abs/10.1002/2014JC010605.

Roberts, C. D., F. K. Garry, and L. C. Jackson. 2013. "A Multimodel Study of Sea Surface Temperature and Subsurface Density Fingerprints of the Atlantic Meridional Overturning Circulation." *Journal of Climate* 26, no. 22 (November 15, 2013): 9155–9174. ISSN: 0894-8755, 1520-0442. https://doi.org/10.1175/JCLI-D-12-00762.1. https://journals.ametsoc.org/view/journals/clim/26/22/jcli-d-12-00762.1.xml.

Robson, J., P. Ortega, and R. Sutton. 2016. "A Reversal of Climatic Trends in the North Atlantic since 2005." *Nature Geoscience* 9, no. 7 (7): 513–517. ISSN: 1752-0908. https://doi.org/10.1038/ngeo2727. https://www.nature.com/articles/ngeo2727.

Sarkisyan, A. S. 2006. "Forty Years of JEBAR—the Finding of the Joint Effect of Baroclinicity and Bottom Relief for the Modeling of Ocean Climatic Characteristics." *Izvestiya, Atmospheric and Oceanic Physics* 42, no. 5 (October 1, 2006): 534–554. ISSN: 1555-628X. https://doi.org/10.1134/S0001433806050021. https://doi.org/10.1134/S0001433806050021.

Sarkisyan, A., and V. Ivanov. 1971. "Joint Effect of Baroclinicity and Bottom Relief as an Important Factor in the Dynamics of Sea Currents." *Izv. Acad. Sci. USSR, Atmos. Ocean. Phys.* 7 (January 1, 1971): 116–124.

Schloesser, F., R. Furue, J. P. McCreary, and A. Timmermann. 2012. "Dynamics of the Atlantic Meridional Overturning Circulation. Part 1: Buoyancy-forced Response." *Progress in Oceanography* 101, no. 1 (August): 33–62. ISSN: 00796611. https://doi.org/10.1016/j.pocean.2012.01.002. https://linkinghub.elsevier.com/retrieve/pii/S0079661112000031.

———. 2014. "Dynamics of the Atlantic Meridional Overturning Circulation. Part 2: Forcing by Winds and Buoyancy." *Progress in Oceanography* 120 (January): 154–176. ISSN: 00796611. https://doi.org/10.1016/j.pocean.2013.08.007. https://linkinghub.elsevier.com/retrieve/pii/S0079661113001675.

Schoonover, J., W. Dewar, N. Wienders, J. Gula, J. C. McWilliams, M. J. Molemaker, S. C. Bates, G. Danabasoglu, and S. Yeager. 2016. "North Atlantic Barotropic Vorticity Balances in Numerical Models." *Journal of Physical Oceanography* 46, no. 1 (January 1, 2016): 289–303. ISSN: 0022-3670, 1520-0485. https://doi.org/10.1175/JPO-D-15-0133.1. https://journals.ametsoc.org/view/journals/phoc/46/1/jpo-d-15-0133.1.xml.

Send, U., and J. Marshall. 1995. "Integral Effects of Deep Convection." *Journal of Physical Oceanography* 25, no. 5 (May 1, 1995): 855–872. ISSN: 0022-3670. https://doi.org/10.1175/1520-0485(1995)025<0855:IEODC>2.0.CO;2. https://journals.ametsoc.org/jpo/article/25/5/855/8798/Integral-Effects-of-Deep-Convection.

Sime, L. C., D. P. Stevens, K. J. Heywood, and K. I. C. Oliver. 2006. "A Decomposition of the Atlantic Meridional Overturning." *Journal of Physical Oceanography* 36, no. 12 (December 1, 2006): 2253–2270. ISSN: 0022-3670, 1520-0485. https://doi.org/10.1175/JPO2974.1. https://journals.ametsoc.org/view/journals/phoc/36/12/jpo2974.1.xml.

Smeed, D. A., S. A. Josey, C. Beaulieu, et al. 2018. "The North Atlantic Ocean Is in a State of Reduced Overturning." *Geophysical Research Letters* 45 (3): 1527–1533. ISSN: 1944-8007. https://doi.org/10.1002/2017GL076350. https://agupubs.onlinelibrary.wiley.com/doi/abs/10.1002/2017GL076350.

Smyth, W. D., J. N. Moum, and D. R. Caldwell. 2001. "The Efficiency of Mixing in Turbulent Patches: Inferences from Direct Simulations and Microstructure Observations." *Journal of Physical Oceanography* 31, no. 8 (August 1, 2001): 1969–1992. ISSN: 0022-3670, 1520-0485. https://doi.org/10.1175/1520-0485(2001)031<1969:TEOMIT>2.0.CO;2. https://journals.ametsoc.org/view/journals/phoc/31/8/1520-0485_2001_031_1969_teomit_2.0.co_2.xml.

Spall, M. A. 2003. "On the Thermohaline Circulation in Flat Bottom Marginal Seas." *Journal of Marine Research* 61 (January 1, 2003): 1–25. https://doi.org/10.1357/002224003321586390.

———. 2004. "Boundary Currents and Watermass Transformation in Marginal Seas." *Journal of Physical Oceanography* 34 (January 1, 2004): 17.

Spall, M. A., and R. S. Pickart. 2001. "Where Does Dense Water Sink? A Subpolar Gyre Example." *Journal of Physical Oceanography* 31:17.

Spall, M. A. 2015. "Thermally Forced Transients in the Thermohaline Circulation." *Journal of Physical Oceanography* 45, no. 11 (November 1, 2015): 2820–2835. ISSN: 0022-3670, 1520-0485. https://doi.org/10.1175/JPO-D-15-0101.1. https://journals.ametsoc.org/jpo/article/45/11/2820/12392/Thermally-Forced-Transients-in-the-Thermohaline.

Srokosz, M. A., and H. L. Bryden. 2015. "Observing the Atlantic Meridional Overturning Circulation Yields a Decade of Inevitable Surprises." *Science* 348, no. 6241 (June 19, 2015): 1255575–1255575. ISSN: 0036-8075, 1095-9203. https://doi.org/10.1126/science.1255575. https://www.sciencemag.org/lookup/doi/10.1126/science.1255575.

Stommel, H. 1948. "The Westward Intensification of Wind-Driven Ocean Currents." *Eos, Transactions American Geophysical Union* 29 (2): 202–206. ISSN: 2324-9250. https://doi.org/10.1029/TR029i002p00202. https://onlinelibrary.wiley.com/doi/abs/10.1029/TR029i002p00202.

Straneo, F. 2006. "On the Connection between Dense Water Formation, Overturning, and Poleward Heat Transport in a Convective Basin*." *Journal of Physical Oceanography* 36, no. 9 (September 1, 2006): 1822–1840. ISSN: 1520-0485, 0022-3670. https://doi.org/10.1175/JPO2932.1. https://journals.ametsoc.org/jpo/article/36/9/1822/10606/On-the-Connection-between-Dense-Water-Formation.

Takahashi, T., S. C. Sutherland, R. Wanninkhof, et al. 2009. "Climatological Mean and Decadal Change in Surface Ocean pCO2, and Net Sea–Air CO2 Flux over the Global Oceans." *Deep Sea Research Part II: Topical Studies in Oceanography* 56, nos. 8-10 (April): 554–577. ISSN: 09670645. https://doi.org/10.1016/j.dsr2.2008.12.009. https://linkinghub.elsevier.com/retrieve/pii/S0967064508004311.

Talley, L. 2013. "Closure of the Global Overturning Circulation Through the Indian, Pacific, and Southern Oceans: Schematics and Transports." *Oceanography* 26, no. 1 (March 1, 2013): 80–97. ISSN: 10428275. https://doi.org/10.5670/oceanog.2013.07. https://tos.org/oceanography/article/closure-of-the-global-overturning-circulation-through-the-indian-pacific-an.

Vallis, G. 2006. *Atmospheric and Oceanic Fluid Dynamics.* January 1, 2006. https://doi.org/10.2277/0521849691.

Veronis, G. 1975. "The Role of Models in Tracer Studies." In *Numerical Models of Ocean Circulation,* 133–146. A Symposium Held at Durham, New Hampshire, October 17-20, 1972. National Academy of Sciences. https://cir.nii.ac.jp/crid/1571698599536228480.

Waldman, R., J. Hirschi, A. Voldoire, C. Cassou, and R. Msadek. 2021. "Clarifying the Relation between AMOC and Thermal Wind: Application to the Centennial Variability in a Coupled Climate Model." *Journal of Physical Oceanography* 51, no. 2 (February 1, 2021): 343–364. ISSN: 0022-3670, 1520-0485. https://doi.org/10.1175/JPO-D-19-0284.1. https://journals.ametsoc.org/view/journals/phoc/51/2/jpo-d-19-0284.1.xml.

Wang, C., L. Zhang, S.-K. Lee, L. Wu, and C. R. Mechoso. 2014. "A Global Perspective on CMIP5 Climate Model Biases." *Nature Climate Change* 4, no. 3 (3): 201–205. ISSN: 1758-6798. https://doi.org/10.1038/nclimate2118. https://www.nature.com/articles/nclimate2118.

Watson, A. J., N. Metzl, and U. Schuster. 2011. "Monitoring and Interpreting the Ocean Uptake of Atmospheric CO2." *Philosophical Transactions of the Royal Society A: Mathematical, Physical and Engineering Sciences* 369, no. 1943 (May 28, 2011): 1997–2008. https://doi.org/10.1098/rsta.2011.0060. https://royalsocietypublishing.org/doi/full/10.1098/rsta.2011.0060.

Yan, X., R. Zhang, and T. R. Knutson. 2017. "The Role of Atlantic Overturning Circulation in the Recent Decline of Atlantic Major Hurricane Frequency." *Nature Communications* 8, no. 1 (1 2017): 1695. ISSN: 2041-1723. https://doi.org/10.1038/s41467-017-01377-8. https://www.nature.com/articles/s41467-017-01377-8.

Yeager, S. 2015. "Topographic Coupling of the Atlantic Overturning and Gyre Circulations." *Journal of Physical Oceanography* 45, no. 5 (May 1, 2015): 1258–1284. ISSN: 0022-3670, 1520-0485. https://doi.org/10.1175/JPO-D-14-0100.1. https://journals.ametsoc.org/view/journals/phoc/45/5/jpo-d-14-0100.1.xml.

Yeung, P. K., X. M. Zhai, and K. R. Sreenivasan. 2015. "Extreme Events in Computational Turbulence." *Proceedings of the National Academy of Sciences* 112, no. 41 (October 13, 2015): 12633–12638. https://doi.org/10.1073/pnas.1517368112. https://www.pnas.org/doi/10.1073/pnas.1517368112.

Young, W. R. 1981. "The Vertical Structure of the Wind-Driven Circulation," Massachusetts Institute of Technology and Woods Hole Oceanographic Institution, August. https://doi.org/10.1575/1912/2469. https://darchive.mblwhoilibrary.org/handle/1912/2469.

———. 2012. "An Exact Thickness-Weighted Average Formulation of the Boussinesq Equations." *Journal of Physical Oceanography* 42, no. 5 (May 1, 2012): 692–707. ISSN: 0022-3670. https://doi.org/10.1175/JPO-D-11-0102.1. https://journals.ametsoc.org/jpo/article/42/5/692/11455/An-Exact-Thickness-Weighted-Average-Formulation-of.

Zhang, R., R. Sutton, G. Danabasoglu, Y.-O. Kwon, R. Marsh, S. G. Yeager, D. E. Amrhein, and C. M. Little. 2019. "A Review of the Role of the Atlantic Meridional Overturning Circulation in Atlantic Multidecadal Variability and Associated Climate Impacts." *Reviews of Geophysics* 57 (2): 316–375. ISSN: 1944-9208. https://doi.org/10.1029/2019RG000644. https://agupubs.onlinelibrary.wiley.com/doi/abs/10.1029/2019RG000644.

Zhang, R., and M. Thomas. 2021. "Horizontal Circulation across Density Surfaces Contributes Substantially to the Long-Term Mean Northern Atlantic Meridional Overturning Circulation." *Communications Earth & Environment* 2, no. 1 (1 2021): 1–12. ISSN: 2662-4435. https://doi.org/10.1038/s43247-021-00182-y. https://www.nature.com/articles/s43247-021-00182-y.

Zhao, J., and W. Johns. 2014. "Wind-Forced Interannual Variability of the Atlantic Meridional Overturning Circulation at 26.5°N." *Journal of Geophysical Research: Oceans* 119 (4): 2403–2419. ISSN: 2169-9291. https://doi.org/10.1002/2013JC009407. https://agupubs.onlinelibrary.wiley.com/doi/abs/10.1002/2013JC009407.

Zou, S., M. S. Lozier, F. Li, R. Abernathey, and L. Jackson. 2020. "Density-Compensated Overturning in the Labrador Sea." *Nature Geoscience* 13, no. 2 (2): 121–126. ISSN: 1752-0908. https://doi.org/10.1038/s41561-019-0517-1. https://www.nature.com/articles/s41561-019-0517-1.